

**Exploring weak $n \rightarrow \pi^*$ non-covalent Interaction: Gas
Phase Spectroscopy and Quantum Chemical Calculations**

**A thesis
submitted in partial fulfillment of the requirements
of the degree of
Doctor of Philosophy**

By

Santosh Kumar Singh

ID No. 20112008



INDIAN INSTITUTE OF SCIENCE EDUCATION AND RESEARCH PUNE

(2018)

Dedicated to
My parents



INDIAN INSTITUTE OF SCIENCE EDUCATION AND RESEARCH
(An Autonomous Institution, Ministry of Human Resource Development, Govt. of India)
Dr. Homi Bhabha Road, Pashan Pune – 411008

Declaration

I declare that this written submission represents my ideas in my own words and wherever other's ideas have been included; I have adequately cited and referenced the original sources. I also declare that I have adhered to all principles of academic honesty and integrity and have not misrepresented, fabricated or falsified any ideas/data/fact/sources in my submission. I understand that violation of the above will cause disciplinary action by the Institute and can also evoke penal action from the sources which have thus not been properly cited or from whom proper permission has not been taken when needed.

A handwritten signature in blue ink that reads "Ssingh".

Date: 14/03/2018

Mr. Santosh Kumar Singh

20112008



INDIAN INSTITUTE OF SCIENCE EDUCATION AND RESEARCH
(An Autonomous Institution, Ministry of Human Resource Development, Govt. of
India)

Dr. Homi Bhabha Road, Pashan Pune – 411008

Certificate

Certified that the work incorporated in this thesis entitled “Exploring weak $n \rightarrow \pi^*$ non-covalent Interaction: Gas Phase Spectroscopy and Quantum Chemical Calculations” submitted by Mr. Santosh Kumar Singh represents his original work which was carried out by him at IISER, Pune under my guidance and supervision during the period from 2013 to 2018. The work presented here or any part of it has not been included in any other thesis submitted previously for the award of any degree or diploma from any other University or Institution. I further certify that the above statements made by him in regard to his thesis are correct to the best of my knowledge.

Date: 14/03/2018

A handwritten signature in red ink that reads "Alok Das".

Dr. Alok Das

(Research Supervisor)

Acknowledgements

Firstly, I would like to express my sincere gratitude to my research supervisor Dr. Alope Das for his careful guidance, constant encouragement, inspiration and indispensable suggestions during the course of my Ph. D. research. His expertise and continuous effort in the work has helped me to successfully achieve the research goals. The journey of my Ph. D would not be easy without his help and diligent participation. I would like to thank him for his immense efforts to train me to become a good researcher and develop my skills in the experiments. Apart from helping me to develop my research skills he has also helped me to improve my writing and speaking skills. His teaching on delivering good presentation has helped me to win several prizes in the conferences. All of my learning from him will assist me in future to become an independent researcher.

It's my great pleasure to thank my research advisory committee members Dr. Sayan Bagchi and Dr. Partha Hazra for their fruitful discussions and suggestions to improve our results. I would also like to thank Dr. Anirban Hazra for giving us valuable suggestions to understand our experimental results.

My research work would have been incomplete without the help from the collaborators. I express my sincere thanks to my collaborators Dr. Gary Breton, Dr. Sayan Bagchi, Prof. K. N. Ganesh, Pranab Deb and Shahaji More for working with us.

It is difficult to express my sincere thanks to former group members of the lab, Dr. Sumit Kumar and Jamuna Vaishnav, in words. They have helped me a lot in performing the experiments and it was a great pleasure to work with them. I thank Dr. Sumit Kumar for teaching and assisting me during the experiments. Without his help it would have not been

possible for me to learn all the computational and experimental aspects of the work in a short time. I am grateful to my juniors Kamal Kr. Mishra, Satish Kumar, Kshetrimayum Borish, Surajit Metya, and Prakash Panwaria for assisting me in my work. I deeply thank them for helping me in preparing my thesis.

I am thankful to my friends Aamod and Anindita for their support and lively company.

I wish to express my thanks to Prof K. N. Ganesh, former Director of IISER Pune for providing high quality research environment. I thank IISER, Pune for my JRF and SRF fellowship. I wish to acknowledge all the staff members of the chemistry department for their help.

I want to express my sincere respect to my parents and my sister for their constant support during my research period. It would have been impossible for me to achieve my goal without their blessings.

Santosh Kumar Singh

Contents

List of Abbreviations	v
List of Figures	vii
List of Tables	xix
Synopsis	xxiii
List of Publications	xxxi
Chapter 1: Introduction	
1.1 Non-covalent interactions	3
1.2 The $n \rightarrow \pi^*$ interaction	5
1.2.1 Classification of $n \rightarrow \pi^*$ interaction	6
1.3 Signature of $n \rightarrow \pi^*$ interaction in biomolecules	7
1.3.1 $n \rightarrow \pi^*$ interaction in nucleic acids	7
1.3.2 $n \rightarrow \pi^*$ interaction in proteins	10
1.3.2.1 $n \rightarrow \pi^*$ interaction in the backbone of proteins	10
1.3.2.2. $n \rightarrow \pi^*$ interaction involving side chains of proteins	12
1.3.2.3 Co-operativity between hydrogen bonding and $n \rightarrow \pi^*$ interaction in proteins	14
1.4 Signature of $n \rightarrow \pi^*$ interaction in materials	16
1.4.1 $n \rightarrow \pi^*$ interaction in supramolecular structures	16
1.4.2 $n \rightarrow \pi^*$ interaction in polymers	19
1.5 Significance of $n \rightarrow \pi^*$ interaction in small molecules	19
1.6 Understanding $n \rightarrow \pi^*$ interaction through NMR spectroscopy	23
1.7 Physical nature of $n \rightarrow \pi^*$ interaction	26
1.7.1 $n \rightarrow \pi_{Am}^*$ interaction	26
1.7.2 $n \rightarrow \pi_{Ar}^*$ interaction	28
1.8 Aim of the thesis	29
Chapter 2: Experimental and Computational Methods	
2.1 Experimental methods	37
2.1.1 Supersonic jet expansion	37
2.1.2. Resonance enhanced multi-photon ionization and time of flight mass spectrometry	40
2.1.2.1 REMPI	41

2.1.2.2 Time of Flight mass spectrometry	42
2.1.3. Laser systems used for the experiments	46
2.1.3.1 Dye laser	46
2.1.3.2 UV Tracker (UVT)	48
2.1.3.3 IR OPO/OPA	50
2.1.4. Experimental set-up	53
2.1.5. Experimental Scheme	56
2.1.6. Spectroscopic Techniques	59
2.1.6.1 1C-R2PI spectroscopy	59
2.1.6.2 Resonant ion-dip infrared spectroscopy (RIDIRS)	59
2.1.6.3 IR-UV double resonance spectroscopy	60
2.1.6.4 UV-UV double resonance spectroscopy	61
2.2 Computational Methods	62
2.2.1 Geometry optimization and Frequency calculation	62
2.2.2 Energy decomposition analysis	63
2.2.3. Natural Bond Orbital analysis	63
Chapter 3: Interplay between hydrogen bonding and $n \rightarrow \pi^*$ interaction	
3.1 Introduction	69
3.2 Results and Discussion	72
3.2.1 Structures of complexes of 7-azaindole and fluorosubstituted pyridines	72
Computational studies	
3.2.2 Co-operativity between hydrogen bonding and $n \rightarrow \pi^*$ interaction	75
3.2.3 7-AI...fluorosubstituted pyridine complexes: Experimental studies	80
3.2.3.1 Time of Flight (TOF) mass spectra of the complexes	81
3.2.3.2 Electronic Spectra of 7-AI...2,6-FP and 7-AI...2,3,5,6-FP complexes	82
3.2.3.3 IR spectra of 7-AI...2,6-FP and 7-AI...2,3,5,6-FP complexes	87
3.2.3.4. IR-UV hole-burning spectra of 7-AI...2,6-FP and 7-AI...2,3,5,6-FP complexes	91
3.2.4 Strength of N-H...N hydrogen bonding and $n \rightarrow \pi^*$ interaction	91
3.2.5 Origin of $n \rightarrow \pi_{Ar}^*$ interaction	93
3.3 Conclusion	95
Chapter 4: Gas phase IR spectroscopic evidence for an $n \rightarrow \pi^*$ interaction	

4.1	Introduction	101
4.2	Results and Discussion	102
4.2.1	Conformers of phenyl formate: Electronic spectroscopy and ab initio calculations	102
4.2.2	Gas phase IR spectroscopy: Evidence for the $n \rightarrow \pi^*$ interaction	108
4.2.3	$n \rightarrow \pi^*$ interaction and C=O stretching frequency: NBO analysis	110
4.3	Conclusion	119
Chapter 5: Gas Phase IR spectroscopic signature for C=O...C=O $n \rightarrow \pi^*$ interaction in Cbz-(4R)-Hyp-OMe, a key amino acid residue of collagen		
5.1	Introduction	123
5.2	Results and Discussion	127
5.2.1	Conformations of Cbz-Hyp-OMe: Electronic Spectroscopy	127
5.2.2	Conformational landscape of Cbz-Hyp-OMe: DFT calculations	129
5.2.3	Structures of the observed conformers of Cbz-Hyp-OMe: IR spectroscopy	136
5.2.4	NBO analysis: $n \rightarrow \pi^*$ interaction vs C=O stretching frequency	139
5.3	Conclusion	147
Chapter 6: $n \rightarrow \pi^*$ interaction governs the conformational preference of salicin		
6.1	Introduction	151
6.2	Results and Discussion	153
6.2.1	Conformations of salicin: Electronic spectroscopy	153
6.2.2	Conformational landscape of salicin: DFT calculations	156
6.2.3	Structures of observed conformers of salicin: IR spectroscopy	160
6.2.4	Franck-Condon simulated electronic spectra	164
6.2.5	Conformational preference in salicin: $n \rightarrow \pi^*$ interaction	167
6.2.6	Biological perspective	174
6.3	Conclusion	176
Chapter 7: Summary and future direction		181
Bibliography		187

List of Abbreviations

1C-R2PI	One color resonantly enhanced two-photon ionization
2C-R2PI	Two color resonantly enhanced two-photon ionization
Ar	Argon gas
aVDZ	aug-cc-pVDZ
BSSE	Basis set superposition error
DFT	Density functional theory
disp	Dispersion
EDA	Energy Decomposition Analysis
Es	Electrostatics
Ex	Exchange
IP	Ionization potential
LMO	Localized molecular orbital
MP2	2 nd order Moller-Plesset Perturbation Theory
NBO	Natural bond orbital
Pol	Polarization
Rep	Repulsion
RIDIRS	Resonant ion dip infrared spectroscopy
ZPE	Zero point energy
ΔE_e	BSSE corrected Binding Energy
ΔE_0	BSSE+ZPE corrected Binding Energy
PDB	Protein data bank
CSD	Cambridge structural database
Phe	Phenylalanine
Glu	Glutamic acid
Asp	Aspartic acid
Pro	Proline
Hyp	Hydroxyproline
Gly	Glycine

List of Figures

- Figure 1.1** (a) Example of $n \rightarrow \pi_{Am}^*$ Am (amide) interaction. Angles ω , ψ , θ are the Ramachandran angles. (b) Burgi-Dunitz trajectory for favourable $n \rightarrow \pi_{Am}^*$ interaction. Adapted in part with permission from ref. 61. Copyright [2014] American Chemical Society. (c) Example of $n \rightarrow \pi_{Ar}^*$ Ar (aromatic) interaction. Adapted in part with permission from ref. 3. Copyright [2007] American Chemical Society. 5
- Figure 1.2** NBO view of (a) Overlap of lone pair orbital (n) of nitrogen with σ^* antibonding orbital of the N-H bond in N-H...N hydrogen bonding interaction. (b) Overlap of lone pair orbital of nitrogen with π^* antibonding orbital of the aromatic ring in $n \rightarrow \pi_{Ar}^*$ interaction and (c) lone pair orbital of oxygen with π^* antibonding orbital of the carbonyl group in $n \rightarrow \pi_{Am}^*$ interaction. Figure (c) adapted in part with permission from ref. 61. Copyright [2014] American Chemical Society. 6
- Figure 1.3** (a) Crystal structure of Z-DNA (PDB ID-131D) showing $n \rightarrow \pi_{Ar}^*$ interaction between oxygen atom of the cytidine (C) sugar and guanine ring of the guanidium (G) moiety. (b) Crystal structure of tRNA (PDB ID-1EHZ) showing $n \rightarrow \pi_{Ar}^*$ interaction between oxygen atom of phosphate and cytosine ring at the U-turn. 8
- Figure 1.4** (a) $n \rightarrow \pi_{Am}^*$ interaction in the backbone of PP-II helix of collagen (PDB ID-1CAG) between the carbonyl groups of residue i and $i+1$. (b) Sequence of collagen (pro-Hyp-Gly). (c) $n \rightarrow \pi_{Am}^*$ interaction in the backbone of α -helix (PDB ID-1AL1) between carbonyl groups of residue i and $i+1$. 10

- Figure 1.5** (a) The $n \rightarrow \pi_{Ar}^*$ interaction between backbone carbonyl oxygen of Ala and side chain aromatic ring of Phe residues (PDB ID-1LUC). (b) $n \rightarrow \pi_{Ar}^*$ interaction between side chain carbonyl oxygen of Glu and side chain aromatic ring of Tyr residues (PDB ID-1QL0). (c) $n \rightarrow \pi_{Am}^*$ interaction between side chain carbonyl oxygen and backbone carbonyl group of Asp residue (PDB ID-1AGJ), an example of self contacting Asp residues in proteins. Adapted in part with permission from ref. 5 and 6. Copyright [2007] American Chemical Society. 13
- Figure 1.6** (a) Hydrogen bonding ($n \rightarrow \sigma^*$) interaction in α -helix between carbonyl group of residue i and N-H bond of residue $i+4$. (b) $n \rightarrow \pi_{Am}^*$ interaction in α -helix between carbonyl groups of residue i and $i+1$. Adapted in part with permission from ref. 7. Copyright [2010] Nature Chemical Biology. 15
- Figure 1.7** (a) $lp \dots \pi$ interaction between nitrogen atom of acetonitrile and the aromatic ring of triazine in the crystal structure of $Zn_4(oxodentriz)Cl_8](CH_3CN)_2(H_2O)$ complex. Adapted with permission from ref. 80. Copyright [2006] American Chemical Society. (b) and (c) supramolecular structures generated by $O(lp) \dots \pi$ and $Cl(lp) \dots \pi$ interaction, respectively, along with $C-H \dots \pi$ interaction. Adapted with permission from ref. 88. Copyright [2007] American Chemical Society. 17
- Figure 1.8** Crystal structure of Polylactic acid (PLA) showing $n \rightarrow \pi^*$ interaction between adjacent carbonyl groups, oriented along the Burgi-Dunitz trajectory. (Reproduced from ref. 62 with permission from The Royal Society of Chemistry.) 19
- Figure 1.9** Crystal structure of N-trimethyl homoserine lactone showing $n \rightarrow \pi^*$ interaction between the neighboring carbonyl groups. Adapted in part with permission from ref. 61. Copyright [2014] American Chemical Society. (b) and (c) lowest energy conformers of GABA showing $n \rightarrow \pi^*$ interaction between the nitrogen atom and C=O group of carboxylic acid. 20

- Figure 1.10** (a) and (b) are the lowest energy conformers of aspirin showing $n \rightarrow \pi^*$ interaction Adapted in part with permission from ref. 63. Copyright [2011] American Chemical Society. Structures of small peptoid mimicking (c) $n \rightarrow \pi_{Am}^*$ interaction and (d) $n \rightarrow \pi_{Ar}^*$ interaction. Adapted in part with permission from ref. 1. Copyright [2007] American Chemical Society. 22
- Figure 1.11** (a) Structures of trans conformers of N-acetylproline methylester (AcProOMe), N-acetyl-4S-Fluoroproline methylester (Ac-4S-Flp-OMe) and N-acetyl-4R-fluoroproline methylester (Ac-4R-Flp-OMe) from ref. 42. (b) Crystal structure of Ac-4R-Flp-OMe showing trans conformation of the peptide bond and orientation of adjacent carbonyl groups along the Burgi-Dunitz trajectory. Adapted in part with permission from ref. 10. Copyright [2002] American Chemical Society. 23
- Figure 1.12** Structures of cis and trans conformers of N-formylproline phenylester from ref. 13. $n \rightarrow \pi^*$ interaction in the trans conformer is indicated by the green arrow. X represents the electron donating or withdrawing group. An electron withdrawing group favours the trans conformation while electron donating group favours the cis conformation. 25
- Figure 1.13** Structures of trans conformation of (a) N-thioacetyl-4R-fluoroproline methylester and (b) N-acetyl-4R-fluoroproline methylester. NBO views of the overlap of their respective n and π^* orbitals are shown below. Strong $n \rightarrow \pi^*$ interaction is observed when carbonyl oxygen is replaced by sulphur. Adapted in part with permission from ref. 60. Copyright [2009] American Chemical Society. 26
- Figure 2.1** A schematic representation of supersonic expansion. 38
- Figure 2.2** Velocity distribution curves of (a) effusive molecular beam and (b) supersonic molecular beam. 39
- Figure 2.3** Schematic diagram for (a) 1C-R2PI spectroscopy and (b) 2C-R2PI 41

spectroscopy.

Figure 2.4	Schematic representation of Time of Flight mass spectrometer based on Wiley and McLaren design.	44
Figure 2.5	A schematic diagram of dye laser (ND6000, Continuum) showing its optical configuration.	47
Figure 2.6	A schematic diagram of UV tracker (UVT, Continuum) showing its optical configuration.	49
Figure 2.7	A schematic diagram of IR laser (Laser Vision) showing its optical configuration.	51
Figure 2.8	Schematic diagram of the generation of far-IR wavelength using AgGaSe ₂ crystal.	53
Figure 2.9	Photograph of the home-built jet-cooled REMPI Time of Flight mass spectrometer coupled with laser desorption	54
Figure 2.10	Schematic diagram of the experimental setup of a home-built jet-cooled Time of Flight mass spectrometer coupled with laser desorption. The temporal synchronization between the molecular beam and the lasers is performed using the delay generator.	55
Figure 2.11	A schematic diagram of the laser desorption setup. Sample holder is attached to an XYZ manipulator coupled with the motorized translational assembly which moves the sample holder back forth.	57
Figure 2.12	(a) A schematic demonstration of the RIDIR spectroscopy (b) Cartoon diagram of the IR spectrum obtained from the RIDIRS.	59
Figure 2.13	(a) A schematic diagram of the IR-UV hole-burn spectroscopy (b) Cartoon	61

diagram of the R2PI spectrum and IR-UV hole-burn spectrum.

- Figure 2.14** (a) A schematic diagram of the UV-UV hole-burn spectroscopy (b) 62
Cartoon diagram of the R2PI spectrum and IR-UV hole-burn spectrum.
- Figure 3.1** (a) Hydrogen bonding ($n \rightarrow \sigma^*$) interaction in α -helix between carbonyl 70
group of residue i and N-H bond of residue $i+4$. (b) $n \rightarrow \pi_{Am}^*$ interaction in
 α -helix between carbonyl groups of residue i and $i+1$. Adapted in part with
permission from ref. 37. Copyright [2010] Nature Chemical Biology.
- Figure 3.2** Double hydrogen-bonded structures of all the complexes of 7-AI with 73
fluoropyridines optimized at the M05-2X/cc-pVTZ level of theory.
- Figure 3.3** The initial and final structures of the complexes of 7-AI with 2,6-FP, 2,3,6- 74
FP, 2,4,6-FP, 2,3,4,6-FP, 2,3,5,6-FP and 2,3,4,5,6-FP optimized at the
M05-2X/cc-pVTZ level of theory.
- Figure 3.4** (a) Definition of a few important intermolecular geometrical parameters of 76
the $n \rightarrow \pi_{Ar}^*$ complexes of 7-AI with 2,6-substituted fluoropyridines. (b), (c)
and (d) plots of the $R_{N...Ar}$, $d_{N-H...N}$ and $\theta_{N-H...N}$ values of the six complexes
of 7-AI with 2,6-substituted fluoropyridines calculated at the B3LYP, B97-
D, MP2 and M05-2X levels of theory.
- Figure 3.5** Plots of the BSSE corrected binding energies (ΔE_c) of the complexes of 7- 78
AI with 2,6-substituted fluoropyridines calculated at the MP2 level as well
as various levels of DFT.
- Figure 3.6** Time of Flight mass spectra of (a) 7-AI...2,6-FP and (b) 7-AI...2,3,5,6-FP 81
complexes recorded by fixing the laser at 33889 and 33930 cm^{-1}
respectively.
- Figure 3.7** 1C-R2PI spectra of the (a) 7-AI monomer (b) 7-AI...2,6-FP and (c) 7- 82
AI...2,3,5,6-FP complexes. All the spectra of the monomer and the
complexes are presented in relative wavenumber scale with respect to their

electronic origin bands. The assignment of the spectra shown in the Fig. is described in the text.

- Figure 3.8** R2PI spectrum of 7AI...2,3,5,6-FP complex recorded at (a) 268 K, (b) 258 K, and (c) 247 K temperature of 2,3,5,6-FP keeping the temperature of 7AI fixed at 363 K. 86
- Figure 3.9** RIDIR spectra measured in the N-H stretching frequency region by probing the electronic origin band of the (a) 7-AI monomer, (b) 7AI...2-FP complex, (c) 7-AI...2,6-FP complex and (d) origin +118 cm^{-1} band of the 7-AI...2,3,5,6-FP complex. The theoretical N-H stretching frequencies calculated at the M05-2X/cc-pVTZ level of theory are shown through the stick spectra. Fig. 2(b) is reproduced from ref. 74. The ground state optimized structures of the complexes are shown in the inset of Fig. 2 below their respective RIDIR spectrum. The structures are optimized at the M05-2X/cc-pVTZ level of theory. The green dotted line in the optimized structures represents $n \rightarrow \pi^*$ interaction, the red dotted line represents N-H...N hydrogen bonding interaction and the purple dotted line in the structure of 7AI...2-FP complex represents C-H...N interaction. 88
- Figure 3.10** IR-UV hole burning spectra of (b) 7AI...2,6-FP and (d) 7AI...2,3,5,6-FP recorded by probing N-H stretching frequency at 3414 cm^{-1} and 3451 cm^{-1} respectively. 1C-R2PI spectra of (a) 7AI...2,6-FP and (c) 7AI...2,3,5,6-FP are reproduced along with their respective IR-UV hole burn spectra. 90
- Figure 3.11** The NBO pictures depicting the overlap between the donor and acceptor orbitals corresponding to the $n \rightarrow \pi_{Ar}^*$ and N-H...N interactions present in the complexes of 7-AI with 2,6-FP, and 2,3,5,6-FP 92
- Figure 3.12** Different components of the total interaction energy of the complexes of (a) 7-AI with 2,6-substituted fluoropyridines and (b) doubly hydrogen bonded complexes of 7-AI with 2,3-FP, 2,3,4-FP, 2,3,4,5-FP calculated at the M05-2X/cc-pVDZ level of theory using LMO-EDA method. 94

- Figure 4.1** Electronic spectrum of phenyl formate measured using 1C-R2PI spectroscopy. (b) and (c) represent UV-UV hole-burning spectra of phenyl formate measured by probing the bands at 37673 and 37613 cm^{-1} , respectively, marked by asterisks in the spectrum A. Tentative assignment of the bands in the electronic spectrum is done based on the calculated vibrational frequencies in the excited electronic state at the CIS/6-31+G(d) level of theory. See the text as well as Table S1 for the detailed assignment. The bands marked as A₁ and A₂ belong to the trans conformer only but could not be assigned to S₁←S₀ transition. 103
- Figure 4.2** (a) cis and (b) trans conformers of phenyl formate obtained at the M05-2X/aug-cc-pVDZ level of theory. The atom numbering scheme is shown in the structure of trans conformer. 104
- Figure 4.3** IR spectra by probing (a) 0-0(cis) + 83 cm^{-1} and (c) 0-0(trans) + 126 cm^{-1} bands in the electronic spectrum shown in Fig. 4.1. Theoretical IR spectra of the cis and trans conformers of phenyl formate calculated at the M05-2X/aug-cc-pVDZ level of theory are shown as stick diagrams in 4.3(b) and 4.3(d), respectively. The calculated IR frequency has been scaled with respect to reported experimental carbonyl stretching frequency of methyl lactate. 108
- Figure 4.4** IR spectra measured in the carbonyl stretching region by exciting the (a) 0₀⁰ (trans), (b) 0₀⁰ (trans) + 39 cm^{-1} , (c) 0₀⁰ (trans) + 51 cm^{-1} , (d) 0₀⁰ (trans) + 79 cm^{-1} and (e) 0₀⁰ (trans) + 126 cm^{-1} bands of the electronic spectrum of phenyl formate shown in Figure 4.1(c). 109
- Figure 4.5** NBO view showing the overlap of lone pair orbital (n) of carbonyl oxygen and π^* orbitals of phenyl ring in the cis conformer of phenyl formate. 111
- Figure 4.6.** NBO view of (a) π^* orbital of phenyl ring along with π orbital of the carbonyl group and (b) π orbital of phenyl ring along with π^* orbital of carbonyl group in the cis conformer of phenyl formate. 112

- Figure 4.7** NBO view for the overlap of donor and acceptor orbitals involved in R_1 and R_2 interactions in the cis and trans conformers of phenyl formate. R_1 and R_2 are defined at the footnote of Table 4.3. 113
- Figure 4.8** NBO view for the overlap of donor and acceptor orbitals involved in R_3 interaction in the cis and trans conformers of phenyl formate. R_3 is defined at the footnote of Table 4.3. 114
- Figure 5.1** (a) Crystal structure of collagen tripeptide sequence (Pro-Hyp-Gly) showing $n \rightarrow \pi^*$ interaction (represented by green arrow) between the neighbouring carbonyl groups. (b) General structure of a proline unit in collagen showing the trans conformation of the amide bond. Where X= -H or -OH at 4R-configuration 124
- Figure 5.2** (a) Electron withdrawing group (EWG) in the 4R position favors the gauche conformation which stabilizes the C_4 -exo puckering of the pyrrolidine ring. (b) Newman projection of C_4 and C_5 carbon atoms of the pyrrolidine ring in gauche conformation showing overlap of σ orbital of C_5 -H bond with σ^* orbital of C_4 -EWG bond and σ orbital of C_4 -H bond with σ^* orbital of C_5 -N bond. 126
- Figure 5.3** (a) Electronic spectrum of Cbz-Hyp-OMe measured using 1C-R2PI spectroscopy. (b), (c), (d), and (e) are the UV-UV hole burning spectra of Cbz-Hyp-OMe measured by probing the bands marked by (\blacklozenge), (\blacktriangle), (\blacksquare), and (\bullet) in the R2PI spectrum, respectively. A_0^0 (37677 cm^{-1}), B_0^0 (37703 cm^{-1}), C_0^0 (37656 cm^{-1}), and D_0^0 (37633 cm^{-1}) represents the origin band transition of conformers A, B, C, and D, respectively. 128
- Figure 5.4** Zero-point corrected relative energies of the conformers of Cbz-Hyp-OMe calculated at the M05-2X/aVDZ level of theory. Conformers are classified into four groups (P, Q, R, and S). Conformers of group P, Q and S have exo puckering while group R has endo puckering of the pyrrolidine ring. 130

- Figure 5.5** Structures of all the 16 conformers optimized at the M05-2X/aVDZ level of theory. E_{rel} represents the zero point corrected relative energies (kcal/mol) of the conformers with respect to the most stable conformer (I-c). “c” stands for cis, “t” stands for trans. 131
- Figure 5.6** (a) Symbols for representing the important geometrical parameters. β represents the benzyl ring torsion. Dihedral angles ω (O10-C8-N1-C2), ϕ (C8-N1-C2-C-11) and ψ (CN1-C2-C11-O13) are the Ramachandran angles that define the main chain torsion angles. Distance r represents the N...H-O hydrogen bond distance. (b) Pictorial representation of Burgi-Dunitz parameters. d_{BD} represents the distance between the donor oxygen and carbon atom of the acceptor carbonyl group while θ_{BD} represent the angle O...C=O. Δ represents the degree of pyramidalization of the acceptor carbonyl carbon from the plane of its three substituents. 132
- Figure 5.7** Experimental IR spectra of conformers A, B, C and D shown in comparison with the theoretical IR spectra of group P, Q and R structures of Cbz-Hyp-OMe in the (a) C=O stretching frequency region and (b) O-H stretching frequency region. The calculated amide C=O, ester C=O and OH stretching frequencies are scaled using scaling factor of 0.9441, 0.9546 and 0.9391 respectively. 137
- Figure 5.8** NBO view of overlap of donor and acceptor natural bond orbitals involved in $n \rightarrow \pi^*$, R1 and R2 interactions in the conformers of group P. 140
- Figure 5.9** cis and trans conformers of N-methoxycarbonyl (2S,4R)-4-hydroxypyrrolidine-2-methyl showing no change in the amide C=O stretching frequency in the absence of $n \rightarrow \pi^*$ interaction. Second order perturbative energies of R1 and R2 interactions are shown for cis and trans conformers below their corresponding geometries. R1 and R2 interactions in both the conformers are similar. 143

- Figure 6.1** Skeletal structure of salicin 152
- Figure 6.2** (a) Electronic spectrum of salicin measured using 1C-R2PI spectroscopy. 154
 (b), (c) and (d) are UV-UV hole burning spectra of salicin measured by probing the bands labeled as A (36422), B (36435) and C (36452 cm^{-1}) respectively, in the R2PI spectrum. The electronic band origins of A, B and C conformers are designated as A_0^0 (36422 cm^{-1}), B_0^0 (36435 cm^{-1}) and C_0^0 (36452 cm^{-1}).
- Figure 6.3** Relative energies (including zero-point energy corrections) of the 157
 conformers of salicin calculated at the M06-2X/6-311++G(d,p) level of theory. Conformers are divided into four groups P, Q, R, and S on the basis of their structural similarities.
- Figure 6.4** Structures of 14 low energy conformers of salicin optimized at the M06- 158
 2X/6-311++G(d,p) level of theory.
- Figure 6.5** (a), (c) and (e) show the experimental IR spectra of species A, B, and C, 161
 respectively, in the O-H stretching region measured by probing their respective electronic band origins (for electronic origin bands see Figure 2). The scaled theoretical O-H stretching frequencies of conformers II, I and III are shown in (b), (d) and (f) respectively, calculated at the M06-2X/6-311++G(d,p) level of theory. The structures of conformers I, II, and III are also shown in the inset of the figure. The blue dotted line represents the O-H...O hydrogen bonding, and the green dotted line represents the $n \rightarrow \pi^*$ interaction.
- Figure 6.6** Experimental O-H stretching frequencies of species A, B and C in 162
 comparison with the computed O-H stretching frequencies of (a) Group P, (b) Group Q, (c) Group R, and (d) Group S conformers. The calculated [M06-2X/6-311++G(d,p) level of theory] O-H stretching frequencies are shown as stick spectra (origins scaled by a factor of 0.9333).

- Figure 6.7** (b), (d) and (f) shows experimental electronic spectra of species A, B and C 165 respectively, in comparison with the Franck-Condon simulated electronic spectra of conformers II, I and III presented in (a), (c) and (e), respectively. Assignments of the bands are based on the simulated Franck-Condon spectra.
- Figure 6.8** NBOs of the three lowest energy conformers (I, II, and III) of salicin and 170 the gauche conformer of benzyl alcohol, showing no overlap between the π orbitals of the aromatic ring and σ^* orbital of the benzylic OH group. The electron density was calculated at the M06-2X/6-311++G(d,p) level of theory.
- Figure 6.9** (a) NBOs of the O2-H2...O7' hydrogen bonding interaction and $n \rightarrow \pi^*$ 172 interaction in various conformers (I, II, III, V and VIII) of salicin calculated at the M06-2X/6-311++G(d,p) level of theory. The NBOs of the $n \rightarrow \pi^*$ interaction show overlap between the lone pair orbitals (n_s and n_p) of O7' atom with the π^* orbital of C2'=C3' bond of the aromatic ring. The NBOs of the hydrogen bonding interaction show overlap between lone pair orbitals (n_s and n_p) of O7' atom with the σ^* orbital of the O2-H2 bond. (b) NBOs of the $n \rightarrow \pi^*$ interaction between the lone pair orbital of (n_s and n_p) oxygen atom and the aromatic ring in the gauche and trans conformers of benzyl alcohol.
- Figure 6.10.** (a) X-ray crystal structure of the β -Glucosidase enzyme...salicin complex 175 (PDB ID: 3VIL). (b) Structure of salicin in the enzyme bound state and one of its NBOs showing an $n \rightarrow \pi^*$ interaction between the oxygen atom of the benzylic OH and the aromatic ring. The electron density has been calculated at the M06-2X/6-311++G(d,p) level of theory.

List of Tables

Table 3.1	Binding energies (kcal/mol) and intermolecular geometrical parameters (kcal/mol) of all the double hydrogen bonded complexes of 7-AI and fluoropyridines calculated at the M05-2X/cc-pVTZ level of theory	73
Table 3.2	BSSE corrected binding energies (ΔE_e , kcal/mol) of the complexes of 7-AI with the 2,6-substituted fluoropyridines calculated using various basis sets at the M05-2X level of theory	80
Table 3.3	Observed and calculated low frequency intermolecular vibrations of the 7-AI...2,6-FP and 7-AI...2,3,5,6-FP complexes. Low frequency intermolecular vibrations in the S_1 state are calculated at the TD-M05-2X/6-31+G(d) level of theory	83
Table 3.4	Occupancies of π^* orbital of the fluoropyridine ring and σ^* orbital of the N-H bond of 7-AI in the complexes of 7-AI...2,6-substituted fluoropyridine	93
Table 4.1.	Observed and calculated S_1 state vibrational frequencies (in cm^{-1}) of the cis and trans conformers of phenyl formate. S_1 state vibrational frequencies are calculated at the CIS/6-31+G(d) level of theory	105
Table 4.2	A few selected geometrical parameters of the cis and trans conformers of phenyl formate in the S_0 and S_1 states. The structures in the S_0 state have been calculated at the M05-2X/aug-cc-pVDZ level of theory while the S_1 state structures have been calculated at the CIS/6-31+G(d) level of theory	107
Table 4.3	Second order perturbative energy ($E_{i \rightarrow j^*}^{(2)}$) values for interaction between various donor and acceptor NBOs in the cis and trans conformers of phenyl formate calculated at the M05-2X/cc-pVTZ level of theory	115

Table 4.4	Sum of multiple contributions of second order perturbative energy ($E_{i \rightarrow j^*}^{(2)}$) values for each of the R ₁ , R ₂ , R ₃ and R ₄ interactions in the cis and trans conformers of phenyl formate	116
Table 4.5	Occupancy of the carbonyl oxygen O ₁₅ lone pair electrons (p-type) of the cis conformer of phenyl formate on deletion of specific interaction(s) by performing NBO deletion analysis	117
Table 4.6	NBO occupancies of the $\sigma_{C=O}$, $\sigma^*_{C=O}$, π and π^* orbitals of the carbonyl group in the cis and trans conformers of phenyl formate, calculated at the M05-2X/cc-pVTZ level of theory	118
Table 5.1:	Important geometrical parameters ^a of all the conformers of group P, Q and R calculated at the M05-2X/aVDZ level of theory. “c” and “t” after the conformers number represents the cis and trans conformation	133
Table 5.2	Ramachandran angles (ϕ and ψ) and n $\rightarrow\pi^*$ interaction energy of the trans conformers of Ac-Y-OMe (Where Y=Pro, Hyp and Flp) in comparison with the trans conformer of Cbz-Hyp-OMe	134
Table 5.3	Relative electronic energies (ΔE) and relative Gibbs Free energies (ΔG) of all the Cbz-Hyp –OMe conformers of group P, Q and R calculated at 298 K	135
Table 5.4.	The second-order perturbative energy values of all the possible orbital interactions which involves lone pair and π^* NBOs of amide carbonyl group in the conformers of group P and Q	142
Table 5.5	Change in the occupancy of lone pair orbital of O ₉ (n_p) and π^* orbital of C ₈ = O ₉ upon deletion of specific interactions in the group P conformers of Cbz-Hyp-OMe. ΔE_{scf} represents the change in the SCF energy upon deleting the interaction.	144

Table 5.6	Bond order of $n \rightarrow \pi^*$ donor carbonyl bond ($C_8=O_9$) and acceptor carbonyl bond ($C_{11}=O_{12}$) along with amide bond (N_1-C_8) and ester bond ($O_{10}-C_8$) of the donor carbonyl group, in the group P conformers of Cbz-Hyp-OMe.	145
Table 5.7	The NBO second order perturbative energy values of the resonance effect (R1) and inductive effect (R2) present in the ester carbonyl group ($R1_{\text{ester}}$, $R2_{\text{ester}}$) and amide carbonyl group ($R1_{\text{amide}}$, $R2_{\text{amide}}$), calculated at the M05-2X/aVDZ level of theory. $\partial_{C_8=O_9}$ represents the occupancy of the amide carbonyl group and $\partial_{C_{11}=O_{12}}$ represents the occupancy of the ester carbonyl group.	147
Table 6.1	Experimental and Franck-Condon simulated low frequency intramolecular vibrational modes of the three observed conformers of salicin.	155
Table 6.2	Zero-point energy (ZPE) corrected relative energies (kcal/mol) of various conformers of salicin, calculated at different levels of theory	159
Table 6.3.	Relative electronic energies (ΔE) and relative Gibbs Free energies (ΔG) of all 14 low energy conformers of salicin calculated at 10 K	160
Table 6.4.	Experimental 0_0^0 band transitions of species A, B, and C in comparison with the TDDFT calculated [TD-M06-2X/6-311++G(d)] vertical excitation energies of conformers I, II and III	167
Table 6.5.	Important geometrical parameters ^a of low energy conformers of salicin calculated at the M06-2X/6-311++G(d,p) level of theory	168
Table 6.6.	NBO second-order perturbative estimates of donor-acceptor interactions ($E_{i \rightarrow j}^{(2)}$) of all hydrogen bonding and $n \rightarrow \pi^*$ interactions observed in conformers I, II, III, V and VIII of salicin. NBO calculations were performed at the M06-2X/6-311++G(d,p) level of theory	171

Table 6.7 Occupancy of σ^* orbital of benzylic O-H group in the conformers of salicin 174

Synopsis

Non-covalent interactions are the backbone of biomolecular and material structures as well as biological processes. Thus, an in-depth understanding of these weak interactions may lead to design of efficient functional materials, drugs and also understanding the biological processes. These non-bonding interactions generally have a broad range of classifications depending on their nature, origin and strength. Hydrogen bonding is the most versatile and well understood non-covalent interaction documented in the literature. Intermolecular interactions involving π -systems, which are also very popular and well studied, are π -stacking, π -hydrogen bonding, cation- π interactions and anion- π interactions. Recently, another non-covalent interaction involving π -system and electronegative atom has been recognized by the scientific community. This newly discovered non-covalent interaction is named as $n \rightarrow \pi^*$ interaction.

The $n \rightarrow \pi^*$ interaction is generally classified into two categories: $n \rightarrow \pi_{Am}^*$ (amide) and $n \rightarrow \pi_{Ar}^*$ (aromatic).¹ The $n \rightarrow \pi_{Am}^*$ interaction is widely present in the backbone of proteins and peptoids where the lone pair of electrons on the oxygen atom of a carbonyl group is delocalized into the π^* orbital of a neighbouring carbonyl group.² This interaction follows the Burgi-Dunitz trajectory ($O \dots C=O$ distance $\leq 3.2 \text{ \AA}$ and $\angle O \dots C=O = 109 \pm 10^\circ$) of approach of a nucleophile to an electrophilic system. In the case of the $n \rightarrow \pi_{Ar}^*$ interaction, lone pair electrons on electronegative atom (e.g. oxygen of a carbonyl group) are delocalized into the π^* orbital of an aromatic ring. In this case, the geometrical requirements for the optimum interaction is given by the distance between the carbonyl oxygen and aromatic ring centroid (2.8-3.8 \AA) as well as the angle between the aryl and carbonyl planes ($\leq 90^\circ$). $n \rightarrow \pi_{Ar}^*$ interaction is also termed as lone pair (lp)... π interaction. The $n \rightarrow \pi_{Ar}^*$ interaction is mostly observed in nucleic acids and in the side chains of proteins.³⁻⁶

The widespread presence of the $n \rightarrow \pi^*$ interactions in proteins, nucleic acids, and solid state materials has been documented from an extensive search of X-ray crystal structures in the Protein Data Bank (PDB) as well as Cambridge Structural Database (CSD).^{3,7} The $n \rightarrow \pi_{Ar}^*$ interaction was first reported in Z-DNA by Egli and co-workers in 1995 through analysis of its crystal structure.⁸ Later, Egli and co-workers have reported several nucleic acids (tRNA, hammerhead ribozyme and RNA Pseudoknot) where significant $n \rightarrow \pi^*$ interactions are present.³ Another crystallographic data analysis performed by Sankararamakrishnan and co-workers also provides evidence of $n \rightarrow \pi^*$ interaction in nucleic acids.⁹

Significance of the $n \rightarrow \pi^*$ interaction in proteins was recognised after its discovery in collagen triple helix.¹⁰ The presence of the $n \rightarrow \pi^*$ interactions in the backbone of individual PP-II helix of collagen accounts for very long and robust structure of individual strand in spite of the absence of any intra-strand hydrogen bonding interaction. The $n \rightarrow \pi^*$ interaction exists not only in the backbone but also in the side chains of proteins. Sankararamakrishnan and co-workers have analyzed high resolution crystal structures of about 500 proteins and reported that the oxygen atom of the backbone carbonyl group interacts frequently with side chain carbonyl groups as well as aromatic centers.⁴

On the material front, there are quite extensive reports in the literature demonstrating the role of the $n \rightarrow \pi^*$ interaction in the supramolecular self-assembly of molecules to give rise to specific structures of materials.¹¹ Mostly, $n \rightarrow \pi_{Ar}^*$ type of interaction, which is also referred as lone pair (lp)... π interaction, has been observed in materials. A triazine-based supramolecular self-assembly shows the first evidence of the $n \rightarrow \pi_{Ar}^*$ interaction in the solid state. This interaction has been named as a new supramolecular bond by Reedijk and co-workers who have done a thorough systematic search of the lone pair (lp)... π interaction in the crystal structures deposited in the CSD.¹¹ The $n \rightarrow \pi^*$ interaction also contribute to the stability of polymers and small molecules. The examples are poly Lactic acid (PLA),

peptoids (polymer of N-substituted glycine residues), N-acyl homoserine lactones (AHL), γ -Amino butyric acid (GABA) and analgesics drug aspirin.²

It has been observed from crystallographic and computational studies that $n \rightarrow \pi^*$ interaction is present in the backbone of α -helix along with the hydrogen bonding interaction.⁷ Raines and co-workers have stated that there is a close connection between the hydrogen bond and an $n \rightarrow \pi^*$ interaction,⁷ and interplay or cooperativity between these two interactions is inevitable in the structures of biomolecules. Such interplay between both the interactions can either increase or decrease the strength of the other interaction.¹² Raines and co-workers have also shown the interplay between $n \rightarrow \pi^*$ interaction and hydrogen bonding in the side chains of proteins through crystal structure and computational analysis.¹² They have also used NMR spectroscopy to understand the role of $n \rightarrow \pi^*$ interaction in the stability of biomolecules.¹³ Several proline derivatives have been used as model systems. The prolyl-peptide bonds of proline derivatives can have both cis and trans conformations. Interestingly, the trans amide conformations which have $n \rightarrow \pi^*$ interactions are dominant in proteins. The NMR spectroscopy experiments on model compounds indeed show preferential population of the conformers having an $n \rightarrow \pi^*$ interaction over the conformers without an $n \rightarrow \pi^*$ interaction.

Till now, experimental approaches to determine the presence of the $n \rightarrow \pi^*$ interactions are limited to only NMR spectroscopy and X-ray crystallographic studies. Both of these studies demonstrate the presence of the $n \rightarrow \pi^*$ interaction in various molecular systems. However, the question arises as to whether this close contact between two electron-rich moieties observed in the crystal structures occurs just because of optimization of the arrangement of other molecular units in the macromolecular systems. Further, in solution phase spectroscopy, the solute-solvent interaction may change the equilibrium between the conformers having $n \rightarrow \pi^*$ interaction and without having $n \rightarrow \pi^*$ interaction. In principle,

presence of neighboring intermolecular interactions can obscure the investigation of the $n \rightarrow \pi^*$ interaction as it is very weak in strength.

Isolated gas phase spectroscopy is an ideal means to study this weak $n \rightarrow \pi^*$ interaction as this technique allows to study the structures of molecular moieties in an environment which is free from crystal packing forces and solvent or any other intermolecular interactions. Although there are thorough literature studies on conventional hydrogen bonding, π -stacking and π -hydrogen bonding interactions in isolated gas phase, similar studies on the $n \rightarrow \pi^*$ interaction are scarce in the literature. The scarcity of the gas phase study of the $n \rightarrow \pi^*$ interaction in the literature is definitely due to the weak and counterintuitive nature of this non-covalent interaction. In this thesis, we have employed isolated gas-phase spectroscopic techniques combined with quantum chemistry calculations to explore $n \rightarrow \pi^*$ interaction quantitatively in various molecular systems and addressed the following questions on $n \rightarrow \pi^*$ interaction.

- 1) Can we study $n \rightarrow \pi^*$ interaction in isolated gas phase?
- 2) Can $n \rightarrow \pi^*$ interaction exists along with strong hydrogen bonding interaction?
- 3) Can we directly probe the $n \rightarrow \pi^*$ interaction in a molecular system from gas phase spectroscopic study?
- 4) Can we explore $n \rightarrow \pi^*$ interaction in molecular systems which have direct biological implications using gas phase spectroscopy? (e.g., peptides, drugs, nucleic acid etc.)

In chapter 1, we have introduced the $n \rightarrow \pi^*$ non-covalent interaction. We have discussed its significance in biomolecules, materials, and small molecules. The current understanding of the $n \rightarrow \pi^*$ interaction through NMR spectroscopy has been reviewed in this chapter. We have also discussed the physical nature of the $n \rightarrow \pi^*$ interaction understood so far from the experimental and computational analysis. At the end of this chapter, we have projected the aim of the current thesis.

In chapter 2, we have described the experimental setup and computational methods which have been employed to study the structures of molecules and complexes stabilized by the $n \rightarrow \pi^*$ interaction. We have discussed the principles of supersonic jet expansion, Time of Flight Mass spectrometry and laser based various spectroscopic techniques used to measure high-resolution electronic and vibrational spectroscopy of molecules in isolated gas phase. The spectroscopic techniques include resonant two-photon ionisation spectroscopy (R2PI), resonant ion-dip infrared spectroscopy (RIDIRS), IR-UV and UV-UV hole-burn spectroscopy.

In chapter 3, we have shown the interplay between hydrogen bonding and weak $n \rightarrow \pi^*$ interactions in the complexes of 7-azaindole and several 2,6-substituted fluoropyridines using gas phase spectroscopic techniques (R2PI and IR-UV double resonance spectroscopy) combined with quantum chemical calculations. In literature, the co-operativity between hydrogen bonding and $n \rightarrow \pi^*$ interactions is reported mostly based on crystal structure and computational analysis. Here, our purpose is to show the spectroscopic evidence of the interplay between hydrogen bonding and $n \rightarrow \pi^*$ interactions, by studying judiciously chosen molecular complexes of 7-azaindole and several 2,6-substituted fluoropyridines, as a model system in isolated gas phase. We have found from our experiment and detailed theoretical calculations that the structures of these complexes are stabilized due to subtle balance between N–H...N hydrogen bonding and $n \rightarrow \pi_{Ar}^*$ interactions.

In chapter 4, we have reported gas-phase IR spectroscopic evidence of weak $n \rightarrow \pi^*$ interaction in phenyl formate. Generally, the hydrogen-bonding interaction ($X-H \cdots Y$) in a molecular system can easily be quantitatively characterized by measuring the red-shift in the X-H stretching frequency using IR spectroscopy. However, there is no report to measure the strength of the $n \rightarrow \pi^*$ interaction quantitatively by probing the functional group involved in the interaction using gas phase IR spectroscopy. The central theme of this chapter is to

investigate whether the existence of the $n \rightarrow \pi^*$ interaction can be proven by probing the stretching frequency of the C=O group involved in this interaction using gas phase IR spectroscopic technique. For this purpose, we chose phenyl formate as a model compound and studied its structure in a supersonic jet. We observed both cis and trans conformers of phenyl formate in our experiment. The cis conformer has C=O group oriented towards the phenyl ring while the trans conformer has C=O group oriented away from the phenyl ring. The cis conformer having $n \rightarrow \pi_{Ar}^*$ interaction is more stable than the trans conformer where $n \rightarrow \pi_{Ar}^*$ interaction is absent. IR spectrum of the cis conformer shows significant red-shift in the donor C=O stretching frequency relative to that of the trans conformer. We have shown that the observed red-shift in the C=O stretching frequency of the cis conformer is due to $n \rightarrow \pi_{Ar}^*$ interaction. This study provides the direct evidence for the $n \rightarrow \pi_{Ar}^*$ interaction as the functional group involved in this interaction is directly probed using IR spectroscopy.

Chapter 5 deals with the IR spectroscopic signature for the $n \rightarrow \pi^*$ interaction between two adjacent carbonyl groups (C=O...C=O) in hydroxyl proline derivative, an important amino acid residue of collagen. In chapter 4, we have reported gas phase IR spectroscopic evidence of $n \rightarrow \pi_{Ar}^*$ interaction by probing the C=O stretching frequency. Here, we have used the same spectroscopic technique to show the evidence of $n \rightarrow \pi_{Am}^*$ interaction between two C=O groups which is widely present in the structures of proteins including collagen. The $n \rightarrow \pi_{Am}^*$ interaction stabilizes the structure of collagen, which is the most abundant protein in animals. Collagen has a unique helical structure made up of three polyproline II-type (PP-II) helices which are tightly inter-twisted with each other. Each of the strands consists of the amino acid sequence X-Y-Gly in a repeating manner, where X is usually proline (Pro) and Y is 4R-L-hydroxyproline (Hyp). The prolyl peptide bonds of each PP-II strands of collagen predominantly exist in trans conformer which allows the two proximal carbonyl groups to come close following the Burgi-Dunitz trajectory for favourable

$n \rightarrow \pi_{Am}^*$ interaction. Here, we have studied Cbz-Hyp-OMe to show the gas-phase IR spectroscopic evidence of the $n \rightarrow \pi^*$ interaction between two carbonyl groups. This study demonstrates the first gas phase IR spectroscopic evidence of the $n \rightarrow \pi^*$ interactions between the two carbonyl groups.

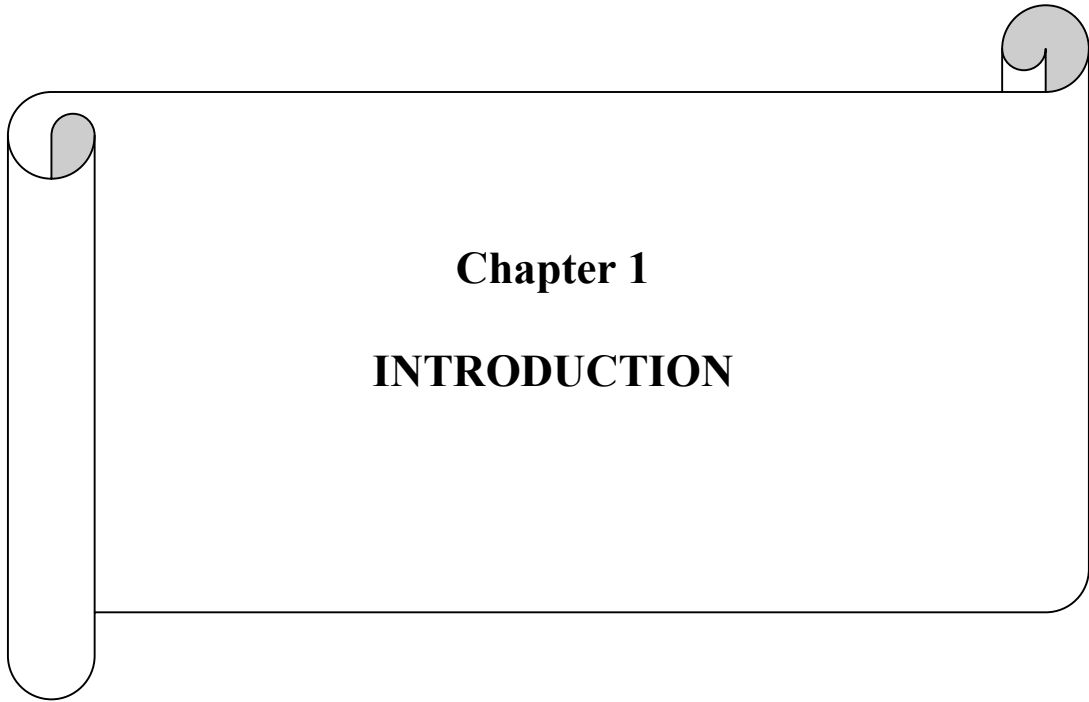
In chapter 6, we have shown the role of the $n \rightarrow \pi^*$ interaction in governing the conformational preferences of an analgesic drug salicin, even in the presence of strong hydrogen bonding interactions in the molecule. Structure of salicin consists of a sugar molecule (β -D-glucopyranoside) and a benzyl alcohol moiety, which are linked through the anomeric oxygen atom of the sugar molecule. In this chapter, we have explored the conformational preferences of salicin in isolated gas-phase. We have observed three lowest energy conformers of salicin in our experiment. All the three conformers show a chain of weak hydrogen bonding interactions between the equatorial hydroxy groups of the sugar moiety. It has been found that the oxygen atom of the CH_2OH group of the benzyl alcohol moiety is involved in hydrogen bonding interaction with one of the equatorial $-\text{OH}$ group of the sugar moiety as well as it takes part in an $n \rightarrow \pi^*$ interaction with the phenyl ring. We observed an interplay between hydrogen bonding and $n \rightarrow \pi^*$ interaction in the most stable conformers of salicin. Presence of the $n \rightarrow \pi^*$ interaction decreases the strength of the hydrogen bonding in these conformers since the same oxygen atom is involved in both hydrogen bonding and $n \rightarrow \pi^*$ interactions, similar to that observed in α -helix. The most significant finding of this study is that higher energy conformers of salicin, possessing stronger hydrogen bonds but negligible $n \rightarrow \pi^*$ interactions are not observed in the experiment suggesting that $n \rightarrow \pi^*$ interaction play a major role in governing the conformational preferences of salicin.

In chapter 7, we have discussed the summary of the present thesis and future perceptive.

List of Publications

1. Kamal Kumar Mishra, **Santosh Kumar Singh**, Paulami Ghosh, Debashree Ghosh* and Alope Das*: *The nature of selenium hydrogen bonding: gas phase spectroscopy and quantum chemistry calculations* **Phys. Chem. Chem. Phys.** **2017**, **19**, 24179.
2. Sumit Kumar, **Santosh Kumar Singh**, Jamuna Vaishnav, J. Grant Hill*, Alope Das*: *Interplay among electrostatic, dispersion and steric interactions: Spectroscopy and quantum chemical calculations of π -hydrogen bonded complexes*. **ChemPhysChem** **2017**, **18**, 828.
3. **Santosh Kumar Singh**, Jamuna Vaishnav and Alope Das*: *Experimental observation of structures with subtle balance between strong hydrogen bond and weak $n \rightarrow \pi^*$ interaction: Gas phase laser spectroscopy of 7-azaindole...fluorosubstituted pyridines*. **J. Chem. Phys.** **145**, **2016**, 104302.
4. **Santosh Kumar Singh**, Alope Das* and Gary W. Breton*: *An ab Initio Study of the effect of Substituents on the $n \rightarrow \pi^*$ interactions between 7-Azaindole and 2,6-Difluorosubstituted Pyridines*. **J. Phys. Chem. A**, **2016**, **120(31)**, 6258-6269.
5. **Santosh Kumar Singh**, Kamal Kumar Mishra, Neha Sharma, and Alope Das*: *Direct spectroscopic evidence for an $n \rightarrow \pi^*$ interaction*. **Angew. Chem. Int. Ed.** **2016**, **55**, 7801-7805.
6. **Santosh Kumar Singh*** and Alope Das*: *The $n \rightarrow \pi^*$ interaction: a rapidly emerging non-covalent interaction*. **Phys. Chem. Chem. Phys.** **2015**, **17**, 9596-9612. (Invited Perspective)
7. Sumit Kumar, **Santosh Kumar Singh**, Camilla Calabrese, Assimo Maris, Sonia Melandri* and Alope Das*, *Structure of saligenin: Microwave, UV and IR spectroscopy studies in a supersonic jet combined with quantum chemistry calculations*. **Phys. Chem. Chem. Phys.** **2014**, **16**, 17163-17171.
8. **Santosh Kumar Singh**, Sumit Kumar and Alope Das*: *Competition between $n \rightarrow \pi^*$ and conventional hydrogen bonding (N-H...N) interactions: An ab initio study of the complexes of 7-azaindole and fluorosubstituted pyridines*. **Phys. Chem. Chem. Phys.** **2014**, **16**, 8819. (Selected for inside front cover page)
9. **Santosh Kumar Singh**, Prasad Joshi, Robert Shaw, Grant J. Hill and Alope Das: *$n \rightarrow \pi^*$ interaction governs the conformational preference of an analgesic drug salicin in presence of hydrogen bonding interaction* (*manuscript under revision*)
10. **Santosh Kumar Singh**, Shahaji Moore, Satish Kumar, Kamal Kumar Mishra, K. N. Ganesh, Alope Das: *Gas Phase IR spectroscopic signature for C=O...C=O $n \rightarrow \pi^*$ interaction in Cbz-(4R)-Hyp-OMe, a key amino acid sequence of collagen*. (*manuscript under preparation*)

11. Santosh Kumar Singh, Kamal Kumar Mishra, Alok Das: *Probing $n \rightarrow \pi^*$ interaction in phenyl acetate. (manuscript under preparation)*



Chapter 1

INTRODUCTION

1.1 Non-covalent interactions

Non-covalent interactions play a central role in dictating the structures and functions of biomolecules as well as materials.¹⁴⁻³⁷ A detailed understanding of these weak non-bonding interactions helps us to understand biological processes and to design new functional materials as well as drugs. There are different types of non-covalent interactions, present in biomolecules and materials, e.g., hydrogen bonding, π - π stacking, cation... π , anion... π etc. These non-bonding interactions are classified depending on their nature, origin, and strength. There are excellent reviews in the literature describing various types of non-covalent interactions in great detail.^{15,28,31,38-45} For the brevity, a brief description of different non-covalent interactions is provided here.

Hydrogen bonding is the most versatile non-covalent interaction present in bimolecular systems and materials.¹⁴⁻¹⁶ This non-covalent interaction is denoted as X-H...Y where X can be any atom which has higher electronegativity than hydrogen and Y can be any atom or group.⁴⁶ Here, X-H is denoted as hydrogen bond donor and Y is denoted as hydrogen bond acceptor. Depending upon the electronegativity of the hydrogen bond donor and acceptor groups/atoms, hydrogen bonding interactions are generally classified into two types, conventional and non-conventional hydrogen bonding.¹⁴ In the case of conventional hydrogen bonding, both X and Y are electronegative atoms like N, O, etc. Conventional hydrogen bonding interactions (for example O-H...O, N-H...N, N-H...O, ionic hydrogen bonds, etc.) fall in the category of strong non-covalent interactions and it is mostly governed by electrostatic forces.¹⁶ Considering the ionic hydrogen bond it is stated that the interaction energy of conventional hydrogen bonding interactions can lie in the range of 5-40 kcal/mol. In the case of the non-conventional hydrogen bonding, X is usually a carbon atom while Y is an electronegative atom, i.e. O, N. The examples are C-H...O, C-H...N, C-H...F, etc. These

non-conventional hydrogen bonding interactions belong to weak non-covalent interactions as the interaction energy lies in the range of 2-5 kcal/mol.

Another type of non-conventional hydrogen bonding interaction, which involves π -electron cloud as an acceptor, is widely studied in the literature.^{39,41,42,47,48} This non-covalent interaction is known as π -hydrogen bonding interaction and it is denoted by X-H... π where, X = C, N, O etc. The interaction energy of π -hydrogen bonding interaction is generally less than 2-5 kcal/mol. In the case of π -hydrogen bonding interactions, both electrostatic and dispersion forces play significant role.³⁸

π -systems are also involved in π - π stacking interaction where, two or more π -systems (aromatic ring) stack upon each other resulting in attractive interaction.^{44,49-51} π - π stacking interaction plays crucial role in the stability of biomolecules and supramolecular assembly of materials. For example, π - π stacking interaction is one of the significant forces for the double helical structure of DNA, drug-DNA intercalation, crystal packing of aromatic molecules etc.²⁰ This non-covalent interaction is mostly driven by dispersion forces which originate because of the polarization of delocalized π -electron cloud.^{44,50}

Another non-covalent interaction which involves π -systems is ion... π interaction where, an ion can be a cation or anion. Cation... π and anion... π interactions are observed in the structures of protein, biological processes like ion recognition and transport as well as supramolecular assembly.^{28,31,52} Both cation... π and anion... π interactions originate mostly from electrostatics (ion-quadrupole) combined with smaller but important contributions of induction (ion-induced polarization) and dispersion forces.^{29,31}

Recently, a non-covalent interaction involving π -system and an electronegative atom has been recognized by the scientific community.^{2,11,53} This non-covalent interaction known as $n \rightarrow \pi^*$ interaction is very weak (0.3-1.5 kcal/mol) compared to other non-covalent interactions. However, the $n \rightarrow \pi^*$ interaction has been found to have potential role in the

stabilization of the structures of bio-molecules and supramolecular architectures.^{3,7,11} The thesis is primarily dealt with gas phase spectroscopy studies and quantum chemical calculation on the molecular systems having $n \rightarrow \pi^*$ interaction.

1.2 The $n \rightarrow \pi^*$ interaction

The $n \rightarrow \pi^*$ interaction is a recently discovered non-covalent interaction which is extensively present in biomolecules and materials. This interaction involves delocalization of lone pair (n) electrons on any electronegative atom or oxygen atom of a C=O group into a π^* orbital of an adjacent C=O group or an aromatic moiety (see Figure 1.1).^{1-13,53-83} The $n \rightarrow \pi^*$ interaction is quite analogous to hydrogen bonding, as both involves a lone pair donor atom

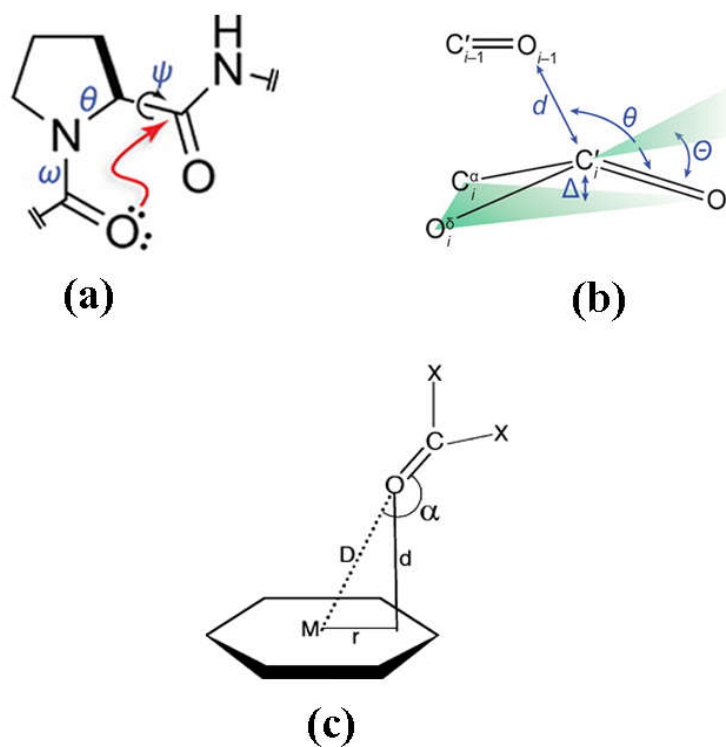


Figure 1.1 (a) Example of $n \rightarrow \pi_{Am}^*$ (amide) interaction. Angles ω , ψ , θ are the Ramachandran angles. (b) Burgi-Dunitz trajectory for favorable $n \rightarrow \pi_{Am}^*$ interaction. Adapted in part with permission from ref. 61. Copyright [2014] American Chemical Society. (c) Example of $n \rightarrow \pi_{Ar}^*$ (aromatic) interaction. Adapted in part with permission from ref. 3. Copyright [2007] American Chemical Society.

which donates its lone pair electron density into an anti-bonding orbital. However, unlike the $n \rightarrow \pi^*$ interaction, the anti-bonding orbital in hydrogen bonding is σ^* of X-H bond (see Figure 1.2).^{2,12} Further, the $n \rightarrow \pi^*$ interaction (~ 0.3 - 1.5 kcal/mol) is much weaker in strength compared to hydrogen bonding (~ 5 - 10 kcal/mol).⁷⁷ It is worth mentioning that the $n \rightarrow \pi^*$ interaction is getting explored only for last 15 years while hydrogen bonding is known in the literature for almost a century. The $n \rightarrow \pi^*$ interaction was overlooked by the scientific community earlier because it is weak and counterintuitive in nature. This interaction seems to be counterintuitive as it involves interaction between two electron rich moieties (lone pair and π -system).

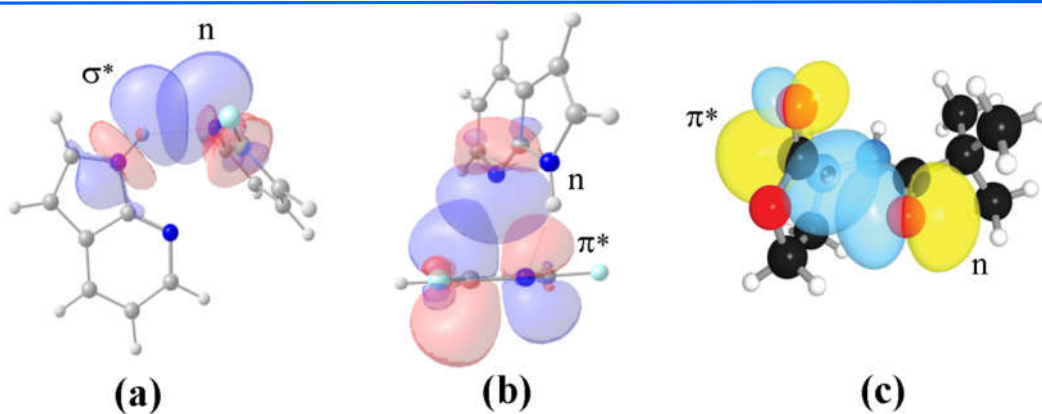


Figure 1.2 NBO view of (a) Overlap of lone pair orbital (n) of nitrogen with σ^* antibonding orbital of the N-H bond in N-H...N hydrogen bonding interaction. (b) Overlap of lone pair orbital of nitrogen with π^* antibonding orbital of aromatic ring in $n \rightarrow \pi_{Ar}^*$ interaction and (c) overlap of oxygen lone pair with π^* antibonding orbital of a carbonyl group in $n \rightarrow \pi_{Am}^*$ interaction. Figure (c) adapted in part with permission from ref. 61. Copyright [2014] American Chemical Society.

1.2.1 Classification of $n \rightarrow \pi^*$ interaction

The $n \rightarrow \pi^*$ interaction is broadly classified into two types, $n \rightarrow \pi_{Am}^*$ (amide) and $n \rightarrow \pi_{Ar}^*$ (aromatic), based on the nature of the acceptor π -system.¹ The $n \rightarrow \pi_{Am}^*$ interaction is delocalization of the lone pair (lp) electrons on the oxygen atom of a carbonyl group into the π^* orbital of an adjacent carbonyl group and this interaction is generally present in the

backbone of proteins. (see Figure 1.1a).^{2,7,57} This interaction follows the Burgi-Dunitz trajectory ($O\dots C=O$ distance ≤ 3.2 Å and $\angle O\dots C=O = 109 \pm 10^0$) required for the optimal overlap during the nucleophilic attack at the carbonyl carbon. On the other hand, the $n \rightarrow \pi_{Ar}^*$ interaction occurs through the overlap between the lone pair (lp) electrons on an electronegative atom (e.g. oxygen of a carbonyl group) with the π^* orbitals of an aromatic ring (See Figure 1.1c). In this case, the geometrical requirements for the optimum interaction is given by the distance between the carbonyl oxygen and aromatic ring centroid (2.8-3.8 Å) as well as the angle between the aryl and carbonyl planes ($\leq 90^0$). The $n \rightarrow \pi_{Ar}^*$ interaction is mostly observed in nucleic acids and in the side chain of proteins.³⁻⁶ $n \rightarrow \pi_{Ar}^*$ interaction is also termed as lone pair (lp)... π interaction.

In the case of the $n \rightarrow \pi_{Am}^*$ interaction, which is also called $C=O\dots C=O$ $n \rightarrow \pi^*$ interaction, the donor carbonyl group distorts the plane of the acceptor carbonyl group and consequently the carbon atom of the acceptor carbonyl group rises above the plane of its substituents and moves towards the oxygen atom of the donor carbonyl group. Such a deviation from the planarity can be measured as degree of pyramidalization (Δ), which is also a characteristic signature of the $n \rightarrow \pi_{Am}^*$ interactions in proteins and other molecules.^{56,57}

1.3 Signature of $n \rightarrow \pi^*$ interaction in biomolecules

Significance of $n \rightarrow \pi^*$ interaction in biomolecules is revealed through their crystal structure analysis. The geometrical parameters for favorable $n \rightarrow \pi_{Am}^*$ and $n \rightarrow \pi_{Ar}^*$ interactions mentioned in the previous section serves as a basis to search the short contacts between two carbonyl groups ($C=O\dots C=O$) or between an electronegative atom and an aromatic ring, in the crystal structures of biomolecules.

1.3.1 $n \rightarrow \pi^*$ interaction in nucleic acids

The $n \rightarrow \pi_{Ar}^*$ interaction was first reported in Z-DNA by Egli and co-workers in 1995 through analysis of its crystal structure.⁸ Z-DNA is found to be stable and rigid even though it does not have proper base stacking like A-DNA and B-DNA have. Crystal structure of Z-DNA reveals that the O4' oxygen of the deoxyribose sugar of the cytidine moiety points directly towards the guanine ring of the guanidium (G) moiety at each GC site (see Figure 1.3a) while the stacking interaction between the guanine and cytosine bases is mostly disrupted. The distance between the oxygen atom of the sugar and one of the carbons of the guanine ring in the Z-DNA has been found to be 2.98 Å, which is less than the sum of the van der Waals radii of the oxygen and the carbon atoms. The angle between the O4 atom

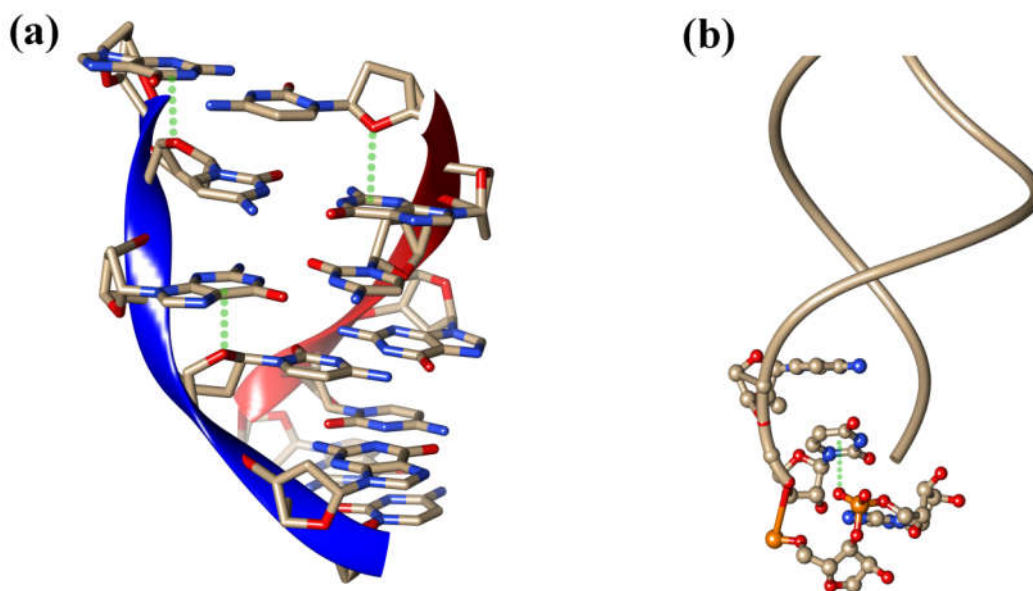


Figure 1.3 (a) Crystal structure of Z-DNA (PDB ID-131D) showing $n \rightarrow \pi_{Ar}^*$ interaction between oxygen atom of the cytidine (C) sugar and guanine ring of the guanidium (G) moiety. (b) Crystal structure of tRNA (PDB ID-1EHZ) showing $n \rightarrow \pi_{Ar}^*$ interaction between oxygen atom of phosphate and cytosine ring at the U-turn.

and the exocyclic C–N bond, i.e. $\angle O4 \dots C=N$, is 105° . It has been demonstrated from this geometrical arrangement of the oxygen atom of the sugar unit and the guanine ring that an attractive $n \rightarrow \pi^*$ interaction between one of the lone pairs of the O4' atom and the π^* orbitals

of the guanine ring contributes to the stability of the Z-DNA, in spite of the poor base stacking present there.

Later, Egli and co-workers have performed Cambridge Structural Database (CSD) analysis and identified several nucleic acids (tRNA, hammerhead ribozyme and RNA Pseudoknot) where significant $n \rightarrow \pi^*$ interactions are present.³ They have pointed out that there is a possibility of the $n \rightarrow \pi^*$ interactions at the U-turns of the tRNA and the hammerhead ribozyme (see Figure 1.3 b). U-turns are actually structural motifs found in diverse three dimensional structures of RNA. At the U-turn, RNA backbone makes a sharp turn of about 120° from the standard helical conformation between the first and second nucleotides of the UNR sequence, where U is uridine, N is any base and R is usually adenine or guanine.³ It is interesting to note that the U-turns are stabilized by two hydrogen bonds and an $n \rightarrow \pi^*$ interaction between an oxygen atom of the phosphate group of the third residue and the face of the nucleobase of the first nucleotide. Egli and co-workers have also reported an $n \rightarrow \pi^*$ interaction between the oxygen of water molecules and the aromatic ring of unstacked nucleobases in the crystal structure of an RNA pseudoknot obtained from beet western yellow virus.⁵⁵

Another crystallographic data analysis performed by Sankararamakrishnan and co-workers also provides evidence of $n \rightarrow \pi^*$ interaction in nucleic acids.⁹ They have analysed several crystal structures of DNA and RNA to find the close contacts between the oxygen atom of one base and aromatic centre of another base. They have analyzed 77 crystal structures of DNA having 110 base sequences and 55 crystal structures of RNA containing 76 base sequences. It has been found that $n \rightarrow \pi^*$ interaction is possible in 91 base pairs in DNA and 18 base pairs in RNA. The authors have reported that oxygen-aromatic close contacts between the base pairs are very less frequent in RNA compared to those in DNA. They have performed *ab-initio* calculations on all the 91 base pairs in DNA showing close

contacts between the oxygen atom and the centre of aromatic ring by taking the co-ordinates of the atoms from the crystal structures. It has been found that such close contacts are indeed attractive in nature.

1.3.2 $n \rightarrow \pi^*$ interaction in proteins

1.3.2.1 $n \rightarrow \pi^*$ interaction in the backbone of proteins.

It has been found that the $n \rightarrow \pi^*$ interaction, in similarity to the hydrogen bonding interaction, plays a significant role in the stability of the backbone of proteins.^{2,7,57,60} The search for the significance of the $n \rightarrow \pi^*$ interaction in proteins began after its recognition in the stability of the collagen triple helix.¹⁰ Collagen is the most abundant protein in animals. It consists of three polyproline II-type (PPII) helices which are tightly intertwined with each

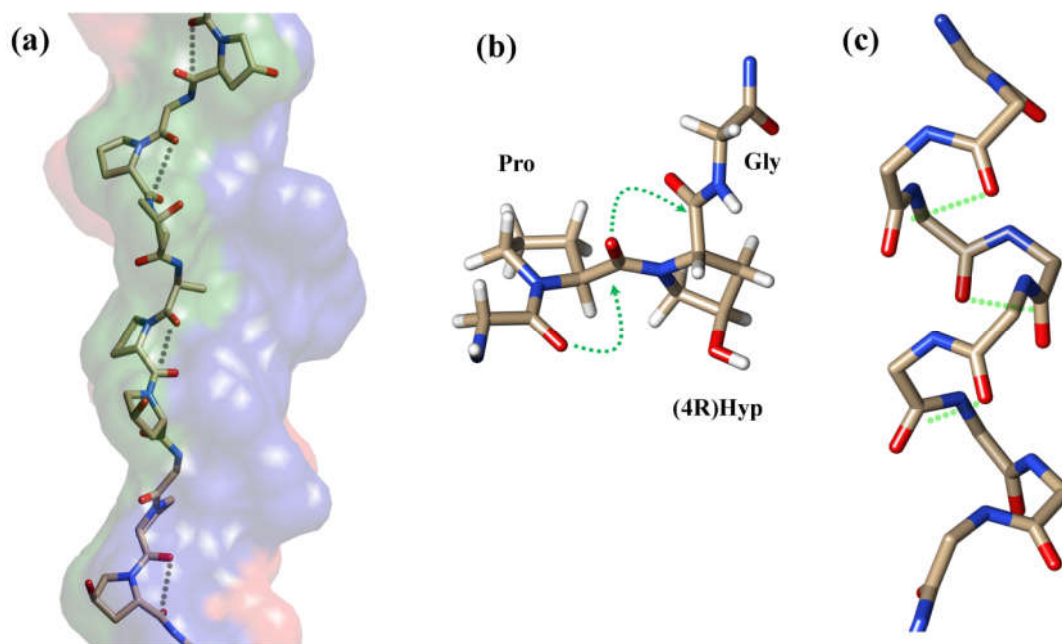


Figure 1.4 (a) $n \rightarrow \pi_{Am}^*$ interaction in the backbone of PP-II helix of collagen (PDB ID-1CAG) between the carbonyl groups of residue i and $i+1$. (b) Sequence of collagen (pro-Hyp-Gly). (c) $n \rightarrow \pi_{Am}^*$ interaction in the backbone of α -helix (PDB ID-1AL1) between carbonyl groups of residue i and $i+1$.

other through hydrogen bonding interaction.^{54,84} The repeating amino acid sequence of each PPII helix is Xaa–Yaa–Gly, where Xaa is proline (Pro) and Yaa is (2S,4R)-4-hydroxyproline (Hyp). The peptide bond between residue Xaa and Yaa (prolyl peptide bond) of collagen predominantly exist in trans conformation, which allows the carbonyl group of residue Xaa and Yaa to come in close contact along the Burgi-Dunitz trajectory (see Figure 1.4).^{10,54,85,86} The crystal structures, NMR spectroscopy and computational analysis of collagen-mimetic peptides also show that the trans conformation of the prolyl peptide bond is more stable compared to the cis conformation.¹⁰ In the trans form, the lone pair orbital of the carbonyl oxygen atom of residue *i-1* overlaps with the π^* orbital of the carbonyl group of residue *i* ($O_{i-1} \dots C_i=O_i$). These studies suggest that the trans conformations of the peptide bond in individual polyproline strand of collagen is stabilized by $n \rightarrow \pi^*$ interaction that operates between the residues *i* and *i+1*.^{7,13,54}

Further, it has been observed that the thermal stability of collagen is enhanced due to the presence of electron-withdrawing substituents (for example hydroxyl group or fluorine) at the 4R configuration of the Yaa residue.⁸⁷ Electron-withdrawing substituents at the 4R position impose the exo pucker of the pyrrolidine ring due to gauche effect.^{54,59} The exo pucker of the pyrrolidine ring favors the $n \rightarrow \pi^*$ between the neighboring carbonyl groups. Conversely, the 4S configuration imposes the endo pucker of the proline ring, which disfavors the $n \rightarrow \pi^*$ interaction between the residue *i* and *i+1*.^{54,85} This clearly explains the choice of nature to choose explicitly the 4R-configuration instead of 4S-configuration in the structure of collagen triple helix. The presence of the $n \rightarrow \pi^*$ interactions in the backbone of individual PP-II helix of collagen accounts for very long and robust structure of individual strand inspite of absence of any intrastrand hydrogen bonding interaction.

After the discovery of the $n \rightarrow \pi^*$ interaction in collagen and PP-II helices, the search for the $n \rightarrow \pi^*$ interaction in other secondary structures of proteins was initiated. Raines and

co-workers have performed computational and PDB analysis to find the presence of the $n \rightarrow \pi^*$ interactions in proteins and other molecules.⁷ Christian Fufezan followed a similar procedure to determine the significance of the $n \rightarrow \pi^*$ interaction in the structural stability of proteins.⁶⁸ Both the studies by Raines and co-workers and those of Christian Fufezan show that there are abundant $n \rightarrow \pi^*$ interactions in the allowed regions of the Ramachandran plot. Further, the computational search of the possible conformations of proteins which can give rise to an $n \rightarrow \pi^*$ interaction correlates well with the actual PDB search.

These studies show that the highest propensity for the $n \rightarrow \pi^*$ interaction is in left and right handed α -helices. It is also present in 3_{10} helices, twisted β -turns and β -bulges. However, the extended β -strands have the least propensity for the $n \rightarrow \pi^*$ interaction between the $i+1$ and i residues, as the neighbouring carbonyl groups in this structure are at a distance greater than 3.2 \AA . These analysis showed that $n \rightarrow \pi^*$ interaction is abundant in the structures of proteins and contribute significantly towards the stability of the protein structures. Very recently, it has been observed through crystal structure and computational analysis that the oxygen atom of the acceptor carbonyl group ($C_{i+1}=O_{i+1}$) can also donate its lone pair electron density back to the π^* orbital of the donor $C_i=O_i$ group.⁸³ This has been called as reciprocal $n \rightarrow \pi^*$ interaction. Although the propensity of this interaction is less, it imparts additional stability to the structures of proteins.

1.3.2.2 $n \rightarrow \pi^*$ interaction involving side chains of proteins

The $n \rightarrow \pi^*$ interaction exists not only in the backbone but also in the side chains of proteins. Sankararamakrishnan and co-workers have analyzed high resolution crystal structures of about 500 proteins and reported that the oxygen atom of the backbone carbonyl group interacts frequently with side chain carbonyl groups as well as aromatic centers.⁵ Thus, both $n \rightarrow \pi^*_{Am}$ and $n \rightarrow \pi^*_{Ar}$ types of interactions are present in proteins. It has been found that there are 249 examples where a close contact of about 3.5 \AA between an aromatic center and

backbone carbonyl oxygen is present. On the other hand, the occurrence of the interaction between a side chain carbonyl oxygen and aromatic center is very less frequent (37 examples). Fig. 1.5(a) shows an example of an $n \rightarrow \pi_{Ar}^*$ interaction between the backbone carbonyl oxygen atom of an alanine residue and the aromatic center of a phenylalanine residue in the protein bacterial luciferase enzyme (PDB ID:1LUC). A similar interaction between the side chain carbonyl oxygen of glutamine and the aromatic center of tyrosine present in the protein *Serratiamarcescens* endonuclease (PDB ID:1QL0) is shown in Fig. 1.5(b).

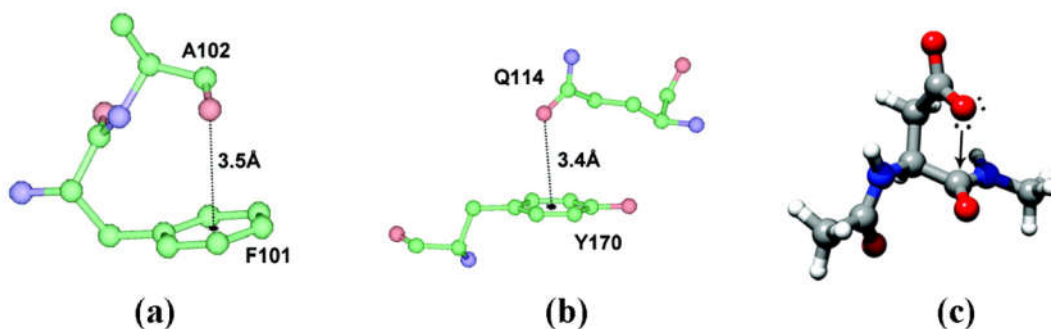


Figure 1.5 (a) The $n \rightarrow \pi_{Ar}^*$ interaction between backbone carbonyl oxygen of Ala and side chain aromatic ring of Phe residues (PDB ID-1LUC). (b) $n \rightarrow \pi_{Ar}^*$ interaction between side chain carbonyl oxygen of Glu and side chain aromatic ring of Tyr residues (PDB ID-1QL0). (c) $n \rightarrow \pi_{Am}^*$ interaction between side chain carbonyl oxygen and backbone carbonyl group of Asp residue (PDB ID-1AGJ), an example of self contacting Asp residues in proteins. Adapted in part with permission from ref. 5 and 6. Copyright [2007] American Chemical Society.

Close contact between the carbonyl groups of the backbone and side chain of the same amino acid residue aspartic acid (Asp) has been identified by Sankararamkrishnan and co-workers from an exhaustive search of high-resolution protein crystal structures in the PDB.⁶ They have found that these intra-residue close contacts between the carbonyl groups are present in about 102 Asp residues. Figure 1.5c shows an example of this interaction in an Asp residue of the protein epidermolytic toxin A (PDB ID:1AGJ). The authors have also

recognized $n \rightarrow \pi^*$ interactions between water oxygen atoms and the π -cloud of aromatic residues in proteins through the detailed analysis of high resolution crystal structures of proteins as well as quantum chemistry calculations of model compounds based on protein structures in the presence of different orientations of water molecules.⁴

1.3.2.3 Co-operativity between hydrogen bonding and $n \rightarrow \pi^*$ interaction in proteins.

It has been found from the PDB search that $n \rightarrow \pi^*$ interaction is present in the backbone of α -helix along with the hydrogen bonding interaction.^{2,7,12,82} In a α -helix, the hydrogen bonding interaction ($n \rightarrow \sigma^*$) is present between i and $i+4$ residues while the $n \rightarrow \pi^*$ interaction is present between i and $i+1$ residues. Interestingly, the same carbonyl oxygen atom of residue i is involved in both hydrogen bonding and $n \rightarrow \pi^*$ interaction.⁷ As oxygen atom has two lone pairs (s-type and p-type), the s-type lone pair is engaged in hydrogen bonding with the N-H bond of the residue $i+4$ while the p-type lone pair takes part in the $n \rightarrow \pi^*$ interaction with the neighbouring C=O group (see Figure 1.6). Since, same oxygen atom is involved in both hydrogen bonding and $n \rightarrow \pi^*$ interactions, strength of both of these interactions are interdependent in α -helix. This induces an interplay between hydrogen bonding and $n \rightarrow \pi^*$ interaction, where one interaction can either increase or decrease the strength of the other interaction.¹²

For example, presence of the $n \rightarrow \pi^*$ interaction between i and $i+1$ residues shortens the $O_i \dots C_{i+1} = O_{i+1}$ distance which causes the compaction of the backbone, that could decrease the distance between residue i and $i+4$ to have stronger hydrogen bonding.⁷ Further, the involvement of $C_{i+1} = O_{i+1}$ in hydrogen bonding with N-H makes it better acceptor for $n \rightarrow \pi^*$ interaction as the hydrogen bonding polarises the $C_{i+1} = O_{i+1}$ bond and makes it electron deficient. This can be called as positive co-operativity between hydrogen bonding and $n \rightarrow \pi^*$ interaction, where one interaction increases the strength of the other. Negative co-operativity

between hydrogen bonding and $n \rightarrow \pi^*$ interaction has also been observed in the peptidic systems where, $n \rightarrow \pi^*$ interaction opposes the hydrogen bonding and vice versa.⁸²

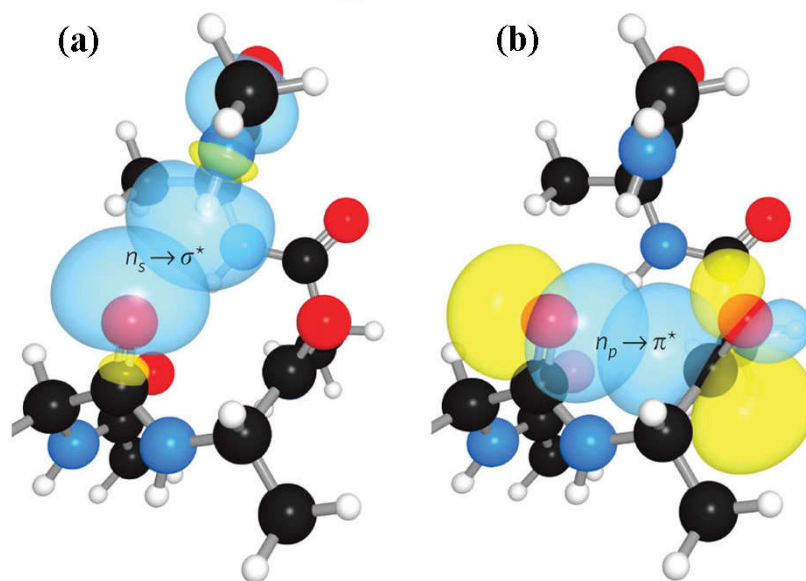


Figure 1.6 (a) Hydrogen bonding ($n \rightarrow \sigma^*$) interaction in α -helix between carbonyl group of residue i and N-H bond of residue $i+4$. (b) $n \rightarrow \pi^*$ interaction in α -helix between carbonyl groups of residue i and $i+1$. Adapted in part with permission from ref. 7. Copyright [2010] Nature Chemical Biology.

Interplay between hydrogen bonding and $n \rightarrow \pi^*$ interaction has been investigated in the proteins using crystallographic as well as computational studies.¹² It has been found that the side-chain carbonyl group of asparagine residues in proteins can involve in $n \rightarrow \pi^*$ interaction with the carbonyl group of the backbone and it can also form hydrogen bond with the N-H group of $i+2$ residue (hydrogen bond between i and $i+2$ residues is called as local hydrogen bond) as well as N-H group of residue $i+n$ where, $n > 5$ (hydrogen bond between i and $i+n$ residue where, $n > 5$ is called as non local hydrogen bond). Crystal structure and computational analysis show that strength of the $n \rightarrow \pi^*$ interaction decreases in the absence of local hydrogen bond, as the side chain carbonyl groups of the asparagine residue are involved in stronger hydrogen bond with $i+n$ ($n > 5$) residue. While in the presence of local

hydrogen bond, which is weaker than non-local hydrogen bond, the $n \rightarrow \pi^*$ interaction is more prominent. Thus a strong hydrogen bond decreases the strength of the $n \rightarrow \pi^*$ interaction while the $n \rightarrow \pi^*$ interaction is stronger in the presence of weak hydrogen bond (local hydrogen bond).

1.4 Signature of $n \rightarrow \pi^*$ interaction in materials.

There are quite extensive reports in the literature demonstrating the existence of the $n \rightarrow \pi^*$ interaction and its role in the supramolecular self assembly of molecules to give rise to specific structures of materials. Mostly, $n \rightarrow \pi^*_{Ar}$ type of interaction, which is also referred as lone pair (lp)... π interaction, has been observed in materials.

1.4.1 $n \rightarrow \pi^*$ interaction in supramolecular structures.

Very first report of the existence of the $n \rightarrow \pi^*$ interaction in material has been provided by Reedijk and co-workers who have called this interaction as a new supramolecular bond.^{11,80} They reported $n \rightarrow \pi^*$ interaction in the crystal structure of $[Zn_4(\text{oxodentriaz})Cl_8](CH_3CN)_2(H_2O)$ complex, which shows that the nitrogen atom of acetonitrile is in close contact with the aromatic ring of triazine (see Fig. 1.7a).⁸⁰ The distance between the nitrogen atom of the acetonitrile molecule and the center of the triazine ring is 3.25 Å and the angle of approach of the nitrogen atom of the acetonitrile molecule towards the center of the triazine ring is 75.21°. These favorable geometrical parameters indicate the presence of an $n \rightarrow \pi^*$ interaction between the nitrogen atom of acetonitrile and heteroaromatic ring triazine.

Later, Reedijk and co-workers have designed two triazine-based compounds which self-assemble to form structures stabilized by both $C-H \dots \pi$ and $n \rightarrow \pi^*$ interactions.⁸⁸ The crystal packing of the self assembled structures of both the compounds has been shown in Fig. 1.7b and c, which shows that each molecular unit interacts with four neighbouring molecules by means of two $n \rightarrow \pi^*$ and two weak $C-H \dots \pi$ interactions. Presence of $n \rightarrow \pi^*$

interaction along with C-H... π imparts additional stability to the structure. Further, the same group reported the crystal structure of a co-ordination complex, $[\text{Cu}(\text{Hspet})(\text{NO}_3)_2](\text{NO}_3)_0.5\text{H}_2\text{O}$ where, double $n \rightarrow \pi^*$ interaction holds the two complexes together in their crystal packing.⁸⁹

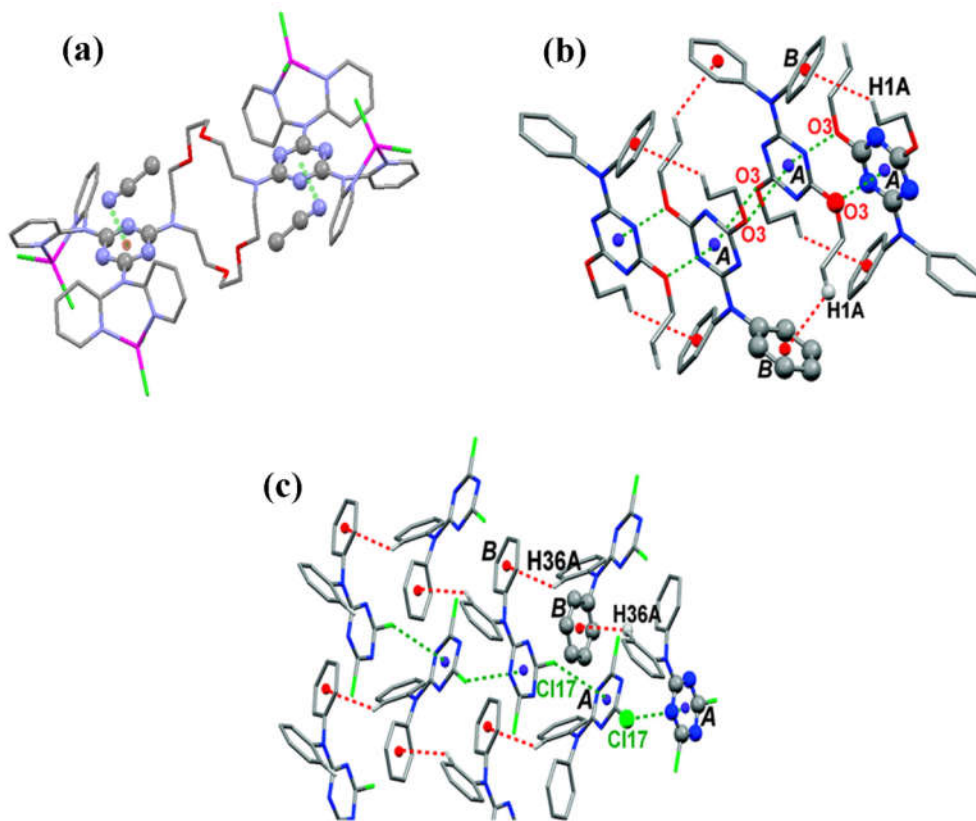


Figure 1.7 (a) $lp \dots \pi$ interaction between nitrogen atom of acetonitrile and aromatic ring of triazine in the crystal structure of $\text{Zn}_4(\text{oxodentriz})\text{C}_{18}](\text{CH}_3\text{CN})_2(\text{H}_2\text{O})$ complex. Adapted with permission from ref. 80. Copyright [2006] American Chemical Society. (b) and (c) supramolecular structures generated by $\text{O}(lp) \dots \pi$ and $\text{Cl}(lp) \dots \pi$ interaction, respectively, along with $\text{C-H} \dots \pi$ interaction. Adapted with permission from ref. 88. Copyright [2007] American Chemical Society.

Mukhopadhyay and co-workers have reported the crystal structure of two co-ordination complexes of nickel II malonate, namely $(\text{C}_5\text{H}_7\text{N}_2)_4[\text{Ni}(\text{C}_3\text{H}_2\text{O}_4)_2(\text{H}_2\text{O})_2](\text{ClO}_4)_2$ and $(\text{C}_5\text{H}_7\text{N}_2)_4[\text{Ni}(\text{C}_3\text{H}_2\text{O}_4)_2(\text{H}_2\text{O})_2](\text{PF}_6)_2$.⁹⁰ The crystal structures of these complexes are stabilized by $n \rightarrow \pi^*$ interaction, $\pi \dots \pi$ stacking interaction and anion... π interaction. All the

three types of non-covalent interactions form a chain which stabilizes the supramolecular network of the complexes. Ghosh and co-workers have also reported three dimensional molecular assembly of $[\text{Cu}_2(\text{pic})_3(\text{Hbyp})(\text{H}_2\text{O})(\text{ClO}_4)_2]$ complex which is stabilized by combination of $n \rightarrow \pi^*$, $\pi \dots \pi$ stacking, anion $\dots \pi$ and hydrogen bonding interactions.⁹¹ The above examples demonstrate that the $n \rightarrow \pi^*$ interaction, in combination with other non-covalent interactions, plays an important role in the self-assembly of the molecules to form large multidimensional structures.

Reedijk and co-workers have also performed an extensive search of the Cambridge Structural Database (CSD) to identify $n \rightarrow \pi^*$ interactions in materials.¹¹ They have analyzed 263007 crystal structures and each one of them contains at least one neutral six membered aromatic ring. The authors have observed several crystal structures (9,168) showing close contact between halogen atoms (fluorine, chlorine, bromine and iodine) and the aromatic ring. Close contact between the oxygen atom of an ether group and an aromatic ring ($\text{O} \dots \pi$) has been observed in 3703 crystal structures, while $\text{C}=\text{O} \dots \pi$ close contact has been found in 5069 crystal structures. Similarly, various crystal structures showing close contact between nitrogen and the aromatic ring have been observed. In fact, they have observed $n \rightarrow \pi^*$ interactions in a large number of crystal structures and their observation has helped in the recognition of $n \rightarrow \pi^*$ interactions in materials.

Not only oxygen, nitrogen and halogen atoms act as lone pair donors in $n \rightarrow \pi^*$ interactions, but also other elements in the periodic table have been demonstrated as potential lone pair donors for the $n \rightarrow \pi^*$ interaction. Caracelli and co-workers have reviewed several crystal structures where antimony (Sb) and bismuth (Bi) participate in the $\text{lp} \dots \pi$ interaction.^{92,93} The $n \rightarrow \pi^*$ interaction between the metal atom (Sb, Bi) and aromatic ring can

lead to the formation of small one dimensional or large three-dimensional structures. The authors have also found the existence of the $Sb(lp)\dots\pi$ interaction in biomolecules.⁹²

1.4.2 $n\rightarrow\pi^*$ interaction in polymers

$n\rightarrow\pi^*$ interaction also contribute to the stability of poly (Lactic acid) (PLA), which is a biodegradable polyester.⁶² The crystal structure of α -PLA shows that its backbone dihedral angles i.e. (ϕ and Ψ) are similar to those of the PPII helix strand of collagen. The neighboring carbonyl groups in PLA are oriented along the Burgi-Duntiz trajectory for favorable $n\rightarrow\pi^*$ interaction (see Figure 1.8). Calculations suggest that energy for every $n\rightarrow\pi^*$ interaction in the PLA is 0.44 kcal/mol. Further, the analysis of crystal structures of small-chain of PLA revealed pyramidalization of the acceptor carbonyl group which is the characteristic of

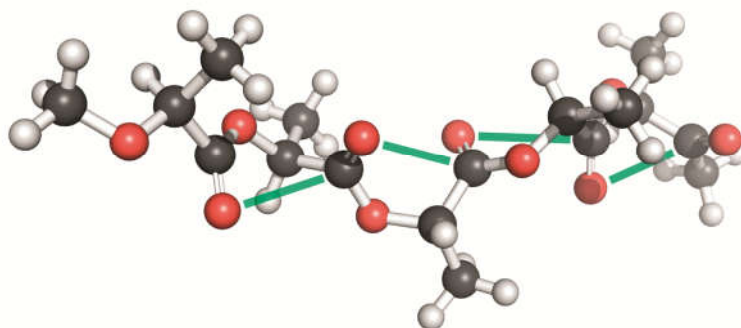


Figure 1.8 Crystal structure of Poly lactic acid (PLA) showing $n\rightarrow\pi^*$ interaction between adjacent carbonyl groups, oriented along the Burgi-Duntiz trajectory. (Reproduced from ref. 62 with permission from The Royal Society of Chemistry.)

$n\rightarrow\pi_{Am}^*$ interaction. This suggests that $n\rightarrow\pi^*$ interaction stabilizes the structure of PLA. Like PPII helix, PLA also lacks intramolecular hydrogen bonding interaction. This indicates that $n\rightarrow\pi^*$ interaction can exist independently and it is not just a short contact imposed by the geometric constraint due to the hydrogen bonding patterns.

1.5 Significance of $n\rightarrow\pi^*$ interaction in small molecules

Importance of $n \rightarrow \pi^*$ interaction is observed in several small molecules like N-acyl homoserine lactones, drugs, neurotransmitters and peptoids.^{1,61,63,72,74,75,94} N-acyl homoserine lactones (AHL) are signalling molecules which mediate quorum sensing in Gram -ve bacteria. N-acyl homoserine lactones have two carbonyl groups adjacent to each other as in proline residue (see Figure 1.9a).⁶¹ The crystal structure of N-trimethyl homoserine lactone (a non-natural homoserine lactone) shows that the two carbonyl groups are in close proximity following the Burgi-Dunitz trajectory for favourable $n \rightarrow \pi^*$ interaction. It has been shown that N-acyl homoserine lactones like proline residue can also exhibit $n \rightarrow \pi^*$ interaction between the proximal carbonyl groups. Further, the crystal structure of N-acyl homoserine lactone in the bound-state with the protein demonstrate that the $n \rightarrow \pi^*$ interaction in the

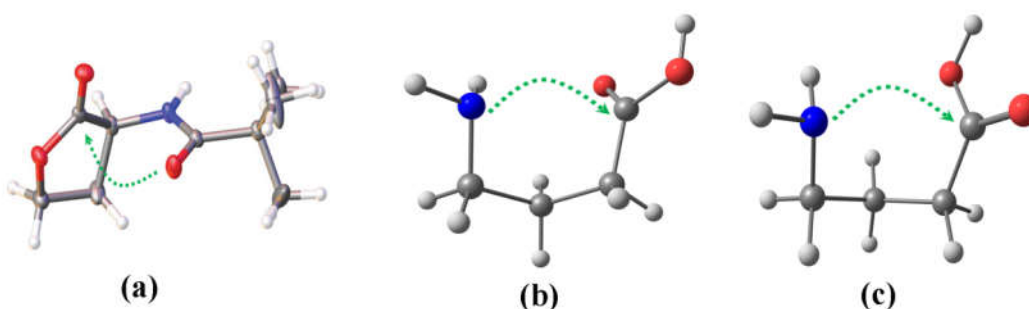


Figure 1.9 (a) Crystal structure of N-trimethyl homoserine lactone showing $n \rightarrow \pi^*$ interaction between the neighbouring carbonyl groups. Adapted in part with permission from ref. 61. Copyright [2014] American Chemical Society. (b) and (c) lowest energy conformers of GABA showing $n \rightarrow \pi^*$ interaction between nitrogen atom and C=O group of carboxylic acid.

molecule is disrupted due to the formation of hydrogen bond between N-acyl carbonyl oxygen and tyrosine residue of the receptor. Thus there is a competition between the hydrogen bonding and the $n \rightarrow \pi^*$ interaction at the time of binding of N-acyl homoserine lactones with its receptor. Any factor that can attenuate the $n \rightarrow \pi^*$ interaction of the AHLs will affect its binding affinity with the receptor.

The $n \rightarrow \pi^*$ interaction have also been reported in γ -Amino butyric acid (GABA), which is an inhibitory neurotransmitter in the brain and spinal cord. Microwave spectroscopy

data shows the evidence of nine conformers of GABA in the gas phase.⁷⁵ Out of 9, five conformers have intramolecular non-covalent interactions while remaining four conformers are without any intramolecular non-covalent interaction. Among the five conformers, three show the possibility of intramolecular hydrogen bonding and two show the possibility of $n \rightarrow \pi^*$ interaction. The conformers which show $n \rightarrow \pi^*$ interaction are observed to be the lowest energy conformers of GABA (see Figure 1.9b and 1.9c). Similarly, four lowest energy conformers of β -alanine has been observed in gas phase through microwave spectroscopy.⁷⁴ Among the four conformers of β -alanine, three conformers are stabilized by intermolecular hydrogen bonding (N-H...O=C) while the fourth conformer is stabilized by $n \rightarrow \pi^*$ interaction between nitrogen lone pair and π^* orbital of carbonyl group. These results clearly indicate that even though $n \rightarrow \pi^*$ interaction is weaker in strength compared to hydrogen bonding it can independently stabilize the conformations of the molecule. Further, the stability of the conformers having $n \rightarrow \pi^*$ interaction is comparable with the stability of the hydrogen bonded conformers.

The significance of the $n \rightarrow \pi^*$ interaction has been observed in analgesic medicine aspirin.⁶³ Crystal structure of aspirin shows close contact between the oxygen atom of the hydroxy group of carboxylic acid and the carbonyl group of the ester along the Burgi-Dunitz trajectory. Calculation shows an $n \rightarrow \pi^*$ interaction energy of 0.95 kcal/mol for this conformer. Another conformer predicted through calculation shows $n \rightarrow \pi^*$ interaction between the carbonyl oxygen atom of carboxylic acid and the carbonyl group of ester with interaction energy of 1.73 kcal/mol. Interestingly, both the conformers of aspirin has been observed in the gas-phase through microwave spectroscopy.⁷² Structures of these two conformers of aspirin are shown in Fig. 1.10a and 1.10b. Thus both crystal structure and microwave spectroscopy data suggest that lowest energy conformers of aspirin is stabilized by $n \rightarrow \pi^*$ interaction. It has been speculated that intermolecular $n \rightarrow \pi^*$ interaction in aspirin

may shield the donor oxygen from interaction with solvent that helps it to pass through the hydrophobic channel without hydrolysis. Thus $n \rightarrow \pi^*$ interaction could facilitate the chemical and pharmacological functions of aspirin.

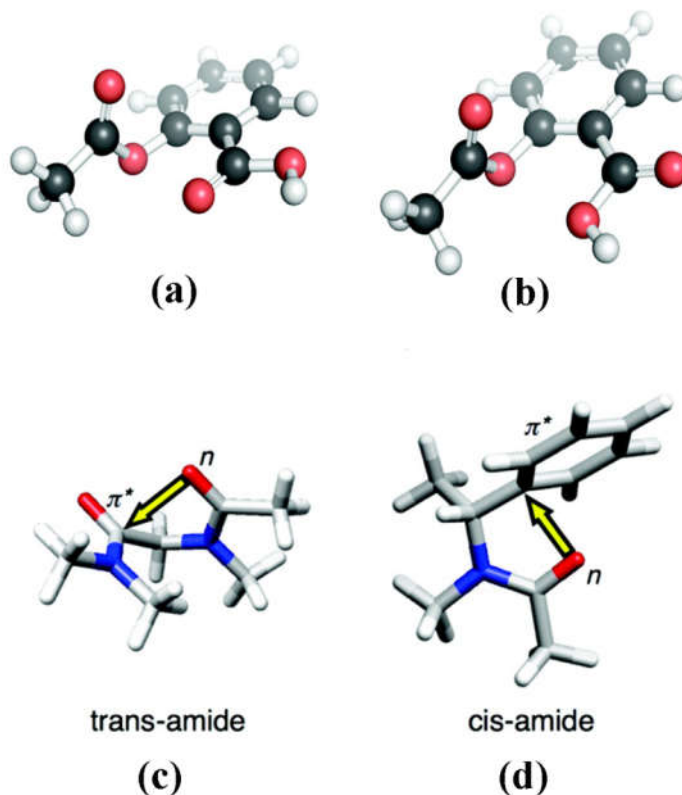


Figure 1.10 (a) and (b) are the lowest energy conformers of aspirin showing $n \rightarrow \pi^*$ interaction. Adapted in part with permission from ref. 63. Copyright [2011] American Chemical Society. Structures of small peptoid mimicking (c) $n \rightarrow \pi_{Am}^*$ interaction and (d) $n \rightarrow \pi_{Ar}^*$ interaction. Adapted in part with permission from ref. 1. Copyright [2007] American Chemical Society.

The $n \rightarrow \pi^*$ interaction is also found to regulate the conformations of peptoids.^{1,70} A peptoid is a polymer of N-substituted glycine residues. It lacks hydrogen bonding interactions in its backbone, like polyproline and poly (lactic acid). It has been observed that the $n \rightarrow \pi_{Am}^*$ interaction stabilizes the backbone of peptoids while $n \rightarrow \pi_{Ar}^*$ interaction is present in the backbone-side chain contacts. Blackwell and co-workers have designed small peptoids to study these interactions. The structures of small peptoids mimicking the $n \rightarrow \pi_{Am}^*$ interaction in the backbone and $n \rightarrow \pi_{Ar}^*$ interaction in the backbone-side chain contacts of peptoids have

been shown in Figure 1.10c and 1.10d, respectively. The $n \rightarrow \pi_{Am}^*$ interaction in the backbone of peptoid favors the trans conformation of the amide while the $n \rightarrow \pi_{Ar}^*$ interaction between backbone carbonyl group and side chain aromatic ring favor the cis conformation. Thus both the interactions could be used to tune the conformations of peptoids.

1.6 Understanding $n \rightarrow \pi^*$ interaction through NMR spectroscopy

NMR spectroscopy has been extensively used to understand the role of $n \rightarrow \pi^*$ interaction in the stability of biomolecules as well as the factors which can affect the $n \rightarrow \pi^*$ interaction.^{10,13,60,66} Raines and co-workers have used NMR spectroscopy to explore $n \rightarrow \pi_{Am}^*$ interaction in several proline derivatives as model systems. The peptide bonds in proline derivatives can have both cis and trans conformations. Since, the $n \rightarrow \pi^*$ interaction is present in only trans conformations, it will tend to increase the population of the trans

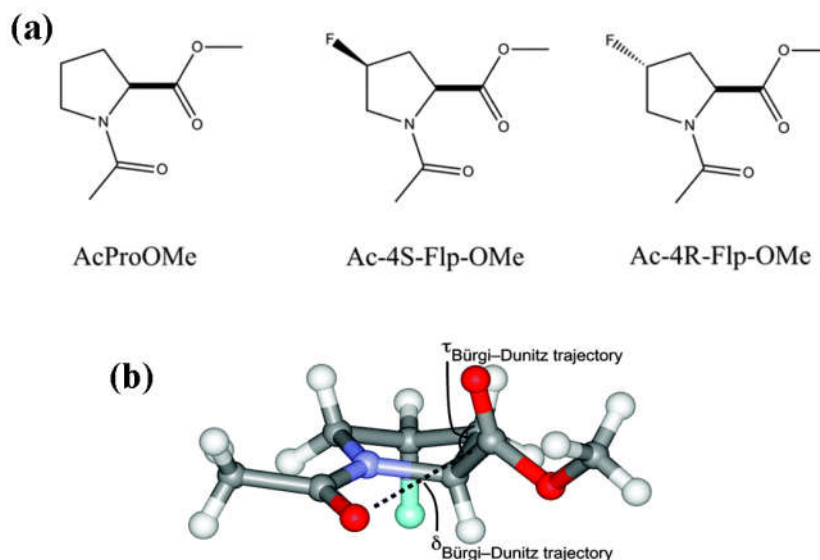


Figure 1.11 (a) Structures of trans conformers of N-acetylproline methylester (AcProOMe), N-acetyl-4S-Fluoroproline methylester (Ac-4S-Flp-OMe) and N-acetyl-4R-fluoroproline methylester (Ac-4R-Flp-OMe) from ref. 10. (b) Crystal structure of Ac-4R-Flp-OMe showing trans conformation of the peptide bond and orientation of adjacent carbonyl groups along the Bürgi-Dunitz trajectory. Adapted in part with permission from ref. 10. Copyright [2002] American Chemical Society.

conformer compared to the cis conformer. Therefore, population difference between the cis and the trans conformers can indicate the strength of the $n \rightarrow \pi_{Am}^*$ interaction between the neighboring carbonyl groups. Using ^1H NMR spectroscopy, Raines and co-workers⁹ have determined the equilibrium constant ($K_{\text{trans/cis}}$) between the trans and the cis conformers of the proline derivatives and this gives information about the relative population of both the conformers in the solution.

For example, the role of the $n \rightarrow \pi^*$ interaction in the stability of collagen has been revealed through NMR spectroscopy of three model compounds (AcProOMe, Ac-4R-Flp-OMe and Ac-4S-Flp-OMe).¹⁰ Structures of all the three model compounds are shown in Figure 1.11. NMR spectroscopy shows that $K_{\text{trans/cis}}$ is greater than 1 for all the three compounds indicating that the population of the trans conformer is more than the cis conformer. This study also proves that the trans form of the prolyl peptide bond in the collagen is more stable than the cis form. This observation is further supported by calculation which shows significant overlap between the lone pair orbital on amide oxygen and the empty π^* orbital of adjacent carbonyl group in the trans conformations. It is also revealed from the NMR spectroscopy that the presence of the electron withdrawing group (hydroxy or fluorine) on the proline ring at the 4R configuration enhances the population of the trans conformer, indicating a stronger $n \rightarrow \pi^*$ interaction. On the other hand, preference for the trans conformer in the 4S configuration is lower compared to that in the 4R configuration. This observation is also supported by computational analysis.

Similarly, NMR spectroscopy of N-formylproline phenylester (see figure 1.12) has been studied to understand the energetics of the $n \rightarrow \pi^*$ interaction.¹³ The substituents (X) at the para position of the phenyl ring has been varied from electron withdrawing group to electron donating groups to attenuate the electrophilicity of the acceptor carbonyl group and to observe its effect on the strength of the $n \rightarrow \pi^*$ interaction. NMR spectroscopy shows that

electron withdrawing groups increase the trans/cis ratio (>2.12) whereas electron donating groups decrease the trans/cis ratio (<2.12). This suggests that the electron withdrawing group decreases the energy of the π^* orbital of the acceptor carbonyl group making it more electrophilic and thus allows more closer overlap of the lone pair orbital of the oxygen and the π^* orbital of the $C_{i+1}=O_{i+1}$ group.

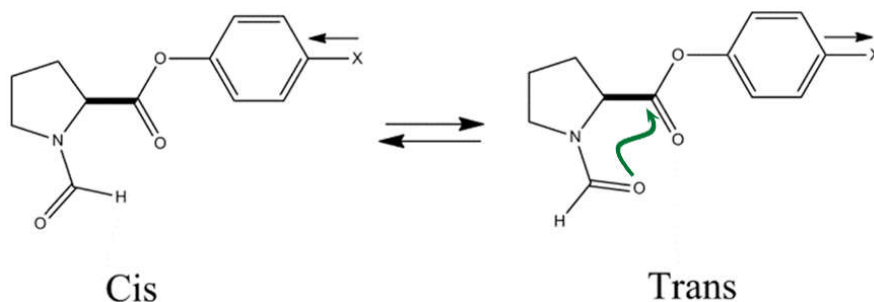


Figure 1.12 Structures of cis and trans conformers of N-formylproline phenylester from ref. 13. $n \rightarrow \pi^*$ interaction in the trans conformer is indicated by green arrow. X represents the electron donating or withdrawing group. An electron withdrawing group favours the trans conformation while electron donating group favours the cis conformation.

Raines and co-workers have further changed the nature of the substituent attached to the donor carbonyl group to observe the effect on $n \rightarrow \pi^*$ interaction.⁶⁶ The methyl group attached to the donor carbonyl group of N-acetylproline methylester is changed to monofluoromethyl group. As a result the trans/cis ratio decreases. Lower value of trans/cis ratio in case of monofluoromethyl group compared to the methyl group indicates that the inductive effect of fluorine decreases the donating ability of the donor oxygen thereby decreasing the population of the trans conformer. Further, substituting the monofluoromethyl group by difluoromethyl group or trifluoromethyl group results in slight decrease in the $n \rightarrow \pi^*$ interaction energy due to the inductive effect of fluorine. However, the trans/cis ratio increases in case of difluoromethyl and trifluoromethyl substitution compared to monofluoromethyl because of the steric interaction between fluorine and acceptor carbonyl group in the cis conformer. This results in increase in the population of the trans conformer.

Raines and co-workers have also studied the effect on the strength of the $n \rightarrow \pi^*$ interaction on changing the nature of the lone pair donor atom. They replaced the donor oxygen of the N-acetylproline methylester by sulphur to form N-thioacetylproline methylester (see Figure 1.13). NMR experiments show that trans/cis ratio of N-

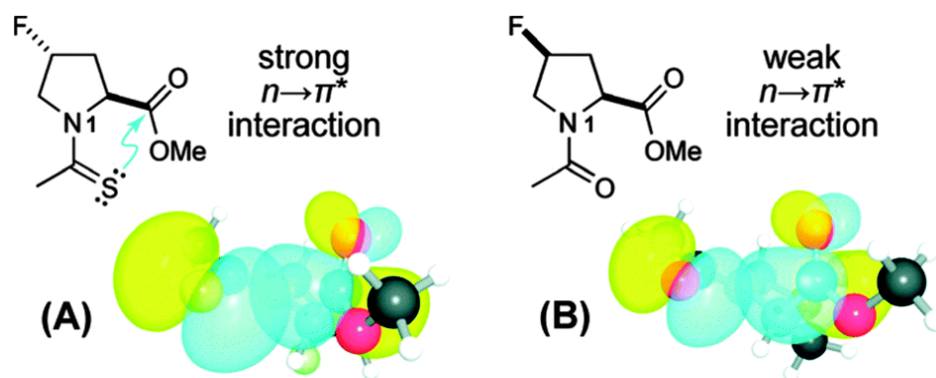


Figure 1.13 Structures of trans conformation of (a) N-thioacetyl-4R-fluoroproline methylester and (b) N-acetyl-4R-fluoroproline methylester. NBO views of the overlap of their respective n and π^* orbitals are shown below. Strong $n \rightarrow \pi^*$ interaction is observed when carbonyl oxygen is replaced by sulphur. Adapted in part with permission from ref. 60. Copyright [2009] American Chemical Society.

thioacetylprolinemethylester is 2 times greater than that measured for N-thioacetylproline methyl ester.⁶⁰ Calculation also shows that the energy of the $n \rightarrow \pi^*$ interaction in N-thioacetylproline methylester (1.3 kcal/mol) is more than N-acetylproline methylester (0.7 kcal/mol). Sulphur, being better electron pair donor, enhances the $n \rightarrow \pi^*$ interaction and favour the trans conformer more over the cis conformer. In general, the $n \rightarrow \pi^*$ interaction between the two neighbouring carbonyl groups is enhanced if electron withdrawing group is present near the acceptor carbonyl group and electron donating group is present near the donor carbonyl group. A stronger $n \rightarrow \pi_{Am}^*$ interaction in proline derivatives increases the population of its trans conformer over the cis conformer.

1.7 Physical nature of $n \rightarrow \pi^*$ interaction

1.7.1 $n \rightarrow \pi_{Am}^*$ interaction

The attractive interaction between two carbonyl groups can be thought of (1) coulombic interaction between the negatively charged oxygen atom of one carbonyl group and positively charged carbon atom of the other carbonyl group, (2) dipolar interaction between two permanent dipoles of the two carbonyl group or (3) a donor-acceptor interaction where electron density is donated from the lone pair orbital of the carbonyl oxygen to the empty π^* antibonding orbital of other carbonyl group.^{58,60} To reveal the nature of the attractive interaction between two carbonyl groups, Raines and co-workers have studied several proline derivatives using NMR spectroscopy. It has been observed that replacement of the oxygen atom of the amide carbonyl group in N-acetylproline methylester by sulfur results in an increase in the $K_{\text{trans/cis}}$ i.e. population of the trans conformer over the cis increases. If the interaction between the two carbonyl groups is electrostatic, then the value of $K_{\text{trans/cis}}$ should decrease as sulfur carries less negative charge compared to oxygen. This indicates that attractive interaction between the carbonyl group is not governed by electrostatic forces rather it could be either dipole...dipole interaction or donor-acceptor interaction.

For favorable dipole...dipole interaction, the two carbonyl groups should be orthogonal to each other and thus there will be restriction of all the four atoms to a fixed orientation. Crystal structure as well as computational analysis of small molecules and proline derivatives, show that there is no such restriction on the C=O...C=O dihedral angle. Further, it has been observed that $K_{\text{trans/cis}}$ value is higher for N-acetylproline methylester compared to that for N-acetylproline dimethylamide. Since the dipole moment of the amide is more than the ester, the $K_{\text{trans/cis}}$ value in the case of dimethylamide should be higher if the interaction between the neighboring carbonyl groups is dominated by dipolar interaction. Thus the interaction between the carbonyl groups of residue i and $i+1$ in proteins is due to

donor-acceptor interaction in which lone pair orbital (n) of carbonyl oxygen atom of residue i overlaps with the π^* antibonding orbital of the carbonyl group of residue $i+1$.

Any factor which decreases the energy gap between the n and π^* orbitals lead to a better overlap between them and hence stronger $n \rightarrow \pi^*$ interaction. For example, replacing donor oxygen with sulphur leads to stronger $n \rightarrow \pi^*$ interaction because energy of the lone pair orbital in thioamide is higher compared to that in amide. Relatively higher energy of the π^* orbitals in alkenes or fluoroalkenes make them poor acceptors for $n \rightarrow \pi^*$ interaction.⁶⁵ Another factor which increases the overlap between donor lone pair and acceptor π^* orbitals is the distance between donor oxygen and carbon atom of the acceptor carbonyl group. A shorter distance allows better overlap between n and π^* orbitals and hence makes stronger $n \rightarrow \pi^*$ interaction. However repulsion between the n orbital of the donor and the filled π orbitals of the acceptor carbonyl groups tends to oppose the $n \rightarrow \pi^*$ interaction.⁶⁴ Above studies clearly indicate that $n \rightarrow \pi^*$ interaction is basically governed by orbital interactions which can be explained only on the basis of quantum mechanics.

1.7.2 $n \rightarrow \pi^*_{Ar}$ interaction

The very first theoretical study performed on $C_6F_6 \dots H_2O$ complex by Dougherty and coworkers predicted that $n \rightarrow \pi^*$ interaction could be governed by electrostatic forces⁹⁵ because the oxygen atom of the water molecule is attracted towards the electron deficient aromatic ring of hexafluorobenzene. However, theoretical studies performed later shows that $n \rightarrow \pi^*$ interaction is even possible between the lone pair containing atom and the electron rich aromatic ring.⁹⁶⁻⁹⁸ It is indeed interesting that $n \rightarrow \pi^*$ interaction is favorable between the oxygen atom of H_2O and polycyclic aromatic hydrocarbons (PAHs, i.e. anthracene, triphenylene, coronene, circumcoronene, etc.) although the same interaction is repulsive in the benzene... H_2O complex.^{99,100} It has been also reported that the $n \rightarrow \pi^*$ interaction in PAH... H_2S complex is much stronger than that in PAH... H_2O .⁹⁹ Interestingly, this

interaction is attractive even in the benzene...H₂S complex.⁹⁹ It has also been demonstrated that substituted benzene with electron donating groups have attractive n→π* interactions with dimethyl ether and trimethyl ammonia while similar interaction is absent with water and ammonia.^{97,98} All of the results mentioned above indicate that increase in the dispersion in these systems switches on the n→π* interaction. Thus dispersion interaction plays a significant role in n→π* interaction.

The n→π* interaction between the oxygen atom and the electron-rich aromatic ring has also been studied through NMR spectroscopy by Gung and co-workers.^{96,101} They designed triptycene scaffold which has anti and syn conformations. The syn conformation allows close contact between aromatic ring and oxygen atom. The syn to anti ratio was determined using different substituents on the aromatic ring through NMR experiment. It has been observed that syn/anti ratio is greater than 2 even if the aromatic ring is substituted with an electron donating group. These studies clearly indicate that n→π*_{Ar} interaction has significant dispersion contribution.

Finally it is important to mention that n→π* non-covalent interaction should not be confused with n→π* electronic transition. The n→π* electronic transition involves electronic excitation from n state to π* state in presence of light. On the other hand n→π* interaction involves orbital overlap between lone pair orbital (n) and π* antibonding orbital which leads to stabilization of the molecular system.

1.8 Aim of the thesis

n→π* interaction has been explored in biomolecules, supramolecular structures and small molecules through X-ray crystallography, NMR spectroscopy and computational analysis. Computational studies show that the short contacts between an electronegative atom and a π system (C=O or aromatic ring) is indeed attractive in nature and it involves transfer of electron density from electronegative atom to π* antibonding orbital of the π system. It has

been revealed from NMR spectroscopy that $n \rightarrow \pi^*$ interaction plays a major role in the structural stability of molecular systems and even dictates their conformational preferences. It is also found that $n \rightarrow \pi^*$ interaction has its own independent existence i.e. it can exist in absence of other non-covalent interactions. It has been observed from crystallographic studies that there is a subtle interplay between the $n \rightarrow \pi^*$ interaction and the hydrogen bonding interaction in the stabilization of molecular systems. However, quantitative nature and strength of this weak $n \rightarrow \pi^*$ interaction and its gas phase IR spectroscopic evidence are yet to be explored. In the present thesis, we have addressed the following points on the $n \rightarrow \pi^*$ non-covalent interaction.

1. Can we study $n \rightarrow \pi^*$ interaction in isolated gas phase?

Till now experimental approaches to determine the presence of $n \rightarrow \pi^*$ interaction is limited to X-ray crystallographic and NMR spectroscopy studies. Both of these studies demonstrate the presence of the $n \rightarrow \pi^*$ interaction in various molecular systems. However, it could be argued that the short contact observed between two molecular units ($C=O \dots C=O$ or $C=O \dots \text{phenyl}$) in the crystal structure designated as the $n \rightarrow \pi^*$ interaction may arise due to optimized orientation of different structural units of large biomolecular systems. On the other hand, if the $n \rightarrow \pi^*$ interaction could be observed in the molecular units in absence of different structural units of biomolecules, it could be inferred that this weak non-covalent interaction detected in biomolecules is not due to mere optimization of those structural units in the macromolecules.

Further, in solution phase spectroscopy, the strength of the $n \rightarrow \pi^*$ interaction may be affected due to solute-solvent interaction as the $n \rightarrow \pi^*$ interaction is weaker in strength compared to other non-covalent interactions. Isolated gas phase spectroscopy can provide accurate strength of the $n \rightarrow \pi^*$ interaction as it allows to study the structures of molecular moieties in an environment which is free from crystal packing forces and solvent interactions. Non-

covalent interactions like conventional hydrogen bonding, π -hydrogen bonding, and $\pi\cdots\pi$ stacking interactions have been studied quantitatively in isolated gas phase. However, similar studies on the $n\rightarrow\pi^*$ interaction is absent in the literature. In the present study, we have employed isolated gas-phase spectroscopic techniques to explore $n\rightarrow\pi^*$ interaction quantitatively in various molecular systems, which includes molecular complexes (7-azaindole...2,6-substituted fluoropyridine), phenyl formate, hydroxyproline derivatives and salicin.

Study of $n\rightarrow\pi^$ interaction in a molecular complex stabilized by both hydrogen bonding and $n\rightarrow\pi^*$ interaction can reveal the answer of the following question.*

2. Can $n\rightarrow\pi^*$ interaction exists along with strong hydrogen bonding interaction?

It has been previously discussed that interplay between hydrogen bonding and $n\rightarrow\pi^*$ interaction contributes significantly to the stability of protein structures. However, this analysis is based only on crystallographic studies. A quantitative knowledge of interplay between various non-covalent interactions can be obtained if judiciously chosen molecular systems or weakly bound complexes can be studied in isolated gas-phase. There are several reports on the gas-phase experimental and theoretical studies of molecular complexes which are stabilized by interplay between various types of non-covalent interactions. However, there is no report of a molecular complex which is stabilized due to subtle balance between hydrogen bonding and $n\rightarrow\pi^*$ interaction.

Herein, we have reported the interplay between hydrogen bonding and $n\rightarrow\pi^*$ interaction in 1:1 complexes of 7-azaindole and 2,6-substituted fluoropyridines using gas phase laser spectroscopic techniques and quantum chemistry calculations. Presence of $n\rightarrow\pi^*$ interaction in the complexes is identified by probing the stretching frequency of the N-H group of 7-azaindole, which is involved in N-H...N hydrogen bonding with the nitrogen atom of fluoropyridine. Measurement of the N-H stretching frequency gives us the

quantitative information about the strength of N-H...N hydrogen bonding present in the complexes. It also demonstrates how $n \rightarrow \pi^*$ interaction can affect the strength of the hydrogen bonding interaction as these two non-covalent interactions are interrelated and influence each other in the complexes. However, this is an indirect approach to probe the $n \rightarrow \pi^*$ interaction in a molecular moiety. Thus the following next question has been asked in our work.

(3) Can we directly probe the $n \rightarrow \pi^*$ interaction in a molecular system from gas phase study?

It is well known that hydrogen bonding interaction (X-H...Y) in a molecular system can be directly probed by measuring the red-shift in the X-H stretching frequency using IR spectroscopy. On the other hand, there is no IR spectroscopic evidence of $n \rightarrow \pi^*$ interaction, which is analogous to hydrogen bonding. Here the point is to identify the presence of the $n \rightarrow \pi^*$ interaction in a molecular system by directly probing the functional groups (C=O group) involved in the $n \rightarrow \pi^*$ interaction using IR spectroscopy. NMR spectroscopy provides the evidence of the $n \rightarrow \pi^*$ interaction in a molecular system by determining the population difference between the two conformers, one with and another without the $n \rightarrow \pi^*$ interaction. However, it does not provide a quantitative information on the $n \rightarrow \pi^*$ interaction present in the molecular system. Further, the solvent polarity may affect the population difference between the conformers.

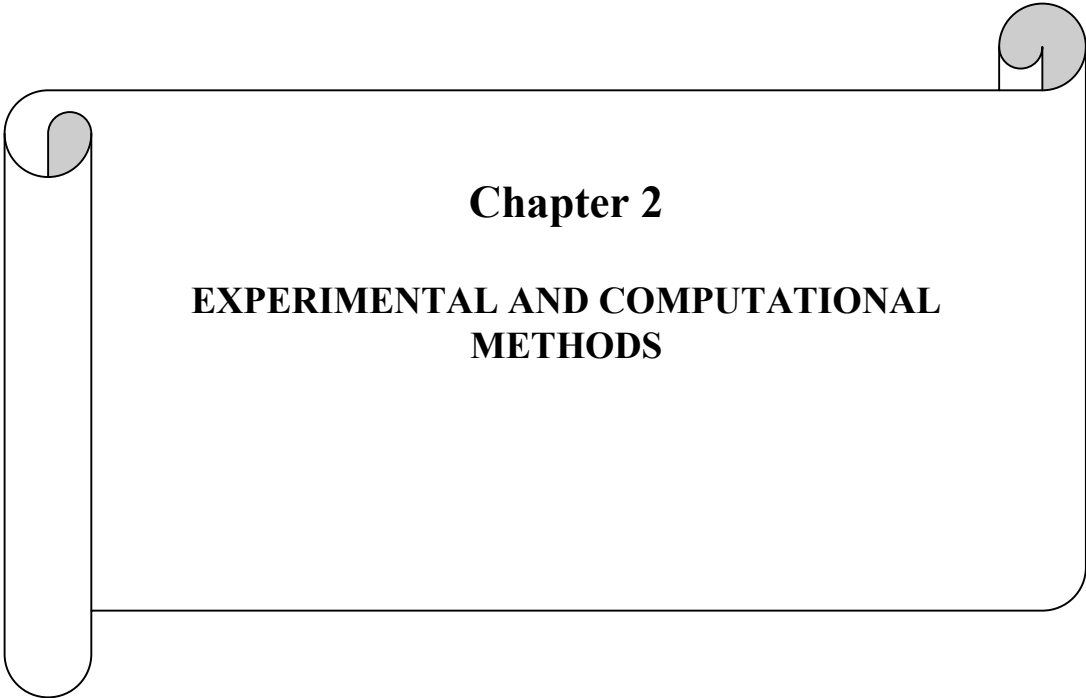
On the other hand, gas phase IR spectroscopy can be used to directly probe the change in the C=O stretching frequency in the conformer which has $n \rightarrow \pi^*$ interaction relative to the one which does not have $n \rightarrow \pi^*$ interaction. Herein, we have used gas phase IR spectroscopic techniques to quantitatively characterize $n \rightarrow \pi^*_{Ar}$ interaction in phenyl formate and $n \rightarrow \pi^*_{Am}$ interaction in hydroxyproline derivative, by measuring the red-shift in the C=O

stretching frequencies of their respective conformers which has $n \rightarrow \pi^*$ interaction relative to the conformers which do not have $n \rightarrow \pi^*$ interaction.

Further question which we have asked in our study is following.

(4) Can we explore $n \rightarrow \pi^*$ interaction in molecular systems which have direct biological implications using gas phase spectroscopy? (for example peptides, drugs, nucleic acid etc.)

We have studied the $n \rightarrow \pi^*$ interaction in a drug salicin which is also known as nature's aspirin. Salicin is an analgesic and antipyretic drug which is obtained from the bark of a willow tree. Salicin is highly rich in conformation due to presence of many flexible coordinates. In our gas-phase experiments, we have observed three lowest energy conformers of salicin which are stabilized by both hydrogen bonding and $n \rightarrow \pi^*$ interaction. A fine interplay between $n \rightarrow \pi^*$ interaction and hydrogen bonding has been found in the observed conformers of salicin. Interestingly, other higher energy conformers which have relatively stronger hydrogen bonding interactions in the absence of $n \rightarrow \pi^*$ interaction, were not observed in the experiment. This indicates that presence of $n \rightarrow \pi^*$ interaction plays a major role in governing the conformational preferences of salicin.



Chapter 2

**EXPERIMENTAL AND COMPUTATIONAL
METHODS**

2.1 Experimental methods

2.1.1 Supersonic jet expansion

Supersonic jet expansion technique has been used to perform high-resolution electronic and vibrational spectroscopy of molecules in isolated gas phase. This technique is the heart of the experiments described in this thesis. Here we can also measure high resolution electronic and IR spectra of non-covalently bonded molecular complexes. This technique brings the molecules in its lowest vibrational and rotational states. The molecules are in an isolated environment as the molecular density is very low after the expansion and the molecules can freely travel in space without any collision from other molecules. The principle and application of supersonic expansion in molecular spectroscopy have been described in detail in many reviews.¹⁰²⁻¹⁰⁴

Supersonic molecular beam is formed when gaseous molecules are expanded from a high-pressure reservoir into a vacuum chamber through a small orifice whose diameter (D) is greater than the mean free path of the gas molecules ($D \gg \lambda_0$) (see Figure 2.1). If the diameter of the orifice is less than the mean free path of the gas molecules ($D \ll \lambda_0$), the molecular beam is called effusive beam. In an effusive flow, there is no change in the internal degrees of freedom of the molecules. In supersonic molecular beam, molecules undergo numerous collisions while passing through the orifice and downstream the orifice. The collisions maximum near the orifice and it decreases with the increase in the distance (X) from the orifice. Due to these collisions, the enthalpy associated with the random motion of molecules is converted to a directed mass flow. As a result, the translational, rotational and vibrational temperatures of molecules decreases and the mass-flow velocity (v) increases. The translational temperature of molecules is directly proportional to the speed of sound (a) according to the equation $a = (\gamma k_B T / m)^{1/2}$ where, γ is the heat capacity ratio C_p / C_v , m , k_B , and T is the mass, Boltzmann constant and temperature, respectively. This suggests that speed of

sound decreases with a decrease in temperature of molecules while mass flow velocity increases to a few km/sec. Hence the flow is termed as supersonic. The Mach number ($M=v/a$) which is given by the ratio of flow velocity to the speed of sound is always greater than 1 for supersonic flow.

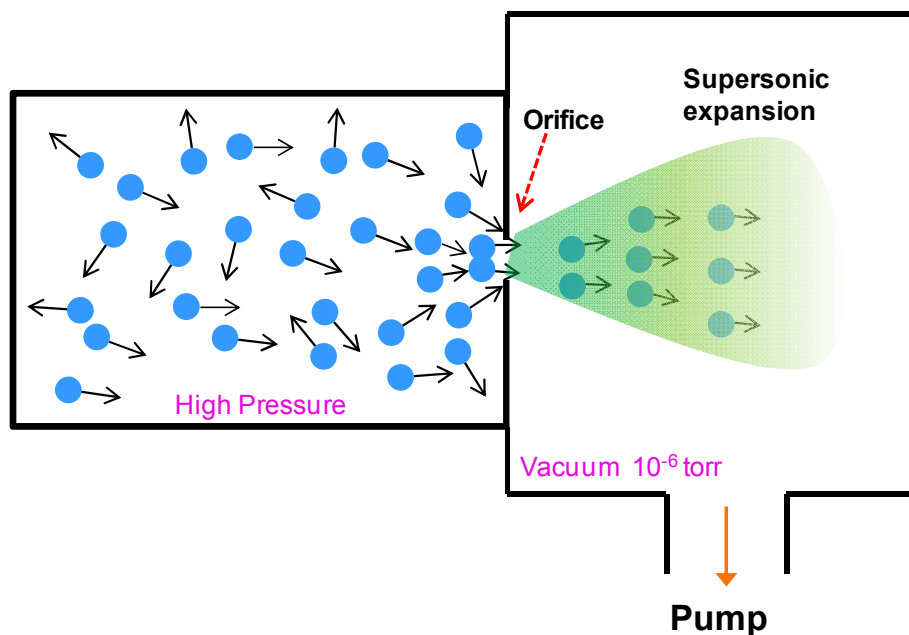


Figure 2.1. A schematic representation of supersonic expansion.

Figure 2.2 shows velocity distribution curve of the gas molecules in the reservoir and the supersonic beam. In a static cell, the velocity distribution is broad (see Figure 2.2a). In supersonic beam, the velocity distribution narrows down and the peak maximum shifts to a higher value as the flow velocity increases (see Figure 2.2b). The width of the Maxwell-Boltzmann velocity distribution curve provides a measurement of the translational temperature of molecules. Narrow velocity distribution of molecules in supersonic beam suggests that translational temperature of molecules significantly decreases. The rate of cooling of the translational degree of freedom is higher compared to that of the other degrees of freedom. Infact, the rotational and vibrational degrees of freedom cool when they come in

equilibrium with the translational cold bath. The rate of rotational-translational equilibration is much faster than that of vibrational-translational equilibration and therefore, rotational cooling is faster compared to vibrational cooling. As the rate of cooling is different for different degrees of freedom, there is no further collision after some point in the expansion and a non-equilibrium state is achieved. There is no further energy exchange between the internal degrees of freedom afterwards. Molecules are frozen in this non-equilibrium state for a long time and one can perform high resolution spectroscopy in isolated gas phase.

The process of supersonic expansion is isentropic under the adiabatic reversible conditions (i.e. in the absence of heat source, shock waves, shear forces, heat sinks and heat conductivity). Therefore, the temperature, pressure, and density of a supersonic molecular

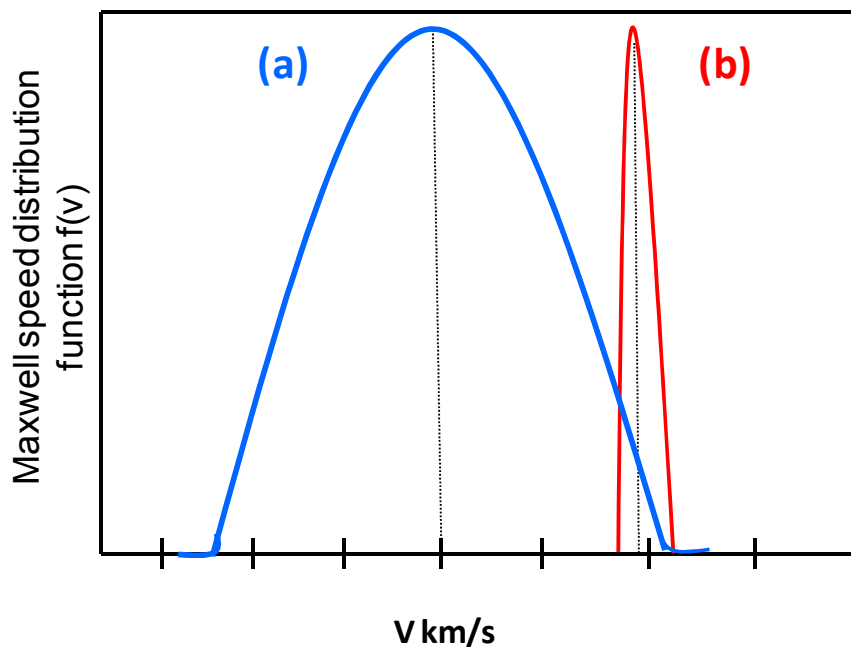


Figure 2.2. Velocity distribution curves of (a) effusive molecular beam and (b) supersonic molecular beam.

beam can be described by the isentropic equation of state of an ideal gas which is given by the equation 2.1.^{102,103}

$$\frac{T}{T_0} = \left(\frac{P}{P_0}\right)^{(\gamma-1)/\gamma} = \left(\frac{\rho}{\rho_0}\right)^{\gamma-1} = \frac{1}{1+\frac{1}{2}(\gamma-1)M^2} \dots\dots\dots (2.1)$$

Where, T_0 , P_0 and ρ_0 are the temperature, pressure, and density of molecules in the reservoir and T , P and ρ are the same quantities in the supersonic molecular beam. γ is the heat capacity ratio (C_p/C_v) and M is the Mach number. If we consider the expanding molecular beam as a continuous medium, the Mach number at a distance (X) from the nozzle can be written by equation 2.2

$$M=A(X/D)^{\gamma-1} \dots\dots\dots(2.2)$$

Where, A is a constant that depends upon the γ and it is 3.26 for monoatomic gas. Equation 2.2 suggests that the Mach number increases with the increase in the distance from the nozzle. However, the Mach number cannot keep on increasing. Fenn and Anderson have shown that Mach number cannot have infinite value as the gas is made up of discrete atoms and molecules and it is not continuous.¹⁰⁵ The total number of collisions is finite and hence the Mach number will also have a finite value. The terminal Mach number, which can be achieved, is given by the equation 2.3 where, ϵ is collisional effectiveness constant.¹⁰⁵

$$M_T = 2.05\epsilon^{-(1-\gamma)/\gamma} (\lambda_0/D)^{(1-\gamma)/\gamma} \dots\dots\dots(2.3)$$

$$=133(P_0D)^{0.4} \text{ for Argon}$$

Thus the terminal Mach number depends upon the pressure in the reservoir and diameter of the orifice. The quantity P_0D actually defines the total number of collision possible for a molecule before achieving a given Mach number. Thus Mach number depends upon the total number of collisions a molecule undergoes during the expansion.

2.1.2. Resonance Enhanced Multiphoton Ionisation and Time of Flight mass spectrometry

Resonance Enhanced Multiphoton Ionisation (REMPI) technique and Time of Flight mass spectrometry have been coupled with supersonic jet assembly to measure mass selected electronic and IR spectra of isolated molecules and non-covalently bound molecular

complexes. The principles of REMPI and TOF mass spectrometry have been described below.

2.1.2.1 REMPI

Figure 2.3 shows a schematic diagram demonstrating the principle of REMPI. The S_0 , S_1 , and D_0 in the figure represent ground electronic state, first excited state, and ground ionic state, respectively. In REMPI technique, multiple photons are used to ionize the molecules. If two photons are used for ionization, it is called as resonant two-photon ionisation (R2PI). R2PI is basically of two types: one color resonant two-photon ionisation (1C-R2PI) technique (see Figure 2.3a) and two color resonant two-photon ionisation (2C-R2PI) technique (see Figure 2.3b). In 1C-R2PI technique, molecules are electronically excited to one of the vibronic levels in the S_1 state by a UV photon and subsequently, another photon of the same energy ionises the molecules. Total energy absorbed by two photons must be more than the ionisation potential of the molecule for successful ionisation of the molecule.

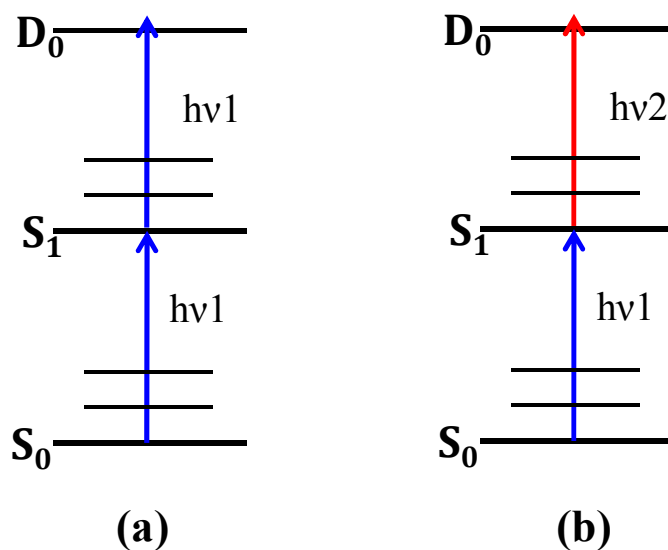


Figure 2.3. Schematic diagram for (a) 1C-R2PI spectroscopy and (b) 2C-R2PI spectroscopy.

In 2C-R2PI spectroscopy, the second photon (ionisation photon) is of different wavelength and from a different laser. 2C-R2PI technique is useful when the energies of the two-photons of the same wavelength is insufficient to cross the ionisation potential of the molecule. To overcome the ionisation potential of the molecule using 2C-R2PI, the second photon should be of higher energy (shorter wavelength) relative to that of the first photon (excitation photon). This technique is also advantageous over the 1C-R2PI technique in studying the electronic spectra of weakly bound molecular complexes as their ionic state is very shallow and excess energy available through 1C-R2PI spectroscopy may break the molecular clusters in the ionic state. Thus the wavelength of the second photon is chosen using such a way that the total energy of two photons should be just above the ionisation potential. The molecular ions formed using R2PI technique are analyzed and detected using TOF mass spectrometry.

2.1.2.2 Time of Flight mass spectrometry

In Time of Flight (TOF) mass spectrometry, the molecular ions of different masses are separated according to their different time of flight (TOF) and then detected by a micro channel plate (MCP) detector. The ions are first accelerated by applying an electric field of a known voltage. The accelerated ions are then allowed to move in a field free region, where they separate out depending upon their masses before reaching to the detector. When the positively charged ions are accelerated, their potential energy is converted into kinetic energy. The potential energy of a charged particle in an electric field is given by:

$$U=qV \quad \dots\dots (2.4)$$

where q is the charge of the particle and V is the potential of the electric field. The kinetic energy of the particle is given by:

$$K=1/2mv^2 \quad \dots\dots (2.5)$$

Where, m is the mass of the particle and v is the velocity of the particle. If the potential energy is converted to kinetic energy then we can show from equation 2.4 and 2.5,

$$qV = \frac{1}{2}mv^2 \dots(2.6)$$

If an ion travels distance d which is the path length of the field free region in time t before reaching to the detector then the velocity is given as:

$$v = d/t \dots\dots (2.7)$$

Using equation 2.7 in equation 2.6 and rearranging we get,

$$t = [(d^2/2qV)m]^{1/2} \dots\dots (2.8)$$

$$\therefore t = k(m)^{1/2} \dots\dots(2.9)$$

where, $k = [d^2/2qV]^{1/2}$ is a constant, since all the ions have the same charge, traveled same distance and experience same electric field. From equation 2.9 it is clear that the time taken by the ions to reach to the detector is directly proportional to the mass of the ions i.e. ions of heavier mass will take more time to reach to the detector compared to the ions of lighter mass.

The TOF mass spectrometer used here is based on three electrodes design given by Wiley and McLaren for improved mass resolution of molecules and clusters.¹⁰⁶ Figure 2.4 shows a schematic diagram of TOF mass spectrometer used in the experiment. It consists of three electrode plates, a field free TOF tube where the ions get separated depending upon their masses and a micro channel plate detector at the end of the TOF tube for detecting the ions. The first and the second electrode plate is called as repeller plate and extraction grid, respectively. The repeller plate has higher positive voltage compared to the extraction grid and the distance between them is denoted by s . The third plate, which is called as accelerating grid is grounded. The positively charged ions are formed between the repeller plate and the extraction grid through R2PI technique. The positively charged ions move towards the

extraction grid due to the effect of uniform electric field (E_s) between the repeller plate and the extraction grid. The ions experience an electric field E_s between the repeller plate and the extraction grid and move towards the accelerating grid. The electric field between the extraction grid and the accelerating grid is represented by E_d and the distance between them is represented by d . Since E_d is more than E_s , the ions in the region with E_d experience much stronger field which causes it to accelerate into the flight tube.

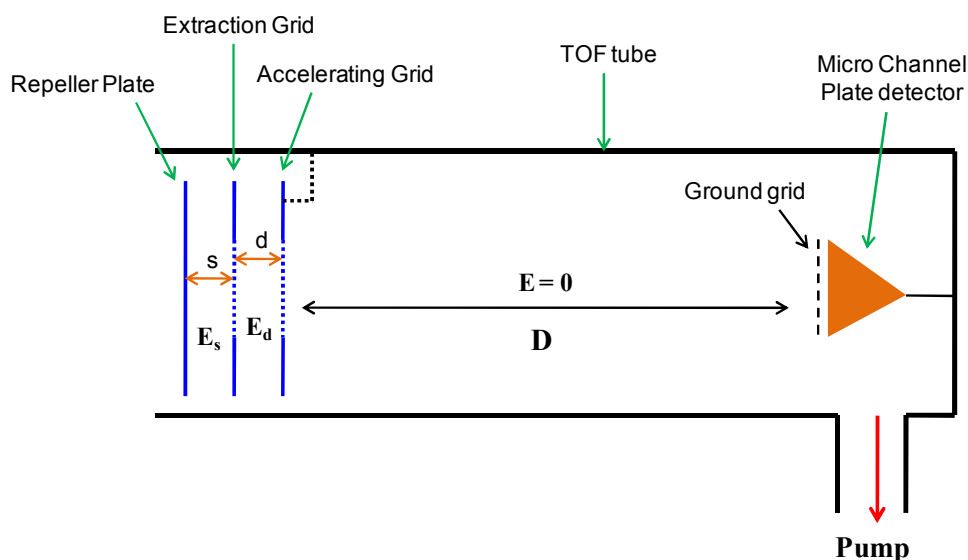


Figure 2.4. Schematic representation of Time of Flight mass spectrometer based on Wiley and McLaren design.

When a pulse laser ionises the molecular beam, a packet of ions is created. These ions are at different positions in space. This variation in positions is known as initial spatial distribution. When accelerated, the ions closer to the repeller plate moves faster than the ions which are closer to extraction grid, this difference in their velocities is known as initial velocity distribution or initial kinetic energy distribution. Due to initial space and energy distributions, the ions of same masses will reach to the detector at slightly different times, which will lead to decrease in the resolution of the TOF mass spectrometer. The dual-source field allows us to adjust the parameter E_d/E_s so that all the ions start moving in the field free

region from the same position, this is called energy focusing or space focussing.¹⁰⁶ This design increases the resolution of the TOF mass spectrometer by reducing the time spread of the ions of same mass.

If U_0 is the initial energy of the ions then it is increased to U when it experiences an electric field E_s between the repeller plate and the extraction grid and electric field E_d between the extraction grid and the accelerating grid.

$$U = U_0 + qsE_s + qdE_d, \dots\dots\dots(2.10)$$

The total time of flight T taken by an ion of mass m and charge q is given by

$$T = T_s + T_d + T_D, \dots\dots\dots(2.11)$$

where T_s is the time taken by ion source to travel the ionization region

$$= 1.02 \frac{(2m)^{1/2}}{qE_d} [(U_0 + qsE_s)^{1/2} \pm (U_0)^{1/2}] \dots\dots\dots(2.12)$$

T_d is the time taken by ion source to travel the acceleration region¹⁰⁶

$$= 1.02 \frac{(2m)^{1/2}}{qE_d} [U^{1/2} - (U_0 + qsE_s)^{1/2}] \dots\dots\dots(2.13)$$

and T_D is the time taken by ion source to travel field free drift tube

$$= 1.02(2m)^{1/2} \left(\frac{D}{2U}\right)^{1/2} \dots\dots\dots(2.14)$$

In our experimental setup, the TOF mass spectrometer (Jordan TOF Products Inc.) is placed mutually perpendicular to the axis of the skimmed molecular beam and the pulse laser beam. The molecular beam is introduced into the space between the repeller plate and the extraction grid which is separated by 1cm. The UV laser interacts with the molecular beam at a right angle to the molecular beam axis and ionises the molecules. The repeller plate and the extracting grid are kept at +3060 V and +2780 V, respectively, while the accelerating grid is grounded. The molecular ions formed between the repeller plate and extraction grid are accelerated into the field free TOF tube which is 1metre long. At the end of the tube, an 18

mm dual chevron type micro channel plate detector (MCP) is placed to detect the ions. The MCP detector is at a negative voltage (-3060 V) and it has several million micro-channels which work as an independent electron multiplier. When an ion enters a micro-channel of the detector, it emits an electron from the channel wall. This secondary electron is accelerated by the electric field developed due to the voltage applied on either side of the MCP. The accelerated electron travels along the parabolic trajectory until it hits the channel wall, thereby producing more secondary electrons. This process is repeated along the channel wall, as a result, the cascade process leads to the generation of several thousand electrons that emerge from the rear end of the plate. The electronic signal generated from the detector due to the bombardment of ions is visualized on the oscilloscope. Signal due to ions of different masses appears at a different time on the oscilloscope.

2.1.3. Laser systems used for the experiments

We have used solid-state lasers pumped tunable dye lasers to measure the electronic and IR spectra of molecules and molecular complexes in the supersonic jet. The working principle of each of the lasers is described here briefly.

2.1.3.1 Dye laser

The dye laser is a liquid laser where the organic dye (Rhodamine 6G, Fluorescein, LDS etc) is used as an active medium for generating laser light in the visible range. The entire visible range can be covered by choosing different dyes.¹⁰⁷⁻¹⁰⁹ In general, the dyes used as an active medium should have good photochemical stability, high quantum yield, strong electronic absorption at the excitation wavelength and minimal intersystem crossing for good performance of the laser.

The dye laser (ND 6000, continuum) used here is pumped by the second harmonic output (532 nm) of an ND-YAG laser (Continuum Surelite, 10 Hz rep. rate, 10ns pulse width) with pulse energy of 250 mJ. Figure 2.5 shows a schematic of the Dye laser used in the experiment. It consists of an oscillator cell and two amplifier cells (pre-amplifier and final-amplifier). The vertically polarized 532 nm light strikes the beam splitter (BS1) which reflects 5% of the total energy towards the oscillator dye cell and the remaining percentage strikes the beam splitter BS2 after passing through a set of dichroic mirrors. Beam splitter BS2 reflects 10% of the light towards the pre-amplifier cell and the rest is transmitted towards the final-amplifier dye cell after passing through a dichroic mirror. The dye laser cavity consists of a beam expander, two gratings which have 2400 lines/mm grooving, a front

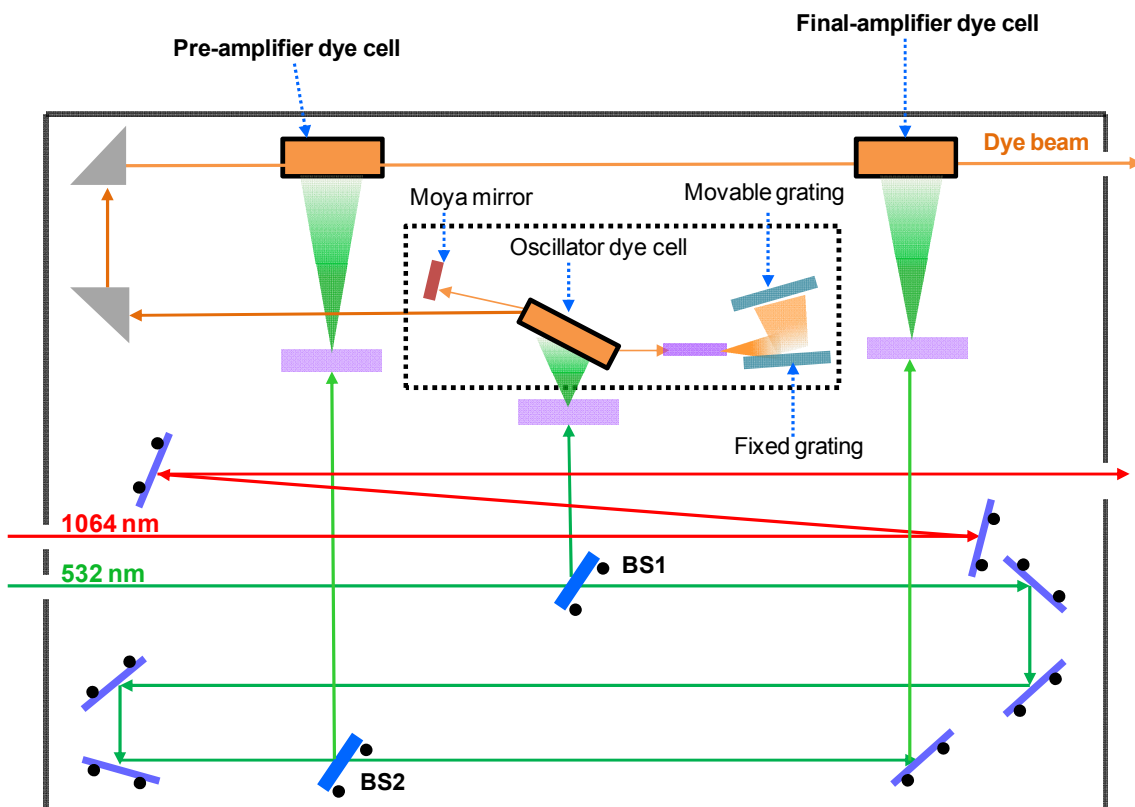


Figure 2.5. A schematic diagram of dye laser (ND6000, Continuum) showing its optical configuration.

mirror which is called Moya mirror and the oscillator dye cell. The light reflected by the beam splitter bs1 passes through a telescope lens before it falls on the oscillator dye cell. The incident 532 nm light excites the dye molecules of the oscillator cell which results into stimulated emission. The laser beam from the oscillator dye cell passes through the beam expander before falling on the grating. The grating provides the wavelength selection from the broad range output of the dye.

The selected monochromatic oscillator laser beam exits the dye laser cavity and passes through the pre-amplifier dye cell where it coincides with the reflected 532 nm laser beam from the beam splitter BS2. The pre-amplified dye output is then allowed to incident on the final amplifier dye cell. The transmitted 532 nm light from the beam splitter BS2 coincides with the pre-amplified dye output in the final amplifier dye cell which results in further amplification of the dye output beam. The dye beam is introduced in UVT tracker where it is allowed to pass through the BBO crystal for generating the doubled output (UV beam).

2.1.3.2 UV Tracker (UVT)

UV tracker allows us to generate the UV beam from the visible output of the dye laser by using a non-linear KDP or BBO crystal. The non-linear crystals are used either to obtain frequency doubled output of the fundamental beam or to get further shorter wavelength by mixing the doubled output of the dye laser with the 1064 nm IR beam from the YAG laser (mixing after doubling). In the doubling mode, only a KDP or BBO crystal is used. The wavelength of the frequency doubled output of the fundamental beam of the dye laser is given by the equation 2.10,

$$\text{Frequency doubled output wavelength} = \text{Fundamental wavelength}/2 \dots\dots\dots(2.15)$$

In the case of mixing after doubling, the doubling crystal is used along with another KDP crystal which is the mixing crystal. The frequency doubled output of the dye laser beam and

the 1064 nm beam from the YAG laser overlap with each other inside the mixing crystal and generates sum frequency output in the shorter UV region. The wavelength of the sum frequency output can be calculated from the following equation:

$$1/(\text{sum frequency output wavelength})=1/(\text{frequency doubled output wavelength}) + 1/(1064 \text{ nm}) \dots\dots\dots (2.16)$$

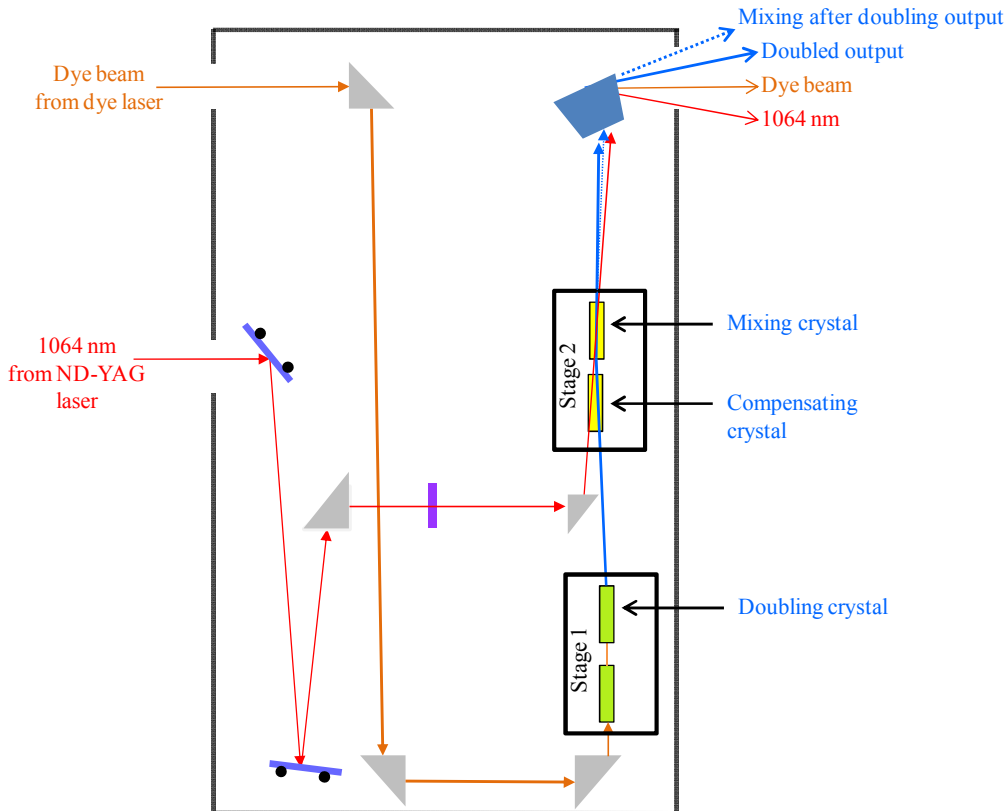


Figure 2.6. A schematic diagram of UV tracker (UVT, Continuum) showing its optical configuration.

Figure 2.6 shows a schematic diagram of the UV tracker. It has two stages, stage 1 and stage 2. In doubling mode, the doubling crystal is placed on stage 2 and it is paired with a compensating crystal to avoid changes in the path of the beam with change in the wavelength. The dye beam is allowed to fall on the doubling crystal by a set of prisms. The vertically polarized dye beam strikes the doubling crystal, at a certain phase match angle. The horizontally polarized doubled output along with the residual dye beam exit the doubling

crystal and falls on a turning prism. The frequency doubled output (UV beam) is separated from the fundamental beam with the help of four Pellin-Broca prisms placed after the exit port of the UVT.

In mixing after doubling mode, the doubling crystal is moved to stage 1 and the mixing crystal is placed on stage 2. Both the crystals are paired with the compensating crystals. The vertically polarized dye beam is changed to horizontally polarized by the help of a turning prism before it strikes the doubling crystal. The doubling crystal on stage 1 is mounted at 90° to the plane of the optical bench so that it is properly oriented with the horizontally polarized dye beam for doubling. The doubled output leaves the stage 1 as vertically polarized and reaches stage 2 where it overlaps with 1064 nm IR light coming from ND:YAG pump laser inside the mixing crystal. A set of mirrors in the dye laser directs the 1064 nm light towards the UV tracker. Inside the UVT the 1064 nm is allowed to incident on the mixing crystal by the help of a mirror and a turning prism. The UV beam generated by mixing after doubling exits the mixing crystal along with the residual doubled output, residual dye beam and 1064 nm light. All the four lights are separated by the help of 4 Pellin-Broca prisms.

2.1.3.3 IR OPO/OPA

The infrared laser (Laser Vision) uses optical parametric oscillation (OPO) and optical parametric amplification (OPA) for generating light in the near-IR region (710 to 885 nm) and the mid-IR region (1.35 to 5 μm). It uses a non-linear KTP crystal for OPO which is pumped by 532 nm light and four non-linear KTA crystals for OPA which is pumped by 1064 nm light. All the OPO and OPA crystals are mounted on stepper motors which allow the crystals to rotate to achieve proper phase matching angle for generating the IR beam of the desired wavelength. Figure 2.7 shows a schematic of the IR OPO/OPA laser used here.

The 1064 nm pump beam from the ND:YAG laser (seeded/unseeded) with pulse energy of 530 mJ is directed into the IR laser using two steering mirrors. Inside the IR laser, the pump beam first passes through the telescope which adjusts the beam profile and then strikes the beam splitter. The beam splitter divides the horizontally polarized pump beam into two separate beam lines. One-third of the total pump beam energy is reflected towards the BBO crystal which generates 532 nm light by frequency doubling. A half-wave plate (attenuator) in a rotation stage placed before the second harmonic generator is used to control the efficiency of the conversion of 1064 nm to 532 nm. The 532 nm light generated by the

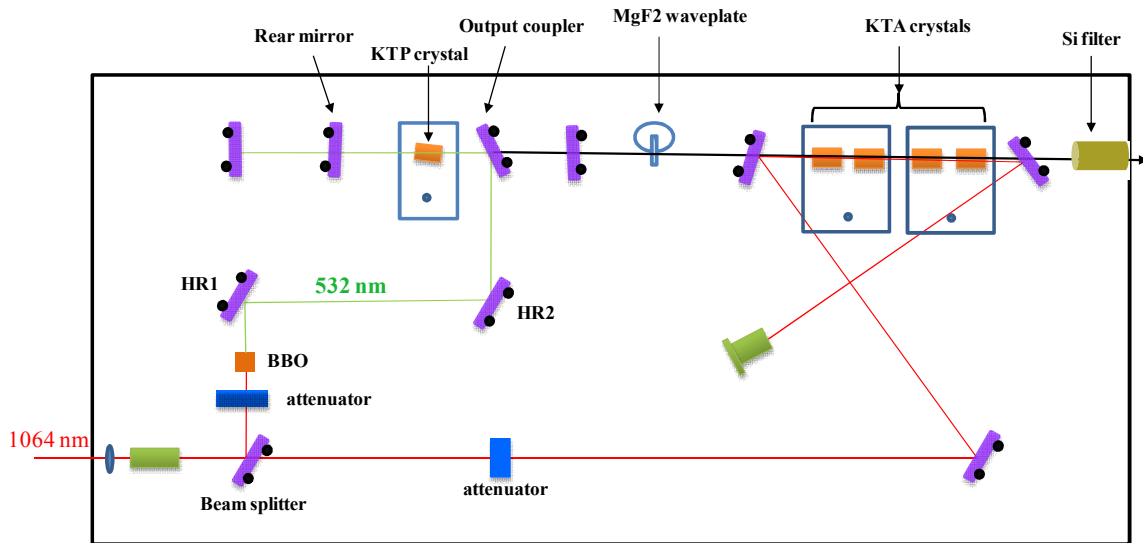


Figure 2.7. A schematic diagram of IR laser (Laser Vision) showing its optical configuration.

second harmonic crystal is directed into the OPO stage using 532 nm reflecting mirror HR1 and HR2. The OPO stage is configured as a linear cavity with a KTP crystal, a rear mirror, and an output coupler. When an intense 532 nm laser beam passes through the KTP crystal two new photons, signal (ω_s) and idler (ω_i), are generated via optical parametric oscillation in such a way that the sum of the signal and idler frequencies is equal to the frequency of the pump beam. The wavelength of the signal and idler output from the OPO is tuned by rotating

the KTP crystal. Both near-infrared signal and intermediate-IR idler beams pass through the dove prism after coming out of the output coupler. The dove prism maintains the collimation of the beam. A MgF₂ waveplate is placed before the OPA stage to change the polarization of the idler beam from vertical to horizontal and hence the OPA crystals are tuned in the horizontal plane. The near-infrared signal (ω_s) is rejected using a silicon filter placed between the OPA stage and MgF₂ waveplate. Thus only the idler beam (ω_i) reaches to the OPA stage.

At the OPA stage, there are two pairs of KTA crystals. Crystals in each pair rotate in opposite direction to compensate the change in the path of the beam. The 1064 nm pump beam transmitted by the beam splitter (bs) passes through the half-wave plate which allows to attenuate the energy of the pump beam delivered to the OPA stage and also changes the horizontal polarization of the 1064 nm to vertical polarization. The pump beam is directed onto the center of the OPA crystals and in the direction of propagation of the intermediate IR idler from the OPO output using mirror M3 and M4. Both intermediate-IR beam from the OPO and 1064 nm beam mix inside the OPA crystals. The intermediate-IR idler becomes the signal for the OPA stage and 1064 nm becomes the pump. Difference frequency generation of both the beams results in the generation of a new idler in the mid-IR region while simultaneously amplifying the intermediate-IR signal. The residual 1064 nm pump beam is removed by the 1064 nm separator mirror towards the beam dump while passing the mid-IR idler and intermediate-IR signal. The mid-IR idler is vertically polarized while the intermediate-IR signal is horizontally polarized. Our requirement is the mid-IR beam, therefore, a “Stack of plates” Si filter is used before the exit port which rejects the intermediate-IR signal and allows only the mid-IR idler beam to pass through. The bandwidth of the IR laser is 2-2.5 cm⁻¹.

In order to generate far-IR wavelength, an AgGaSe₂ crystal is mounted at a distance of one meter from the exit port of the IR laser. The “Stack of plates” Si filter is removed and both mid-IR idler and the intermediate-IR signal from the OPA are allowed to incident on the

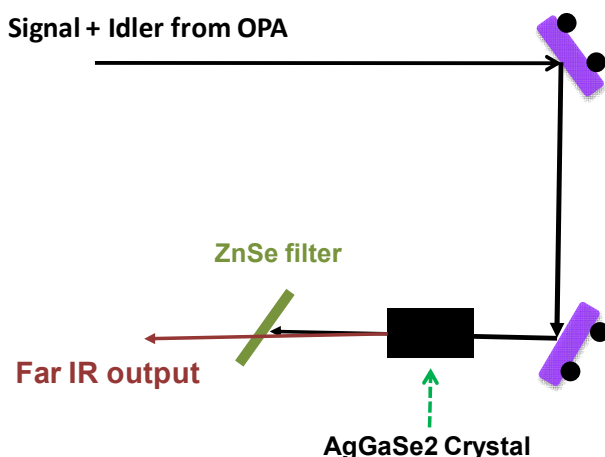


Figure 2.8. Schematic diagram of generation of far-IR wavelength using AgGaSe₂ crystal.

AgGaSe₂ crystal collinearly using a set of mirrors (see Figure 2.8). The AgGaSe₂ crystal generates a far-IR wavelength at a certain phase-match angle from the intermediate-IR signal and mid-IR idler beams by difference frequency mixing (see equation 2.12). The residual signal and idler coming out of the AgGaSe₂ crystal are removed by ZnSe filter while allows the far-IR beam to pass through.

$$\omega_{\text{far-IR}} = \omega_{\text{signal}} - \omega_{\text{idler}} \dots\dots\dots(2.17)$$

where, $\omega_{\text{far-IR}}$, ω_{signal} and ω_{idler} are the frequencies of far-IR output, intermediate-IR signal and mid-IR idler, respectively.

2.1.4. Experimental set-up

Figure 2.9 shows the photograph of our home-built jet-cooled REMPI-TOF mass spectrometer used for the experiment. The set up consists of two differently pumped vacuum chambers (molecular beam chamber and ionization chamber). Both the chambers are connected through the skimmer having a diameter of 2mm. A commercial pulse valve

(General valve, series 9, 10 Hz repetition rate) with orifice diameter of 0.5 mm and operated by a pulse driver (IOTA ONE, Parker instrumentation) is used for the experiment. The pulse valve is connected with a long stainless steel pipe which is connected with a XYZ manipulator. The XYZ manipulator allows us to align the pulse valve orifice with the skimmer. The whole assembly of the pulse valve is incorporated in the molecular beam chamber.

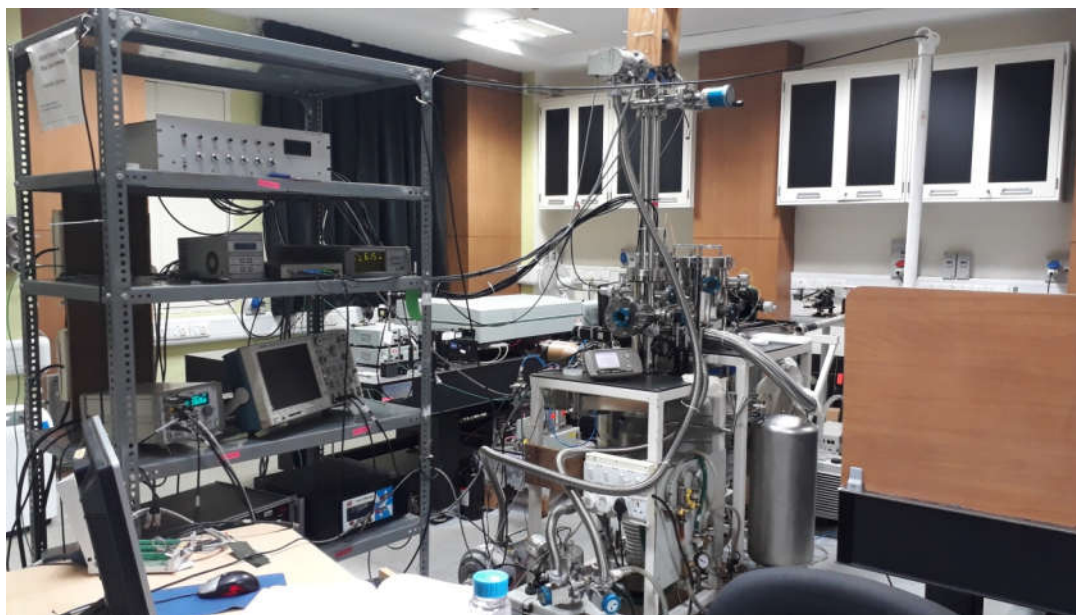


Figure 2.9. Photograph of the home-built jet-cooled REMPI Time of Flight mass spectrometer coupled with laser desorption

The molecular beam chamber is pumped by a 10-inch diffstack diffusion pump (OD 250, Hind Hivac) with a pumping speed of 2000 L/s and this diffusion pump is backed by a roughing pump (FD-60, Hind Hivac) having a pumping speed of 17 L/s. The ionization chamber is pumped by a 4.5-inch diffstack diffusion pump (OD-114, Hind Hivac) with a pumping speed of 280 L/s and it is backed by a roughing pump (ED-21, Hind Hivac) having a pumping speed of 6 L/s. The walls of the diffusion pumps are cooled by circulating water (temperature 18° C) from a chiller (Refricon Hvac System). Vacuum chambers are separated

from the diffusion pump by gate valves. Liquid nitrogen traps are present between the vacuum chambers and the diffusion pump which prevents the oil contamination in the vacuum chambers. The pressure in the vacuum chambers is measured by cold cathode ion gauges. The base pressure in the molecular chamber and ionization chamber is 1×10^{-7} torr and 8×10^{-8} torr, respectively.

The time of flight (TOF) tube is connected with the ionization chamber and placed perpendicular to the molecular beam axis. An 18 mm MCP detector (Jordon TOF Products) is housed in a small vacuum chamber which is placed at the end of the TOF tube. The detector chamber is pumped by a turbo molecular pump with a pumping speed of 70 L/s. The turbo

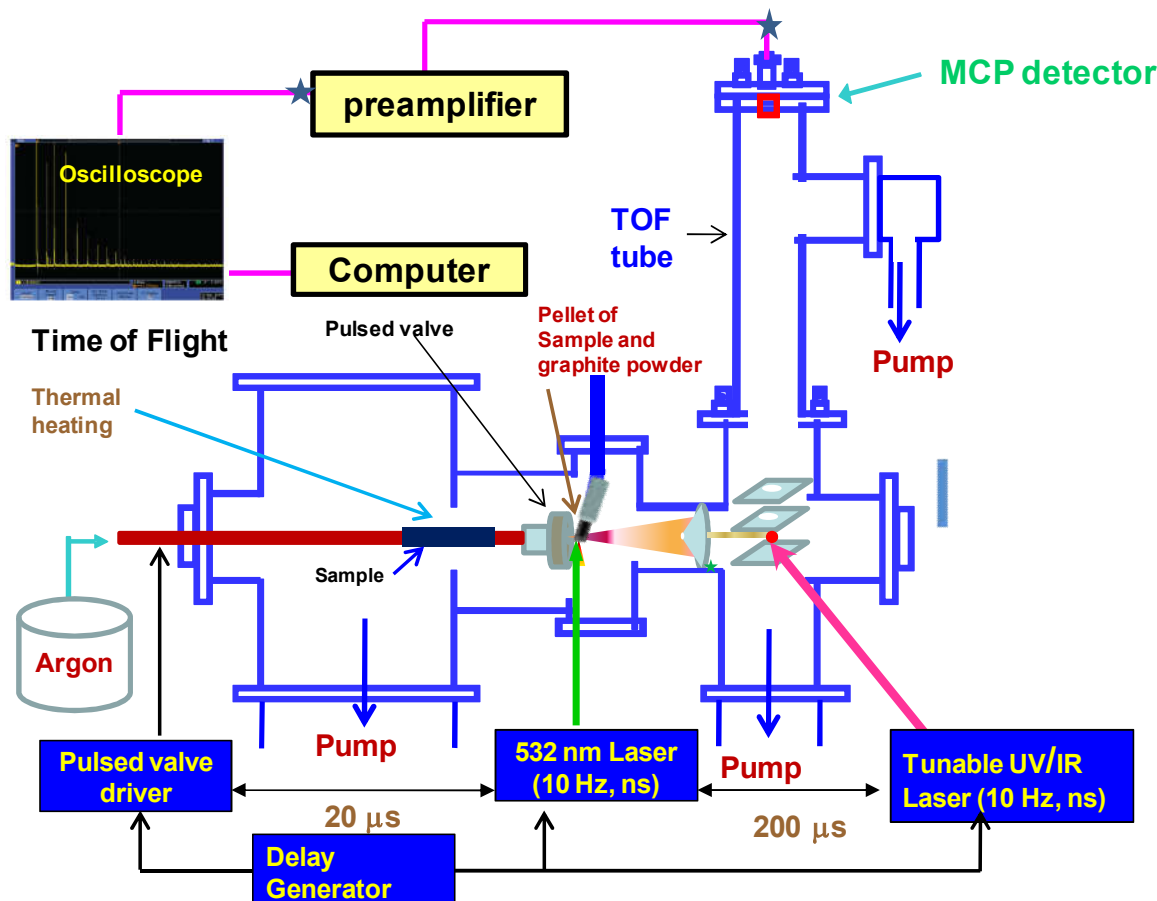


Figure 2.10. Schematic diagram of the experimental setup of a home-built jet-cooled Time of Flight mass spectrometer coupled with laser desorption. The temporal synchronisation between the molecular beam and the lasers is performed using the delay generator.

pump is backed by a dry scroll pump (SH-110, Varian, Pumping speed 1.5 L/s). A TOF power supply (Jordon TOF products) is used to supply negative voltage to the detector and the positive voltage to the electrode plates. The ion signal generated from the detector is amplified by a preamplifier (SRS, Model SR445A) and sent to a digital oscilloscope (Tektronix, 350 MHz, DPO 4034) which is interfaced with a computer using USB interface. Temporal synchronization among the pulse valve, UV laser, and IR laser is performed by a delay generator (BNC, Model 575).

2.1.5. Experimental Scheme

Figure 2.10 shows a schematic diagram of our experimental setup. Generally, the sample of our interest (solid or liquid) having low vapor pressure is heated inside a stainless steel container, which is placed just behind the pulse valve, to generate its vapor. The samples which have very high vapor pressure is taken in a sample holder which is cooled using an appropriate freezing bath and kept outside the chamber. The sample vapor seeded in Argon or He/Ne carrier gas is allowed to expand through the orifice of the pulse valve into the expansion chamber. Typical operating pressure of the expansion chamber and ionization chamber is 2.0×10^{-6} torr and 4.0×10^{-7} torr, respectively.

In order to generate vapor of those molecules which have very low vapor pressure and decomposes on heating, for example peptides, nucleic acid, drugs etc, we use a technique called laser desorption.¹¹⁰⁻¹¹² This technique is useful to bring the molecules in the gas phase without any thermal decomposition. The molecule of our interest is first mixed with graphite to form a matrix. When a short pulse (10 ns, 10 Hz) laser beam strikes the surface of the matrix, the temperature of the surface rises to 1000K for 10 ns.¹¹³ Since a very high temperature is achieved in very small time duration, the chemical bonds of the molecules do not break and vapor of the sample is then seeded in the jet-cooled molecular beam of the carrier gas. To perform laser desorption, the (solid) sample of our interest is mixed with

graphite powder in a 2:1 weight ratio to form a pellet in a hydraulic press under 2-3 tons of pressure. If the sample is liquid, it is first dissolved in a solvent and then coated on the surface of the graphite pellet. Figure 2.11 shows a schematic diagram of the laser desorption setup coupled with the jet-cooled Time of Flight mass spectrometer.

The sample pellet was placed in a sample holder attached with an XYZ manipulator coupled with a motorized translational assembly (Fourvac Technology, Pune) for translation of the sample pellet along the Z-axis. Second harmonic output (532 nm) of a Nd:YAG laser (Continuum, Minilite-I, 10 Hz, ns) was used for desorption of the sample from the surface of the pellet. The 532 nm laser beam of about 500 μJ pulse energy was fed into an optical fiber (multimode, 400 μm core diameter, 4 m length) through an optical coupler and focused on the sample.¹¹⁰ The distance between the edge of the pellet and the center of the orifice of the

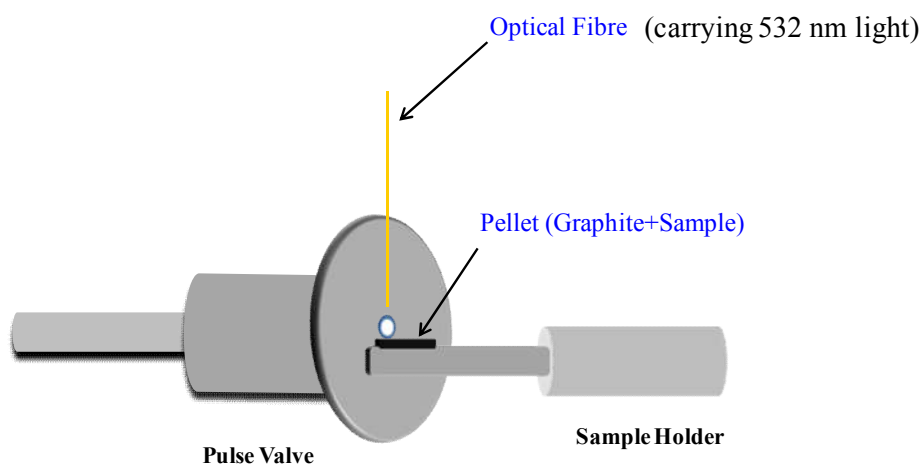


Figure 2.11. A schematic diagram of the laser desorption setup. Sample holder is attached to an XYZ manipulator coupled with the motorized translational assembly which moves the sample holder back forth.

pulsed valve was maintained at about 1 mm while the distance between the surface of the pellet and the axis of the molecular beam was kept at about 2 mm. The sample pellet was translated back and forth to ensure exposure of a fresh spot of the sample surface by the laser. The desorbed molecules were entrained in a supersonic expansion of Ar gas (~ 5 bar) through a pulsed nozzle of 500 μm diameter (General valve, series 9, 10 Hz).

The central coldest part of the jet-cooled molecular beam passes through the skimmer and reaches the ionization chamber. The pulsed UV laser beam intersects the molecular beam in the ionization chamber at a right angle to the molecular beam axis. To ensure that the UV beam intersects the molecular beam, firing of the UV laser is delayed by about 400 μ s from that of the pulse valve. Temporal synchronization between the molecular beam and the UV laser beam is controlled by a delay generator. Molecules are ionized by the tunable UV beam using REMPI technique. The ions thus formed are accelerated into the field free time of flight tube by applying a positive voltage to the repeller plate (+3060 V) and the extraction grid (+2780 V). Ions get separated in the time of flight tube depending upon their masses before reaching the MCP detector. Ions of lighter mass reach the detector earlier in time compared to the ions of heavier mass. The ion signal from the detector is further amplified by a preamplifier and sent to an oscilloscope which is interfaced with a computer via a USB port.

A LabVIEW based programme has been used to scan the laser wavelength and obtain data from the oscilloscope. The ion signal of different masses is displayed on the oscilloscope as a function of time of flight. The time of flight of different ions are converted to their corresponding masses following the equation $t_2 = (m_1/m_2)^{1/2} * t_1$, where t_1 and m_1 are the time of flight and mass of an unknown molecule, respectively, while t_2 and m_2 are the time and mass of a reference molecule, respectively. This equation is derived based on the fact that kinetic energy of all the ions of different masses is same in the field free time of flight tube. Derivation of this equation is discussed in section 2.1.2. Mass of different molecules and molecular complexes are identified in the TOF mass spectrum. The time window of a particular mass is selected using the LabVIEW base program and the UV laser is tuned using the same program to measure the mass selected electronic spectrum. Various UV and IR lasers based spectroscopic techniques have been used to determine the structure and

conformations of the molecules and complexes in a supersonic jet. These spectroscopic techniques have been described below.

2.1.6. Spectroscopic Techniques

We have used various spectroscopic techniques to analyze the structures of molecules and molecular complexes in a supersonic jet. 1C-R2PI spectroscopy¹¹⁴ has been used to measure the mass selected electronic spectra of molecules and complexes. Presence of different conformations of molecules and complexes in the experiment has been determined using UV-UV and IR-UV double resonance spectroscopy techniques. Resonant ion dip infrared spectroscopy has been used to measure the IR spectra of the molecules and clusters. The quantum chemical calculation is combined with our experimental IR spectra to determine the structure of the molecules and molecular clusters.

2.1.6.1 1C-R2PI spectroscopy

This technique has already been discussed in the section 2.1.2.1.

2.1.6.2 Resonant ion-dip infrared spectroscopy (RIDIRS)

Figure 2.12 shows a schematic diagram of RIDIR spectroscopy. In this technique, one

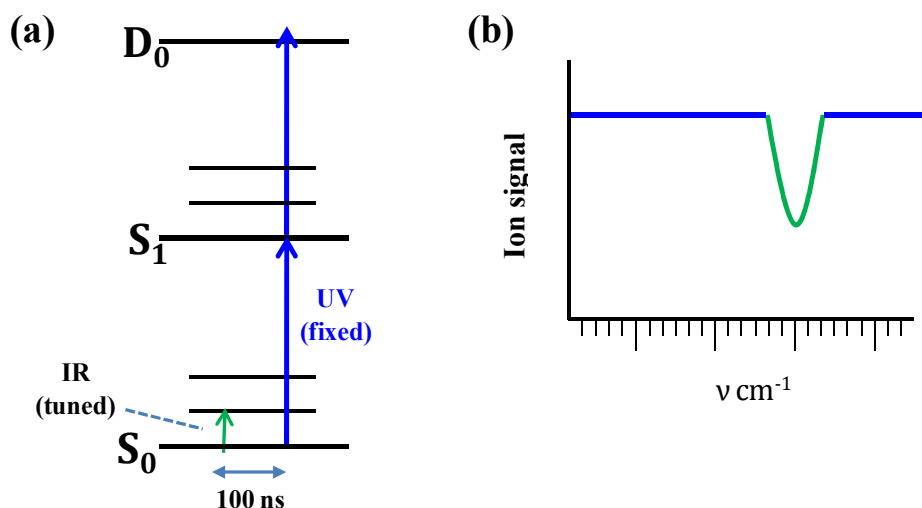


Figure 2.12. (a) A schematic demonstration of the RIDIR spectroscopy (b) Cartoon diagram of the IR spectrum obtained from the RIDIRS.

UV and one IR laser are used. The UV and IR beams are spatially overlapped and intersected with the molecular beam at a right angle to the molecular axis. IR laser beam with pulse energy of 3-4 mJ is focused using a CaF₂ lens of focal length 100 cm while the UV laser beam with pulse energy of 0.3-0.4 mJ is unfocused. The IR laser is fired about 120 ns prior to the UV laser and the time delay between these two lasers is achieved using delay generator. The IR laser is scanned while the UV laser is fixed to a particular transition in the R2PI spectrum of the molecule or complex. The IR spectrum is obtained as a depletion in the ion signal whenever the IR frequency matches with any vibrational transition of the molecule or complex in the ground electronic state. Figure 2.12(b) shows a cartoon diagram of the IR spectrum obtained using the RIDIRS technique.

2.1.6.3 IR-UV double resonance spectroscopy

IR-UV double resonance spectroscopy has been used to determine whether a single conformer or multiple conformers of the molecules or complexes are present in the experiment. Figure 2.13 shows a schematic diagram of the IR-UV double resonance spectroscopy which is also known as IR-UV hole-burning spectroscopy as the IR laser burn the population of the molecules in the lowest vibrational level of the ground electronic state. In this technique, the IR laser is fixed at a particular vibrational frequency of a conformer of the molecule or complex while the UV laser is scanned along the entire R2PI spectrum.¹¹⁵ The IR laser depletes the population of a conformer through a vibrational transition and the electronic band transitions belonging to that particular conformer show reduced intensity compared to those in the R2PI spectrum while the electronic band transitions belonging to other conformers remain unaffected. Figure 2.13 (b) shows a cartoon diagram of IR-UV hole burn spectrum measured by fixing the IR laser at the vibrational frequency of the electronic band B. The IR-UV hole-burn spectrum shows depletion in the intensity of the electronic band B while the intensity of the electronic band A remains unaltered.

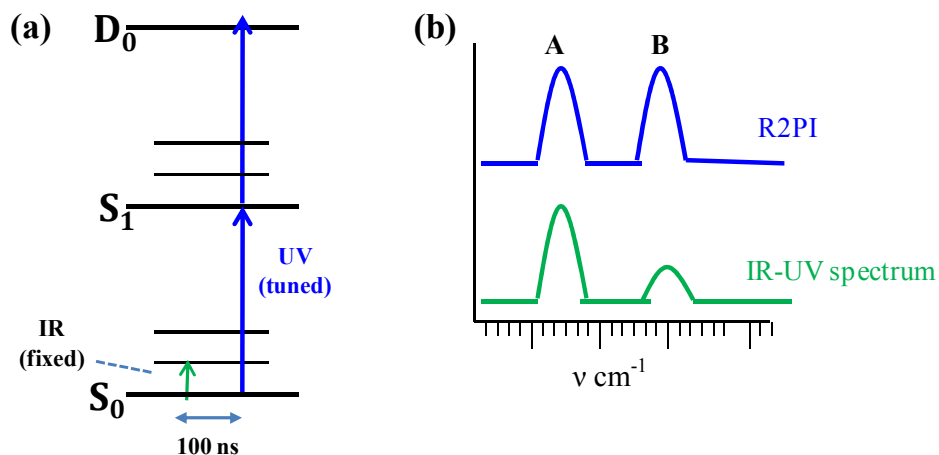


Figure 2.13. (a) A schematic diagram of the IR-UV hole burn spectroscopy (b) Cartoon diagram of the R2PI spectrum and IR-UV hole burn spectrum.

2.1.6.4 UV-UV double resonance spectroscopy

UV-UV double resonance spectroscopy has been used to discriminate the presence of multiple conformers of molecules in the experiment. Two UV lasers are used in this experiment. The probe UV probe laser (pulse energy $\sim 0.2\text{-}0.3$ mJ) is fixed to a particular transition in the R2PI (electronic) spectrum while the UV pump laser (pulse energy $\sim 0.6\text{mJ}$) fired about 100 ns prior to the probe laser is scanned through the whole R2PI spectral region of the molecule. The counter-propagating pump and probe UV laser beams are spatially overlapped and intersect with the molecular beam at a right angle to the molecular beam axis. Depletion in the probe ion signal is observed whenever the pump UV excites the bands which belong to the same ground state as that of the electronic band which is being probed, while the bands which belong to the different ground state do not give any depletion in the probe ion signal. Figure 2.14 (b) shows a cartoon diagram of UV-UV hole burn spectrum measured

by fixing the probe UV laser at peak B. No depletion is observed for peak A in the UV-UV hole-burn spectrum and therefore peak A belongs to a different conformer.

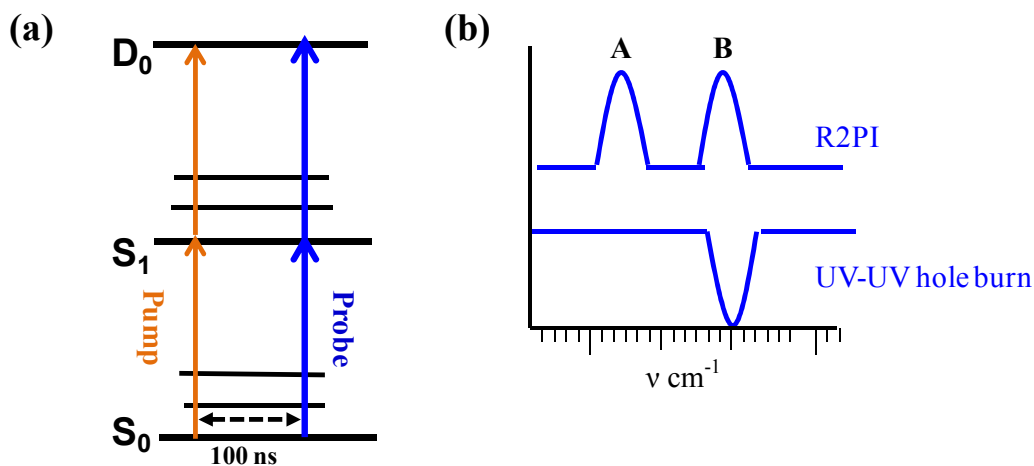


Figure 2.14. (a) A schematic diagram of the UV-UV hole burn spectroscopy (b) Cartoon diagram of the R2PI spectrum and IR-UV hole burn spectrum.

2.2 Computational Methods

Our experimental results are compared with the quantum chemical calculations to determine the structures of the molecules or complexes observed in the experiment. The comparison between experimental and theoretical results also helps to validate the accuracy of the results obtained from the quantum chemistry calculation. Here, we have used Gaussian G09¹¹⁶, NBO6.0¹¹⁷ and GAMESS program¹¹⁸ packages to perform the quantum chemical calculations.

2.2.1 Geometry optimization and Frequency calculation

We have used both wave function theory (WFT)¹¹⁹ and Density functional theory (DFT)^{120,121} to calculate the ground state geometry and harmonic vibrational frequencies of molecules and complexes. We have used MP2 level of theory and various dispersion-corrected DFT functionals (M05-2X, M06-2X, B97-D)¹²²⁻¹²⁴ with Pople type as well as Dunning's correlation consistent basis sets to perform the geometry optimization and frequency calculation of

various possible conformers of molecules and complexes. The initial geometries are either chosen from chemical intuition or generated using molecular mechanics force field incorporated in CONFLEX¹²⁵⁻¹²⁷ and Marvin Sketch programme packages. “Ultrafine” numerical integration has been used to perform the DFT calculations. All calculations have been performed using “opt=tight” convergence criteria for geometry optimization.

Relative energies of various conformers of molecules are calculated with respect to the most stable conformer of the molecules. The binding energies of various conformers of the complexes have been corrected for basis set superposition error (BSSE) as well as zero-point energy (ZPE) correction. BSSE correction has been performed using the counterpoise method given by Boys and Bernardi.¹²⁸ To determine the structures of the molecules or complexes the experimental IR spectra is compared with the computed IR spectra of different possible conformers of molecules or complexes. The computed harmonic IR frequencies are scaled with respect to the vibrational frequency of a known molecule. Gaussian G09 has been used to perform the geometry optimization and frequency calculations.

2.2.2 Energy decomposition analysis

We have used GAMESS program package for energy decomposition analysis (EDA) of the complexes.¹¹⁸ A localized molecular orbital (LMO) method introduced by Su and Li has been used for the energy decomposition analysis.¹²⁹ Using the LMO-EDA method, the total binding energy of the molecular complexes is decomposed into electrostatic, exchange, repulsion, polarization, and dispersion terms.

2.2.3. Natural Bond Orbital analysis

NBO program developed by Weinhold and co-workers has been used to determine the strength of the $n \rightarrow \pi^*$ and the hydrogen bonding interactions present in molecule or complexes.^{130,131} The NBO method enables to understand the fundamental concept of the

localized Lewis-like chemical bonds. The delocalized molecular orbitals are converted into localized natural bond orbitals. These natural bond orbitals are localized orbitals on either one center, two center or three center. NBOs represents the Lewis like molecular bonding environment, in other words, it shows the localized electron density picture of the molecular system. Its mathematical algorithm first converts the input atomic orbital basis set into natural atomic orbitals (NAOs). Natural atomic orbitals can be defined as localized atomic orbitals of the atoms. Three types of NAOs are generated, core, valence and Rydberg. Only Core and valence NAOs have significant occupancies of the electron. Linear combination of NAOs give rise to natural hybrid orbitals (NHOs). The NHOs is a complete orthonormal set that spans the entire basis space. Natural bond orbitals (NBOs) are composed of a linear combination of natural hybrid orbitals (NHOs). For a 2-center bond, the linear combination of two natural hybrid orbitals can result in a generation of bonding NBO (Lewis type) or anti-bonding NBO (non-Lewis type). A bonding NBO, also called as donor orbital, has filled electrons and lower in energy while the anti-bonding NBO, also called as acceptor orbital, has low occupancy (vacant).

Non-covalent interactions like $n \rightarrow \pi^*$ and hydrogen bonding, involves delocalization of electron density from the filled bonding NBO to anti-bonding NBO which results in the stabilization of the system. Thus, to understand the non-covalent interactions one of the most important parameter which can be derived from the NBO analysis is the NBO delocalization energy which is determined by the second order perturbative energy, $E_{i \rightarrow j^*}^{(2)}$ where, i and j^* stand for the donor and acceptor orbitals. It measures the extent of the overlap of donor orbital (i) with the acceptor (j^*) anti-bonding orbital and hence the strength of the interaction. Since these interactions lead to loss of occupancy from the localized NBOs of the idealized Lewis structure into the empty non-Lewis orbitals (and thus, to departures from the idealized Lewis structure description), they are referred to as “delocalization” corrections to the zeroth-

order natural Lewis structure. For each donor NBO (i) and acceptor NBO (j), the donor-acceptor stabilization energy $E^{(2)}$ associated with $i \rightarrow j$ delocalization is estimated as

$$E^{(2)} = \Delta E_{ij}^{(2)} = q_i F(i,j)^2 / (\epsilon_j - \epsilon_i) \dots\dots\dots(2.18)$$

where q_i is the donor orbital occupancy (2 for closed-shell, 1 for open-shell), ϵ_i , ϵ_j are diagonal elements (orbital energies), and $F(i,j)$ is the off-diagonal NBO Fock matrix element.

Higher the second order perturbative energy value for a given donor-acceptor pair, greater is the strength of the interaction. NBO analysis has been used extensively to visualize the $n \rightarrow \pi^*$ interaction in the molecules, to determine its strength and its effect on nearby orbital interactions.

In this thesis, we have also used NBO deletion analysis. The NBO deletion analysis provides an opportunity to calculate the interaction energy within a single molecular fragment or between many by deleting certain NBOs. By deleting certain NBOs, this method sets their value in corresponding Fock matrix as zero and it re-diagonalizes the Fock matrix. The interaction energy obtained by this method can be compared with the original interaction energy. This method is basis set independent hence interaction energy values can also be compared at different levels of theory.

We have also used Wiberg bond indices implemented in the Gaussian G09 program to calculate the bond order of the bond. Bond order (B) of a chemical bond is defined as

$$B = \frac{N_b - N_{ab}}{2} \dots\dots\dots(2.19)$$

Where, N_b and N_{ab} are the numbers of electrons occupying the bonding and antibonding orbitals, respectively. However, the bond order calculated from the above equation cannot be

considered as quantum chemical quantity as it is not calculated from the wave function following the rules of quantum mechanics.

The first quantum mechanical approach to calculate the bond order was given by Coulson which is denoted as Coulson's bond order. The equation defining the Coulson's bond order is given as

$$D_{\mu\nu} = 2\sum C_{\mu i} C_{\nu i}^* \dots\dots\dots (2.20)$$

Where, $D_{\mu\nu}$ is the off-diagonal matrix element of the "Coulson's charge-bond order matrix", $C_{\mu i}$ is the coefficients of orbital i , μ and ν are the basis functions. Coulson's bond order was very useful to determine the bond order of C-C bonds in π -system. However, it cannot be applied for Pople's CNDO-all valence-electrons semiempirical theory.

Wiberg introduced a new equation for calculating the bond order at the CNDO semiempirical MO theory which is called as Wiberg bond order. Later the Wiberg's bond order was generalized for *ab initio* SCF wavefunctions. The Wiberg's bond order is defined as

$$W_{AB} = \sum_{\mu \in A} \sum_{\nu \in B} (PS)_{\mu\nu} (PS)_{\nu\mu}^* \dots\dots\dots (2.21)$$

Where, μ, ν are the basis functions, A, B represents the nuclei while P and S represent the one particle density and overlap matrices, respectively. Bond order calculated using Wiberg's equation correlates very well with the calculated bond order from equation 2.19.



Chapter 3

INTERPLAY BETWEEN HYDROGEN BONDING AND $n \rightarrow \pi^*$ INTERACTION

3.1 Introduction

Structures of biomolecules and materials are governed by delicate balance among multiple types of non-covalent interactions.^{14,19-21,34,132} For example, structures of nucleic acids are stabilized by hydrogen bonding and π -stacking interactions.²⁰ Similarly, specific folding structures of proteins are controlled by multiple non-covalent interactions like N-H...O, N-H...N, N-H... π , π -stacking etc.^{19,133,134} Self-assembly of molecular systems are also regulated by various types of intermolecular interactions.^{17,18} Thus, in-depth analysis of the interplay between different types of non-covalent interactions will help us to understand the biological processes and to design new functional materials as well as efficient drugs.

It has been discussed in section 1.3 that a previously unexplored and counterintuitive weak non-covalent interaction named as $n \rightarrow \pi^*$ interaction has been recently proved to be of significant importance in the stabilization of the structures of biomolecules as well as materials. It has been found that $n \rightarrow \pi^*$ interaction is quite analogous to the hydrogen bonding interaction in terms of electron delocalization. $n \rightarrow \pi^*$ interaction is delocalization of lone pair electrons on an electronegative atom into a π^* orbital of an adjacent C=O group or phenyl ring while hydrogen bonding involves delocalization of lone pair electrons into a σ^* orbital. It has been also observed that co-operativity between hydrogen bonding and $n \rightarrow \pi^*$ interaction contributes to the stability of protein structures as well as supramolecular assemblies.^{2,7,11,12,56,57,88} A subtle balance between both the interactions stabilizes the backbone as well as the backbone-side chain contacts of the proteins.^{2,7,12} It has been argued that in the backbone of α -helix, the carbonyl group of residue i is involved in hydrogen bonding with residue $i+4$ as well as in $n \rightarrow \pi^*$ interaction with residue $i+1$.^{2,7,12} As the carbonyl oxygen atom of residue i has two lone pairs, one of the lone pairs (s-type) is engaged in hydrogen bonding with the N-H group of the residue $i+4$ while the other lone pair

(p-type) takes part in $n \rightarrow \pi^*$ interaction with the neighboring carbonyl group (see Figure 3.1). Since, same carbonyl oxygen atom is involved in both hydrogen bonding and $n \rightarrow \pi^*$ interaction, strength of both of these interactions are interdependent in α -helix or they can influence each other. In other words, the strength of the hydrogen bonding could be compromised due to the presence of the $n \rightarrow \pi^*$ interaction or the $n \rightarrow \pi^*$ interaction itself could be attenuated due to the presence of strong hydrogen bonding interaction.^{12,82} Sometime, the presence of the $n \rightarrow \pi^*$ interaction can also strengthen the hydrogen bonding interaction.⁷

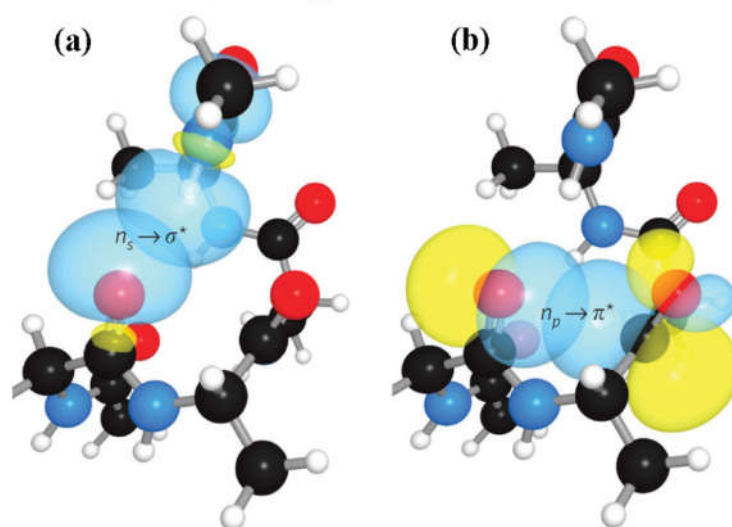


Figure 3.1 (a) Hydrogen bonding ($n \rightarrow \sigma^*$) interaction in α -helix between carbonyl group of residue i and N-H bond of residue $i+4$. (b) $n \rightarrow \pi^*$ interaction in α -helix between carbonyl groups of residue i and $i+1$. Adapted in part with permission from ref. 7. Copyright [2010] Nature Chemical Biology.

The co-operativity between the hydrogen bonding and the $n \rightarrow \pi^*$ interactions reported in the literature is mostly based on the PDB searches.^{7,12} However, one can obtain quantitative knowledge of the interplay among different types of intermolecular interactions if judiciously chosen molecules or weakly bound complexes can be studied as model systems in isolated gas phase. There is one advantage of studying the

physical nature of the interplay between these noncovalent interactions in the isolated gas phase over the crystal structures. In the case of the crystal structures, it could be argued that the close contacts between various atoms or moieties could be due to mere optimization of the orientation of different structural units in the supramolecular systems but this could not be true for the model systems studied in the gas phase. There are plenty of reports on gas phase experimental and theoretical studies on molecules and complexes stabilized due to subtle balance among various types of non-covalent interactions.^{47,135-140} However, gas phase study of the structures stabilized by subtle balance between $n \rightarrow \pi^*$ interaction and other non-covalent interactions is scarce in literature.

In this chapter, we have reported experimental as well as theoretical investigation of subtle interplay between hydrogen bonding and weak $n \rightarrow \pi^*$ interaction by studying 1:1 complexes of 7-azaindole (7-AI) and 2,6-substituted fluoropyridines, using gas-phase spectroscopic techniques (R2PI and IR-UV double resonance spectroscopy) and quantum chemistry calculations. The results show that the most stable geometries of these complexes are stabilized due to subtle balance between N-H...N hydrogen bonding and $n \rightarrow \pi^*$ interaction. The most significant observation of the present study is that a very weak $n \rightarrow \pi^*$ interaction can modulate the overall structural motif of the complexes in the presence of a very strong hydrogen bonding interaction. As 7-azaindole is a model for the nucleic acid base adenine, the present study mimics the $n \rightarrow \pi_{Ar}^*$ interaction present in the Z-DNA, which is reported by Egli and co-workers.⁸ We have probed the N-H stretching frequency in the complexes using gas phase IR spectroscopy to determine the observed structures of the complexes. The measurement of the N-H stretching frequencies in the complexes with variation of the fluorine substitution has been used to monitor the change in the strength of

the hydrogen bonding in the presence of $n \rightarrow \pi^*$ interaction. This is probably the first gas-phase study on the complexes stabilized due to $n \rightarrow \pi^*$ interaction and hydrogen bonding.

3.2 Results and Discussion

3.2.1 Structures of complexes of 7-azaindole and fluorosubstituted pyridines:

Computational studies

We have studied the structures of the complexes of 7-azaindole (7-AI) and fluorosubstituted pyridines in great detail using density functional theory (DFT) as well as wave functional theory (WFT) calculations. 1:1 complexes of 7-AI have been studied with all possible fluorosubstituted pyridines. The fluoropyridines considered for the complex formation are: 2-fluoropyridine (2-FP), 3-fluoropyridine (3-FP), 4-fluoropyridine (4-FP), 5-fluoropyridine (5-FP), 2,3-difluoropyridine (2,3-FP), 2,4-difluoropyridine (2,4-FP), 2,5-difluoropyridine (2,5-FP), 2,6-difluoropyridine (2,6-FP), 3,5-difluoropyridine (3,5-FP), 4,5-difluoropyridine (4,5-FP), 2,3,4-trifluoropyridine (2,3,4-FP), 2,3,5-trifluoropyridine (2,3,5-FP), 2,3,6-trifluoropyridine (2,3,6-FP), 2,4,5-trifluoropyridine (2,4,5-FP), 2,4,6-trifluoropyridine (2,4,6-FP), 3,4,5-trifluoropyridine (3,4,5-FP), 2,3,4,5-tetrafluoropyridine (2,3,4,5-FP), 2,3,4,6-tetrafluoropyridine (2,3,4,6-FP), 2,3,5,6-tetrafluoropyridine (2,3,5,6-FP), and 2,3,4,5,6-pentafluoropyridine (2,3,4,5,6-FP).

Gas phase experimental as well as computational studies of 7AI...2-FP complex has already been reported in the literature.¹⁴¹ Two in-plane double hydrogen bonded cyclic structures of 7AI...2-FP complex have been predicted from DFT calculation. It has been found that the structure with the N-H...N and C-H...N hydrogen bonds is more stable than the one with the N-H...F and C-H...N hydrogen bonds. Only the most stable structure of the dimer has been observed in the gas phase experiment. Therefore, only the structures primarily bound by N-H...N hydrogen bond have been considered for computational analysis of the 7-AI...fluorosubstituted pyridines studied here.

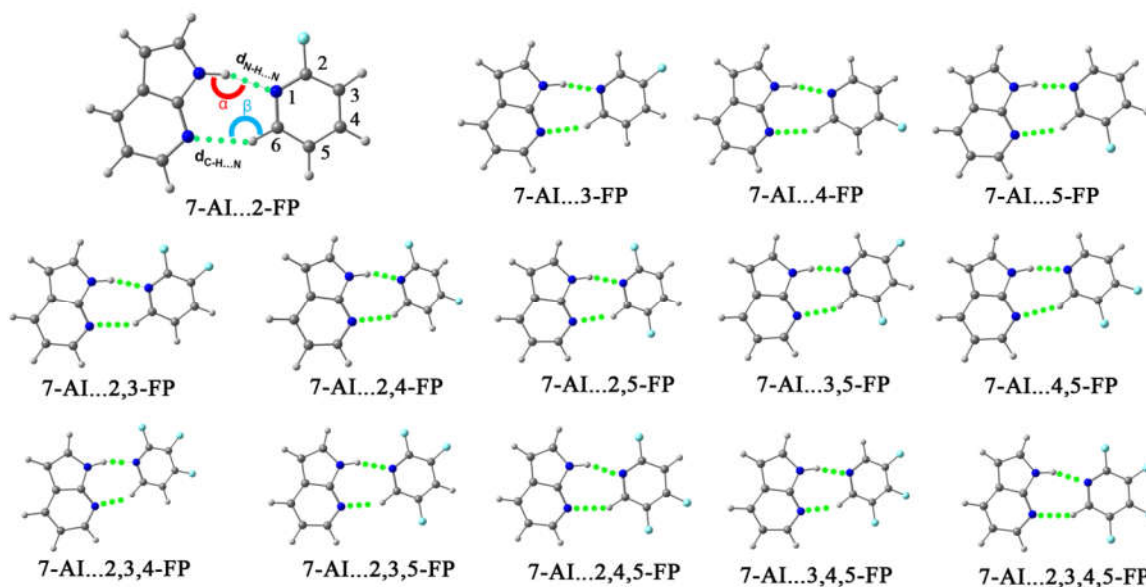


Figure 3.2 Double hydrogen bonded structures of all the complexes of 7-AI with fluoropyridines optimized at the M05-2X/cc-pVTZ level of theory.

Table 3.1 Binding energies (kcal/mol) and intermolecular geometrical parameters (kcal/mol) of all the double hydrogen bonded complexes of 7-AI and fluoropyridines calculated at the M05-2X/cc-pVTZ level of theory

	$d_{N-H...N}$ (Å)	$d_{C-H...N}$ (Å)	α ($^{\circ}$)	β ($^{\circ}$)	ΔE_0^a
7-AI...2-FP	2.04	2.48	165	149	-7.42
7-AI...3-FP	2.02	2.47	168	152	-7.23
7-AI...4-FP	2.01	2.45	168	152	-7.53
7-AI...5-FP	2.02	2.44	167	150	-7.16
7-AI...2,3-FP	2.07	2.46	164	149	-7.02
7-AI...2,4-FP	2.06	2.44	163	149	-7.39
7-AI...2,5-FP	2.08	2.42	162	147	-7.10
7-AI...3,5-FP	2.05	2.42	166	150	-6.86
7-AI...4,5-FP	2.04	2.40	165	150	-7.27
7-AI...2,3,4-FP	2.08	2.42	163	150	-7.03
7-AI...2,3,5-FP	2.10	2.41	161	148	-6.78
7-AI...2,4,5-FP	2.09	2.39	161	148	-7.23
7-AI...3,4,5-FP	2.06	2.39	165	151	-6.96
7-AI...2,3,4,5-FP	2.12	2.36	160	149	-6.92

^a ΔE_0 represents the BSSE+ZPE corrected binding energies of the complexes.

It has been found that all the fluoropyridines, except the ones with fluorine substitutions at both 2 and 6 positions, prefer planar double hydrogen bonded structure while forming complexes with 7-AI. Figure 3.2 shows the most stable double hydrogen bonded structure (N-H...N and C-H...N bound) of all the complexes of 7-AI with fluoropyridines optimized at the M05-2X/cc-pVTZ level of theory. The atom numbering scheme in the fluoropyridine has been shown in one of the complexes presented in Figure 3.1. Binding energies and a few selected geometrical parameters of these complexes calculated at the M05-2X/cc-pVTZ level of theory have been provided in Table 3.1. It appears that there is no drastic change in the geometry as well as the stability of these complexes by increasing the fluorine substitution.

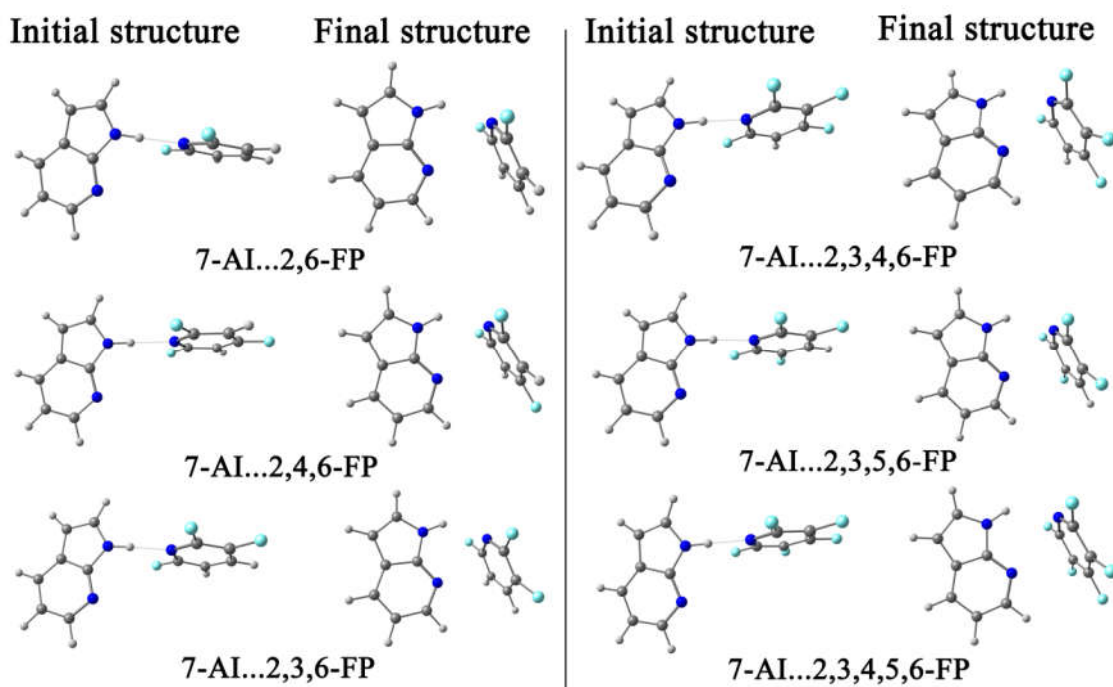


Figure 3.3 The initial and final structures of the complexes of 7-AI with 2,6-FP, 2,3,6-FP, 2,4,6-FP, 2,3,4,6-FP, 2,3,5,6-FP and 2,3,4,5,6-FP optimized at the M05-2X/cc-pVTZ level of theory.

However, it is quite interesting to see how the N-H...N bound structure of the fluorosubstituted complexes of 7-AI changes for the fluorine substitution at 2 and 6 positions of pyridine simultaneously. Fig. 3.3 shows the initial and final structures of the complexes of 7-AI with 2,6-FP, 2,4,6-FP, 2,3,6-FP, 2,3,4,6-FP, 2,3,5,6-FP and 2,3,4,5,6-FP. The

optimization of the initial structures has been done at the M05-2X/cc-pVTZ level of theory. It is obvious that the fluoropyridines having fluorine substitution at 2 and 6 positions cannot make C-H...N hydrogen bond with 7-AI while the N-H...N hydrogen bond is present there.

Thus we have considered the initial geometries of these six complexes provided in Fig. 3.3 as non-planar where the interplanar angle between 7-AI and fluoropyridine is 90^0 and only one hydrogen bond (N-H...N) is present. It is quite intriguing to note that the optimized structures of these six complexes show close contact between the nitrogen atom (N7) of 7AI and the aromatic ring of fluoropyridine (FP) moiety in addition to the presence of the strong N-H...N hydrogen bonding interaction (see Figure 3.3). The attractive interaction between the nitrogen atom (N7) of 7AI and the fluoropyridine ring is due to the $n \rightarrow \pi^*_{Ar}$ interaction which provides additional stability to the structure.

3.2.2 Co-operativity between hydrogen bonding and $n \rightarrow \pi^*$ interaction.

We will now focus the discussion on only those complexes which are stabilized by both hydrogen bonding and $n \rightarrow \pi^*$ interaction since our primary aim is to study the interplay between these two interactions. The geometrical parameters of N-H...N hydrogen bonding and $n \rightarrow \pi^*$ interaction in the complexes of 7-AI and 2,6-substituted fluoropyridines will provide us some evidence of interplay between hydrogen bonding and $n \rightarrow \pi^*$ interaction. Figure 3.4a shows the definition of a few important intermolecular geometrical parameters of the complexes of 7-AI and 2,6-substituted fluoropyridines. The N-H...N hydrogen bond distance and angle are denoted by $d_{N-H...N}$ and $\theta_{N-H...N}$, respectively. The parameter $R_{N...Ar}$ indicates the distance between the nitrogen atom of 7-AI and the centroid of the aromatic ring of the fluoropyridine and this distance dictates the strength of the $n \rightarrow \pi^*_{Ar}$ interaction. Figure 3.4b-d shows the plots of the $R_{N...Ar}$, $d_{N-H...N}$ and $\theta_{N-H...N}$ values as a function of increase of the fluorine substitution in the fluoropyridine moiety of the six complexes of 7-AI with 2,6-

substituted fluoropyridines calculated at the B3LYP, M05-2X, B97-D and MP2 levels of theory. In the case of the M05-2X level, the data have been presented for both cc-pVTZ and aug-cc-pVDZ (aVDZ) basis sets but only aVDZ basis set has been used for other levels of calculation.

It is quite obvious from the results provided in Fig. 3.4b that the $R_{N...Ar}$ values in the six complexes of 7-AI with 2,6-substituted fluoropyridines calculated at all the levels of theory except the B3LYP one falls in the regime of the designated distance (2.8-3.8 Å) for

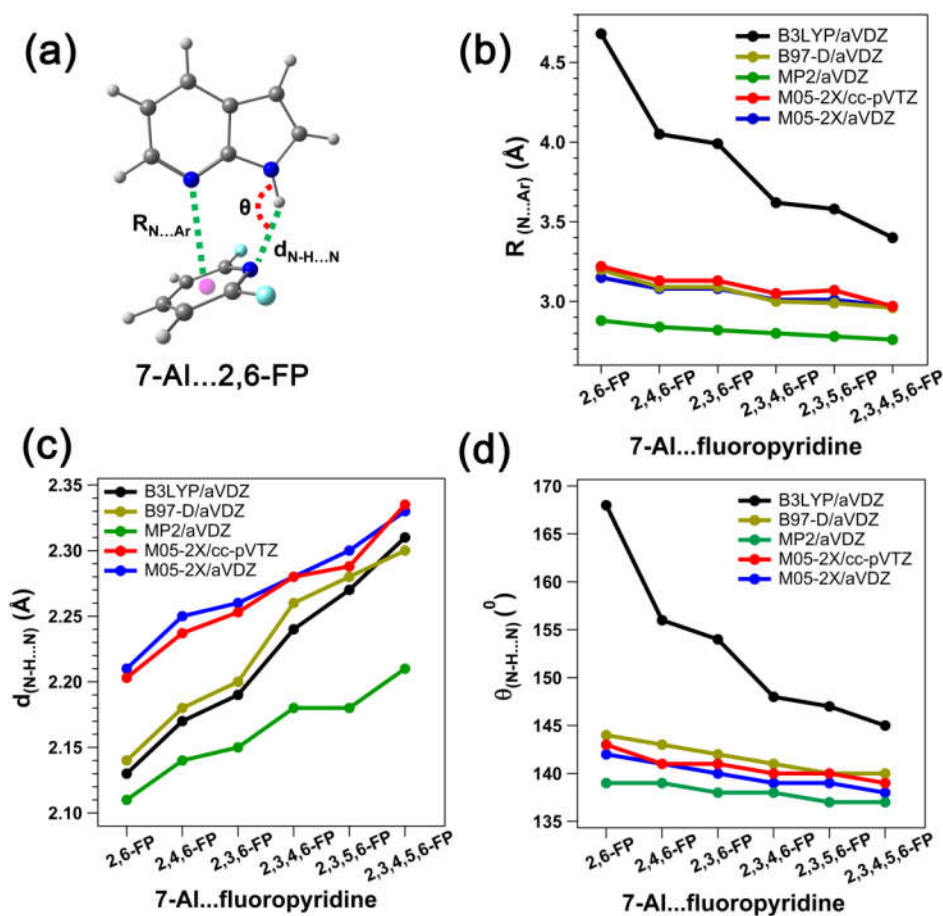


Figure 3.4 (a) Definition of a few important intermolecular geometrical parameters of the $n \rightarrow \pi^*$ complexes of 7-AI with 2,6-substituted fluoropyridines. (b), (c) and (d) plots of the $R_{N...Ar}$, $d_{N-H...N}$ and $\theta_{N-H...N}$ values of the six complexes of 7-AI with 2,6-substituted fluoropyridines calculated at the B3LYP, B97-D, MP2 and M05-2X levels of theory.

the $n \rightarrow \pi_{Ar}^*$ interaction reported in the literature. We observe a large difference in the $R_{N...Ar}$ values of the complexes calculated at the B3LYP level, from those calculated at the other levels of theory. B3LYP theory fails to provide the right value of $R_{N...Ar}$ as it does not consider any dispersion interaction. This result clearly indicates that the dispersion force has a significant contribution for the stability of the $n \rightarrow \pi_{Ar}^*$ interaction. It is also observed from Fig. 3.4b that the $R_{N...Ar}$ value gradually decreases with increasing the number of fluorine substitution in the fluoropyridine moiety of the complexes at all the levels of theory including the B3LYP. This result indicates that there is an increase in the electrostatic interaction between the nitrogen atom of the 7-AI and π -electron cloud of the FP with increasing the number of the fluorine atoms. Thus the $n \rightarrow \pi_{Ar}^*$ interaction is facilitated through the increase of the fluorine substitution in the pyridine ring by making it electron deficient. But it should be noted that the close proximity between the nitrogen atom and the aromatic ring is mostly due to the dispersion dominated $n \rightarrow \pi_{Ar}^*$ interaction unless the B3LYP theory would give correct result.

The plots in Figure 3.4c and 3.4d show that there is an increase in the N-H...N hydrogen bond distance ($d_{N-H...N}$) and decrease in the N-H...N angle ($\theta_{N-H...N}$) as the fluorine substitution in the pyridine ring increases. Similar trends have been observed at all the levels of calculation. The $d_{N-H...N}$ and $\theta_{N-H...N}$ values calculated at the M05-2X/cc-pVTZ level of theory in the six complexes of 7-AI with the 2,6 substituted fluoropyridines are in the range of 2.20-2.33 Å and 143-139°, respectively, while the corresponding values in the double hydrogen bonded complexes of 7-AI and fluoropyridines are 2.01-2.12 Å and 168-160°, respectively (see Table 3.1). According to the definition, the hydrogen bond is stronger if the the hydrogen bond angle is closer to 180°, as well as if the hydrogen bond distance is smaller.⁴⁶ The results clearly show that the strength of hydrogen bonding in the complexes of

7-AI and 2,6-substituted fluoropyridines decreases as the fluorine substitution in the pyridine ring increases. However, the strength of $n \rightarrow \pi_{Ar}^*$ interaction increases as the fluorine substitution in the pyridine ring increases. Thus it is noteworthy that the strength of the $n \rightarrow \pi_{Ar}^*$ interaction increases at the cost of decrease in the strength of the conventional hydrogen bonding interaction. It is quite spectacular to note here that despite the subtle competition between the strong hydrogen bonding and weak $n \rightarrow \pi_{Ar}^*$ interactions in the structures of these complexes, it is mostly the latter interaction that modulates the specific geometry shown in Figure 3.3.

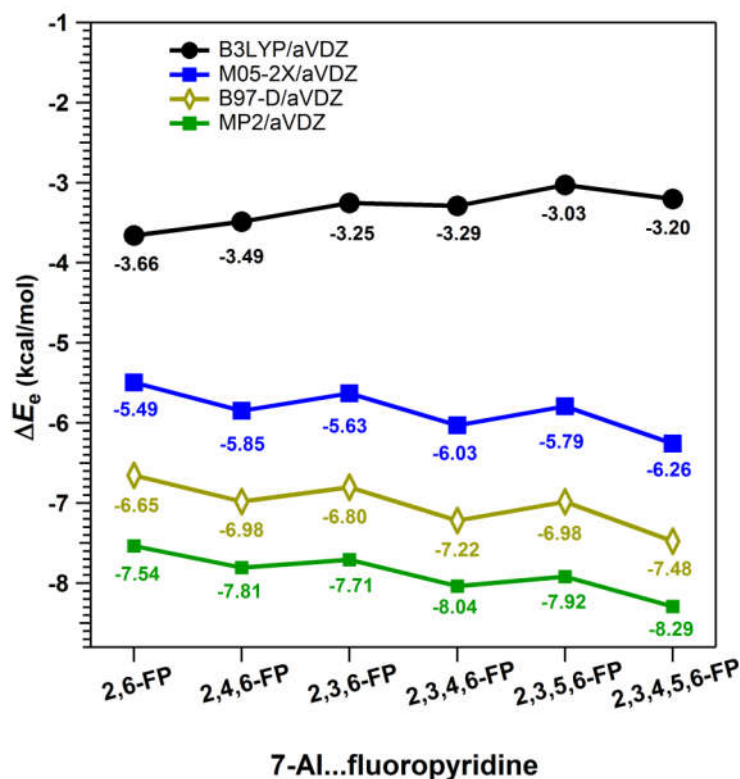


Figure 3.5 Plots of the BSSE corrected binding energies (ΔE_c) of the complexes of 7-AI with 2,6-substituted fluoropyridines calculated at the MP2 level as well as various levels of DFT.

It is interesting to see how the binding energies of these $n \rightarrow \pi_{Ar}^*$ bound complexes of 7-AI and fluorosubstituted pyridines get affected by increasing the fluorine substitution in the

fluoropyridine ring. Figure 3.5 shows the plots of the BSSE corrected binding energies (ΔE_e) of the complexes of 7-AI with 2,6-substituted fluoropyridines as a function of the increase of the fluorine substitution in the fluoropyridine ring calculated at the MP2 level as well as various levels of DFT using aVDZ basis set. A gradual increase in the binding energy (about 0.3 kcal/mol increase for each fluorine substitution) of the complexes with increasing the fluorine substitution has been observed at the MP2, M05-2X, and B97-D levels of theory. On the other hand, it is fascinating to note that there is a decrease in the binding energy of the complexes with increasing fluorine substitution at the B3LYP level of theory. This decrease in the binding energy at the B3LYP level is observed as the strength of the N-H...N hydrogen bond decreases with increasing fluorine substitution in the fluoropyridine moiety of the complexes and the B3LYP theory does not include the dispersion interaction, which contributes significantly to the $n \rightarrow \pi_{Ar}^*$ interaction present there.

It could be argued that the B3LYP theory would show a systematic increase in the binding energy of these complexes with increasing fluorine substitution in the fluoropyridine ring if the close proximity of the electron deficient aromatic ring and nitrogen atom in 7-AI would be governed by mostly electrostatic interaction. In fact, it has been found that the binding energies of the complexes of 7-AI with 2,6-substituted fluoropyridines calculated at the B3LYP level of theory is lower by about 3-4 kcal/mol relative to those obtained at the B97-D level of theory. Thus it is proved from the comparison of the results obtained from the B3LYP and dispersion-corrected DFT (B97-D, M05-2X) as well as MP2 calculations that the nitrogen atom in 7-AI and fluoropyridine ring comes close to each other due to the $n \rightarrow \pi_{Ar}^*$ interaction dominated by the dispersion forces.

BSSE corrected binding energies (ΔE_e) of the complexes of 7-AI with the 2,6-substituted fluoropyridines have also been calculated using various other basis sets at the M05-2X level of theory and this comparison has been presented in Table 3.2. It is interesting

to note that the binding energy values of all the complexes calculated at the M05-2X level using all the basis sets except the cc-pVDZ are very much similar. Thus it is obvious that the cc-pVTZ basis set is sufficient enough to calculate the binding energies of these complexes with reasonable accuracy. It is also apparent here that the basis set effect at the M05-2X level is minimal if the basis set higher than cc-pVDZ is used.

Table 3.2 BSSE corrected binding energies (ΔE_c , kcal/mol) of the complexes of 7-AI with the 2,6-substituted fluoropyridines calculated using various basis sets at the M05-2X level of theory

	cc-pVDZ	cc-pVTZ	cc-pVQZ	aVDZ
7-AI...2,6-FP	-4.90	-5.48	-5.47	-5.49
7-AI...2,4,6-FP	-5.19	-5.86	-5.82	-5.85
7-AI...2,3,6-FP	-5.04	-5.64	-5.60	-5.63
7-AI...2,3,4,6-FP	-5.37	-6.05	-6.01	-6.03
7-AI...2,3,5,6-FP	-5.24	-5.82	-5.76	-5.79
7-AI...2,3,4,5,6-FP	-5.64	-6.27	-6.23	-6.26

3.2.3 7-AI...fluorosubstituted pyridine complexes: Experimental studies

Our theoretical analysis shows that the complexes of 7-AI and 2,6-substituted fluoropyridines are stabilized due to subtle interplay between N-H...N hydrogen bond and $n \rightarrow \pi_{Ar}^*$ interaction. It is noticed that the strength of the hydrogen bond is compromised to accommodate the weak $n \rightarrow \pi_{Ar}^*$ interaction. However, it will be interesting to find out whether we can observe the calculated structures of the 7-AI...2,6-substituted fluoropyridine complexes bound by strong hydrogen bond and $n \rightarrow \pi_{Ar}^*$ interaction in our gas phase experiment. It could be possible then to monitor the interplay between N-H...N hydrogen bond and $n \rightarrow \pi_{Ar}^*$ interactions by probing the N-H stretching frequency. Although we have calculated the structures of six complexes of 7-AI and 2,6-substituted fluoropyridines, we

have performed experiments only on 7-AI...2,6-FP and 7-AI...2,3,5,6-FP complexes in the gas-phase as the remaining complexes will also provide similar results.

3.2.3.1. Time of Flight (TOF) mass spectra of the complexes.

TOF mass spectra of 7-AI...2,6-FP and 7-AI...2,3,5,6-FP complexes measured by fixing the laser wavelength at their corresponding electronic bands at 33889 and 33930 cm^{-1} , respectively, are provided in Figure 3.6. Several other mass peaks corresponding to the water clusters of 7-AI monomer as well as 7-AI complexes are also observed in both of the mass spectra. 7-AI...2-FP and 7-AI...2,3,5,6-FP complexes were synthesized in a supersonic expansion of mixed vapor of 7-AI (heated at 360 K) and fluoropyridines (cooled at 250 K) seeded in 3 bar of 70% Ne/30% He mixture and Ar carrier gases, respectively.

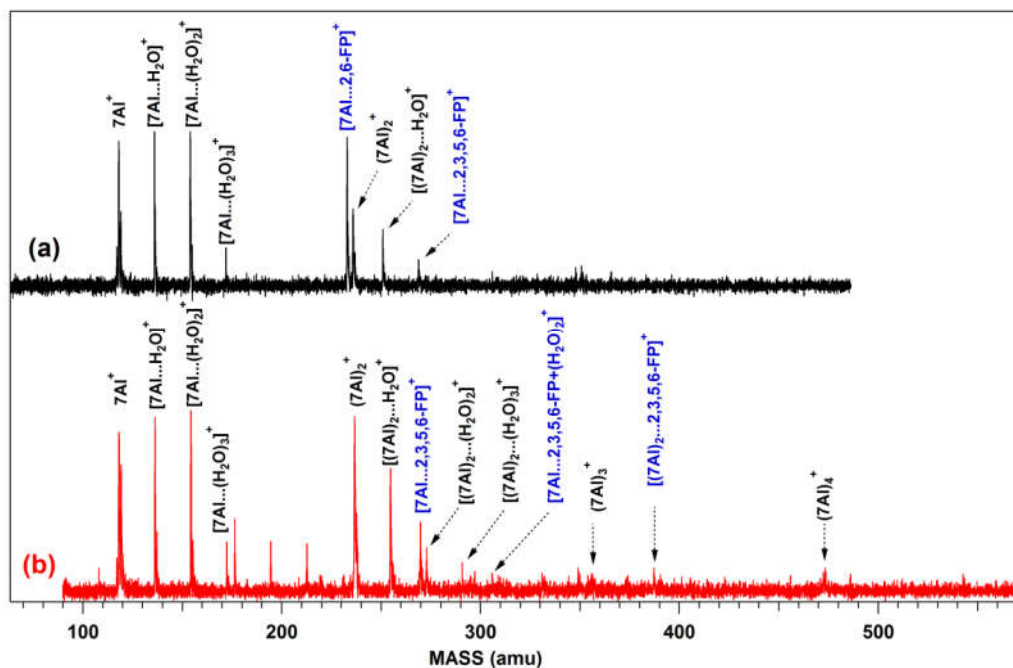


Figure 3.6 Time of Flight mass spectra of (a) 7-AI...2,6-FP and (b) 7-AI...2,3,5,6-FP complexes recorded by fixing the laser at 33889 and 33930 cm^{-1} respectively.

3.2.3.2. Electronic Spectra of 7-AI...2,6-FP and 7-AI...2,3,5,6-FP complexes.

Mass-selected electronic spectra of the 7-AI monomer, 7-AI...2,6-FP, and 7-AI...2,3,5,6-FP complexes measured using 1C-R2PI spectroscopy are shown in Figures 3.7a, 3.7b, and 3.7c, respectively. The spectra of the complexes are obtained by electronic excitation of the 7-AI moiety. The origin band (0_0^0) for the $S_1 \leftarrow S_0$ transition of the 7-AI monomer appears at 34637 cm^{-1} while the same for the 7-AI...2,6-FP and 7-AI...2,3,5,6-FP complexes are observed at 33889 and 33897 cm^{-1} , respectively.¹⁴² The spectra of the monomer and the complexes are presented in relative wavenumber scale with respect to their electronic origin bands. The electronic spectra of both the complexes have been measured up to $\sim 300 \text{ cm}^{-1}$ above their respective origin bands. The 0_0^0 band for the $S_1 \leftarrow S_0$ transition of both the

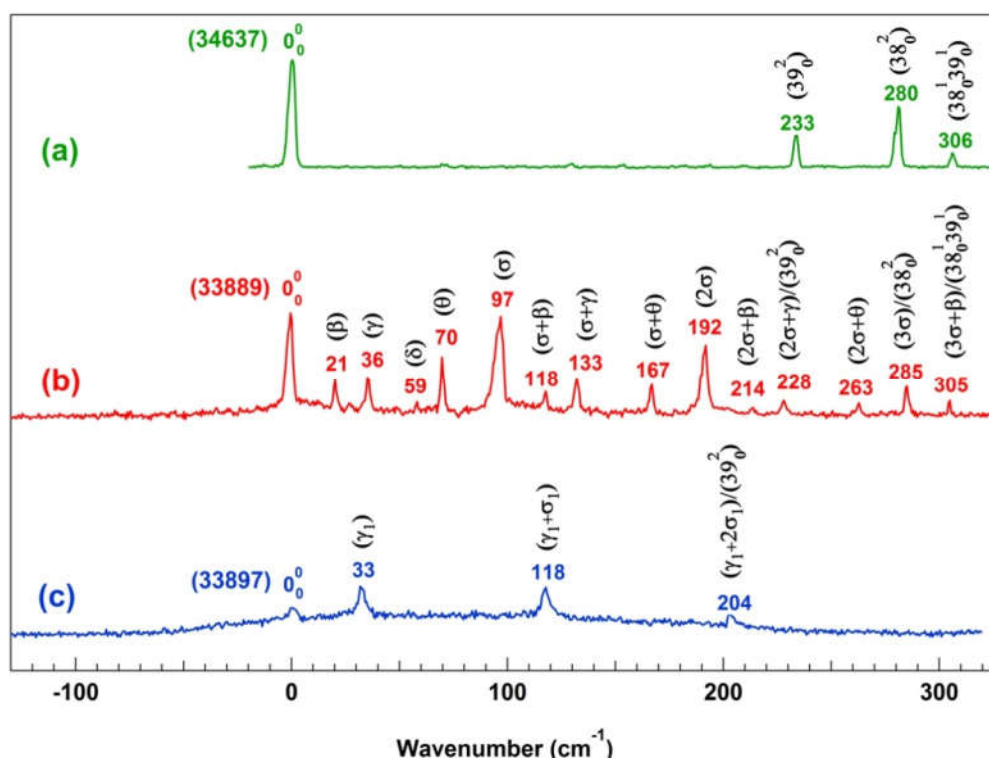


Figure 3.7 1C-R2PI spectra of the (a) 7-AI monomer (b) 7-AI...2,6-FP and (c) 7-AI...2,3,5,6-FP complexes. All the spectra of the monomer and the complexes are presented in relative wavenumber scale with respect to their electronic origin bands. The assignment of the spectra shown in this Fig. is described in the text.

complexes of 7-AI is red-shifted by a similar amount ($\sim 740 \text{ cm}^{-1}$) with respect to that of the 7-AI monomer. The observed red-shift in the electronic origin band of these complexes indicates that the stability of both of the complexes with respect to that of the monomer in the S_1 state is more than that in the S_0 state.

Table 3.3 Observed and calculated low frequency intermolecular vibrations of the 7-AI...2,6-FP and 7-AI...2,3,5,6-FP complexes. Low frequency intermolecular vibrations in the S_1 state are calculated at the TD-M05-2X/6-31+G(d) level of theory

7AI...2,6-FP			7AI...2,3,5,6-FP		
Obs.	Calc.	Assignments	Obs.	Calc.	Assignments
(cm^{-1})	(cm^{-1})		(cm^{-1})	(cm^{-1})	
	8	α		-10	α_1
21	22	β		20	β_1
36	39	γ	33	36	γ_1
59	56	δ		55	δ_1
70	76	θ		79	θ_1
97	97	Σ		87	σ_1
118		$(\sigma + \beta)$	118		$(\gamma_1 + \sigma_1)$
133		$(\sigma + \gamma)$			
167		$(\sigma + \theta)$			
192		2σ			
214		$(2\sigma + \beta)$	204		$(\gamma_1 + 2\sigma_1)/39_0^2$
228		$(2\sigma + \gamma)/39_0^2$			
263		$(2\sigma + \theta)$			
285		$3\sigma/38_0^2$			
305		$(3\sigma + \beta)/38_0^1 39_0^1$			

It is interesting to note that the R2PI spectra of the two complexes presented in Figures 3.7b and 3.7c are quite different. The electronic spectrum of the 7-AI...2,6-FP complex is rich in vibronic structures while that of the 7-AI...2,3,5,6-FP complex shows only a few sharp peaks over a broad background. The difference in the electronic spectra of these complexes could be due to the difference in the strength of the non-covalent interactions (hydrogen bond and $n \rightarrow \pi^*$ interaction) present there as a

result of varying fluorine substitution. The geometrical parameters presented in Figure 3.4 indeed show that the strength of the N-H...N hydrogen bond in the 7-AI...2,6-FP is more than that in the 7-AI...2,3,5,6-FP while it is reverse for the $n \rightarrow \pi^*$ interaction.

Electronic spectra of both the complexes show sharp bands which may correspond to low-frequency intermolecular vibrations of the complexes in the S_1 state. In order to assign these electronic bands, the observed and calculated (TD-M05-2X/6-31+G(d)) S_1 state low-frequency intermolecular vibrations of 7-AI...2,6-FP as well as 7-AI...2,3,5,6-FP complexes are compared in Table 3.3. The agreement between the observed and calculated low-frequency intermolecular modes is reasonably well. These intermolecular vibrations observed here are generally originated due to stretching as well as in-plane and out-of-plane bending of the N-H...N hydrogen bond. Most of the transitions in the electronic spectrum of these two complexes displayed in Figure 3.7b and Figure 3.7c can be assigned tentatively in terms of the fundamental modes, overtones and combination bands of the intermolecular vibrations.

In the case of the 7-AI...2,6-FP complex, all the intermolecular vibrational modes except the lowest frequency mode (8 cm^{-1}) designated as α are observed in the experiment. It is possible that the transition for the lowest frequency intermolecular mode of this complex is very weak in intensity and masked underneath the broad tail of the origin band. It is apparent from the electronic spectrum presented in Figure 3.7b that the hydrogen bond (N-H...N) stretching vibration (σ) at 97 cm^{-1} is the most active intermolecular mode which appears as 1st and 2nd overtones (2σ , 3σ) as well as combination bands with other intermolecular modes (β , γ , and θ). Thus the major change in the geometry of the 7-AI...2,6-FP complex after electronic excitation may occur along the hydrogen bond stretching mode. The comparison of the R2PI

spectrum of the 7-AI...2,6-FP complex with that of the 7-AI monomer¹⁴¹⁻¹⁴³ indicates that the bands observed at 228, 285, and 305 cm^{-1} in Figure 3.7b could be due to 39_0^2 , 38_0^2 , and $38_0^1 39_0^1$ intramolecular vibrations of 7-AI moiety, respectively. Modes 39 and 38 are butterfly and ring twisting vibrations, respectively in 7-AI.¹⁴² Generally, single quantum excitation in a non-totally symmetric vibration is very weak in intensity or absent in the electronic spectrum but the transitions due to two quantum excitations in these out-of-plane modes are allowed.¹⁴² Alternatively, the bands at 228, 285, and 305 cm^{-1} (see Figure 3.7b) could be assigned as intermolecular vibrations designated as $2\sigma + \gamma$, 3σ , and $3\sigma + \beta$, respectively.

The lowest energy sharp band (very weak in intensity) observed in the electronic spectrum depicted in Figure 3.7c is assigned as 0_0^0 band of the 7-AI...2,3,5,6-FP complex. Table 3.3 shows one imaginary frequency of -10 cm^{-1} obtained from the TD-M05-2X/6-31+G(d) level of calculation of the 7-AI...2,3,5,6-FP complex in the S_1 state. TDDFT calculation of this complex has been performed using various basis sets as well as different DFT functionals. However, an imaginary frequency of similar small magnitude has always been found. Such a low frequency of imaginary value indicates that the potential well for this complex in the S_1 state is extremely shallow and the geometry of the complex obtained from the calculation should be very close to the minimum energy structure. The vibronic bands at 33 and 118 cm^{-1} are tentatively assigned as γ_1 and $\gamma_1 + \sigma_1$ (Theoretical value: 113 cm^{-1}) intermolecular vibrations, respectively, where γ_1 is one of the bending modes and σ_1 is the stretching mode of the hydrogen bond. The band at 204 cm^{-1} could be due to either 39_0^2 intramolecular vibration of the 7-AI moiety or $\gamma_1 + 2\sigma_1$ (Theoretical value: 210 cm^{-1}) intermolecular vibration of the complex. The broad background observed in the electronic spectrum of the 7-AI...2,3,5,6-FP complex could be explained tentatively

due to the electronic transition of the larger clusters fragmented into the dimer mass channel upon ionization. Observation of broad background in the R2PI spectrum of dimer due to fragmentation of larger clusters has been reported earlier in the jet-cooled studies of various aromatic complexes.^{137,144}

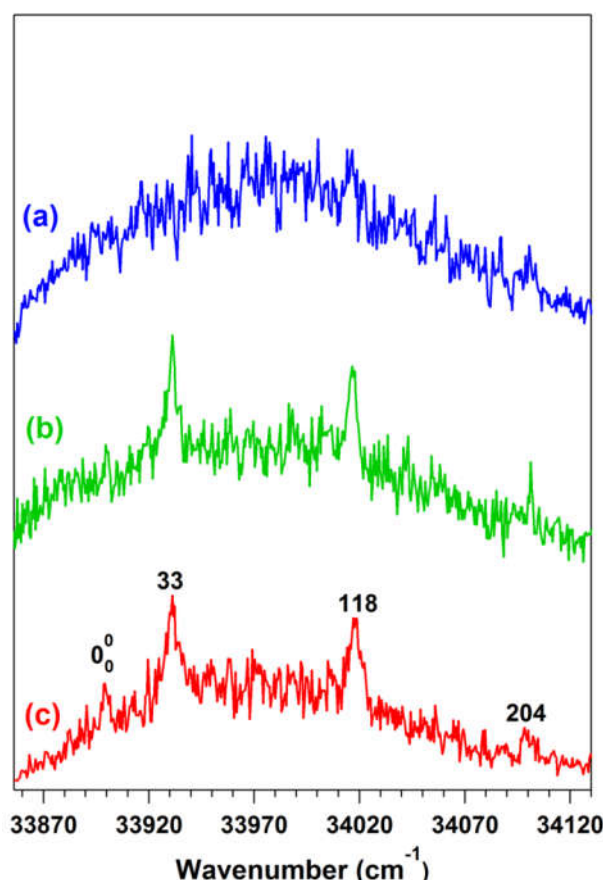


Figure 3.8 R2PI spectrum of 7AI...2,3,5,6-FP complex recorded at (a) 268 K, (b) 258 K, and (c) 247 K temperature of 2,3,5,6-FP keeping the temperature of 7AI fixed at 363 K.

In order to confirm that the broad background in the R2PI spectrum is due to the fragmentation of larger clusters, we have measured the R2PI spectra in the mass channel of 7-AI...2,3,5,6-FP complex by varying the temperature (concentration) of 2,3,5,6-FP while keeping the temperature of 7-AI fixed at 363 K and vice versa. The R2PI spectra recorded in the mass channel of 7-AI...2,3,5,6-FP complex at different

temperatures of 2,3,5,6-FP (keeping temperature of 7-AI fixed at 363 K) have been provided in Figure 3.8.

It is observed that the broad background gradually increases with the increase of the temperature of 2,3,5,6-FP and the sharp features of the R2PI spectrum is completely lost at a temperature of 268 K. Similar enhancement of the broad background with the increase of the temperature of 7-AI from 346 K to 363 K has been observed in the R2PI spectra measured in the 7-AI...2,3,5,6-FP mass channel. It should be pointed out that the R2PI spectra of the 7-AI...2,3,5,6-FP complex could not be measured either at the temperature of 7-AI lower than 346 K or that of 2,3,5,6-FP lower than 247 K due to very weak ion signal of the complex. Signature of formation of larger clusters of 7-AI with 2,3,5,6-FP has also been noticed in the mass spectrum provided in Figure 3.6. The larger clusters consisting both 7-AI and 2,3,5,6-FP observed in the mass spectrum are (7-AI)₂...2,3,5,6-FP trimer and (7AI)...(2,3,5,6-FP)...(H₂O)₂ tetramer. The results obtained from the studies with varying temperature (concentration) of 7-AI as well as 2,3,5,6-FP indicate that the broad background observed in the R2PI spectrum of 7-AI...2,3,5,6-FP is most likely due to larger clusters of 7-AI with 2,3,5,6-FP. However, it is not possible to tell the exact composition of the larger clusters responsible for the broadening.

3.2.3.3 IR spectra of 7-AI...2,6-FP and 7-AI...2,3,5,6-FP complexes

We have measured IR spectra of the 7-AI monomer, 7-AI...2,6-FP and 7-AI...2,3,5,6-FP complexes in the N-H stretching frequency region using RIDIR spectroscopy. The N-H stretching frequency of the 7-AI monomer appears at 3521 cm⁻¹, which matches well with the literature report (see Figure 3.9a).¹⁴⁵ The RIDIR spectrum of 7-AI...2,6-FP measured by exciting the electronic origin band at 33889 cm⁻¹ (Figure 3.7b) while the RIDIR spectrum of 7-AI...2,3,5,6-TTFP shown in Figure 3.9d has been obtained

by exciting the origin + 118 cm^{-1} band (Figure 3.7c). The N-H stretching frequency in 7-AI...2,6-DFP and 7-AI...2,3,5,6-TTFP complexes has been observed at 3414 and 3452 cm^{-1} , respectively. IR spectrum of 7-AI...2-FP complex reported earlier by Das

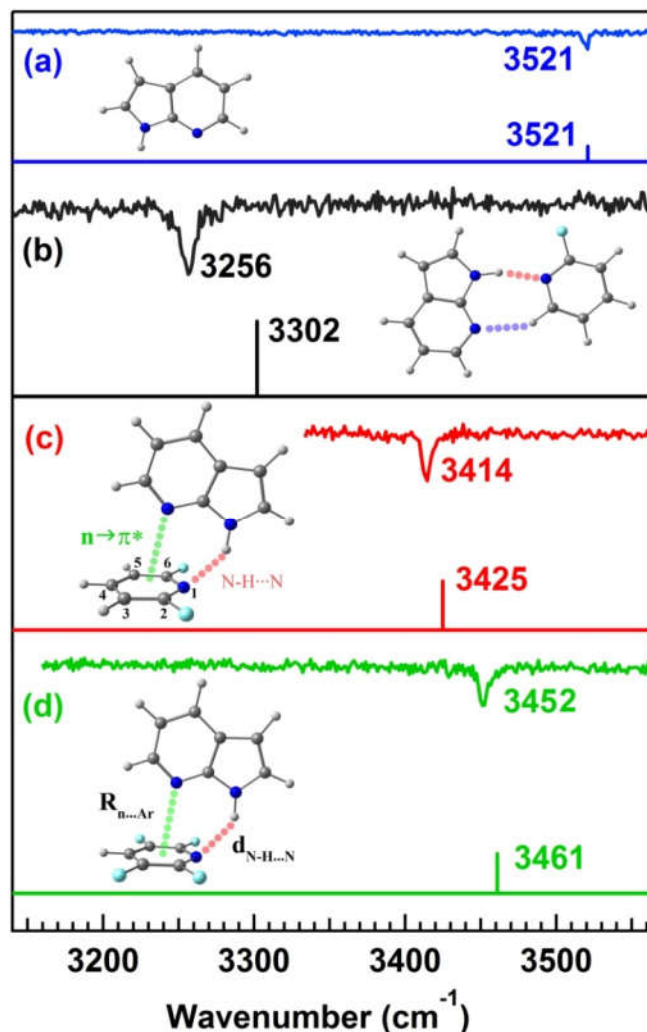


Figure 3.9 RIDIR spectra measured in the N-H stretching frequency region by probing the electronic origin band of the (a) 7-AI monomer, (b) 7AI...2-FP complex, (c) 7-AI...2,6-FP complex and (d) origin +118 cm^{-1} band of the 7-AI...2,3,5,6-FP complex. The theoretical N-H stretching frequencies calculated at the M05-2X/cc-pVTZ level of theory are shown through the stick spectra. Fig. 2(b) is reproduced from ref. 74. The ground state optimized structures of the complexes is shown in the inset of Fig. 2 below their respective RIDIR spectrum. The structures are optimized at the M05-2X/cc-pVTZ level of theory. The green dotted line in the optimized structures represents $n \rightarrow \pi^*$ interaction, the red dotted line represents N-H...N hydrogen bonding interaction and the purple dotted line in the structure of 7AI...2-FP complex represents C-H...N interaction.

and co-workers¹⁴¹ has been reproduced in Figure 3.9b which depicts the N-H stretching frequency at 3256 cm^{-1} . Theoretical stick IR spectra of the 7-AI monomer and its complexes along with their optimized structures calculated at the M05-2X/cc-pVTZ level are provided with the experimental spectra. The theoretical N-H stretching frequencies are scaled using a factor (0.94397) obtained from the ratio of the experimental and theoretical (M05-2X/cc-pVTZ) N-H stretching frequency of the 7-AI monomer.

The strength of a hydrogen bond, e.g. X-H...Y is generally determined by the red-shift in the X-H stretching frequency in the complex compared to that in the monomer.⁴⁶ The red-shift in the N-H stretching frequency in the 7-AI...2-FP complex, which has a planar structure stabilized by N-H...N and C-H...N hydrogen bonds, is 265 cm^{-1} with respect to that in the 7-AI monomer. On the other hand, the red-shift in the N-H stretching frequency in 7-AI...2,6-FP and 7-AI...2,4,5,6-FP complexes compared to that in the 7-AI monomer are 107 and 70 cm^{-1} . These results clearly indicate that the strength of the hydrogen bonding in the 7-AI...2,6-FP and 7-AI...2,4,5,6-FP complexes is much weaker compared to that in the 7-AI...2-FP complex. The structural motif in the 7-AI...2,6-substituted fluoropyridines is drastically different compared to that in 7-AI...2-FP due to the absence of the C-H...N hydrogen bond in the former one. The structures of 7-AI...2,6-substituted fluoropyridines could be much stronger if the N-H...N hydrogen bond would remain close to linear. But this kind of probable structure (see Figure 3.3) is not stable, and the structure is converged to the optimized geometry shown in the inset of Figures 3.9c and 3.9d. However, the significant deviation of the N-H...N hydrogen bond from linearity reveals that there is definitely a delicate balance between the hydrogen bond and the $n \rightarrow \pi^*$ interaction to refine the structures of these complexes.

Further, the N-H stretching frequency of 7-AI...2,3,5,6-FP complex increases by 37 cm^{-1} compared to that in the 7-AI...2,6-FP complex due to increase in the fluorination. This shows that with the increase in fluorination the hydrogen bond strength decreases but it also favours the $n \rightarrow \pi^*$ interaction which modulates the overall structural motif. As the strength of the hydrogen bond in the complexes studied here is affected by several factors, it is difficult to quantify the role of the $n \rightarrow \pi^*$ interaction on the strength of the hydrogen bond. Nevertheless, the IR spectroscopy results shown in Figure 3.9 demonstrate that the structures of the 7-AI...2,6-DFP and 7-AI...2,3,5,6-TTFP complexes observed in the experiment are stabilized by a subtle interplay between the N-H...N hydrogen bond and $n \rightarrow \pi^*$ interaction.

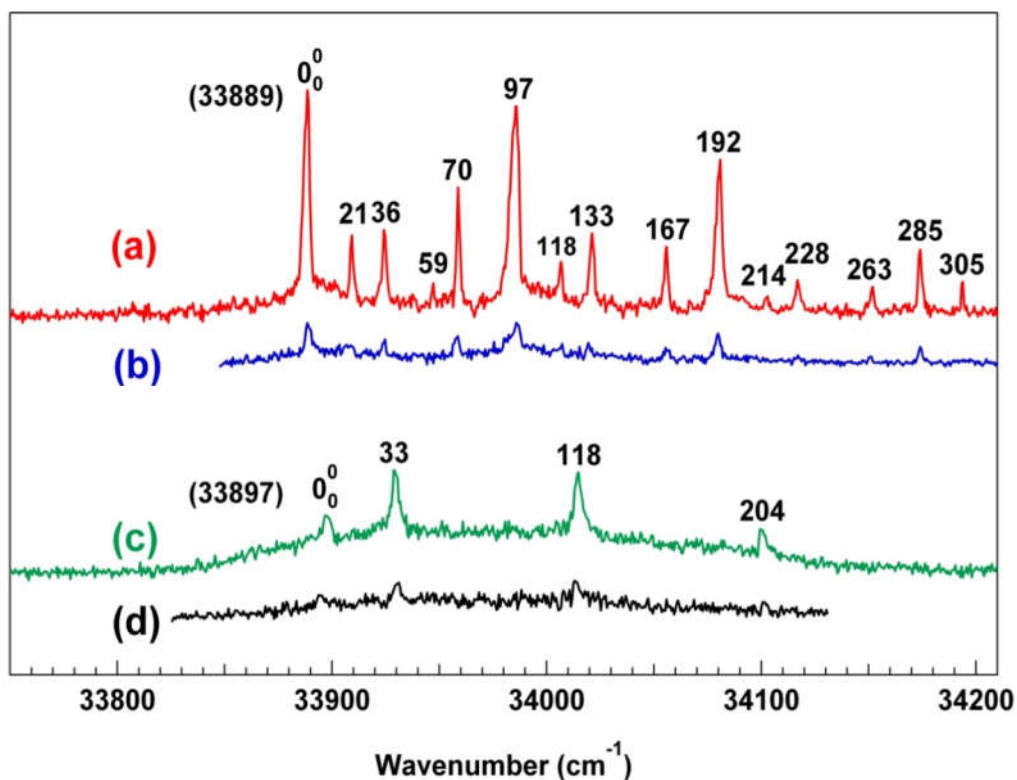


Figure 3.10 IR-UV hole burning spectra of (b) 7AI...2,6-FP and (d) 7AI...2,3,5,6-FP recorded by probing N-H stretching frequency at 3414 cm^{-1} and 3451 cm^{-1} respectively. 1C-R2PI spectra of (a) 7AI...2,6-FP and (c) 7AI...2,3,5,6-FP are reproduced along with their respective IR-UV hole burn spectra.

3.2.3.4 IR-UV hole-burning spectra of 7-AI...2,6-FP and 7-AI...2,3,5,6-FP complexes

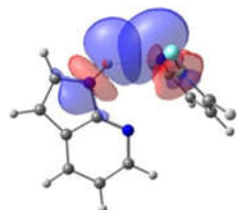
Figures 3.10(b) and 3.10(d) show IR-UV hole-burning spectra of the 7-AI...2,6-FP and 7-AI...2,3,5,6-FP complexes, respectively. The spectra provided in the Figure 3.10(b) and 3.10(d) have been measured by probing the vibrational bands at 3414 cm^{-1} (see Figure 3.9(c), 7-AI...2,6-DFP) and 3452 cm^{-1} (see Figure 3.9(d), 7-AI...2,3,5,6-FP), respectively. The R2PI spectra of 7-AI...2,6-DFP and 7-AI...2,3,5,6-FP have been reproduced in Figures 3.10a and 3.10c, respectively for comparison with the hole-burning spectra. It is apparent from both the hole-burning spectra that there is depletion in the ion signal for all the sharp bands in the R2PI spectra of the two complexes. Thus the IR-UV hole-burning spectra confirm the presence of a single conformer of both the 7-AI...2,6-DFP and 7-AI...2,3,5,6-TTFP complexes in the experiment.

3.2.4 Strength of N-H...N hydrogen bonding and $n \rightarrow \pi^*$ interaction

NBO analysis has been used for the quantitative determination of the strength of the individual N-H...N and $n \rightarrow \pi_{Ar}^*$ Interactions present in the complexes of 7-AI with 2,6-substituted fluoropyridines. In the case of the N-H...N hydrogen bonding interaction, there is a charge transfer delocalization of the lone pair orbital on the nitrogen atom ($n_{N(FP)}$) of the fluoropyridine ring over the antibonding orbital of the N-H group ($\sigma_{N-H(7-AI)}^*$) of 7-AI. On the other hand, the $n \rightarrow \pi_{Ar}^*$ interaction involves delocalization of the lone pair orbital of the nitrogen atom ($n_{N(7-AI)}$) in the pyridine moiety of 7-AI over the antibonding π -orbitals (π_{FP}^*) of the fluoropyridine. The NBO interaction energy is given by the second order perturbative energy $E_{i \rightarrow j}^{(2)}$, where i and j denote the donor and acceptor orbitals, respectively.¹³¹ The overlap between the donor and acceptor orbitals involving the N-H...N and $n \rightarrow \pi_{Ar}^*$ interactions present in the complexes of 7AI...2,6-FP and 7-AI...2,3,5,6-FP has been depicted in Figure 3.11. In the case of the $n \rightarrow \pi_{Ar}^*$ interaction, the $E_{n \rightarrow \pi}^{(2)}$ value has a

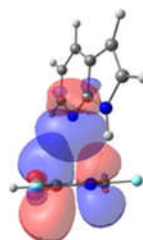
contribution from the overlap of the $n_{N(7-AI)}$ orbital with one of the antibonding π -orbitals ($\pi_{C=N}^*$ and $\pi_{C=C}^*$) of fluoropyridine ring.

7-AI...2,6-FP



$$n_{N(FP)} \rightarrow \sigma_{NH(7-AI)}^*$$

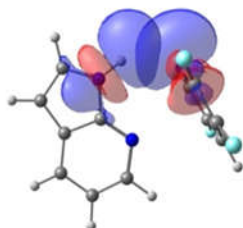
$$E_{i \rightarrow j}^{(2)} = 6.58 \text{ kcal/mol}$$



$$n_{N(7-AI)} \rightarrow \pi_{C-N(FP)}^*$$

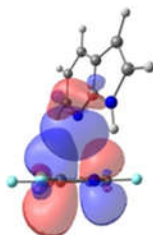
$$E_{i \rightarrow j}^{(2)} = 0.41 \text{ kcal/mol}$$

7-AI...2,3,5,6-FP



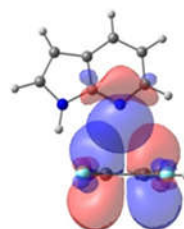
$$n_{N(FP)} \rightarrow \sigma_{NH(7-AI)}^*$$

$$E_{i \rightarrow j}^{(2)} = 4.92 \text{ kcal/mol}$$



$$n_{N(7-AI)} \rightarrow \pi_{C-N(FP)}^*$$

$$E_{i \rightarrow j}^{(2)} = 0.39 \text{ kcal/mol}$$



$$n_{N(7-AI)} \rightarrow \pi_{C-C(FP)}^*$$

$$E_{i \rightarrow j}^{(2)} = 0.08 \text{ kcal/mol}$$

Figure 3.11 The NBO pictures depicting the overlap between the donor and acceptor orbitals corresponding to the $n \rightarrow \pi_{Ar}^*$ and N-H...N interactions present in the complexes of 7-AI with 2,6-FP, and 2,3,5,6-FP .

The strength of $n \rightarrow \pi_{Ar}^*$ interaction increases with the increase of fluorine substitution on fluoropyridine ring. This trend in the $E_{n \rightarrow \pi^*}^{(2)}$ corresponds very well to the slow decrease of the $R_{N...Ar}$ values of the complexes presented in Figure. 3b. It is important to note that very small magnitude of the $n \rightarrow \pi_{Ar}^*$ interaction of these complexes obtained here is quite reasonable because the two aromatic moieties have a constraint to optimize this interaction in

the presence of the strong N-H...N interaction. On the other hand, $E_{n \rightarrow \sigma^*}^{(2)}$ value decreases systematically with increasing the number of fluorine substitution in the fluoropyridine ring. Thus, the increase in the N-H...N hydrogen bond distance as well as a decrease in \angle N-H...N with increasing fluorine substitution for these complexes shown in Figure 3.4c and 3.4d is correctly reflected in the NBO interaction energy of the hydrogen bond. It is worth mentioning here that the $n \rightarrow \pi_{Am}^*$ interaction energy reported for the N-acetylproline dimethylamide is only 0.27 kcal/mol and this small magnitude of interaction energy contributes significantly to the protein stability by showing the conformational preference of the trans amide over the cis configuration.⁶⁰ We also observe here that very weak $n \rightarrow \pi_{Ar}^*$ interaction present in the complexes of 7-AI and 2,6-substituted fluoropyridines can govern the basic structural motif. We have also looked into the occupancies of the π^* orbital of the fluoropyridine ring (FP) and σ^* orbital of the N-H bond of 7-azaindole (7-AI). Table 3.4 shows the occupancies of π^* orbital of the fluoropyridine ring and σ^* orbital of the N-H bond of 7-AI in the complexes of 7-AI...2,6-substituted fluoropyridine. It is observed that with the increase in fluorine substitution the occupancy of π^* orbital of fluoropyridine ring increases while that of σ^* orbital decreases. This further suggests that strength of $n \rightarrow \pi^*$ interaction increases and strength of N-H...N hydrogen bonding decreases with the increase in fluorine substitution on the fluoropyridine ring.

Table 3.4. Occupancies of π^* orbital of the fluoropyridine ring and σ^* orbital of the N-H bond of 7-AI in the complexes of 7-AI...2,6-substituted fluoropyridine

Complex	Occupancy of $\pi_{N=C}^*$ (FP)	Occupancy of σ_{N-H}^* (7-AI)
7-AI...2,6-FP	0.439	0.029
7-AI...2,4,6-FP	0.448	0.028
7-AI...2,4,5,6-FP	0.476	0.025

3.2.5 Origin of $n \rightarrow \pi_{Ar}^*$ interaction

Decomposition of the total interaction energy present in the complexes into different components can help in determining the origin of the $n \rightarrow \pi^*_{Ar}$ interaction. Localized Molecular Orbital (LMO) method has been used to fragment the total interaction energy (ΔE_{total}) of the complexes into electrostatic (ΔE_{ele}), exchange (ΔE_{ex}), repulsion (ΔE_{rep}), polarization (ΔE_{pol}), and dispersion (ΔE_{disp}) components.¹²⁹ These different components of the total interaction energy of the complexes of 7-AI with 2,6- substituted fluoropyridines stabilized by the $n \rightarrow \pi^*_{Ar}$ and N-H...N interactions calculated at the M05-2X/cc-pVDZ level of theory have been presented graphically in Fig. 3.12a.

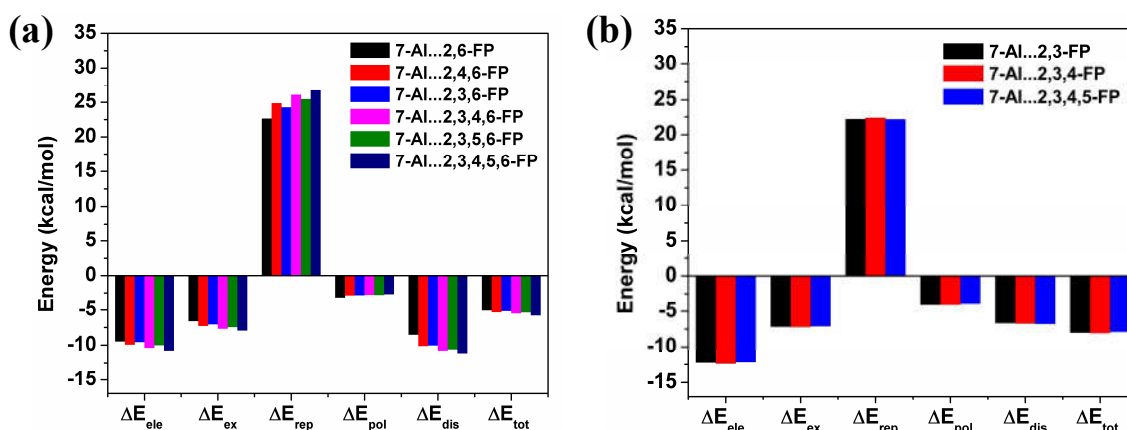


Figure 3.12 Different components of the total interaction energy of the complexes of (a) 7-AI with 2,6-substituted fluoropyridines and (b) doubly hydrogen bonded complexes of 7-AI with 2,3-FP, 2,3,4-FP, 2,3,4,5-FP calculated at the M05-2X/cc-pVDZ level of theory using LMO-EDA method.

The result indicates that all the six complexes comprising of the $n \rightarrow \pi^*_{Ar}$ interaction have comparable amount of electrostatic and dispersion components. A close look into the electrostatic and dispersion components of the total interaction energy of the complexes bound by both the $n \rightarrow \pi^*_{Ar}$ and N-H...N interactions reveals that even the dispersion interaction is more compared to the electrostatic one as the number of fluorine substitution in the fluoropyridine ring increases. It is quite interesting to compare the different components

of the interaction energy in these complexes with those present in the double hydrogen bonded (N-H...N and C-H...N) complexes of 7-AI and fluoropyridines. Fig. 3.12b depicts the components of the interaction energy in the double hydrogen bonded complexes of 7-AI with 2,3-FP, 2,3,4-FP and 2,3,4,5-FP. It is apparent here that the dispersion contribution is almost half of the electrostatic component in all the three complexes of 7-AI and FP bound by double hydrogen bonding interactions. For the brevity, energy decomposition of only three complexes has been presented in Figure 3.12b.

It can be concluded from the energy decomposition analysis that the close proximity of the fluoropyridine ring and nitrogen atom of the pyridine moiety of 7-AI in the complexes of 7-AI and 2,6-substituted fluoropyridines could be due to major contribution from the dispersion interaction. Otherwise the electrostatic component would increase rapidly compared to the dispersion one with increasing the fluorination in the pyridine ring of the 2,6-substituted fluoropyridines as the π -electron cloud of the pyridine ring becomes more electron deficient. Thus it is proved that the dispersion interaction has a significant contribution for the $n \rightarrow \pi^*$ interaction.

3.3 Conclusion

We have studied 1:1 complexes of 7-AI with a series of fluorosubstituted pyridines using various gas-phase spectroscopic techniques (R2PI, RIDIR and IR-UV hole-burning spectroscopy) and quantum chemistry calculations. We have found from detailed theoretical calculations that the most stable structure of the complexes of 7-AI with all the fluoropyridines except the ones with fluorine substitution at 2 and 6 positions is planar and double hydrogen bonded (N-H...N and C-H...N). However, the most stable structure of the complexes of 7-AI with 2,6-substituted fluoropyridines has a geometry consisting of the N-H...N hydrogen bonding and $n \rightarrow \pi_{Ar}^*$ interactions. It has been found that the strength of the $n \rightarrow \pi^*$ interaction increases while the strength of the N-H...N hydrogen bond decreases with

the increase in fluorine substitution on the fluoropyridine ring. Increase in the strength of the $n \rightarrow \pi^*$ interaction compensates the loss in the strength of hydrogen bonding and provides an additional stability to the complex. The $n \rightarrow \pi^*$ interaction also plays a major role in modulating the overall structure of the complex. Our computational results show that the structures of the complexes of 7-AI and 2,6-substituted fluoropyridines are stabilized due to subtle interplay between N-H...N hydrogen bonding and $n \rightarrow \pi^*$ interaction. We have verified the structures of two of these complexes (7AI...2,6-FP and 7AI...2,3,5,6-FP) through gas phase electronic and IR spectroscopy.

IR spectra combined with quantum chemistry calculations confirm that the structures of the observed complexes, 7AI...2,6-FP and 7AI...2,3,5,6-FP, are indeed stabilized due to subtle balance between hydrogen bonding and $n \rightarrow \pi^*$ interaction. The strength of the N-H...N hydrogen bond in the 7AI...2,6-FP complex has found to be weaker compared to that in the 7AI...2,3,5,6-FP complex. However, 7AI...2,3,5,6-FP complex is slightly more stable compared to 7AI...2,6-FP due to the presence of stronger $n \rightarrow \pi^*$ interaction in the former complex. IR-UV hole-burning spectra confirm the presence of a single conformer of both 7AI...2,6-FP and 7AI...2,3,5,6-FP complexes.

The presence of both N-H...N hydrogen bond and $n \rightarrow \pi^*$ interaction in 7-AI...2,6-substituted fluoropyridines has also been confirmed from NBO analysis. It has been established that the close proximity of the two electronegative centers in 7-AI...2,6-substituted fluoropyridines is due to very weak $n \rightarrow \pi_{Ar}^*$ interaction, which is facilitated through the increase in fluorination in the fluoropyridine ring. The $n \rightarrow \pi_{Ar}^*$ interaction cannot be governed by the electrostatic interaction; otherwise the B3LYP level of calculation would capture this non-covalent interaction. Binding energies of these complexes calculated at the B3LYP level are also substantially underestimated compared to those calculated at the

dispersion corrected DFT or MP2 levels. Thus it has been concluded that dispersion has significant contribution to the stability of the $n \rightarrow \pi^*$ interaction. Energy decomposition analysis also supports this conclusion as the increase of the dispersion component is more rapid compared to that of the electrostatic component with increase in fluorination of the fluoropyridine ring. In addition to this, analysis of different components of the total interaction energy of the double hydrogen bonded complexes of 7-AI and fluoro-substituted pyridines reveals that the dispersion contribution is almost half of the electrostatic component and the dispersion contribution in the binding energy is independent of the increase of the fluorination in fluoropyridine.

In this chapter, we have shown first experimental evidence of interplay between hydrogen bonding and $n \rightarrow \pi^*$ interaction using gas phase electronic and IR spectroscopy combined with quantum chemistry calculation. However, the current work determines the presence of the $n \rightarrow \pi^*$ interaction in the molecular complexes by probing the strength of the hydrogen bond (N-H...N) present there by measuring the N-H stretching frequency as these two interactions influence each other. This is an indirect approach to probe $n \rightarrow \pi^*$ interaction in a given molecular moiety. In fact, the molecular complexes studied here do not have any functional group which could be probed through IR spectroscopy to obtain direct spectroscopic evidence for an $n \rightarrow \pi^*$ interaction. In the latter chapters, we will choose suitable molecular systems where the vibrational frequency of the C=O group itself, involved in the $n \rightarrow \pi^*$ interaction, can be probed using gas phase IR spectroscopy.



Chapter 4

**GAS PHASE IR SPECTROSCOPIC
EVIDENCE FOR AN $n \rightarrow \pi^*$
INTERACTION**

4.1 Introduction

In the previous chapter, we have shown signature of the $n \rightarrow \pi^*$ interaction in the molecular complexes of 7-azaindole and 2,6-substituted fluoropyridines by monitoring the strength of the hydrogen bond (N-H...N) through measurement of the stretching frequency of the N-H group of 7-azaindole. This can be called as an indirect spectroscopic approach to show the evidence of the $n \rightarrow \pi^*$ interaction in the molecular system. However, a direct spectroscopic approach will be to probe the vibrational frequencies of the functional groups (for example C=O group) which are involved in the $n \rightarrow \pi^*$ interaction. Generally, the hydrogen bonding interaction (X-H...Y) in a molecular system can easily be characterized in a quantitative fashion by measuring the red-shift in the X-H stretching frequency using IR spectroscopy.^{146,147} Here the point is whether the existence of the $n \rightarrow \pi^*$ interaction, a non-covalent interaction analogous to the hydrogen bonding interaction in terms of electron delocalization, can be proved by directly probing the stretching frequency of the C=O group involved in this interaction using similar IR spectroscopic technique. It has been mentioned in chapter 1 that the $n \rightarrow \pi^*$ interaction is generally of two types.¹ One is $n \rightarrow \pi^*$ (amide) interaction between two neighboring C=O groups and this type of interaction is widely present in the backbone of proteins.^{2,57,60} The other one is $n \rightarrow \pi^*$ (aryl) interaction between a C=O group or any electronegative atom with an aromatic ring.¹ The $n \rightarrow \pi^*_{Ar}$ interaction has been found to play a significant role in the stabilization of nucleic acids, side chain aryl groups with backbone C=O groups, supramolecular assemblies of materials etc.^{3,5,8,11}

The existence of the $n \rightarrow \pi^*$ interaction has been demonstrated in the literature mostly from the analysis of X-ray crystal structures of biomolecules and materials in protein data bank (PDB) and Cambridge structural database (CSD), respectively, by identifying the close contact between an electronegative atom and carbonyl group or aromatic ring.^{7,9,11} However, the question arises whether this close contact between two electron rich moieties occurs just

because of optimization of the arrangement of other molecular units in the macromolecular systems. Preferential stabilization of the conformers of various organic molecules (small peptides, peptoids etc.) having $n \rightarrow \pi^*$ interaction over the ones without this interaction has been also studied by measuring the equilibrium constants from NMR spectroscopy.^{10,13,58,60,64,66} However, no direct spectroscopic evidence or quantitative information on the $n \rightarrow \pi^*$ interaction has not been established from NMR spectroscopy. Further, the NMR studies have been performed in solution phase, where the solvent polarity may affect the population difference between the conformers. On the other hand, IR spectroscopy could be used to probe the vibrational frequencies of different conformers of a given molecule in the presence or absence of the $n \rightarrow \pi^*$ interaction. However, given that the $n \rightarrow \pi^*$ interaction is very weak, it is not easy to identify the presence of this interaction from solution-phase IR spectroscopy because the spectroscopic signature of this weak interaction could be masked by the presence of various other interactions. Instead, IR spectroscopy carried out in an isolated collision-free environment, that is, in a supersonic jet, could be an ideal means to study this weak interaction quantitatively.

In this chapter, we have shown the first IR spectroscopic evidence of the $n \rightarrow \pi_{Ar}^*$ interaction by studying phenyl formate in the isolated gas phase using electronic, vibrational, and UV-UV hole-burning spectroscopy combined with *ab initio* calculations. Two conformers of phenyl formate have been observed in the experiment. One of the conformers (cis) is preferentially stabilized by the $n \rightarrow \pi_{Ar}^*$ interaction over the other conformer (trans) which does not have any $n \rightarrow \pi_{Ar}^*$ interaction. The C=O group of both the conformers were probed with IR radiation to determine whether the carbonyl stretching frequency in the cis conformer is different compared to that in the trans conformer.

4.2 Results and Discussion

4.2.1 Conformers of phenyl formate: Electronic spectroscopy and *ab initio* calculations

Figure 4.1a shows electronic spectrum of phenyl formate measured by one-color resonant 2-photon ionization (1C-R2PI) spectroscopy. The spectrum contains many sharp bands, making the assignment non-trivial. As phenyl formate is a flexible molecule, it can exist as cis and trans conformers depending on the orientation of the carbonyl group with respect to the phenyl group. Figure 4.2 shows the structures of the cis and trans conformers of phenyl formate optimized at the M05-2X/aug-cc-pVDZ level of theory. Zero-point energy (ZPE) corrected relative energies of the two conformers have been provided in the figure. The cis conformer is more stable than the trans conformer by 1.32 kcal/mol. The lowest

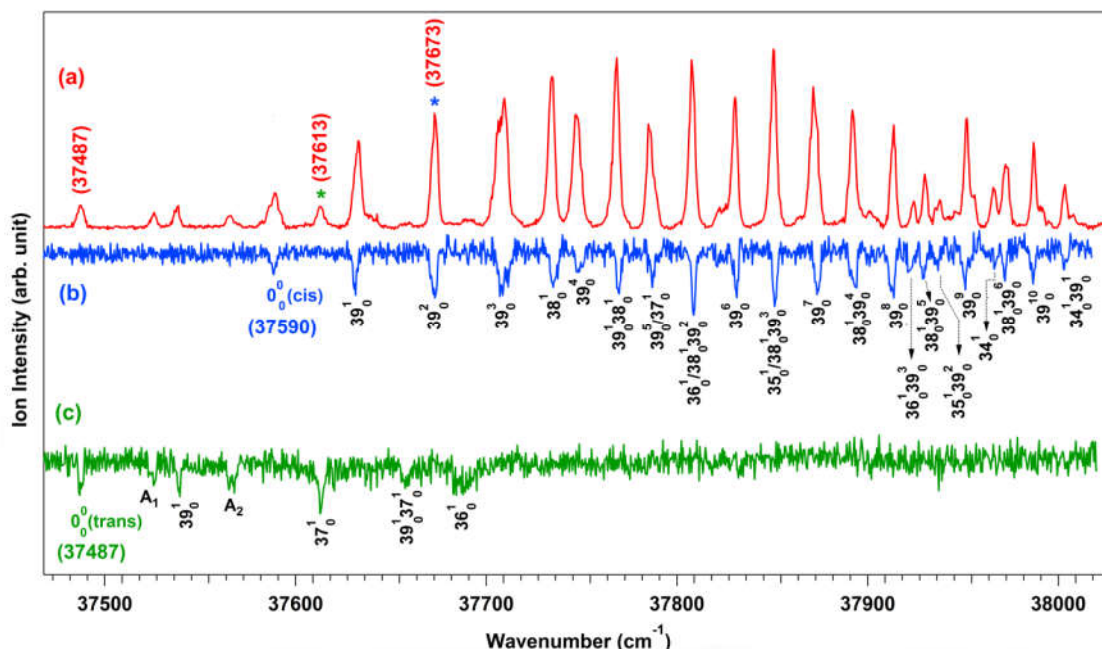


Figure 4.1. (a) Electronic spectrum of phenyl formate measured using 1C-R2PI spectroscopy. (b) and (c) represent UV-UV hole-burning spectra of phenyl formate measured by probing the bands at 37673 and 37613 cm⁻¹, respectively, marked by asterisks in the spectrum A. Tentative assignment of the bands in the electronic spectrum is done based on the calculated vibrational frequencies in the excited electronic state at the CIS/6-31+G(d) level of theory. See the text as well as Table S1 for the detailed assignment. The bands marked as A₁ and A₂ belong to the trans conformer only but could not be assigned to S₁←S₀ transition.

energy transition at 37487 cm^{-1} displayed in the electronic spectrum (Fig. 4.1a) could be assigned to the origin band resulting from the $S_1 \leftarrow S_0$ electronic excitation of one of the conformers of phenyl formate. However, the question arises whether multiple bands present in the spectrum are due to electronic excitation of a single conformer or both of the conformers.

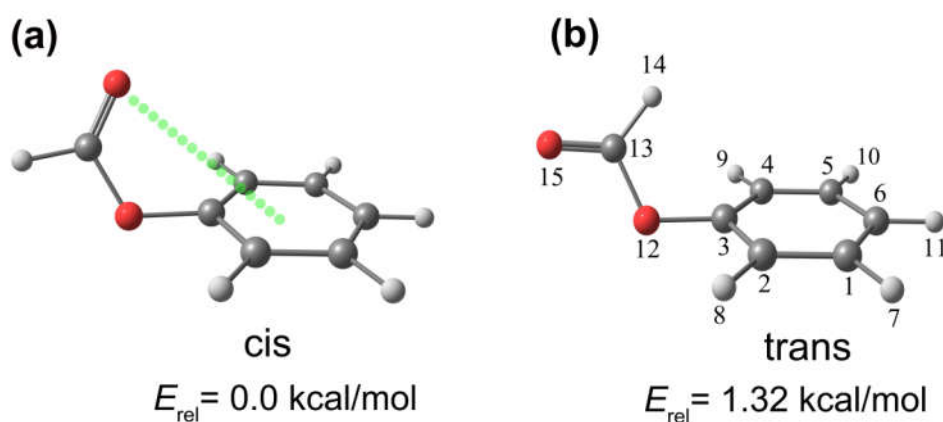


Figure 4.2 (a) cis and (b) trans conformers of phenyl formate obtained at the M05-2X/aug-cc-pVDZ level of theory. The atom numbering scheme is shown in the structure of trans conformer.

Figs. 4.1b and 4.1c show UV-UV hole-burning spectra by probing the bands at 37673 and 37613 cm^{-1} , respectively (marked by asterisks in the R2PI spectrum; Fig. 4.1a). The hole-burning spectra displayed in Fig. 4.1b,c clearly indicate the presence of the two conformers of phenyl formate in the experiment. This is evident through the depletion of the ion signal of the set of transitions originated from the ground electronic state of each individual conformer. The electronic transitions corresponding to the hole-burning spectrum in Fig. 4.1c are much weaker compared to those corresponding to the hole-burning spectrum in Fig. 4.1b. A comparison of the relative intensities of the bands in Fig. 4.1b and 4.1c indicates that the

bands in Fig. 4.1b are due to electronic excitation of the most stable i.e. cis conformer and the bands in Fig. 4.1c originate from excitation of the trans conformer of phenyl formate. The structural assignment of the two detected conformers has been confirmed by IR spectroscopy discussed later.

Table 4.1. Observed and calculated S_1 state vibrational frequencies (in cm^{-1}) of the cis and trans conformers of phenyl formate. S_1 state vibrational frequencies are calculated at the CIS/6-31+G(d) level of theory

cis conformer				trans conformer			
Obs. ^a	Calc.	Assignment	Description	Obs. ^b	Calc.	Assignment	Description
0.0		0_0^0		0.0		0_0^0	
43	46	39_0^1	Ph-O Torsion	39			
83		39_0^2		51	56	39_0^1	Ph-O Torsion
120		39_0^3		79			
145	137	38_0^1	Ring bend (boat)+C-O-C bend		110		O-CO torsion
157		39_0^4		126	134	37_0^1	Ring bend
179		$38_0^1 39_0^1$		171		$39_0^1 37_0^1$	
195	197	$37_0^1 / 39_0^5$	Ring Twist + O-CO torsion	204	208	36_0^1	Ring bend (boat)+Ph-O torsion
218	220	$36_0^1 / 38_0^1 39_0^2$	Ring Twist				
241		39_0^6					
261	259	$35_0^1 / 38_0^1 39_0^3$	Ring bend (boat) + O-CO torsion				
282		39_0^7					
302		$38_0^1 39_0^4$					
324		39_0^8					
335		$36_0^1 39_0^3$					
340		$38_0^1 39_0^5$					
348		$35_0^1 39_0^2$					
362		39_0^9					
376	373	34_0^1	Ring bend (chair)				
383		$38_0^1 39_0^6$					
397		39_0^{10}					
414		$34_0^1 39_0^1$					

^aRelative to the 0_0^0 band observed at 37590 cm^{-1} . ^bRelative to the 0_0^0 band observed at 37487 cm^{-1} . Mulliken notation has been followed to number the vibrational modes.

It is apparent from Fig. 4.1 that the electronic spectrum of the cis conformer of phenyl formate is richer in vibronic structure than that of the trans conformer. The vibronic bands of the two conformers (Figs. 4.1b, c) have been tentatively assigned by calculating their structures and vibrational frequencies in the excited electronic state at the CIS/6+31G(d) level of theory. The assignment of the bands has been provided in Fig. 1b and 1c. A detailed description of the assignment of the bands of the cis and trans conformers of phenyl formate has been listed in Table 4.1.

The band at 37590 cm^{-1} in the spectrum shown in Fig. 4.1b is assigned to the 0-0 band for the $S_1 \leftarrow S_0$ electronic excitation of the cis conformer of phenyl formate. It is interesting to note that the origin band of the cis conformer is very weak in intensity compared to that of the vibronic bands present in the spectrum. The electronic spectrum of the cis conformer is dominated by a long progression of the Ph-O torsion (mode 39) of 43 cm^{-1} as well as combination bands of mode 39 with the ring bending vibration (mode 38) of 145 cm^{-1} (Figure 4.1b). The observation of this strong Franck-Condon activity in the electronic spectrum demonstrates that the most significant change in the geometry of the cis conformer of phenyl formate occurs along the Ph-O torsional co-ordinate ($\angle C_4-C_3-O_{12}-C_{13}$, see Table 4.2). The comparison of a few important geometrical parameters of both the conformers of phenyl formate provided in Table 4.2 indeed corroborates this observation.

The spectrum shown in Fig. 4.1c shows the 0-0 band for the $S_1 \leftarrow S_0$ electronic excitation of the trans conformer of phenyl formate at 37487 cm^{-1} . A few low frequency vibrational modes of the trans conformer of phenyl formate calculated at the S_1 state are provided in Table 4.1. Here the spectrum does not show any significant progression of any normal mode, rather single quantum excitations of a few vibrational modes (mode 39, 37 and 36) are detected in the experiment. The geometrical parameters listed in Table 4.2 supports this observation. It has been found that the bands at $0-0+39$ and $0-0+79 \text{ cm}^{-1}$, marked as A_1 and A_2 in the

spectrum shown in Fig. 4.1c, cannot be assigned from the S_1 state calculated vibrational frequencies of the trans conformer of phenyl formate. This is quite intriguing as both of these bands show depletion in the ion signal simultaneously with all other bands in the hole-burning spectrum of Fig. 4.1c. Thus the A_1 and A_2 bands share the ground state of the trans conformer only. It could be speculated that these two bands could be due to the transition to the S_2 state of the trans conformer which is close to the S_1 state. Detection of a similar $S_2 \leftarrow S_0$ band at 123 cm^{-1} above the S_1 origin transition in the jet-cooled electronic spectrum of diphenylmethane has been reported by Zwier and co-workers.¹⁴⁸ As the focus of this work is to obtain spectroscopic evidence for the $n \rightarrow \pi^*$ interaction by determining the ground state structures of the two conformers of phenyl formate, high level ab initio calculations of the excited electronic states to confirm the assignment of these two bands (A_1 and A_2) was not pursued here.

Table 4.2 A few selected geometrical parameters of the cis and trans conformers of phenyl formate in the S_0 and S_1 states. The structures in the S_0 state have been calculated at the M05-2X/aug-cc-pVDZ level of theory while the S_1 state structures have been calculated at the CIS/6-31+G(d) level of theory

	cis conformer		trans conformer	
	S_0	S_1	S_0	S_1
$r_{\text{C=O}}$ (Å)	1.20	1.18	1.19	1.17
$r_{\text{C}_{13}\text{-H}_{14}}$ (Å)	1.10	1.082	1.10	1.085
$d_{\text{C=O}\dots\text{Ring center}}$ (Å)	3.75	3.91	-	-
$d_{\text{H}_{14}\dots\text{Ring center}}$ (Å)	-	-	3.41	3.50
$a\theta$	48°	35°	-	-
$\angle \text{C}_3\text{-O}_{12}\text{-C}_{13}$	118°	124°	117°	120°
$\angle \text{O}_{12}\text{-C}_{13}\text{-O}_{15}$	126°	127°	122°	122°
${}^b\angle \text{C}_3\text{-O}_{12}\text{-C}_{13}\text{-O}_{15}$	-0.04°	-3°	175°	171°
${}^c\angle \text{C}_4\text{-C}_3\text{-O}_{12}\text{-C}_{13}$	-57°	-40°	-56°	-53°

^a θ is the angle between the plane containing the carbonyl oxygen atom and the aromatic plane; ^b $\angle \text{C}_3\text{-O}_{12}\text{-C}_{13}\text{-O}_{15}$: O-CO torsional angle; ^c $\angle \text{C}_4\text{-C}_3\text{-O}_{12}\text{-C}_{13}$: Ph-O torsional angle

4.2.2 Gas phase IR spectroscopy: Evidence for the $n \rightarrow \pi^*$ interaction

Figs. 4.3a and 4.3c show IR spectra measured in the carbonyl stretching region by excitation of the [0-0 (cis) + 83 cm^{-1}] and [0-0 (trans) + 126 cm^{-1}] bands, respectively, in the electronic spectrum (Fig. 4.1a) of phenyl formate using resonant ion dip infrared (RIDIR) spectroscopy. Theoretical IR spectra calculated at the M05-2X/aug-cc-pVDZ level of theory displaying carbonyl stretching frequency of the cis and trans conformers of phenyl formate

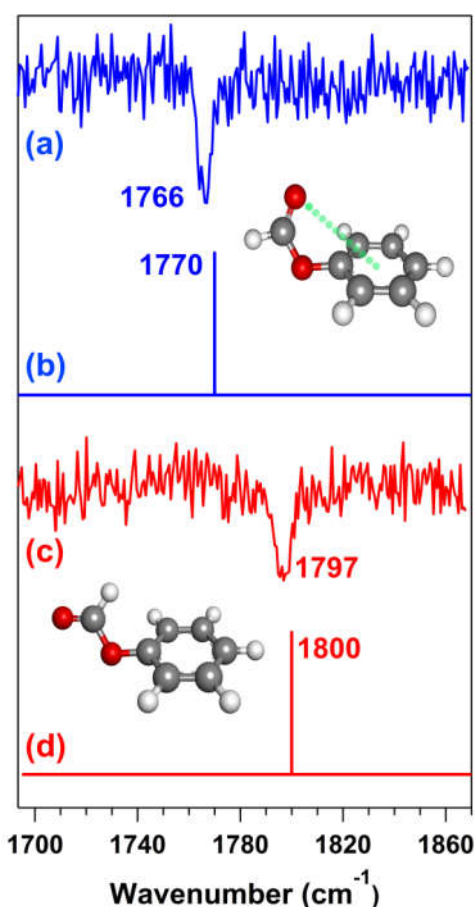


Figure 4.3. IR spectra by probing (a) 0-0(cis) + 83 cm^{-1} and (c) 0-0(trans) + 126 cm^{-1} bands in the electronic spectrum shown in Fig. 4.1. Theoretical IR spectra of the cis and trans conformers of phenyl formate calculated at the M05-2X/aug-cc-pVDZ level of theory are shown as stick diagrams in 4.3(b) and 4.3(d), respectively. The calculated IR frequency has been scaled with respect to reported experimental carbonyl stretching frequency of methyl lactate.

are provided in Fig. 4.3b and 4.3d, respectively. The calculated IR stretching frequency has been scaled using a factor (0.9577) obtained from the ratio of a reported experimental carbonyl stretching frequency (1746 cm^{-1}) and M05-2X/aug-cc-pVDZ level calculated carbonyl stretching frequency (1823 cm^{-1}) of methyl lactate, a similar ester like phenyl formate. The experimental carbonyl stretching frequency of methyl lactate reported in the literature was measured using matrix isolation FTIR spectroscopy.

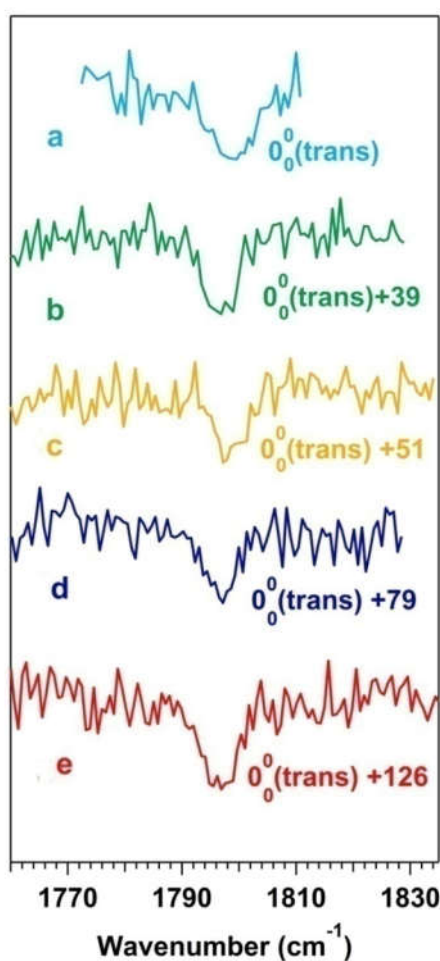


Figure 4.4 IR spectra measured in the carbonyl stretching region by exciting the (a) 0_0^0 (trans), (b) 0_0^0 (trans) + 39 cm^{-1} , (c) 0_0^0 (trans) + 51 cm^{-1} , (d) 0_0^0 (trans) + 79 cm^{-1} and (e) 0_0^0 (trans) + 126 cm^{-1} bands of the electronic spectrum of phenyl formate shown in Figure 4.1(c).

There is an excellent agreement between the experimental and theoretical IR spectra of the two conformers of phenyl formate (Fig. 4.3). The IR band observed at 1766 cm^{-1} in the vibrational spectrum shown in Fig. 4.3a is assigned to the carbonyl stretching frequency in the cis conformer of phenyl formate where the carbonyl group is pointed towards the phenyl ring. On the other hand, the IR band observed at 1797 cm^{-1} in the vibrational spectrum shown in Fig. 4.3c is assigned to the carbonyl stretching frequency in the trans conformer of phenyl formate where the carbonyl group is pointed away from the phenyl ring. The IR spectroscopic data demonstrate that an attractive interaction between the carbonyl group and the π -cloud of the phenyl ring in the cis conformer contributes to the observed red-shift of 31 cm^{-1} in the carbonyl stretching frequency of the cis conformer compared to that of the trans conformer. It is important to mention here that the IR spectra measured by excitation of the A_1 [0-0 (trans) + 39 cm^{-1}] and A_2 [0-0 (trans) + 79 cm^{-1}] bands in the electronic spectrum of phenyl formate (Figure 4.1c) reconfirms that these two bands originate from the trans conformer only. These IR spectra have been provided in Figure 4.4.

4.2.3 $n \rightarrow \pi^*$ interaction and C=O stretching frequency: NBO analysis

NBO analysis of phenyl formate performed at the M05-2X/cc-pVTZ level of theory confirms the presence of the $n \rightarrow \pi^*$ interaction in the cis conformer. NBO calculations also shed light on the role of the $n \rightarrow \pi^*$ interaction in reducing the C=O frequency in the cis conformer of phenyl formate with respect that in the trans conformer. The second order perturbative energy ($E_{n \rightarrow \pi^*}^{(2)}$) for the $n \rightarrow \pi^*$ interaction between the lone pair orbital and π^* orbitals of the phenyl ring in the cis conformer is 1.03 kcal/mol while the same is absent in the trans conformer of the phenyl formate. Figure 4.5 displays NBOs showing the overlap between the carbonyl oxygen lone pair orbital and π^* orbital of the phenyl ring in the cis conformer. Further NBO analysis of both cis and trans conformers of phenyl formate has

been carried out to look into all of the orbital interactions present and to determine the role of the $n \rightarrow \pi^*$ interaction to decrease the C=O stretching frequency in the cis conformer relative to the trans. Second order perturbative energy values as well as energies of donor and acceptor orbitals for interactions between various NBOs in the cis and trans conformers of phenyl formate have are provided in Tables 4.3. The NBOs corresponding to the interactions defined in Table 4.3 showing overlap between various orbitals in the cis and trans conformers of phenyl formate are shown in Figures 4.7-4.8.

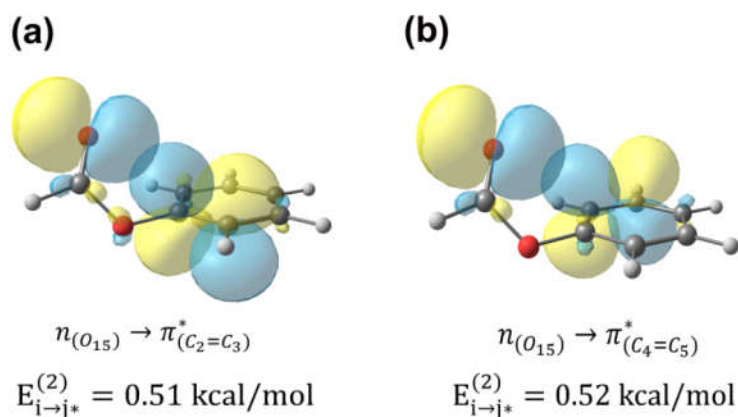


Figure 4.5 NBO view showing the overlap of lone pair orbital (n) of carbonyl oxygen and π^* orbitals of phenyl ring in the cis conformer of phenyl formate.

First of all, the NBO data show that there is no significant overlap (interaction) between the π -orbitals of the carbonyl group and the π^* orbitals of the phenyl ring in the cis conformer of phenyl formate (See Figure 4.6). This result indicates that the stability of the cis conformer of phenyl formate over the trans conformer is not due to π - π interactions between the C=O group and the phenyl ring. Interestingly, there are two opposing electronic effects which influence the carbonyl stretching frequency in phenyl formate. One of the factors denoted by R_1 (see Table 4.3), which reduces the carbonyl stretching frequency or weakens the C=O bond, is the delocalization of the lone pair electrons (p-type and σ -type) on ether oxygen

(O₁₂) into carbonyl π^* and σ^* orbitals (C₁₃=O₁₅). This is also called resonance effect. The reduction in the C=O stretching frequency will be more as the overlap between these lone pair and carbonyl π^*/σ^* orbitals increases. Another factor denoted by R₂, which increases the carbonyl stretching frequency or strengthens the C=O bond, is the delocalization of the lone pair electrons (p-type and σ -type) on the carbonyl oxygen (O₁₅) into the σ^* orbital of O₁₂-C₁₃. Thus the increase in the C=O stretching frequency will be more as there will be more efficient overlap between these two orbitals. Additionally, interaction (denoted as R₃) of the lone pair electrons (p-type and σ -type) on the ether oxygen (O₁₂) with the π^* and σ^* orbitals of the phenyl ring opposes the R₁ factor and favors the R₂ factor. R₂ factor is generally called inductive effect (here it is -I effect). All of these electronic interactions are present in both cis and trans conformers of phenyl formate. However, the $n \rightarrow \pi^*$ interaction (denoted by R₄, see Table 4.3) between the lone pair electrons on the carbonyl oxygen and the π -cloud of the phenyl ring is present only in the cis conformer of phenyl formate but not in the trans conformer.

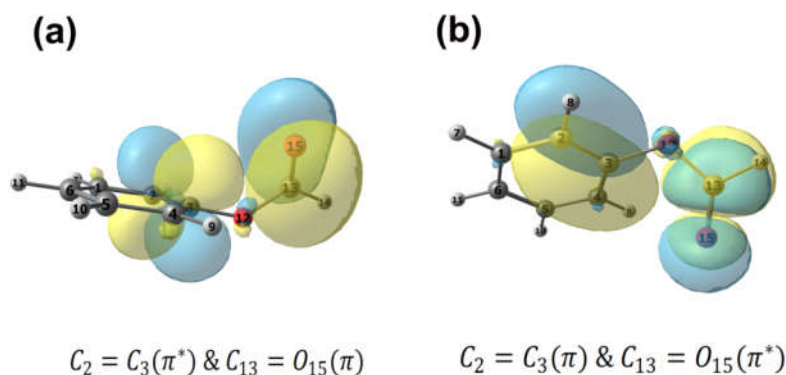


Figure 4.6. NBO view of (a) π^* orbital of phenyl ring along with π orbital of carbonyl group and (b) π orbital of phenyl ring along with π^* orbital of carbonyl group in the cis conformer of phenyl formate.

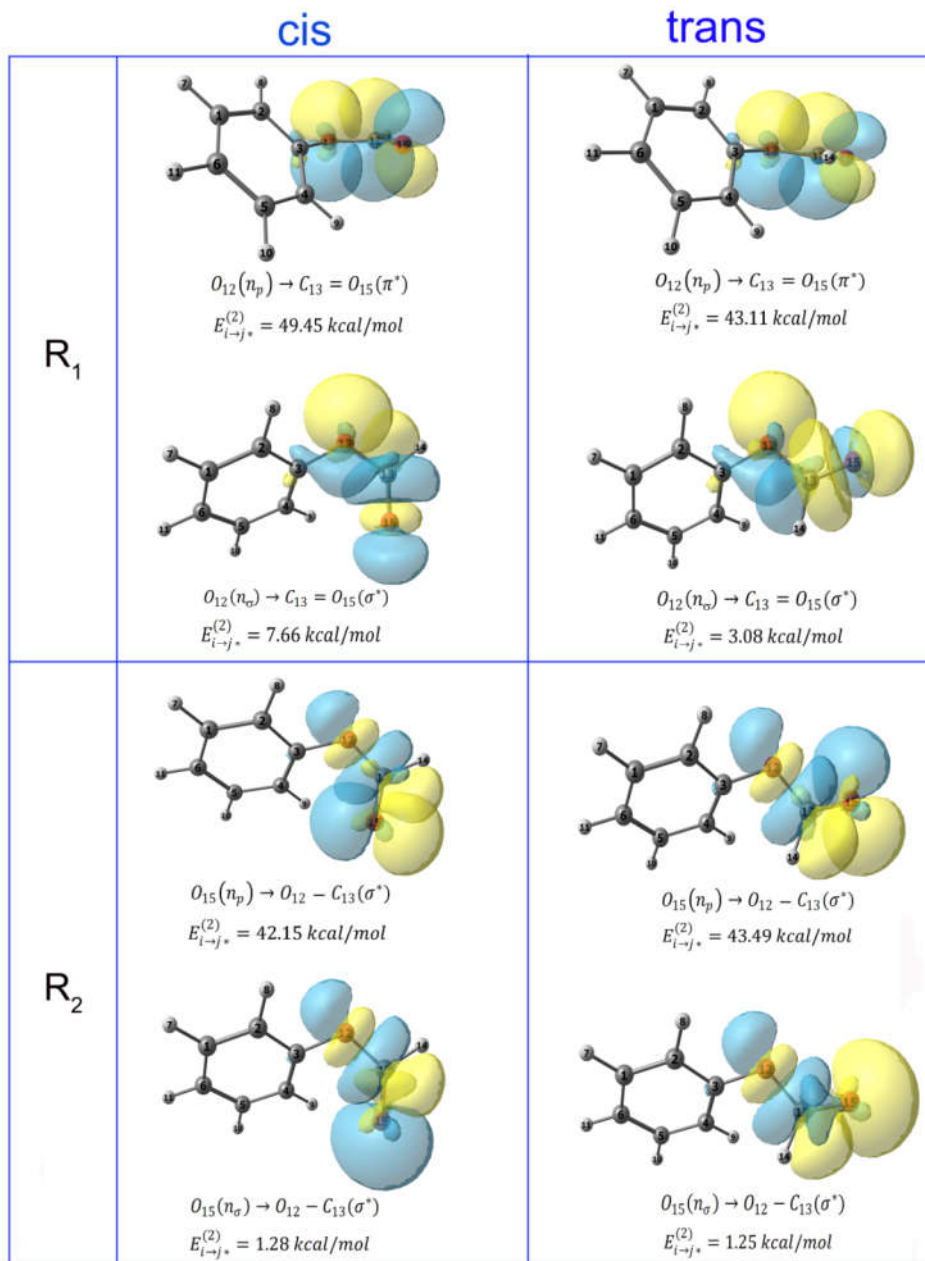


Figure 4.7 NBO view for the overlap of donor and acceptor orbitals involved in R_1 and R_2 interactions in the cis and trans conformers of phenyl formate. R_1 and R_2 are defined at the footnote of Table 4.3.

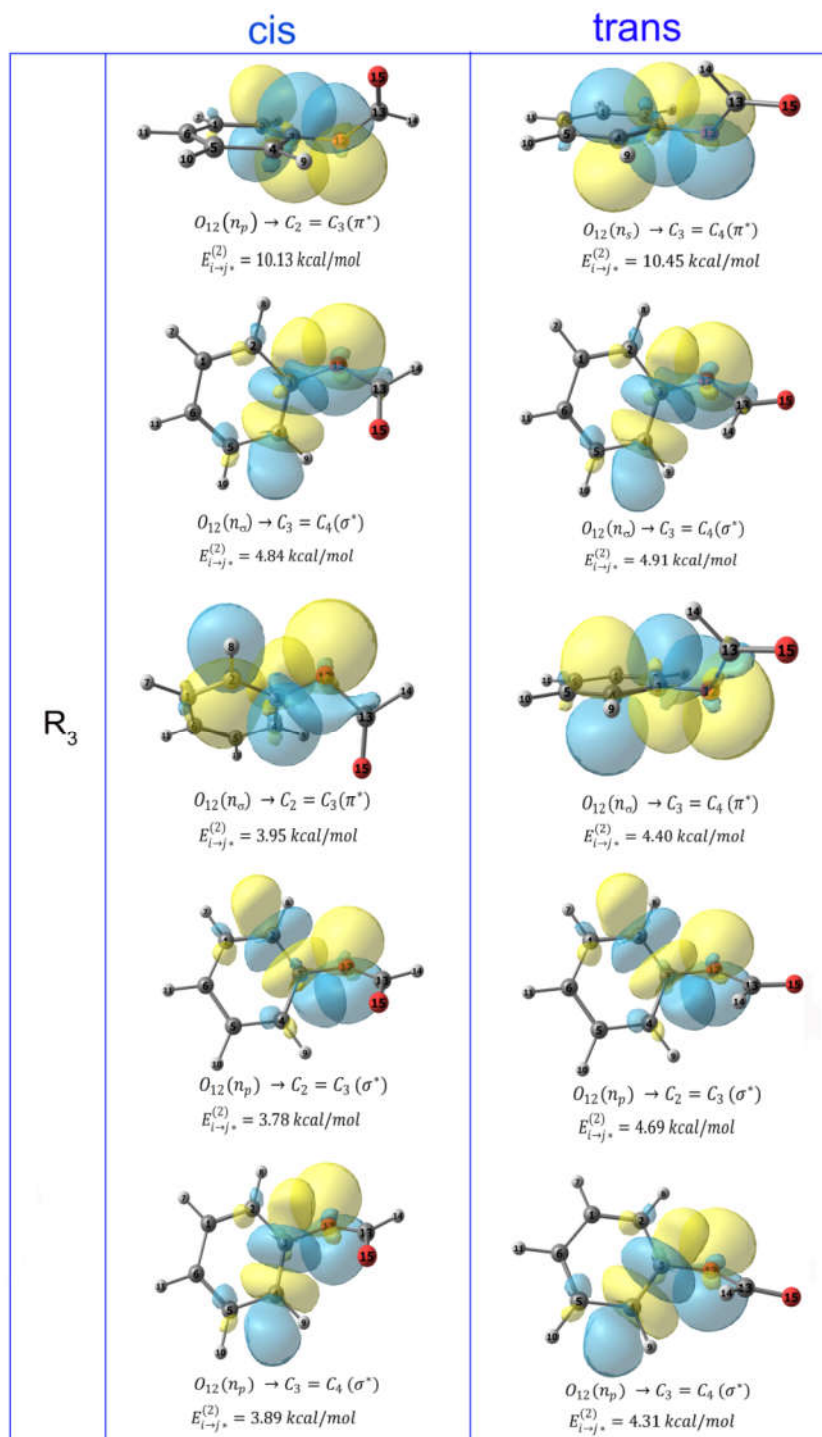


Figure 4.8 NBO view for the overlap of donor and acceptor orbitals involved in R_3 interaction in the cis and trans conformers of phenyl formate. R_3 is defined at the footnote of Table 4.3.

Table 4.3 Second order perturbative energy ($E_{i \rightarrow j^*}^{(2)}$) values for interaction between various donor and acceptor NBOs in the cis and trans conformers of phenyl formate calculated at the M05-2X/cc-pVTZ level of theory

Interaction ^a	cis			trans		
	Donor (<i>i</i>)	Acceptor (<i>j</i> [*])	$E_{i \rightarrow j^*}^{(2)}$ (kcal/mol)	Donor (<i>i</i>)	Acceptor (<i>j</i> [*])	$E_{i \rightarrow j^*}^{(2)}$ (kcal/mol)
R ₁	O ₁₂ (n _p)	C ₁₃ =O ₁₅ (π^*)	49.45	O ₁₂ (n _p)	C ₁₃ =O ₁₅ (π^*)	43.11
	O ₁₂ (n _{σ})	C ₁₃ =O ₁₅ (σ^*)	7.66	O ₁₂ (n _{σ})	C ₁₃ =O ₁₅ (σ^*)	3.08
R ₂	O ₁₅ (n _p)	O ₁₂ -C ₁₃ (σ^*)	42.15	O ₁₅ (n _p)	O ₁₂ -C ₁₃ (σ^*)	43.49
	O ₁₅ (n _{σ})	O ₁₂ -C ₁₃ (σ^*)	1.28	O ₁₅ (n _{σ})	O ₁₂ -C ₁₃ (σ^*)	1.25
R ₃	O ₁₂ (n _p)	C ₂ =C ₃ (π^*)	10.13	O ₁₂ (n _p)	C ₃ =C ₄ (π^*)	10.45
	O ₁₂ (n _{σ})	C ₃ =C ₄ (σ^*)	4.84	O ₁₂ (n _s)	C ₃ =C ₄ (σ^*)	4.91
	O ₁₂ (n _{σ})	C ₂ =C ₃ (π^*)	3.95	O ₁₂ (n _s)	C ₃ =C ₄ (π^*)	4.40
	O ₁₂ (n _p)	C ₂ =C ₃ (σ^*)	3.78	O ₁₂ (n _p)	C ₃ =C ₄ (σ^*)	4.31
	O ₁₂ (n _p)	C ₃ =C ₄ (σ^*)	3.89	O ₁₂ (n _p)	C ₂ =C ₃ (σ^*)	4.69
R ₄	O ₁₅ (n _p)	C ₂ =C ₃ (π^*)	0.52	-	-	-
	O ₁₅ (n _p)	C ₄ =C ₅ (π^*)	0.51	-	-	-

^aR₁ interaction denotes the overlap between the lone pair orbitals (p-type and σ type) on the ether oxygen (O₁₂) and carbonyl π^* orbital. This interaction reduces the carbonyl stretching frequency.

^aR₂ interaction stands for the overlap between the lone pair orbitals (p-type and σ type) on carbonyl oxygen (O₁₅) and the σ^* orbital of the O₁₂-C₁₃ bond. This interaction increases the carbonyl stretching frequency or strengthen the C=O bond.

^aR₃ interaction denotes the overlap between the lone pair orbitals (p-type and σ type) on the ether oxygen (O₁₂) and the π^* and σ^* orbitals of the phenyl ring. This interaction tends to oppose the R₁ interaction i.e. increase the C=O stretching frequency.

^aR₄ interaction denotes the $n \rightarrow \pi^*$ interaction which involves overlap of lone pair orbital of carbonyl oxygen (O₁₅) and π^* orbitals of phenyl ring

Combined values for multiple contributions in terms of overlap of the orbitals to each of the four interactions (R₁, R₂, R₃, and R₄) are listed in Table 4.4. A close inspection into the NBO stabilization energy values listed in the Table reveals that the R₁ value which favors the reduction of the C=O stretching frequency in phenyl formate is higher by 11 kcal/mol in the

case of the cis conformer compared to the trans conformer. On the other hand, the R_2 and R_3 values, which support the increase of the C=O stretching frequency, are lower by 1.35 kcal/mol and 2 kcal/mol, respectively, for the cis conformer in comparison to the trans conformer. Thus the overall orbital interaction values favor the reduction of the C=O stretching frequency in the cis conformer compared to that in the trans conformer of phenyl formate. Wiberg Bond Index calculation also shows that the bond order of C=O for the cis conformer is 1.81 while the same for the trans conformer is 1.84. The lower bond order of C=O for the cis conformer compared to that for the trans conformer indeed supports for the lower C=O stretching frequency in the former one relative to the latter one.

Table 4.4 Sum of multiple contributions of second order perturbative energy ($E_{i \rightarrow j}^{(2)}$) values for each of the R_1 , R_2 , R_3 and R_4 interactions in the cis and trans conformers of phenyl formate^b

Interaction	cis	trans
	Total $E_{i \rightarrow j}^{(2)}$ (kcal/mol)	Total $E_{i \rightarrow j}^{(2)}$ (kcal/mol)
R_1	57.11	46.19
R_2	43.43	44.74
R_3	26.6	28.75
R_4	1.03	-

^b R_1 , R_2 , R_3 and R_4 are defined at the footnote of Table S3.

The $n \rightarrow \pi^*$ interaction, which is present only in the cis conformer, affects the R_1 , R_2 , and R_3 interactions in favor of the reduction of the carbonyl force constant in the cis conformer compared to that in the trans conformer. In fact, the $n \rightarrow \pi^*$ interaction in the cis conformer partially reduces the electron density on the carbonyl oxygen (O_{15}) and consequently this reduction in the electron density induces the enhancement in the R_1 interaction (resonance effect) i.e. overlap between the carbonyl π^* orbital and ether oxygen

(O₁₂) lone pair orbital. As the lone pair electrons on ether oxygen (O₁₂) are involved more in the R₁ interaction in the cis conformer, the value of the R₃ interaction involving the same lone pair electrons decreases there. Similarly, as the lone pair electrons on the carbonyl oxygen (O₁₅) is involved in the $n \rightarrow \pi^*$ interaction in the cis conformer, the R₂ factor i.e. the NBO stabilization energy for the interaction between the lone pair orbital on carbonyl oxygen (O₁₅) and σ^* orbital of O₁₂-C₁₃ is less in the cis conformer compared to that in the trans conformer.

Table 4.5 Occupancy of the carbonyl oxygen O₁₅ lone pair electrons (p-type) of the cis conformer of phenyl formate on deletion of specific interaction(s)^c by performing NBO deletion analysis

	Interactions	Occupancy of O ₁₅ (n _p) lone pair orbital
Case I	R ₁ , R ₂ , R ₃ , R ₄ (Not deleted)	1.84426
	R ₁ , R ₂ , R ₃ (Not deleted) R ₄ (deleted)	1.84501
	R ₁ , R ₃ (Not deleted) R ₂ , R ₄ (deleted)	1.93023
Case II	R ₁ , R ₃ , R ₄ (Not deleted) R ₂ (deleted)	1.92841

^cR₁, R₂, R₃ and R₄ are defined at the footnote of Table 4.3.

Further, we have performed NBO deletion analysis to prove that the $n \rightarrow \pi^*$ interaction in the cis conformer of phenyl formate indeed favors the neighboring orbital interactions which decreases the C=O stretching frequency. Table 4.5 shows occupancy of the lone pair electrons on the carbonyl oxygen (O₁₅) in the cis conformer with deletion of specific NBO interactions. The case I in Table 4.5 reveals that the deletion of the $n \rightarrow \pi^*$ interaction increases the occupancy of the carbonyl oxygen lone pair electrons. Thus the presence of the $n \rightarrow \pi^*$ interaction reduces the occupancy of the carbonyl oxygen (O₁₅), which in turn reduces the R₂ factor responsible for the strengthening of the C=O bond. The case II demonstrates that the change in the occupancy of carbonyl oxygen lone pair orbital is less when only R₂ interaction is deleted against the deletion of both R₂ and R₄ interactions.

We have also analyzed the occupancies of $\sigma_{C=O}$, $\sigma^*_{C=O}$, $\pi_{C=O}$ and $\pi^*_{C=O}$ orbitals of the carbonyl group. Table 4.6 shows the occupancies of the $\sigma_{C=O}$, $\sigma^*_{C=O}$, $\pi_{C=O}$ and $\pi^*_{C=O}$ orbitals of the carbonyl group in the cis and trans conformers. It is revealed that the occupancies of $\sigma_{C=O}$, and $\pi_{C=O}$ orbitals of the carbonyl group are very similar for both trans and cis conformers. The major change is observed in the occupancy of σ^* and π^* orbitals, although the change in the occupancy of the π^* orbital is more significant. It is observed that the occupancy of the π^* orbital drastically increases in the cis conformer relative to the trans conformer. Increase in electron density of the π^* orbital of the C=O group decreases the force constant of the C=O bond in the cis conformer relative to the trans conformer. The occupancy of the π^* orbital of the C=O group increases because of the drastic increase in delocalization of lone pair electron density of the ester oxygen (O12) to the π^* orbital of the C=O group (R1 effect). This statement is evident based on the increase in the second order perturbative value of R1 interaction in the cis conformer relative to the trans conformer.

Table 4.6. NBO occupancies of the $\sigma_{C=O}$, $\sigma^*_{C=O}$, π and π^* orbitals of the carbonyl group in the cis and trans conformers of phenyl formate, calculated at the M05-2X/cc-pVTZ level of theory

	cis	trans
$\sigma_{C=O}$	1.997	1.996
$\sigma^*_{C=O}$	0.013	0.018
$\pi_{C=O}$	1.998	1.998
$\pi^*_{C=O}$	0.159	0.141

Thus it is clear that the $n \rightarrow \pi^*$ interaction present in the cis conformer of phenyl formate contributes to the red-shift in its C=O stretching frequency compared to that in the trans conformer which lacks $n \rightarrow \pi^*$ interaction. This observation will hold true for any

molecule/complex having a carbonyl group attached to a neighboring electronegative atom (O, N, etc.), i.e. -HN-C=O or RO-C=O where the C=O group is involved with $n \rightarrow \pi^*$ or other non-covalent interactions.

4.3 Conclusion

We have reported the IR spectroscopic evidence of weak $n \rightarrow \pi^*$ interaction for the first time by probing the C=O stretching frequency of phenyl formate using IR-UV double resonance spectroscopy in isolated gas phase. Two conformers of phenyl formate have been observed in the experiment. The cis conformer having the $n \rightarrow \pi_{Ar}^*$ interaction between the carbonyl group and the phenyl ring is more stable relative to the trans conformer which does not have any $n \rightarrow \pi_{Ar}^*$ interaction. Detection of a significant amount of red-shift in the C=O stretching frequency of the cis conformer with respect to that of the trans conformer provides the direct evidence for the $n \rightarrow \pi_{Ar}^*$ interaction. It has been found that the C=O stretching frequency of the donor carbonyl group is affected even though the $n \rightarrow \pi_{Ar}^*$ interaction is weak in strength. This is because the $n \rightarrow \pi_{Ar}^*$ interaction induces the enhancement in the resonance effect (i.e. overlap of lone pair orbital of ether oxygen with the antibonding orbital of the carbonyl group) which tends to reduce the force constant of the C=O bond. This chapter deals with the IR spectroscopic evidence for the $n \rightarrow \pi_{Ar}^*$ interaction between the carbonyl group and the aromatic ring. However, the other type of the $n \rightarrow \pi^*$ interaction ($n \rightarrow \pi_{Am}^*$) between two neighboring C=O groups, which is more abundant in the proteins, is not explored yet from gas phase IR spectroscopy. The next chapter deals with the IR signature of the $n \rightarrow \pi_{Am}^*$ interaction where both donor and acceptor C=O groups are probed using IR-UV double resonance spectroscopy to determine the effect of this non-covalent interaction on the C=O stretching frequencies.



Chapter 5

**GAS PHASE IR SPECTROSCOPIC
SIGNATURE FOR C=O...C=O $n \rightarrow \pi^*$
INTERACTION IN Cbz-(4R)-Hyp-OMe, A KEY
AMINO ACID RESIDUE OF COLLAGEN**

5.1 Introduction

In the previous chapter, we have shown the IR spectroscopic evidence for the n→π* interaction (n→π*_{Ar}) between a carbonyl group and an aromatic ring in phenyl formate by probing the carbonyl stretching frequency. The observed red-shift in the C=O stretching frequency of the conformer (cis) of phenyl formate, which has n→π*_{Ar} interaction relative to that of the conformer (trans) without having n→π*_{Ar} interaction, can be considered as a signature for the n→π*_{Ar} interaction. It will be interesting to observe similar IR spectroscopic signature for the n→π* (n→π*_{Am}) interaction between two carbonyl groups, which is widely present in proteins including collagen.

It has been discussed in section 1.3.2 that n→π*_{Am} interaction stabilizes the structure of collagen, which is the most abundant protein in animals. Collagen is specifically present in skin, bones, muscles, blood vessels, ligaments, cartilage, tendons and many other connective tissues of the body.^{54,84,149-152} It has a very unique triple helical structure made of tight interwinding of three parallel left-handed polyproline II (PPII) strands where each of the strands consists of the amino acid sequence X-Y-Gly in a repeating manner.^{54,84,151,152} Generally, the amino acid residue X in collagen is L-proline (Pro) while the residue Y is 4(R)-L-hydroxyproline (Hyp).^{54,87,152} The prolyl peptide bonds between Pro and Hyp predominantly exist in trans conformation, which allows the proximal carbonyl groups to come close along the Burgi-Dunitz trajectory for favourable n→π* interaction (see Figure 5.1). In collagen, there are interstrand hydrogen bonding interactions, albeit limited, between the carbonyl groups of the proline residues of one strand and -N-H groups of the glycine residues of another strand. However, there is no intrastrand hydrogen bonding interaction in individual polypeptide chain due to lack of amide hydrogens in the proline residues.^{10,54,84,87,153} Nevertheless presence of n→π* interaction all along the polypeptide chain makes the

collagen surprisingly stable with approximately 300 repeats of the tripeptide sequence (Pro-Hyp-Gly) for each strand which provides immense tensile strength and flexibility for the connective tissues.¹⁰

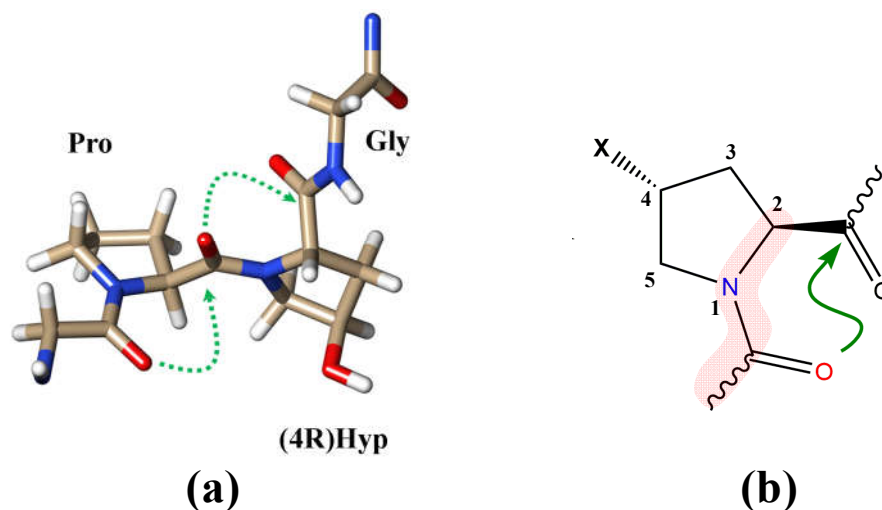


Figure 5.1 (a) Crystal structure of collagen tripeptide sequence (Pro-Hyp-Gly) showing $n \rightarrow \pi^*$ interaction (represented by green arrow) between the neighbouring carbonyl groups. (b) General structure of a proline unit in collagen showing the trans conformation of the amide bond. Where X= -H or -OH at 4R-configuration

The mechanism for the unique stability of the triple helix structure of collagen has been debated extensively in the literature.^{87,154,155} It has been found that 4R-hydroxyproline at the Y position of the tripeptide sequence is the key player for the thermal stability of the collagen triple helix.^{87,156} Surprisingly, the proline residues only at the Y position of the tripeptide sequence undergo hydroxylation during collagen biosynthesis and selectively 4R-hydroxyproline but not 4S-hydroxyproline is produced. Thus the hydroxylation of the proline residues in collagen is stereospecific as well as amino acid position (sequence) specific. Initially, it has been proposed that the enhanced stability of the collagen triple helix is due to

formation of water mediated hydrogen bonded chain between the hydroxyl group of Hyp of one strand and amide C=O group of another strand.¹⁵⁴

Subsequently there are vast amount of studies on various collagen mimics to better understand the role of Hyp in the stability of the collagen triple helix.^{10,59,76,87,155-158} Raines and co-workers have studied thermal denaturation of collagen mimics by varying the 4-substitution group of the proline residue at Y position of the tripeptide using temperature dependent CD spectroscopy.⁸⁷ They have found that the triple helix melting temperature increases in the order (ProProGly)₁₀ < (ProHyPGly)₁₀ < (ProFlpGly)₁₀, where Flp is 4R-fluoroproline. It has been also reported that the triple helix of (ProHyPGly)₁₀ is more stable than that of (ProProGly)₁₀ even in anhydrous environment.¹⁵⁵ Thus water mediated hydrogen bonding interaction through the hydroxy group of the Hyp residues is not significant for the stability of the collagen triple helix. It has been found that interplay of multiple factors originated from the inductive effect of the electronegative substituent, at the 4-position of the proline residue located at the Y position of the peptide sequence, with appropriate stereochemistry governs the stability of the triple helix.^{10,54,87,151-153}

Specifically, the gauche effect emerg from the electronegative substituent at the 4R position of the proline residue at Y position dictates the C⁴-exo puckering of the pyrrolidine ring which determines the main chain torsional angles Φ , Ψ to be suitable for effective n→π* interaction between two adjacent C=O groups and hence stabilizes the trans conformation over the cis conformation of the amide bond (see Figure 5.2).^{54,152} Eventually n→π* interactions in the backbone of individual PPII strands are one of the most significant factors for the stability of the triple helices of collagen or collagen mimics.^{86,159,160} Raines and co-workers have studied the collagen residue mimics i.e. AcProOMe, AcHypOMe and AcFlpOMe by probing the C=O...C=O distance/angle criteria in X-ray crystallography or

$K_{\text{trans/cis}}$ (equilibrium constant for trans to cis ratio) in ^1H NMR spectroscopy to find the presence of the $n\rightarrow\pi^*$ interaction.¹⁰ However, there is no direct gas phase IR spectroscopic signature for the presence of this interaction in collagen or building block of collagen, given the weak nature of this interaction which should be measured in absence of other interactions i.e. solvent perturbation etc.

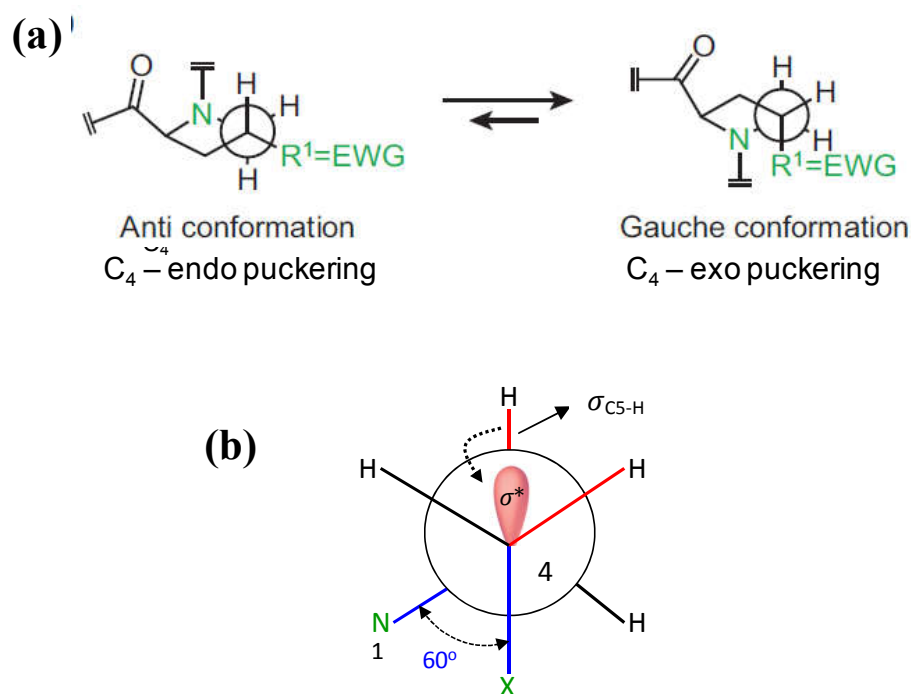


Figure 5.2 (a) Electron withdrawing group (EWG) in the 4R position favours the gauche conformation which stabilizes the $\text{C}_4\text{-exo}$ puckering of the pyrrolidine ring. Adapted with permission from ref. 152. Copyright [2009] Annual Review of Biochemistry (b) Newman projection of C4 and C5 carbon atoms of the pyrrolidine ring in gauche conformation showing overlap of σ orbital of C5-H bond with σ^* orbital of C4-EWG bond and σ orbital of C4-H bond with σ^* orbital of C5-N bond.

In the present work, we have probed the $n\rightarrow\pi^*$ interaction between two adjacent C=O groups in carboxybenzyl(Cbz)-Hyp-OMe using isolated gas phase electronic and IR spectroscopy combined with quantum chemistry calculations. Cbz-Hyp-OMe is the analogue of Ac-Hyp-OMe only where a benzyl group has been incorporated as an electronic

chromophore in the proline derivative. As both the N- and C-terminals of the amino acid Hyp are terminated by Cbz and OMe, respectively, Cbz-Hyp-OMe represents the interactions present in peptides or proteins. The current work is extremely significant as it involves studies involving Hyp which is the most important amino acid residue responsible for the stability of the collagen triple helix. On the other hand, the structures of the amino acids 4R-hydroxyproline (Hyp) and 4S-hydroxyproline (hyp) studied earlier by Alonso and workers using microwave spectroscopy cannot represent the interactions present in peptides or proteins due to lack of protection of the terminal atoms.⁷³ Moreover, the study on these amino acids also cannot address the C=O...C=O n→π* interactions in collagen which is the major focus of the present investigation.

Herein, we have observed both the cis and trans (amide) conformers of Cbz-Hyp-OMe. It has been found that the donor as well as the acceptor C=O stretching frequencies of the trans conformers having n→π* interaction are red-shifted compared to those of the cis conformers without any n→π* interaction. This is the first gas phase IR spectroscopic proof for the presence of C=O...C=O n→π* (amide) interaction in building block of collagen triple helix.

5.2 Results and Discussion

5.2.1 Conformations of Cbz-Hyp-OMe: Electronic Spectroscopy

Figure 5.3(a) shows electronic spectrum of Cbz-Hyp-OMe measured using 1C-R2PI spectroscopy. The spectrum shows several sharp bands in the range of 37610–37750 cm⁻¹. To identify whether the observed bands in Figure 1(a) correspond to same conformer or multiple conformers of Cbz-Hyp-OMe, we have performed UV-UV hole-burning spectroscopy. Figures 5.3(b), (c), (d), and (e) show UV-UV hole-burning spectra of Cbz-Hyp-OMe measured by probing the electronic bands denoted by symbols (♦), (▲), (■), and (●),

respectively, present in Figure 5.3(a). The hole-burning spectra (Figure 5.3(b), (c), (d), and (e)) clearly show the presence of four distinct conformers of Cbz-Hyp-OMe in the experiment and these conformers are denoted as A, B, C and D. Figure 5.3(b), (c), (d), and (e) actually represents conformation-specific electronic spectra of the conformers A, B, C, and D, respectively, of Cbz-Hyp-OMe..

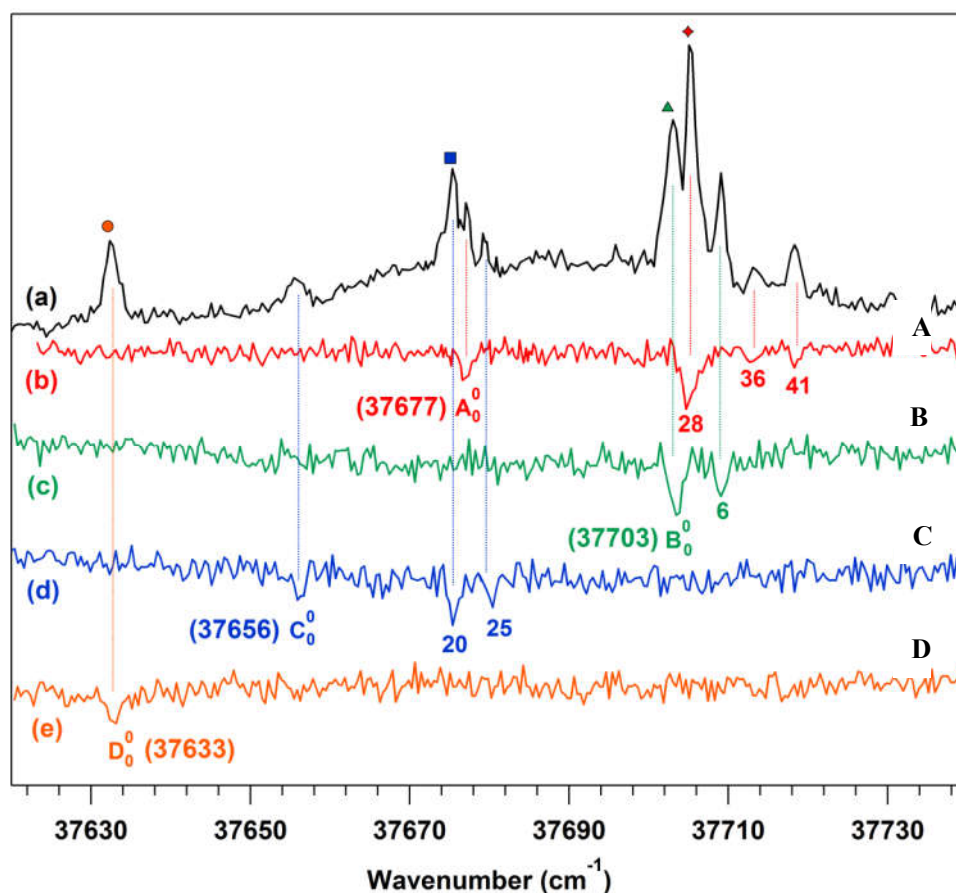


Figure 5.3 (a) Electronic spectrum of Cbz-Hyp-OMe measured using 1C-R2PI spectroscopy. (b), (c), (d), and (e) are the UV-UV hole burning spectra of Cbz-Hyp-OMe measured by probing the bands marked by (♦), (▲), (■), and (●) in the R2PI spectrum, respectively. A_0^0 (37677 cm^{-1}), B_0^0 (37703 cm^{-1}), C_0^0 (37656 cm^{-1}), and D_0^0 (37633 cm^{-1}) represents the origin band transition of conformers A, B, C, and D, respectively.

The electronic spectrum of Cbz-Hyp-OMe presented in Figure 5.3(a) exhibits a broad background, though weak, underneath the sharp bands. This broad background in the electronic spectrum can be due to inefficient cooling of the molecules in the supersonic jet as

the desorbed molecules are seeded in the jet after the expansion of the carrier gas. Similar broad background has also been observed in the electronic spectra of several peptides studied by different groups.^{161,162} The bands denoted by A_0^0 (37677 cm⁻¹), B_0^0 (37703 cm⁻¹), C_0^0 (37656 cm⁻¹), and D_0^0 (37633 cm⁻¹) in Figures 5.3(b), 5.3(c), 5.3(d), and 5.3(e), respectively, are the origin bands for the $S_1 \leftarrow S_0$ transition of respective conformers A, B, C and, D. It is worth noting that conformer D unlike other three conformers does not exhibit any vibronic feature except the origin band. Comparison of relevant geometrical parameters in the S_0 and S_1 states of the four conformers provided in Table S1 in the supporting information supports this observation as the change in the geometry in the S_0 and S_1 states of conformer D is minimum.

5.2.2 Conformational landscape of Cbz-Hyp-OMe: DFT calculations

Though we observed four conformers of Cbz-Hyp-OMe in the experiment, the assignment of their structures is not trivial as the molecule is conformationally rich due to the presence of many flexible co-ordinates. Therefore, a conformational search program (Marvin Sketch) along with chemical intuition has been used to generate probable initial structures in the conformational space of Cbz-Hyp-OMe. We generated 32 conformations of Cbz-Hyp-OMe using MMFF94 force field calculation and chemical intuition. Structures of all the 32 conformers were optimized at the M05-2X/aVDZ level of theory. Eventually, out of the 32 conformers, we selected only 16 conformers and eliminated the rest as they were isoenergetic with the selected 16 conformers. Relative energies of all the 16 conformers and their classification into four groups (P, Q, R, and S) have been shown in Figure 5.4. The optimized structures of all the 16 conformers are shown in Figure 5.5. The symbols for representing the important geometrical parameters, which distinguish various conformers of Cbz-Hyp-OMe, are shown in Figure 5.6.

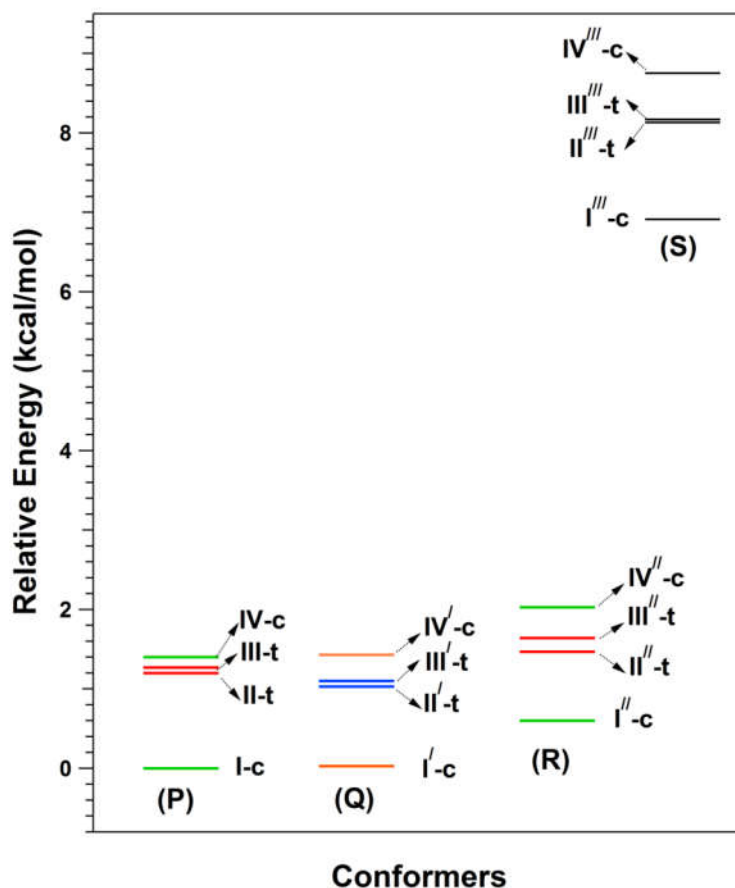


Figure 5.4. Zero-point corrected relative energies of the conformers of Cbz-Hyp-OMe calculated at the M05-2X/aVDZ level of theory. Conformers are classified into four groups (P, Q, R and S). Conformers of group P, Q and S have exo puckerings while group R has endo puckerings of the pyrrolidine ring.

Within each group of P, Q, R, and S, the structures of the conformers differ in the orientation of the amide bond represented by dihedral angle “ ω ” and the orientation of the phenyl ring denoted by angle “ β ” (see Figure 5.5). Change in the orientation of the amide bond generates cis and trans conformers of Cbz-Hyp-OMe and thus the conformers are named as X-c and X-t, respectively, where X represents the conformer number. A close look in figure 5.5 reveals that conformers of Group Q differ from all other groups by the presence of a weak O-H...N hydrogen bonding interaction between the 4-hydroxy group and the nitrogen atom of the pyrrolidine ring. The puckerings of the pyrrolidine ring in the conformers

of group P, Q and S is exo while the conformers of group R has endo puckering. Puckering of the proline ring is represented by dihedral angle α (C2-C3-C5-C4; see figure 3b) which is positive for exo and negative for endo puckering. Group S conformers are generated through the rotation of the methoxy group along C11-O13 bond. Dihedral angles ϕ and ψ are the Ramachandran angles which represent the orientation of the backbone of Cbz-Hyp-OMe conformations.

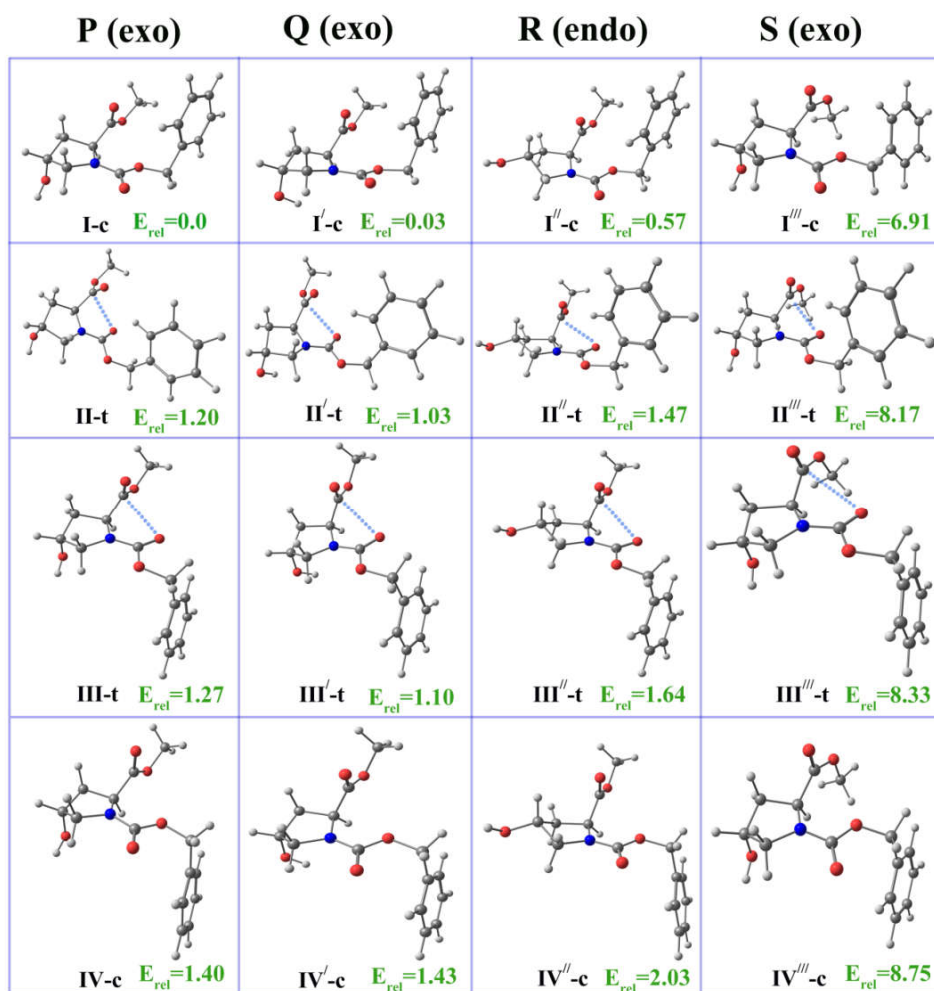


Figure 5.5 Structures of all the 16 conformers optimized at the M05-2X/aVDZ level of theory. E_{rel} represents the zero point corrected relative energies (kcal/mol) of the conformers with respect to the most stable conformer (I-c). “c” stands for cis, “t” stands for trans.

The values of the dihedral angles α , β , and Ramachandran angles (ψ , ϕ , ω) for all the 16 conformers are listed in Table 5.1 along with the second order perturbative energies of the $n\rightarrow\pi^*$ interaction for the trans conformers. The $n\rightarrow\pi^*$ interaction between the carbonyl groups of N and C-terminus is possible only in the trans conformers, where the oxygen atom of the N-terminus carbonyl group donates its lone pair electron density into the π^* orbital of the C-terminus carbonyl group. The calculated values of the angle ω for the trans and cis conformers are $\sim 175^\circ$ and $\sim -10^\circ$, respectively, in all the groups. It is worth noting that the exo pucker angle (α) for the conformers of group Q is lower than that of groups P and S

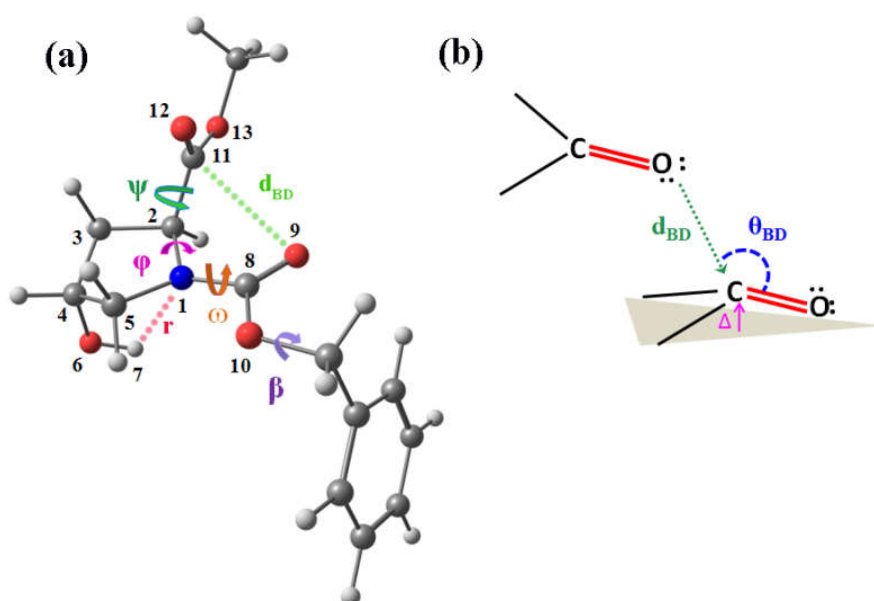


Figure 5.6 (a) Symbols for representing the important geometrical parameters. β represents the benzyl ring torsion. Dihedral angles ω (O10-C8-N1-C2), ϕ (C8-N1-C2-C-11) and ψ (CN1-C2-C11-O13) are the Ramachandran angles that define the main chain torsion angles. Distance r represents the N...H-O hydrogen bond distance. (b) Pictorial representation of Burgi-Dunitz parameters. d_{BD} represents the distance between the donor oxygen and carbon atom of the acceptor carbonyl group while θ_{BD} represents the angle O...C=O. Δ represents the degree of pyramidalization of the acceptor carbonyl carbon from the plane of its three substituents.

due to the presence of the O-H...N hydrogen bond in the former ones.

Table 5.1: Important geometrical parameters^a of all the conformers of group P, Q and R calculated at the M05-2X/aVDZ level of theory. “c” and “t” after the conformers number represents the cis and trans conformation

Conformers	ϕ (°)	ψ (°)	ω (°)	α (°)	d_{BD} (Å)	θ_{BD} (°)	Δ (Å)	β (°)	$r_{O-H...N}$ (Å)	$E_{n\rightarrow\pi^*}^{(2)}$	
P	I-c	-51.26	135.49	-9.91	-25.14	-	-	0.013	-112.44	-	-
	II-t	-48.41	140.32	172.65	-25.76	2.75	94.54	0.024	93.91	-	2.73
	III-t	-55.51	140.37	177.93	-25.63	2.83	98.06	0.023	-87.24	-	1.92
	IV-c	-63.02	144.60	4.38	-28.11	-	-	0.020	84.20	-	-
Q	I'-c	-48.11	138.73	-19.64	-16.17	-	-	0.013	-105.30	2.50	-
	II'-t	-50.30	146.33	167.87	-16.69	2.80	93.36	0.023	95.14	2.51	1.88
	III'-t	-50.84	146.24	170.54	-17.25	2.86	95.76	0.022	-83.96	2.51	1.39
	IV'-c	-57.38	151.06	-8.95	-17.50	-	-	0.020	84.85	2.52	-
R	I''-c	-52.75	141.64	-16.64	31.08	-	-	0.013	-105.07	-	-
	II''-t	-58.26	153.16	171.71	32.19	2.89	93.08	0.022	94.03	-	1.20
	III''-t	-63.49	152.38	174.48	31.89	2.97	96.16	0.022	-84.83	-	0.69
	IV''-c	-63.72	155.30	-6.06	31.72	-	-	0.020	86.10	-	-

^a Dihedral angle ϕ , ψ , ω represents the Ramachandran angles. α represent the puckering angle of the proline ring. The distance and angle of the Burgi-Dunitz trajectory for n→π* interaction is given by d_{BD} and θ_{BD} respectively. Δ represents the pyramidalization of the ester carbonyl group. β represents the orientation of the aromatic ring and $r_{O-H...N}$ represents the O-H...N hydrogen bond distance.

The data presented in Table 1 point out that the change in the amide bond orientation (ω) from trans to cis or change in the puckering angle (α) from exo to endo generally results in significant change in the Ramachandran angles (ϕ and ψ). Interestingly, increase in the ϕ and ψ angles upon changing the puckering of the pyrrolidine ring from exo to endo affects the strength of the n→π* interaction. It is found that the n→π* interaction energy in the trans-exo conformers is higher by ~1 kcal/mol than that in the trans-endo conformers. This is also reflected in the Burgi-Dunitz parameters (d_{BD} and θ_{BD}) of the trans-exo and trans-endo conformers. In general, the n→π* interaction is favorable while d_{BD} is ≤ 3.2 Å and θ_{BD}

≈109°±10°. . Similar results have been reported from a comparative study of the geometric parameters of the endo and exo conformers of Ac-Pro-OMe.¹⁰ It is important to mention here that the geometrical parameters of the conformers of Cbz-Hyp-OMe are quite similar to those of Ac-Hyp-OMe reported in the literature (see Table 5.2).¹⁵² Thus the replacement of the -Ac group by the -Cbz group does not significantly change the important geometrical parameters of the conformers and more specifically, the peptide backbone as well as the Burgi-Dunitz parameters for the n→π* interactions in the trans conformers.

The relative Gibbs free energy (ΔG) of the conformers of group P, Q and R are provided at 298K in table 5.3. It has been found that the trend in ΔE and ΔG of the conformers are not similar. At higher temperature conformer III-t becomes the most stable conformer. This indicates that energy gap between the most stable conformer and higher energy conformers of the group decreases with the increase in temperature. This shows that higher energy conformers are likely to be observed under low cooling condition of the seeded molecules in the supersonic jet.

Table 5.2 Ramachandran angles (ϕ and ψ) and n→π* interaction energy of the trans conformers of Ac-Y-OMe (Where Y=Pro, Hyp and Flp) calculated at the M05-2X/aVDZ level of theory in comparison with the trans conformer of Cbz-Hyp-OMe

	Ring Puckering	ϕ (°)	ψ (°)	$E_{n\rightarrow\pi^*}^{(2)}$ (kcal/mol)
Ac-Pro-OMe	Exo	-53.7	140.50	2.46
Ac-Pro-OMe	endo	-64.4	153.2	0.89
Ac-Hyp-OMe	exo	-54	138.5	2.62
Ac-Hyp-OMe	endo	-62.2	149.0	1.21
Ac-Flp-OMe	exo	-54.2	141	2.64
Ac-Flp-OMe	endo	-62.0	148.7	1.16
Cbz-Hyp-OMe	exo	-48	140	2.47
Cbz-Hyp-OMe	endo	-58	153	1.20

Table 5.3 Relative electronic energies (ΔE) and relative Gibbs Free energies (ΔG) of all the Cbz-Hyp –OMe conformers of group P, Q and R calculated at 298 K

	Conformers	ΔE (kcal/mol)	ΔG (kcal/mol)
P	I-c	0.0	0.25
	II-t	1.20	0.71
	III-t	1.27	0.00
	IV-c	1.40	0.20
Q	I'-c	0.03	0.44
	II'-t	1.03	0.37
	III'-t	1.10	0.38
	IV'-c	1.43	0.33
R	I''-c	0.57	0.67
	II''-t	1.47	0.48
	IV''-c	2.03	1.01

In general, the trans-amide conformers of Ac-Hyp-OMe are reported to be more stable than the cis-amide conformers due to the presence of the $n \rightarrow \pi^*$ interaction between the two neighboring C=O groups in the former ones.¹⁵² Similar trend is also observed in the backbone of proteins.^{7,57} In the case of Cbz-Hyp-OMe studied here, we have observed that the trans-amide conformers are typically more stable than the cis-amide conformers except for one of the cis-amide conformers (I-c, I'-c, I''-c, and I'''-c) of each of the groups of P, Q, R, and S (see Figure 5.4). In fact, conformers I-c, I'-c, I''-c, and I'''-c are the global minima for the groups P, Q, R, and S, respectively and these conformers are significantly lower in energy than all other conformers in their respective groups. It is found that the stability of these cis conformers over the trans conformers is due to the presence of C-H... π interaction between the phenyl ring and CH₃ group of the ester moiety in the former ones. The general trend of the stability of the trans amide over the cis amide holds well in the case of all other conformers of Cbz-Hyp-OMe which do not have any C-H... π interaction. Figure 5.4 also reveals that the conformers of group S are very high in energy compared to those of other groups. Such high energy conformers will have too low population to be observed in the

experiment. Thus the conformers of group S have been eliminated and only the conformers of P, Q and R groups are considered for the comparison of the calculated IR spectra with the experimental IR spectra, which are described in the following section.

5.2.3 Structures of the observed conformers of Cbz-Hyp-OMe: IR spectroscopy

The probable structures of the four conformers (marked as A, B, C and D in Figure 5.3) of Cbz-Hyp-OMe observed in the experiment can be elucidated by comparing their experimental IR spectra with the calculated IR spectra of all the conformers in group P, Q, and R. The IR spectra of the conformers A, B, C and D were measured by probing the electronic bands marked by the symbols (♦), (▲), (■), and (●), respectively, in Figure 5.3(a), using RIDIR spectroscopy. Figures 5.7(a) and 5.7(b) show experimental IR spectra of the four conformers in the C=O and O-H stretching frequency regions, respectively. The IR spectra of all the four conformers in the C=O stretching frequency region (Figure 5.8(a)) show two bands as there are two carbonyl groups (amide and ester) in Cbz-Hyp-OMe.

It is quite intriguing to note that the IR spectra in the C=O stretching region are not different for all the four conformers although the UV-UV hole-burning spectra (Figure 5.3b-e) indicates the presence of four conformers (A, B, C, D) in the experiment. The IR spectra of both the conformers A and C show the two C=O peaks at 1685 and 1759 cm^{-1} while the C=O peaks for conformers B as well as D appear at 1699 and 1764 cm^{-1} . Thus the IR spectral data in the C=O stretching region reveal that A and C conformers have similar C=O environment and the same is true for B and D. However, the orientation of the O-H group in the conformers A and C could be different and again the same could hold true for B and D. IR spectra of the four conformers of Cbz-Hyp-OMe in the O-H stretching region are shown in Figure 5.7(b). It is indeed true that the O-H bands of the conformers A (3646 cm^{-1}) and C (3611 cm^{-1}) appear at significantly different position and also similar difference in the O-H

band position of the conformers B (3642 cm^{-1}) and D (3608 cm^{-1}) is observed. It is noteworthy that the O-H band positions of the conformers A and B are similar while the conformers C and D also exhibit similar O-H stretching frequency. Thus the IR spectra of the four observed conformers in the C=O stretching region is complementary with those in the O-H stretching region in terms of the assignment of their structures.

To determine the probable structures of all the four conformers observed in the

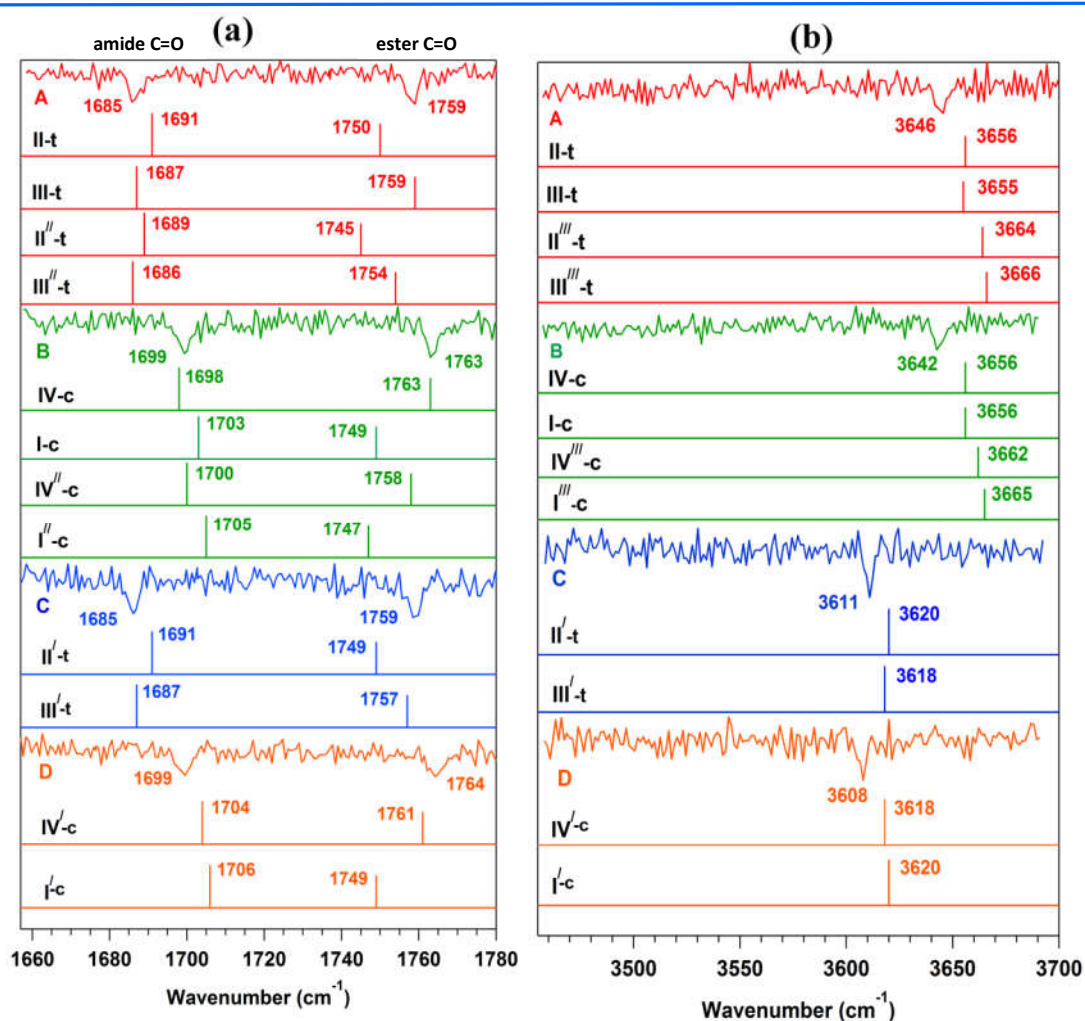


Figure 5.7 Experimental IR spectra of conformers A, B, C and D shown in comparison with the theoretical IR spectra of group P, Q and R structures of Cbz-Hyp-OMe in the (a) C=O stretching frequency region and (b) O-H stretching frequency region. The calculated amide C=O, ester C=O and OH stretching frequencies are scaled using scaling factor of 0.9441, 0.9546 and 0.9391 respectively.

experiment, the experimental IR spectra are compared with the theoretical IR spectra, of 12 conformers classified into P, Q, and R groups, obtained at the M05-2X/aVDZ level of calculation. The theoretical IR spectra in the C=O and O-H stretching frequencies of all the conformers are shown as stick plots with the corresponding experimental spectra in Figure 5.7(a) and 5.7(b), respectively. The comparison of the theoretical and the experimental IR spectra presented in Figure 5.8 reveals that conformers A and C have trans-amide structure while conformers B and D have cis-amide structure. Although both conformers A and C have trans structure, their O-H stretching frequencies are significantly different. In the case of the conformer C, the O-H group of proline is involved in O-H...N hydrogen bonding interaction with the nitrogen atom of the proline ring while the O-H group in conformer A is free. Similarly, conformer cis-D has O-H...N interaction but the O-H group of cis-B is free. The O-H group of both conformers C and D is red-shifted by $\sim 35 \text{ cm}^{-1}$ compared to that of conformers A and B.

We can now assign conformer A to either structure II-exo-trans, III-exo-trans, II'-endo-trans or III'-endo-trans while conformer C can be assigned to either structure II'-exo-trans or III'-exo-trans. Similarly, conformer B can be assigned to either structure IV-exo-cis, I-exo-cis, IV'-endo-cis or I'-exo-cis while conformer D can be assigned to either structure IV'-exo-cis or I'-exo-cis. It should be noted that each of the conformers cannot be assigned easily to a particular structure as multiple structures have similar IR frequencies and energetics. However, the primary aim of the present investigation is to observe cis and trans – amide conformation of Cbz-Hyp-OMe and obtain direct IR spectroscopic evidence of the C=O...C=O n→π* interaction in the trans-amide. We find here that the conformers A and C have trans-amide structure with amide C=O group appearing at 1685 cm^{-1} and ester C=O group at 1759 cm^{-1} . On the other hand, the conformers B and D have cis-amide structure with

amide C=O frequency at 1699 cm^{-1} and ester C=O frequency at 1764 cm^{-1} . The amide C=O frequency of the trans conformers of Cbz-Hyp-OMe is found to be red-shifted by 14 cm^{-1} with respect to that of the cis conformers. It is interesting to note that the ester C=O frequency of the trans conformers is also red-shifted, albeit by small amount, 5 cm^{-1} , with respect to that of the cis conformers. The red-shift in the vibrational frequency of both the C=O groups in the trans conformer with respect to that in the cis conformer indicates the presence of the n→π* interaction in the former one. The C=O groups in the trans conformer are oriented in the same side while the C=O groups are away from each other in the cis conformer.

Burgi-Dunitz parameters i.e. the distance between the two C=O groups (d_{BD}) and their angle (θ_{BD}) as well as pyramidalization of the ester C=O group in the trans conformers of Cbz-Hyp-OMe (Table 5.1) calculated at the M05-2X/aVDZ level of theory supports for the presence of the n→π* interaction there. Detailed NBO analysis of various conformers of Cbz-Hyp-OMe described in the next section is focused on understanding the features of the various orbital interactions present there and the role of the n→π* interaction on the red-shift of the C=O stretching frequencies in the trans conformers with respect to those in the cis conformers.

5.2.4 NBO analysis: n→π* interaction vs C=O stretching frequency

The most significant finding of the present study is the observation of the red-shift in the stretching frequencies of both n→π* donor as well as acceptor C=O groups in the trans conformers of Cbz-Hyp-OMe compared to those in the cis conformers. Here, the n→π* interaction in the trans conformer occurs due to delocalization of the lone pair electrons on donor carbonyl oxygen atom into the π* orbital of the acceptor C=O group. The red-shift

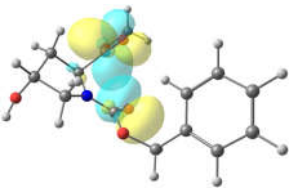
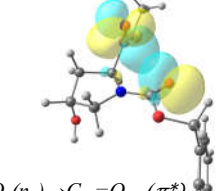
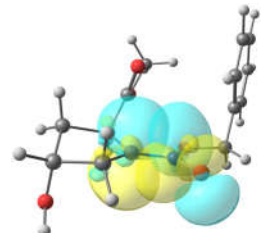
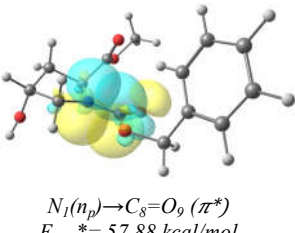
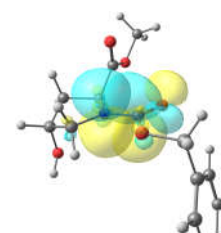
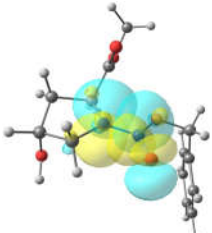
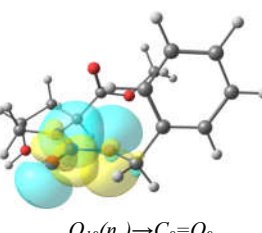
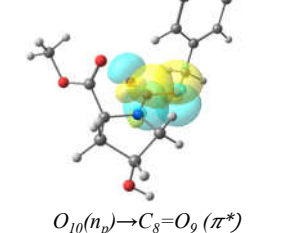
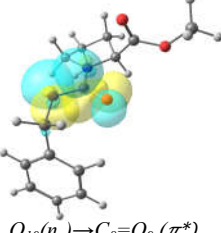
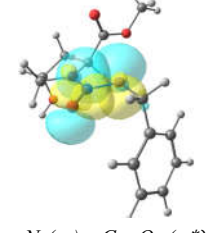
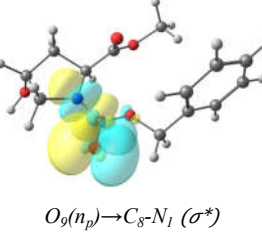
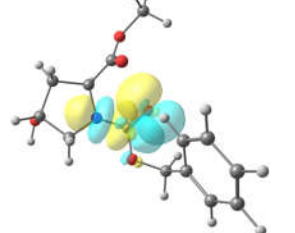
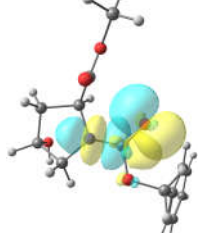
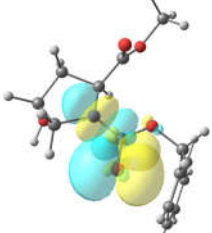
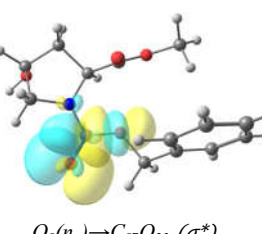
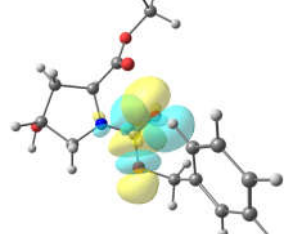
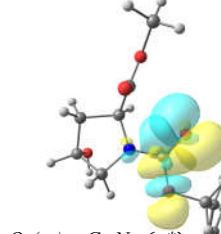
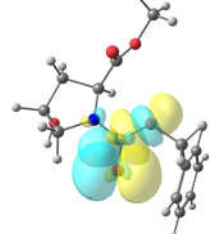
	I	II	III	IV
n→π*	-		 $O_9(n_p) \rightarrow C_{11}=O_{12} (\pi^*)$ $E_{i \rightarrow j}^* = 1.92 \text{ kcal/mol}$	-
R1	 $N_1(n_p) \rightarrow C_8=O_9 (\pi^*)$ $E_{i \rightarrow j}^* = 13.50 \text{ kcal/mol}$	 $N_1(n_p) \rightarrow C_8=O_9 (\pi^*)$ $E_{i \rightarrow j}^* = 57.88 \text{ kcal/mol}$	 $N_1(n_p) \rightarrow C_8=O_9 (\pi^*)$ $E_{i \rightarrow j}^* = 82.81 \text{ kcal/mol}$	 $N_1(n_p) \rightarrow C_8=O_9 (\pi^*)$ $E_{i \rightarrow j}^* = 39.55 \text{ kcal/mol}$
	 $O_{10}(n_p) \rightarrow C_8=O_9$ $E_{i \rightarrow j}^* = 13.50 \text{ kcal/mol}$	 $O_{10}(n_p) \rightarrow C_8=O_9 (\pi^*)$ $E_{i \rightarrow j}^* = 40.86 \text{ kcal/mol}$	 $O_{10}(n_p) \rightarrow C_8=O_9 (\pi^*)$ $E_{i \rightarrow j}^* = 52.23 \text{ kcal/mol}$	 $N_1(n_p) \rightarrow C_8=O_9 (\pi^*)$ $E_{i \rightarrow j}^* = 28.80 \text{ kcal/mol}$
R2	 $O_9(n_p) \rightarrow C_8-N_1 (\sigma^*)$ $E_{i \rightarrow j}^* = 41.03 \text{ kcal/mol}$	 $O_9(n_p) \rightarrow C_8-N_1 (\sigma^*)$ $E_{i \rightarrow j}^* = 40.42 \text{ kcal/mol}$	 $O_9(n_p) \rightarrow C_8-N_1 (\sigma^*)$ $E_{i \rightarrow j}^* = 39.88 \text{ kcal/mol}$	 $O_9(n_p) \rightarrow C_8-N_1 (\sigma^*)$ $E_{i \rightarrow j}^* = 40.22 \text{ kcal/mol}$
	 $O_9(n_p) \rightarrow C_8-O_{23} (\sigma^*)$ $E_{i \rightarrow j}^* = 27.93 \text{ kcal/mol}$	 $O_9(n_p) \rightarrow C_8-N_1 (\sigma^*)$ $E_{i \rightarrow j}^* = 27.43 \text{ kcal/mol}$	 $O_9(n_p) \rightarrow C_8-N_1 (\sigma^*)$ $E_{i \rightarrow j}^* = 27.17 \text{ kcal/mol}$	 $O_9(n_p) \rightarrow C_8-N_1 (\sigma^*)$ $E_{i \rightarrow j}^* = 27.75 \text{ kcal/mol}$

Figure 5.8. NBO view of overlap of donor and acceptor natural bond orbitals involved in n→π*, R1 and R2 interactions in the conformers of group P.

observed in the donor (amide) and acceptor (ester) C=O groups in the trans conformer of Cbz-Hyp-OMe with respect to those in the cis conformer are about 14 and 5 cm⁻¹, respectively. The red-shift in both of the C=O groups can be explained in terms of the n→π* interaction. The red-shift in the acceptor C=O frequency is easily understood as the lone pair electrons are donated to the π* orbital of the acceptor C=O group and this red-shift is very small because the n→π* interaction is very weak (~ 2 kcal/mol). However, relatively larger (14 cm⁻¹) red-shift in the frequency of the donor C=O group in the trans conformer has to be understood in terms of the relationship of the n→π* interaction with the neighboring orbital interactions which are responsible for the reduction of the C=O frequency in the trans conformer compared to that in the cis conformer. A detailed NBO analysis has been performed for all the trans and cis conformers of Cbz-Hyp-OMe. The second-order perturbative energy values ($E_{n\rightarrow\pi^*}^{(2)}$) of all the possible orbital interactions which involve lone pair and π* NBOs of the donor C=O in the conformers of P and Q groups (Figure 5.5) are shown in Table 5.4 and the NBO view for the overlap between corresponding orbitals are provided in Figure 5.8. For the brevity, NBO view has been shown only for the conformers in the group P.

In general, there are two opposing effects (resonance and inductive) which determine the C=O stretching frequency in esters and amides. In Cbz-Hyp-OMe, overlap between the π* orbital of the amide C₈=O₉ with the lone pair orbitals of the neighboring nitrogen atom in the proline ring as well as ether oxygen (R1_O), decreases the amide C₈=O₉ stretching frequency. This can be called resonance effect as it involves delocalization of lone pair orbital of neighbouring electronegative atom into the π* orbital of the carbonyl group. This orbital interaction involving the neighboring nitrogen atom is marked as R_N while the same

comprising the neighboring oxygen atom is tagged as R_O. The reduction in the C=O stretching frequency will be more as the overlap between the lone pair orbital of the electronegative

Table 5.4. The second-order perturbative energy values of all the possible orbital interactions which involves lone pair and π* NBOs of amide carbonyl group in the conformers of group P and Q

	$E_{n \rightarrow \pi^*}^{(2)}$	$N_1 \rightarrow C_8=O_9$ (R1 _N) ^a	$O_{10} \rightarrow C_8=O_9$ (R1 _O)	$O_9 \rightarrow C_8-O_{10}$ (R2 _N) ^b	$O_9 \rightarrow C_8-N_1$ (R2 _O)	Total R1	Total R2
I-c	-	13.50	13.81	41.03	27.93	27.31	68.96
II-t	2.73	57.88	40.86	40.42	27.43	98.74	67.85
III-t	1.92	82.81	52.23	39.88	27.17	135.04	67.05
IV-c	-	39.55	28.80	40.22	27.75	68.35	67.97
I'-c	-	24.68	25.59	41.10	28.55	50.27	69.65
II'-t	1.88	45.14	38.14	40.07	28.03	83.28	68.1
III'-t	1.39	48.60	35.70	39.50	27.69	84.3	67.19
IV'-c	-	24.68	47.38	40.43	28.36	72.06	68.79

^a R1 interaction represents the resonance effect i.e. delocalization of lone pair electrons of neighboring electronegative atom into the π* orbital of the carbonyl group.

^b R2 interaction represents the inductive effect i. e. delocalization of lone pair electrons of carbonyl oxygen (O) into the σ* orbital of C-N bond and C-O bond.

atom and the π* orbital of the carbonyl group increases. On the other hand, overlap between the lone pair orbitals (p-type and s-type) of carbonyl oxygen (O₉) with the σ* orbital of C₈-N₁ bond as well as C₈-O₁₀ bond increases the C₈=O₉ stretching frequency. This orbital interaction is marked as R2_N and R2_O involving C₈-N₁ and C₈-O₁₀ bonds, respectively. A combined values for all R1 and R2 interactions are also listed in Table 5.3. Inspection of Table 5.4 shows that R1 values are always much larger than the R2 values in the trans conformers having the n→π* interaction. On the other hand, the R1 values are either equal or less than the R2 values for the cis conformers which is lacking any n→π* interaction. Thus larger R1 values in the trans conformers compared to those in the cis conformers are induced

by the n→π* interaction which is absent in the cis conformers. In the trans conformer, electron density on the donor carbonyl oxygen (O₉) is partially reduced due to the n→π* interaction and consequently the R1 interactions (resonance effect) are enhanced to compensate the loss of the electron density on the carbonyl oxygen. Similar mechanism has been discussed in section 4.2.3 for the red-shift observed in the C=O stretching frequency of the cis conformer of phenyl formate with respect to that of the trans conformer where the cis has n→π* interaction and the trans does not have.⁷⁹

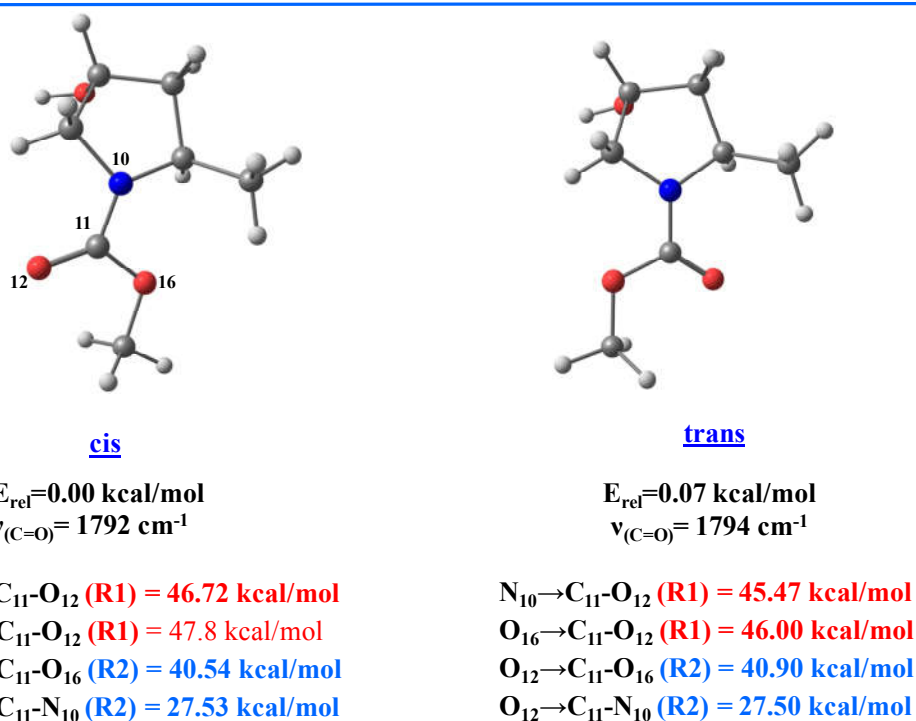


Figure 5.9. cis and trans conformers of N-methoxycarbonyl (2S,4R)-4-hydroxypyrrolidine-2-methyl showing no change in the amide C=O stretching frequency in the absence of n→π* interaction. Second order perturbative energies of R1 and R2 interactions are shown for cis and trans conformers below their corresponding geometries. R1 and R2 interactions in both the conformers are similar.

To check whether the red-shift in the stretching frequency of the amide carbonyl in the trans conformer of Cbz-Hyp-OMe with respect to that of the cis conformer is not simply due to the change in the orientation of the C=O group in the two conformers, we have performed NBO calculation on N-methoxycarbonyl (2S,4R)-4-hydroxypyrrolidine-2-methyl.

In the case of N-methoxycarbonyl (2S,4R)-4-hydroxypyrrolidine-2-methyl, both cis and trans conformers do not have any n→π* interaction due to lack of the ester group at 2-position of the pyrrolidine ring. The structures of the two conformers of N-methoxycarbonyl (2S,4R)-4-hydroxypyrrolidine-2-methyl and their NBO analysis are provided in Figure 5.9.

Table 5.5. Change in the occupancy of lone pair orbital of O₉ (n_p) and π* orbital of C₈=O₉ upon deletion of specific interactions in the group P conformers of Cbz-Hyp-OMe. ΔE_{scf} represents the change in the SCF energy upon deleting the interaction.

	Interaction deleted	Interaction not deleted	Occupancy of O ₉ lone pair orbital		Occupancy of C ₈ =O ₉ (π*) orbital		Change in SCF energy (ΔE _{scf}) (kcal/mol)
			before deletion O ₉ (n _p)	after deletion O ₉ (n _p)	before deletion C ₈ =O ₉ (π*)	after deletion C ₈ =O ₉ (π*)	
I-c	R1	R2	1.83803	1.83804	0.13412	0.02288	109.733
	R2	R1	1.83803	1.98222	0.13412	0.13414	63.499
	R1,R2	-	1.83803	1.98232	0.13412	0.02299	158.063
II-t	R1	R2, n→π*	1.8353	1.83514	0.32925	0.01992	112.321
	R2	R1, n→π*	1.83528	1.97167	0.32932	0.32932	61.728
	R1,R2	n→π*	1.83531	1.97160	0.32925	0.01989	159.398
	n→π*, R1	R2	1.83531	1.84219	0.32925	0.01989	112.952
	n→π*, R2	R1	1.83531	1.98177	0.32925	0.32923	63.838
	n→π*	R1,R2	1.83531	1.84233	0.32925	0.32925	1.192
III -t	R1	R2, n→π*	1.83969	1.83965	0.34674	0.01802	115.157
	R2	R1, n→π*	1.83969	1.97374	0.34674	0.34679	60.788
	R1,R2	n→π*	1.83969	1.97375	0.34674	0.01805	161.338
	n→π*, R1	R2	1.83969	1.84518	0.34674	0.01800	115.574
	n→π*, R2	R1	1.83969	1.98169	0.34674	0.34676	62.374
	n→π*	R1,R2	1.83969	1.84523	0.34674	0.34672	0.888
IV-c	R1	R2	1.84268	1.84237	0.22972	0.02404	111.376
	R2	R1	1.84268	1.98270	0.22972	0.22970	62.505
	R1,R2	-	1.84268	1.98251	0.22972	0.02396	159.050

Interestingly, the C=O stretching frequencies as well as electronic energies of the cis and trans conformers are similar. It is also found that the values for the R1 and R2 factors, which favor and oppose the reduction of the C=O stretching frequency, respectively, are similar for both cis and trans conformers of this compound. This indicates that orientation of

the amide carbonyl group from trans conformation to cis conformation in the absence of n→π* interaction does not change the resonance and inductive effect of the amide carbonyl group. Thus, this results validate that the enhancement of the R1 factor induced by the n→π* interaction is responsible for the red-shift in the C=O frequency of the trans conformer compared to that of the cis conformer of Cbz-Hyp-OMe. Further, NBO deletion analysis (see table 5.5) performed for the cis and trans conformers corroborate this explanation.

NBO deletion analysis performed for the cis and trans conformers of Cbz-Hyp-OMe corroborate our explanation for the reduction of the C=O frequency in the trans compared to the cis. Table 5.5 shows change in the occupancy of the lone pair and the π* orbital of the amide (donor) carbonyl group after deletion of the specific NBO interactions. Close inspection of Table 5.5 reveals that occupancy of the lone pair electrons on the amide carbonyl oxygen (O₉) increases when n→π* interaction is deleted in the trans conformer. This suggests that occupancy of the amide carbonyl oxygen decreases due to the n→π* interaction. Furthermore, decrease in the occupancy of the π* orbital of the amide C=O upon deletion of the R1 interaction is more (value is more negative) in the trans conformers compared to the cis conformers. This concludes that occupancy of the π* orbital of the donor carbonyl group increases due to the enhancement of the R1 interaction in the trans conformer compared to the cis conformer.

Table 5.6. Bond order of n→π* donor carbonyl bond (C₈= O₉) and acceptor carbonyl bond (C₁₁= O₁₂) along with amide bond (N₁-C₈) and ester bond (O₁₀-C₈) of the donor carbonyl group, in the group P conformers of Cbz-Hyp-OMe.

	C ₈ = O ₉	C ₁₁ = O ₁₂	N ₁ -C ₈	O ₁₀ -C ₈
I-c	1.6140	1.7093	1.1284	0.9669
II-t	1.5941	1.7036	1.1297	0.9818
III-t	1.5889	1.7183	1.1335	0.9829
IV-c	1.6060	1.7259	1.1286	0.9728

Reduction in the strength of both amide and ester carbonyl groups in the trans conformer compared to that in the cis conformer is also supported by the bond order calculation provided in Table 5.6. It shows that bond order of both donor and acceptor carbonyl groups decreases in the trans conformer compared to the cis conformer. It could be concluded from all of these calculations that the red-shift in the C=O stretching frequency of the acceptor and donor carbonyl group in the trans conformers compared to that in the cis conformers is due to the presence of the n→π* interaction in the former conformer.

NBO second order perturbative energy value of the resonance effect and inductive effect (hyperconjugation) present in the ester carbonyl group ($R1_{\text{ester}}$, $R2_{\text{ester}}$) is provided in the Table 5.7 along with the total resonance effect and inductive effect present in the amide carbonyl group ($R1_{\text{amide}}$, $R2_{\text{amide}}$). It is evident from the Table 5.7 that the R1 interaction (tends to decrease the C=O stretching frequency) in the ester carbonyl group is similar in the trans and cis conformers of Cbz-Hyp-OMe. This result reveals that hyperconjugation of the ester carbonyl group does not change as significantly as that of the amide carbonyl group. However, we observe red-shift in the ester carbonyl group of the trans conformer. This red shift in the ester C=O stretching frequency of the trans conformer relative to that of the cis conformer is observed because of the n→π* interaction in the trans conformer which involves delocalization of lone pair electron density of amide carbonyl oxygen to π* orbital of the ester C=O carbonyl group. This is evident because the occupancy of the π* orbital of the ester C=O group is more in the trans conformer relative to that of the cis conformer. This increase in the occupancy of π* orbital of the ester C=O group due to R1 effect is ruled out because the NBO value for the R1 effect is similar in both cis and trans conformer. It is also revealed that resonance effect (R1), which tends to decrease the C=O stretching frequency, is more in the amide carbonyl group compared to that of the ester carbonyl group. Therefore,

C=O stretching frequency of an amide carbonyl group red-shifted relative to that of the ester carbonyl group.

Table 5.7. The NBO second order perturbative energy values of the resonance effect (R1) and inductive effect (R2) present in the ester carbonyl group ($R1_{\text{ester}}$, $R2_{\text{ester}}$) and amide carbonyl group ($R1_{\text{amide}}$, $R2_{\text{amide}}$), calculated at the M05-2X/aVDZ level of theory. $\partial\pi^*_{\text{C8=O9}}$ represents the occupancy of the π^* orbital of amide carbonyl group and $\partial\pi^*_{\text{C11=O12}}$ represents the occupancy of the π^* orbital of ester carbonyl group.

Conformer	$E_{i \rightarrow j}^{(2)}$ (kcal/mol)				Occupancy	
	$R1_{\text{amide}}^{\text{a}}$	$R2_{\text{amide}}^{\text{b}}$	$R1_{\text{ester}}^{\text{c}}$	$R2_{\text{ester}}^{\text{d}}$	$\partial\pi^*_{\text{C8=O9}}$	$\partial\pi^*_{\text{C11=O12}}$
I-c	27.31	68.96	66.86	41.75	0.220	0.218
II-t	98.74	67.85	67.21	41.64	0.314	0.222
III-t	135.04	67.05	66.63	42.51	0.353	0.221
IV-c	68.35	67.97	66.84	42.33	0.265	0.216

^a $R1_{\text{amide}}$ interaction represents delocalization of lone pair electrons of neighboring electronegative atom (Nitrogen and oxygen) into the π^* orbital of the amide carbonyl group.

^b $R2_{\text{amide}}$ interaction represents delocalization of lone pair electrons of carbonyl oxygen (O) into the σ^* orbital of C-N bond and C-O bond.

^c $R1_{\text{ester}}$ interaction represents delocalization of lone pair electrons of ester oxygen (O) into the π^* orbital of the ester carbonyl group.

^d $R2_{\text{ester}}$ interaction represents delocalization of lone pair electrons of carbonyl oxygen (O) into the σ^* orbital ester C-O bond.

5.3 Conclusion

The $n \rightarrow \pi^*$ interaction between two adjacent carbonyl groups ($n \rightarrow \pi^*_{\text{Am}}$) is studied in different conformers of Cbz-Hyp-OMe by probing the C=O stretching frequencies using gas phase IR spectroscopy combined with quantum chemistry calculations. Four conformers of Cbz-Hyp-OMe are observed in the experiment. Two of the conformers have trans-amide orientation with $n \rightarrow \pi^*$ interaction while the other two are cis-amide without having any $n \rightarrow \pi^*$ interaction between the two carbonyl groups. One of the pairs of the trans as well as

the cis conformers has a weak O-H...N hydrogen bonding interaction between the 4-hydroxy group and the nitrogen atom of the proline ring. The stretching frequencies of both donor and acceptor carbonyl groups of the trans conformers are red-shifted compared to that of the cis conformers and the red-shift for the donor carbonyl group (15 cm^{-1}) is more than that of the acceptor carbonyl group (5 cm^{-1}). The red-shift of both the C=O groups is explained by detailed NBO analysis. The present study on Cbz-Hyp-OMe demonstrates first gas phase IR spectroscopic evidence of the n→π* interactions between the two carbonyl groups in individual strand of the collagen triple helix as well as polyproline-II helices and α-helix proteins.

In the present and previous chapters we have explored n→π* interaction in model compounds using gas phase spectroscopic techniques. However, it will be more compelling to investigate the role of n→π* interaction in molecules which are directly involved in biological processes for example drugs, signaling molecules, etc using the current spectroscopic techniques. In the next chapter, we have shown the importance of n→π* interaction in dictating the conformational preferences of an analgesis drug, salicin.



Chapter 6

$n \rightarrow \pi^*$ INTERACTION GOVERNS THE CONFORMATIONAL PREFERENCE OF SALICIN

6.1 Introduction

In the previous chapters, we have investigated the interplay between n→π* interaction and hydrogen bonding as well as demonstrated the IR spectroscopic evidence for n→π* interaction using model compounds. It will be more interesting to explore the n→π* interaction in the molecules which have direct biological implications and understand the role of n→π* interaction in governing their structures and functions using similar spectroscopic techniques. In this chapter, the structure of an analgesic drug, salicin, has been studied and it is shown to be stabilized by n→π* interactions in addition to hydrogen bonds. Pharmacological activities of salicin are similar to those of the popular drug aspirin.¹⁶³⁻¹⁶⁸ It has been reported by Raines and co-workers that n→π* interaction plays a significant role in controlling the preferred structure and biological activity of aspirin.⁶³ Generally, clinical efficacy of a drug depends upon its interaction with biomolecules, which further depends upon the structure of the drug molecule and its possible conformations.

In fact, medicinal properties of salicin are manifold. Salicin is the major chemical constituent of white willow bark (*salix alba*), also known as “nature’s aspirin”, which has been used as a medicine for the treatment of fever, pain, and inflammation in the body for thousands of years.¹⁶³⁻¹⁶⁷ Salicin is a glycoside and its chemical structure (Figure 6.1) consists of a sugar molecule (β-D-glucopyranoside) and a benzyl alcohol moiety, which are linked through the anomeric oxygen atom of the sugar molecule. Salicin acts as a prodrug which is metabolized in our body to form the drug salicylic acid.^{163,164,166-168} Upon ingestion, salicin undergoes hydrolysis to form salicyl alcohol (saligenin), which is further oxidized to generate the salicylic acid that acts as an antipyretic, analgesic, and anti-inflammatory agent in the body.^{166,168} Historically, the discovery of aspirin (acetyl salicylic acid) was triggered by the extraction of salicin from willow bark and subsequent synthesis of salicylic acid from

salicin.¹⁶⁶ Recently it has been reported that salicin also shows antitumor properties by inhibiting angiogenesis, a process which supplies oxygen and nutrients to tumor cells.^{169,170} Several *in vitro* and *in vivo* clinical trials are being carried out to discover and understand its full range of clinical properties.¹⁷⁰⁻¹⁷³

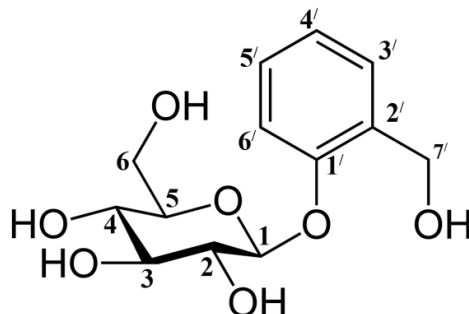


Figure 6.1. Skeletal structure of salicin

Herein, we have explored the conformational preferences of salicin in isolated gas phase using mass-selected Resonance Two Photon Ionization (R2PI), IR-UV and UV-UV double resonance spectroscopic techniques in combination with density functional theory calculations and calculated Franck-Condon spectra. Three low energy conformers of salicin have been observed in the experiment. These conformers show a chain of weak hydrogen bonding interactions between the equatorial hydroxyl groups of the sugar unit while the $-\text{CH}_2\text{OH}$ group of the benzyl alcohol moiety gives rise to an additional strong $\text{O-H}\cdots\text{O}$ hydrogen bonding interaction with one of the $-\text{OH}$ groups of the sugar moiety. In addition to this, the oxygen atom of the $-\text{CH}_2\text{OH}$ group of the benzyl alcohol moiety takes part in an $n \rightarrow \pi^*$ interaction with the phenyl ring. In fact we observed interplay between hydrogen bond and $n \rightarrow \pi^*$ interaction in the most stable conformers of salicin, similar to that in α -helix.

It has been discussed in section 1.3 that the carbonyl oxygen atom of residue i in a α -helix is involved in hydrogen bonding and $n \rightarrow \pi^*$ interaction with residue $i+4$ and residue $i+1$,

respectively. Since oxygen has two lone pairs, one of the lone pairs participates in the hydrogen bonding while the other lone pair of the same oxygen atom takes part in the $n \rightarrow \pi^*$ interaction. As a consequence, the presence of the $n \rightarrow \pi^*$ interaction weakens the hydrogen bond and vice versa. The interesting point is that the hydrogen bond alone could be stronger than the combination of the compromised hydrogen bond and the $n \rightarrow \pi^*$ interaction. However, the latter arrangement may be preferable from an optimal structure point of view.⁷⁷ Even in the present study we noticed that a few higher energy conformers of salicin, possessing stronger hydrogen bonds but negligible $n \rightarrow \pi^*$ interactions, are not observed in the experiment. Gas phase spectroscopic studies of salicyl alcohol (saligenin), which is the hydrolyzed product of salicin, have been reported in the literature.^{174,175} However, the structure of saligenin is much simpler than that of salicin.

The present research demonstrates that the conformational preferences of salicin are governed by a weak $n \rightarrow \pi^*$ interaction, even in the presence of strong hydrogen bonding interactions in the molecule. This result also indicates that a fine balance between a strong hydrogen bond and a weak $n \rightarrow \pi^*$ interaction is essential for the stability of the molecular systems. A close analog of salicin is phenyl β -D-glucopyranoside, which has been studied by Simons and co-workers as well as other groups using gas phase laser spectroscopy.¹⁷⁶⁻¹⁷⁸ However, phenyl β -D-glucopyranoside lacks the strong intramolecular hydrogen bonding interaction as well as an $n \rightarrow \pi^*$ interaction due to absence of the $-\text{CH}_2\text{OH}$ group at 2' position of the aromatic ring and these missing interactions form the basis of the major focus of the current work.

6.2 Results and discussion

6.2.1 Conformations of salicin: Electronic spectroscopy

The electronic spectrum of salicin measured by 1C-R2PI spectroscopy is shown in Figure 6.2(a). The spectrum shows several sharp bands in the range of $36400 - 36600 \text{ cm}^{-1}$.

To determine whether all the electronic bands shown in Figure 6.2(a) correspond to single or multiple conformers of salicin, UV-UV hole-burning spectroscopy was performed. Figures 6.2(b), (c) and (d) show UV-UV hole-burning spectra measured by probing the bands labelled as A, B, and C, respectively, in the spectrum displayed in Figure 6.2(a). In general, a hole-burning spectrum probing a particular band in the electronic spectrum provides depletion of ion signals for all the electronic bands which belong to a specific conformer. The spectra shown in Figures 6.2(b), 6.2(c) and 6.2(d) clearly show the presence of three distinct conformers of salicin in the experiment. The hole-burning spectra shown in Figures 6.2(b),

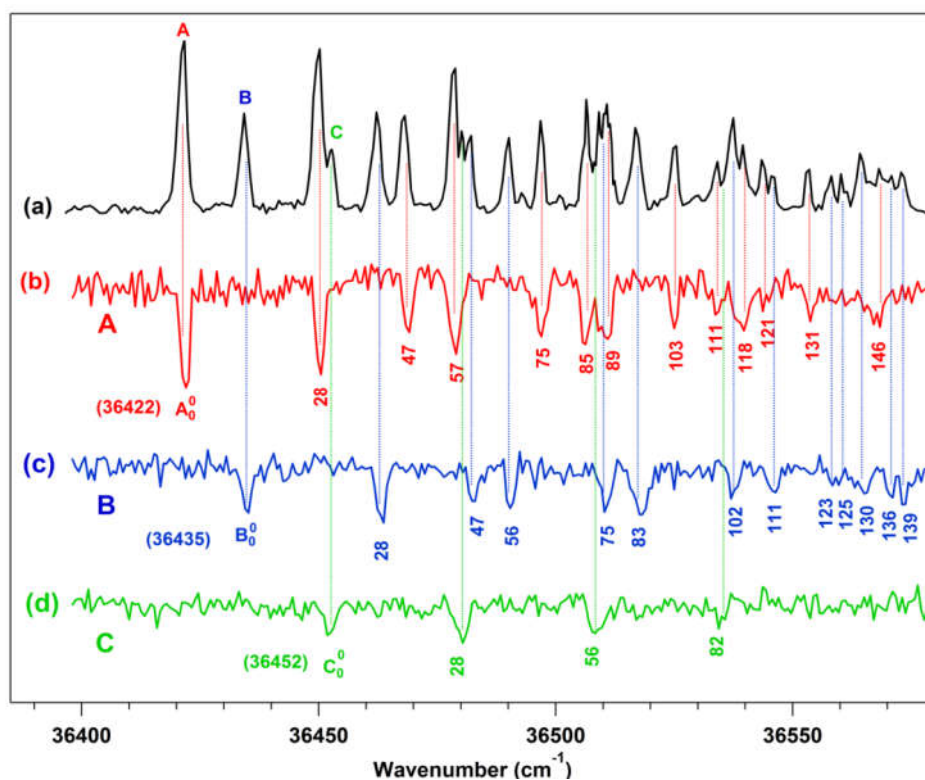


Figure 6.2 (a) Electronic spectrum of salicin measured using 1C-R2PI spectroscopy. (b), (c) and (d) are UV-UV hole burning spectra of salicin measured by probing the bands labeled as A (36422), B (36435) and C (36452 cm^{-1}) respectively, in the R2PI spectrum. The electronic band origins of A, B and C conformers are designated as A_0^0 (36422 cm^{-1}), B_0^0 (36435 cm^{-1}) and C_0^0 (36452 cm^{-1}).

6.2(c) and 6.2(d) are basically conformation-specific electronic spectra of conformers A, B, and C, respectively, of salicin. The $S_1 \leftarrow S_0$ origin bands (0_0^0) of conformers A, B, and C

labeled as A₀⁰, B₀⁰ and C₀⁰ appear at 36422, 36435, and 36452 cm⁻¹, respectively. The intensity pattern of the electronic bands of the three conformers reveals that the most populated conformer is A, while the C conformer is least populated. All three conformers show a progression of a low-frequency vibrational mode of 28 cm⁻¹. The electronic spectra of conformers A and B show some other low frequency modes (e.g. 47 cm⁻¹) and their combination bands apart from the 28 cm⁻¹ mode. The detailed assignment of the electronic bands of the three conformers made through their S₁ state vibrational frequency calculations and simulated Franck-Condon spectra is provided below in Table 6.1 and in the Figure 6.7.

Table 6.1: Experimental and Franck-Condon simulated low frequency intramolecular vibrational modes of the three observed conformers of salicin.

A			B			C		
Obs. (cm ⁻¹)	Cal. (cm ⁻¹)	Assign.	Obs. (cm ⁻¹)	Cal. (cm ⁻¹)	Assign.	Obs. (cm ⁻¹)	Cal. (cm ⁻¹)	Assign.
28	27	α	28	28	α	28	29	α
47	47	β	47	48	β	-	48	β
57	55	2α	56	56	2α	56	58	2α
	59	γ						
75	74	α+β	75	76	α+β	-	78	α+β
	79	δ						
85	86	α+γ	83	84	3α	82	88	3α
89	92	ε	-	88	α+γ	-		
	94	2β		97	2β			
103	102	2α+β	102	103	α+δ	-		
	106	β+γ		104	2α+β		107	2α+β
111	113	2α+γ	111	112	4α	-		
				116	2α+γ		118	2α+γ
118	119	α+ε	123	124	α+2β	-	126	α+2β
121	121	α+2β	130	131	2α+δ	-		
131	134	2α+δ	136	132	3α+β	-	136	3α+β
146	148	2α+2β	139	144	3α+γ	-		

As salicin is a close analogue of β-phenyl D-glucopyranoside having additional substitution of a hydroxymethyl group at 2-position of the phenyl group, it is worth comparing the electronic spectrum of salicin with that of the β-phenyl D-glucopyranoside reported in the literature.¹⁷⁶ It is interesting to note that the electronic spectrum of β-phenyl

D-glucopyranoside also indicates the presence of three conformers in the experiment. The low frequency vibronic bands observed in the electronic spectra of the three conformers of β -phenyl D-glucopyranoside are also similar to those of salicin.

6.2.2 Conformational landscape of salicin: DFT calculations

Although only three conformers are observed in the experiment, salicin can have many possible conformations due to its flexible shape. Thus proper assignment of the structures of the observed conformers is not straightforward. Firstly, the CONFLEX program was used to generate probable initial structures in the conformational space of salicin. A total of 60 conformers were generated from the force field calculation and 22 structures were selected from there on the basis of an energy cut-off of 4 kcal/mol relative to the most stable conformer. As a number of the structures obtained from the force field calculations in this way were very similar in both geometry and energy, DFT calculations were subsequently performed on 14 structures at the M06-2X/6-311++G(d,p) level of theory. The optimized structures of these conformers were then arranged in order of increasing energy from the global minimum as well as into different groups according to their structural similarities.

An energy landscape of the 14 low energy conformers and their classification into four groups (P, Q, R, S) in terms of structural similarities is shown in Figure 6.3. While the structures of all the 14 conformers are provided in Figure 6.4. It is observed that major structural changes of these conformations occur mostly due to the change in the orientation of the hydroxy methyl (-CH₂OH) groups present in the pyranose and phenyl groups of salicin. The structural details of the conformers in the four groups have been visualized in Figure 6.4. The general structural motif of all the conformers is a chain of hydrogen bonds among the -OH groups of the pyranose ring and benzyl alcohol moiety.

Conformer I of group P is the global minimum. In this conformer, the -CH₂OH group of the aromatic ring (benzyl alcohol part) is strongly hydrogen bonded to the -O2H2

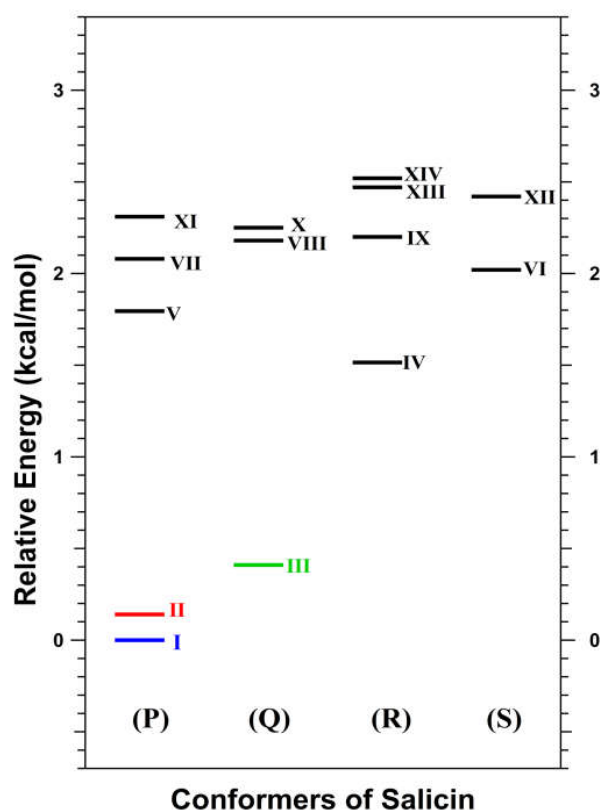


Figure 6.3. Relative energies (including zero point energy corrections) of the conformers of salicin calculated at the M06-2X/6-311++G(d,p) level of theory. Conformers are divided into four groups P, Q, R, and S on the basis of their structural similarities.

group of the sugar moiety. Furthermore, $-O4H4$, $-O3H3$, and $-O2H2$ groups of the sugar unit are weakly hydrogen bonded in a chain fashion, while the $-CH_2OH$ group of the sugar moiety is hydrogen bonded to the oxygen atom of the sugar ring. The other conformers in group P are related by rotation of the $-OH$ group of the benzyl alcohol moiety of salicin when retaining all the same hydrogen bonding structural motifs. The lowest energy conformer (III) in group Q is generated by rotating the $-CH_2OH$ group of the sugar moiety along the C-C bond of conformer I by 180° . This $-CH_2OH$ group forms a hydrogen bond with the neighbouring $-O4H4$ group of the sugar moiety instead of the oxygen atom in the pyranose ring, while the other hydrogen bonding interactions remain intact. The remaining two

conformers of group Q are again obtained from the rotation of the –OH group of the benzyl alcohol moiety of conformer III.

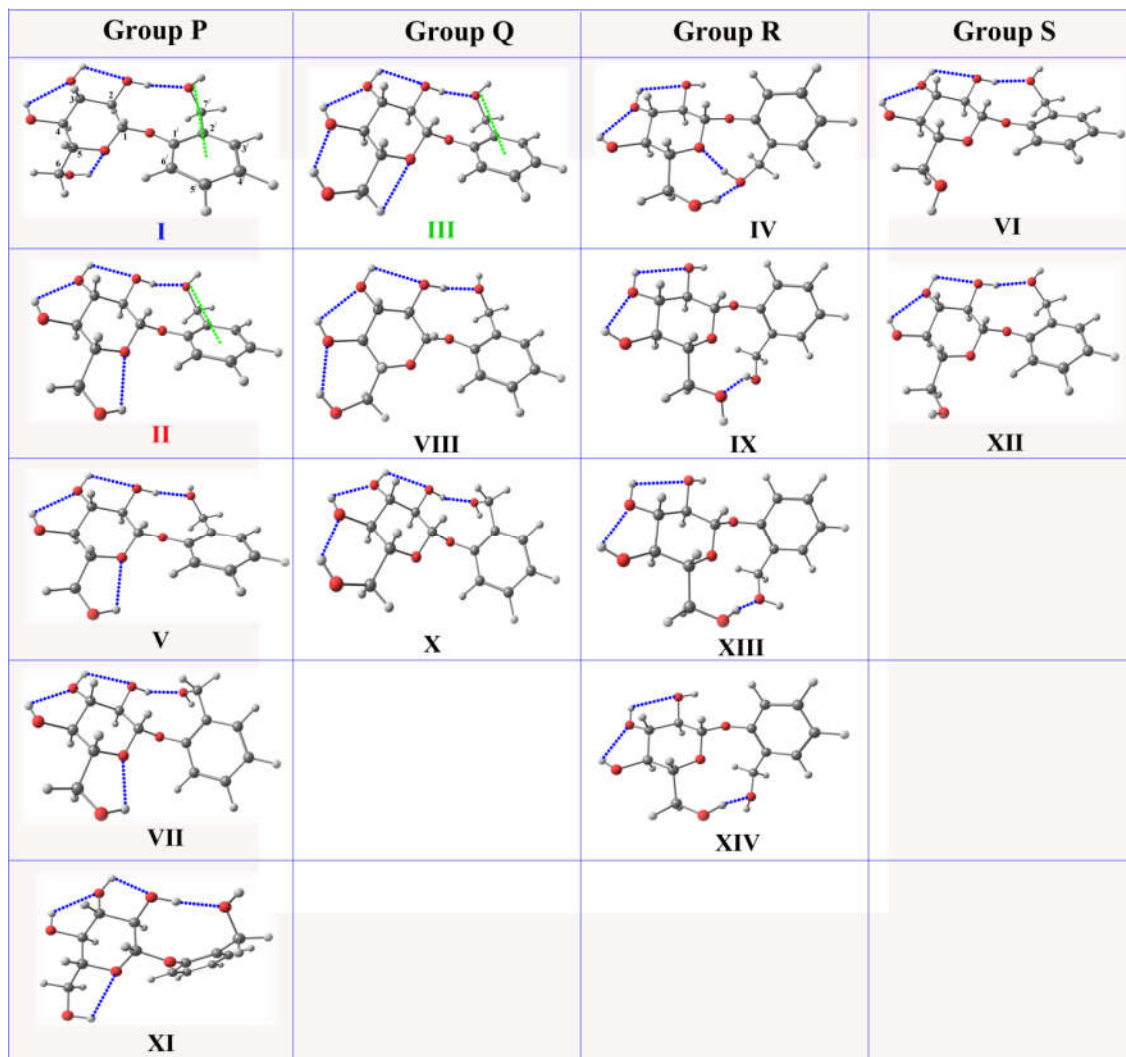


Figure 6.4. Structures of 14 low energy conformers of salicin optimized at the M06-2X/6-311++G(d,p) level of theory.

Conformer IV in group R is obtained by rotation of the whole benzyl alcohol moiety along the inter-ring O-C bond by 180° relative to conformer I of group P. In the R group conformers, –CH₂OH groups of the sugar moiety and aromatic ring are hydrogen bonded to each other, while all three –OH groups of the sugar ring and the inter-ring oxygen atom are

weakly hydrogen bonded in a chain fashion. Different conformers in the R group originate due to rotation of either the –OH group of the benzyl alcohol group or the OH group of the –CH₂OH of the sugar moiety. Conformer VI in group S is generated by rotating the –CH₂OH group of the sugar moiety in conformer I along the C-C bond by 90° and losing the hydrogen bond to the oxygen atom of the sugar ring while keeping all other hydrogen bonding motifs the same. Another conformer in group S, namely conformer XII, arises due to rotation of the –CH₂OH group of the sugar moiety at a different angle.

The most interesting feature of Figure 6.3 is that the three lowest energy conformers of salicin are conformers I, II, and III, which are within 0.5 kcal/mol relative energy (ΔE). The next highest energy conformer (conformer IV) is comparatively high in energy with a relative energy of roughly 1.5 kcal/mol. As three conformers of salicin are observed in the experiment, conformers I, II, and III are probable candidates for the observed conformers. Similar trends in the relative energies of various conformers of salicin were obtained with other density functionals and basis sets, and these results have been listed in Table 6.2.

Table 6.2. Zero-point energy (ZPE) corrected relative energies (kcal/mol) of various conformers of salicin, calculated at different levels of theory

Method	I	II	III	IV	V	VI
M06-2X/6-311++G(d,p)	0.00	0.14	0.41	1.51	1.78	2.02
M05-2X/6-311++G(d,p)	0.00	0.16	0.52	1.51	1.80	2.19
M05-2X/6-31+G(d)	0.00	0.12	0.33	1.86	1.93	2.33
M05-2X/cc-pVTZ	0.00	0.10	0.49	1.74	1.83	1.91
M05-2X/aug-cc-pVDZ	0.00	0.042	0.59	1.68	1.64	1.87

Relative Gibbs free energies (ΔG) of all the conformers have been calculated at 298 K and these data have been provided in Table 6.3. It has been found that the trend in ΔE and ΔG of the conformers are quite similar. Thus, despite salicin being a flexible molecule and having an abundance of conformers, the determination of the structures of the experimentally

observed conformers becomes relatively straightforward when paired with the output of quantum chemical calculations.

Table 6.3. Relative electronic energies (ΔE) and relative Gibbs Free energies (ΔG) of all 14 low energy conformers of salicin calculated at 298 K

Conformer	ΔE (kcal/mol)	ΔG (kcal/mol)
I	0.00	0.00
II	0.14	0.28
III	0.42	0.58
IV	1.51	1.34
V	1.80	1.62
VI	2.02	1.83
VII	2.09	1.78
VIII	2.19	2.19
IX	2.21	1.96
X	2.26	2.24
XI	2.32	2.34
XII	2.43	2.22
XIII	2.48	2.29
XIV	2.53	2.66

6.2.3 Structures of observed conformers of salicin: IR spectroscopy

The primary aim of the present work is to determine the structures of the conformers of salicin observed in the experiment and understand the interplay between the non-covalent interactions that govern their energetics. Figures 6.5(a), 6.5(c), and 6.5(e) show experimental IR spectra of the three conformers (marked as A, B and C in the R2PI spectrum of Figure 6.2) of salicin in the O-H stretching region measured by probing their respective electronic origin band using RIDIR spectroscopy. As there are a total of five OH groups in salicin, five bands should be observed in the O-H stretching frequency region of the IR spectra if all the bands are well resolved. The IR spectra of all three conformers show a strong band around the 3460 cm^{-1} region. On the other hand, the remaining four IR bands appearing in the $3590\text{--}3640 \text{ cm}^{-1}$ region are quite weak, broad and unresolved. Although the position of the strong IR band is very close across all three conformers, their respective positions (3464 , 3466 , and 3460 cm^{-1}) have been confirmed through repeated IR scans. Conformers A and B show the

weak broad features centering around 3630 cm^{-1} while conformer C shows a distinct band at 3597 cm^{-1} in addition to the broad feature at 3630 cm^{-1} . Thus, it is apparent that the structures of conformers A and B are quite similar, while the structure of conformer C is a little different compared to the other two.

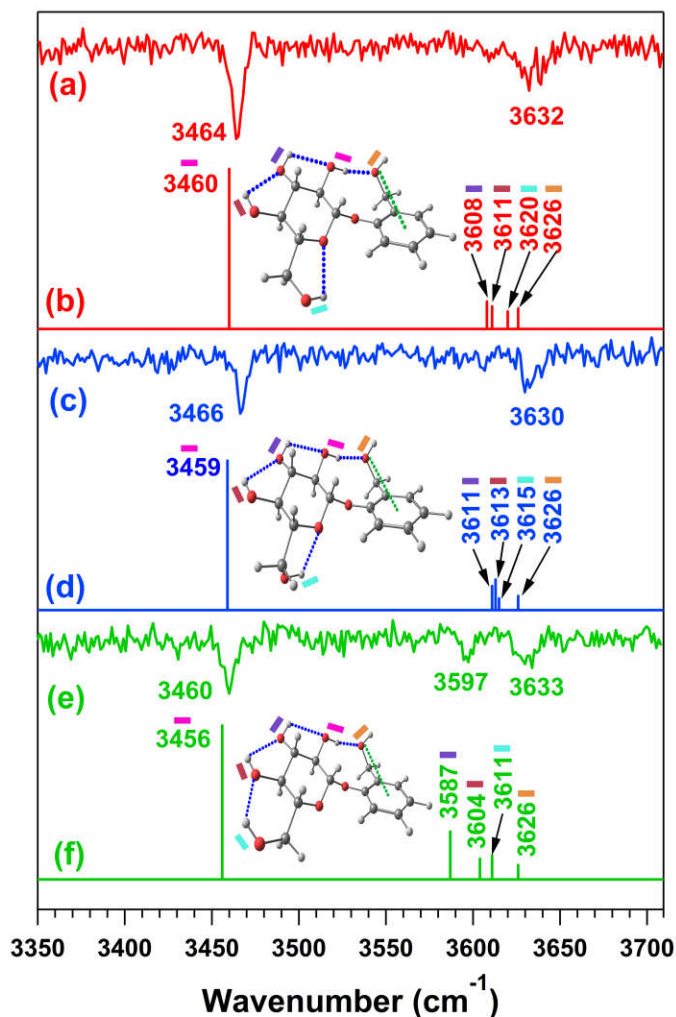


Figure 6.5. (a), (c) and (e) show the experimental IR spectra of species A, B and C, respectively, in the O-H stretching region measured by probing their respective electronic band origins (for electronic origin bands see Figure 2). The scaled theoretical O-H stretching frequencies of conformers II, I and III are shown in (b), (d) and (f) respectively, calculated at the M06-2X/6-311++G(d,p) level of theory. The structures of conformers I, II, and III are also shown in the inset of the figure. The blue dotted line represents the O-H...O hydrogen bonding and the green dotted line represents the $n \rightarrow \pi^*$ interaction.

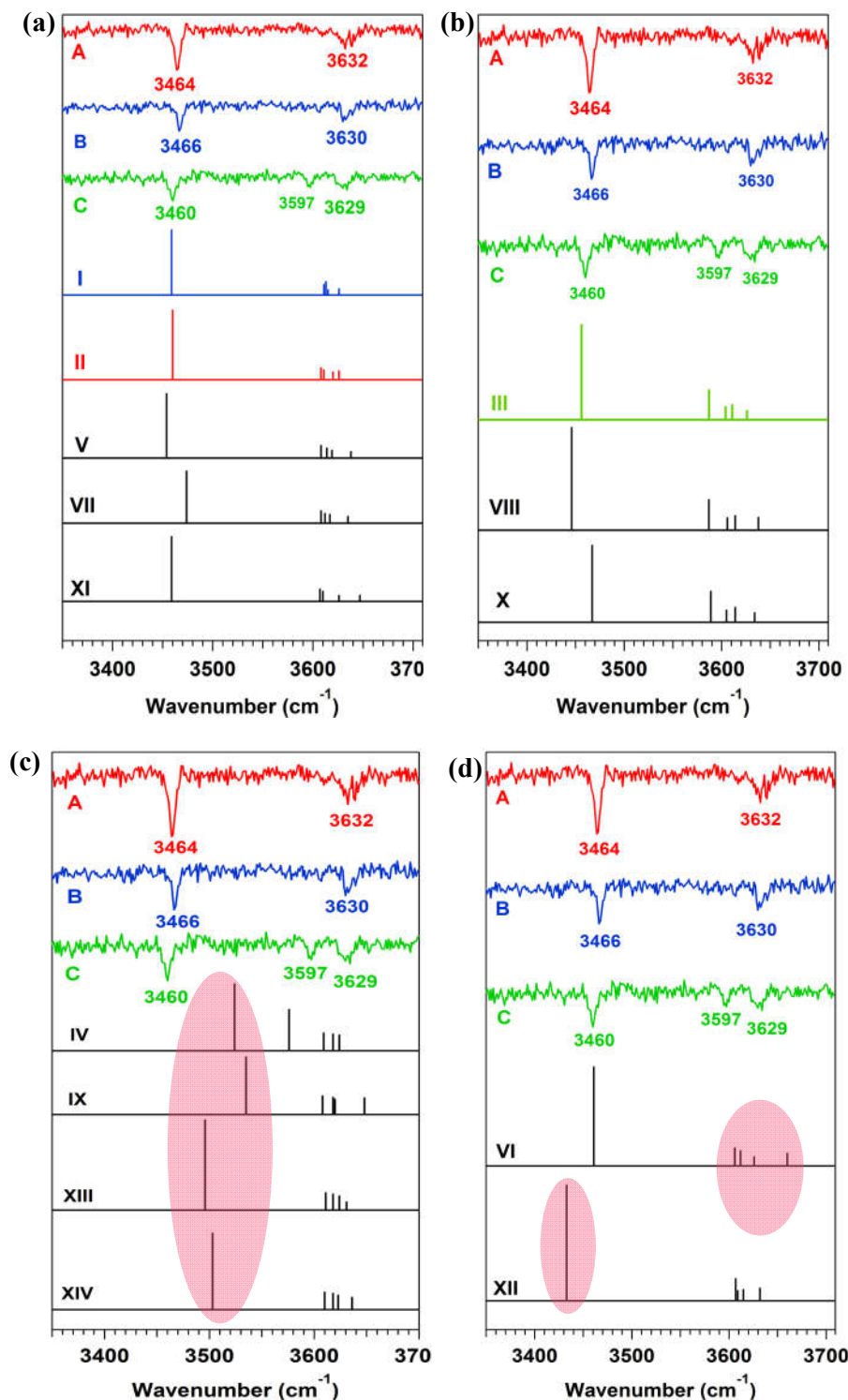


Figure 6.6. Experimental O-H stretching frequencies of species A, B and C in comparison with the computed O-H stretching frequencies of (a) Group P, (b) Group Q, (c) Group R, and (d) Group S conformers. The calculated [M06-2X/6-311++G(d,p) level of theory] O-H stretching frequencies are shown as stick spectra (origins scaled by a factor of 0.9333).

Experimental IR spectra of these three conformers are then compared with the theoretical IR spectra of the conformers classified into P, Q, R, and S groups computed at the M06-2X/6-311++G(d,p) level of theory. The calculated O-H harmonic stretching frequencies of all fourteen conformers are scaled using a factor of 0.9333, which is the ratio of the experimental to calculated OH stretching frequency of benzyl alcohol¹⁷⁹ at the same level of theory. The interesting point here is that the pattern of the experimental OH stretching frequencies serves as a guide to choosing probable observed conformers from the pool of structures obtained from the series of calculations.

Theoretical IR spectra of the three lowest energy conformers (I, II and III) of salicin along with their computed structures are shown in Figure 6.5 while the comparison of the experimental IR spectra of the three conformers of salicin with the theoretical IR spectra of all 14 conformers is provided in Figure 6.6. Each of the five O-H groups in the structures and the corresponding IR band in the theoretical IR spectra (Figure 6.4) are marked with a specific colour bar. It is clear that the C(2)-OH group of the sugar moiety is very strongly hydrogen bonded to the oxygen atom of the OH group of the benzyl alcohol moiety, while the hydrogen bonds involving other OH groups of the sugar moiety are very weak and similar in nature. It can be concluded from the comparison shown in Figure 6.5 that the IR spectra of conformers A and B are due to structures I and II. However, it is not straightforward to tell whether conformer A has structure I and conformer B has structure II, or vice versa. On the other hand, conformer C can easily be assigned to structure III from the comparison of the experimental and theoretical IR spectra provided in Figures 6.5(e) and 6.5(f), respectively, as the IR spectrum of conformer C is different from those of conformers A and B in the 3590-3650 cm^{-1} region. In structure III, the $-\text{CH}_2\text{OH}$ group of the sugar moiety is hydrogen bonded to the neighbouring OH group, while the $-\text{CH}_2\text{OH}$ group of the sugar moiety in both structures I and II is hydrogen bonded to the oxygen atom of the sugar ring. The IR band of

conformer C at 3597 cm^{-1} [Figure 6.5(e)] is assigned to the OH vibration of the $-\text{CH}_2\text{OH}$ group of the sugar moiety. Theoretical IR spectra of the remaining higher energy conformers (structures IV-XIV) presented in Figure 6.6 can be disregarded based on either the higher relative energy or the significantly different IR spectra of these conformers compared to the three lowest energy conformers (I, II, III).

It is intriguing to compare the IR spectra of the three conformers of salicin with those of β -phenyl D-glucopyranoside reported by Simons and co-workers.¹⁷⁶ It can be seen that the IR spectra of the two major conformers of β -phenyl D-glucopyranoside are similar to those of conformers A and B of salicin in the broad and weak spectral region ($3620\text{--}3650\text{ cm}^{-1}$). The IR spectrum of the minor conformer of β -phenyl D-glucopyranoside matches well with that of the conformer C of salicin in the $3590\text{--}3650\text{ cm}^{-1}$ region. However, the strong IR band of salicin around 3460 cm^{-1} is absent in the IR spectra of all conformers of β -phenyl D-glucopyranoside. The comparison of the IR spectra of salicin and β -phenyl D-glucopyranoside thus indicates that the strong band ($3460\text{--}3466\text{ cm}^{-1}$) observed in the IR spectrum of salicin could be due to a strong hydrogen bonding interaction between the benzylic CH_2OH group and $\text{O}2\text{H}2$ group. On the other hand, the weak unresolved broad peaks are due to the OH groups in the sugar moiety present as a chain of intramolecular O-H...O hydrogen bonds. The hydrogen bonded structural motifs of the three observed conformers of β -phenyl D-glucopyranoside are quite similar to those of the three observed conformers of salicin. Thus comparison between salicin and β -phenyl D-glucopyranoside data provides extra confidence to the assignment of the structures of the observed salicin conformers. It should also be noted that the substitution of the $-\text{CH}_2\text{OH}$ group in the phenyl moiety of the sugar derivative does not change the basic structural motif of the sugar unit.

6.2.4 Franck-Condon simulated electronic spectra

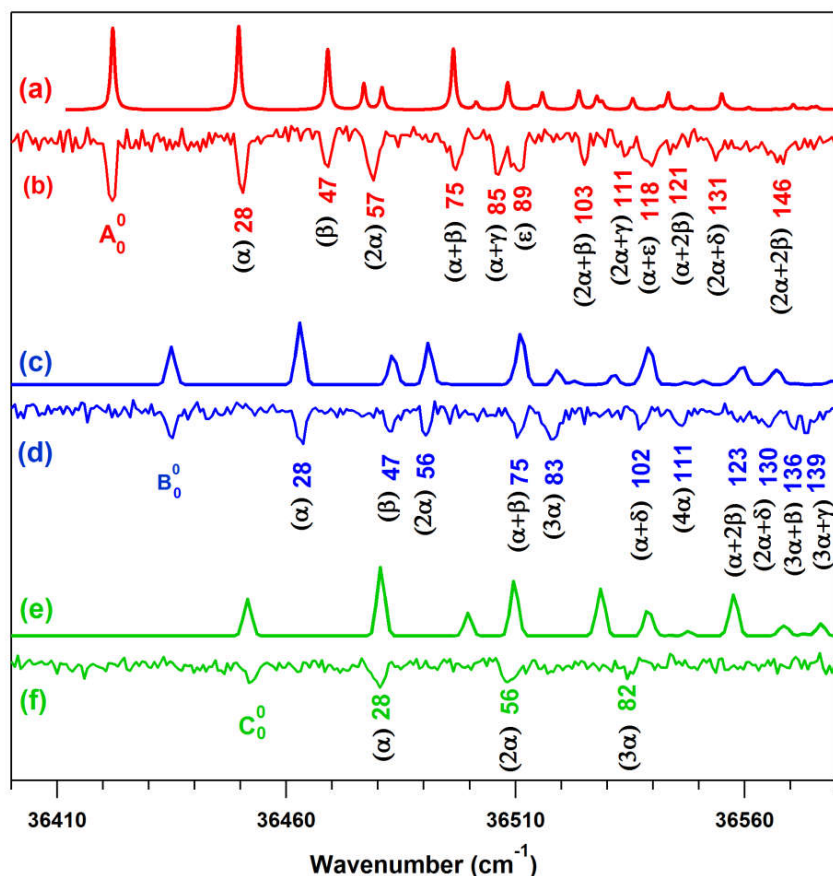


Figure 6.7. (b), (d) and (f) shows experimental electronic spectra of species A, B and C respectively, in comparison with the Franck-Condon simulated electronic spectra of conformers II, I and III presented in (a), (c) and (e), respectively. Assignments of the bands are based on the simulated Franck-Condon spectra.

As mentioned earlier, it is difficult to predict which of the two lowest energy conformers (I and II) of salicin belongs to species A and B in the electronic spectrum due to the similarity in their IR spectra. However, Franck-Condon (FC) simulated electronic spectra of different conformers of salicin and their vertical excitation energies can further aid in assigning the structures of the observed conformers.^{180,181} Figures 6.7(b), 6.7(d), and 6.7(f) show experimentally observed electronic spectra of species A, B, and C, respectively, while FC simulated electronic spectra of conformers II, I, and III are shown in Figures 5(a), (c), and (e), respectively. There is excellent agreement (in terms of the frequency of vibration as well as intensity of the bands) between the experimentally observed and FC simulated electronic

spectra of the three conformers of salicin. It can be seen that the origin band of conformer B (B_0^0) is weaker in intensity when compared to the 28 cm^{-1} vibration of conformer B, while for conformer A the intensities of the origin band (A_0^0) and 28 cm^{-1} vibration are comparable in magnitude. It is noteworthy that this specific intensity pattern of experimental electronic spectra of species A and B corroborates that of the FC simulated electronic spectra of conformers II and I, respectively. Thus species A and B can be assigned as conformers II and I.

Vertical excitation energies of the three lowest energy conformers (I, II, and III) calculated at the TD-M06-2X/6-311++G(d) level of theory lend additional support to the assignment of the structures of the conformers observed in the experiment. Vertical excitation energies (scaled with respect to the origin band of species A) of conformers I, II, and III of salicin are provided in Table 6.4. Conformer II has lowest vertical excitation energy. The order of relative vertical excitation energies of conformers II, I, and III match well with the electronic origin band positions of species A, B, and C, respectively. This suggests that species A, B, and C should be assigned as conformers II, I, and III. FC simulated electronic spectra of a few higher energy conformers of salicin were also calculated. However, large geometric changes between S_0 and S_1 states mean the calculated spectra have almost zero intensity.

Low frequency vibronic bands present in the electronic spectra of the three conformers of salicin are assigned with the help of the simulated Franck-Condon spectra (see Figure 6.7). A list of the experimental and calculated (S_1) low-frequency vibrational modes (based on FC simulation) as well as a tentative assignment of all the low frequency bands in the electronic spectra of the three lowest energy conformers of salicin is also provided in Table 6.1.

Table 6.4. Experimental 0_0^0 band transitions of species A, B and C in comparison with the TDDFT calculated [TD-M06-2X/6-311++G(d)] vertical excitation energies of conformers I, II and III

Observed Species	Experimental 0_0^0 band transitions (cm^{-1}) ^a	Assigned conformer	Calculated vertical excitation energies (cm^{-1}) ^b
A	36422 (0)	II	42877 (0)
B	36435 (13)	I	42912 (35)
C	36452 (30)	III	42930 (53)

^aValues in parentheses represent the relative frequencies with respect to the 0_0^0 band transition of conformer A. ^bValues in parentheses represent the relative frequencies with respect to the calculated vertical excitation energy of conformer II.

It is found that there is a long progression of the 28 cm^{-1} vibration (α) in the electronic spectra of all three conformers. This 28 cm^{-1} vibration is assigned as an inter-ring twisting vibration along the $\angle\text{O7-C1-O8-C1}'$ dihedral angle. Another prominent low frequency vibrational mode of 47 cm^{-1} is observed for both conformers A and B while the same is not observed for conformer C. The electronic spectra of A and B can be assigned mostly by the overtones of the α mode and its combination bands with other modes. Thus, the interpretation of the electronic spectra suggests that major geometrical changes in salicin after electronic excitation may occur along this α mode.

6.2.5 Conformational preference in salicin: $n \rightarrow \pi^*$ interaction

The structures of the conformers I, II and III calculated at the M06-2X/6-311++G(d,p) level of theory are provided in Figure 6.4 and Figure 6.5, with their important geometrical parameters in Table 6.5. It is evident that all three observed conformers differ mainly in the orientation of the hydroxy group (O6-H6) of the $-\text{CH}_2\text{OH}$ group in the sugar moiety, which is represented by the dihedral angle O6-C6-C5-O5. In both conformers I and II, O6-H6 has gauche orientation with $\angle\text{O6-C6-C5-O5}$ of $+57^\circ/-57^\circ$. The O6-H6 group of conformer I and II is involved in a weak hydrogen bonding interaction with the O5 atom of

the pyranose ring (O6-H6...O5). The O6-H6...O5 hydrogen bond distance (d_i) and angle (θ_i) are around 2.3 Å and 105°, respectively, in both conformers I and II. Conformer III differs from I and II as the O6-H6 group in the former has trans orientation ($d\angle O6-C6-C5-O5 = 164.5^\circ$). Unlike conformers I and II, the O6-H6 group of conformer III is involved in a hydrogen bonding interaction with the O4-H4 group (O6-H6...O4). Purely based on a hydrogen bond distance and angle point of view (see Table 6.5), the O6-H6...O4 hydrogen bond in conformer III is stronger than the O6-H6...O5 hydrogen bond present in I and II.

Table 6.5. Important geometrical parameters^a of low energy conformers of salicin calculated at the M06-2X/6-311++G(d,p) level of theory

	I	II	III	V	VIII
d_e (O3-H3...O2)	2.43	2.45	2.46	2.47	2.48
θ_e ($\angle O3-H3...O2$)	101.1	104.6	104.3	104.0	103.7
d_e (O5-H5...O3)	2.41	2.38	2.36	2.38	2.36
θ_e ($\angle O5-H5...O3$)	105.1	107.4	107.3	107.5	107.4
d_i (O6-H6...O5)	2.30	2.34	-	2.33	-
θ_i ($\angle O6-H6...O5$)	106.2	104.5	-	104.9	-
d_l (O6-H6...O4)	-	-	2.05	-	2.04
θ_l ($\angle O6-H6...O4$)	-	-	134.4	-	134.5
d_s (O2-H2...O7 [/])	1.94	1.95	1.93	1.94	1.92
θ_s ($\angle O2-H2...O7$)	164	164.2	164.4	172.6	172.4
r_O (O7 [/] ...Ar)	3.68	3.67	3.68	3.64	3.64
r_H (O7 [/] ...Ar)	3.65	3.65	3.65	4.52	4.53
$\angle O6-C6-C5-O5$	-56.5	57.5	164.9	57.7	164.9
$\angle H6-O6-C6-C5$	55.2	-58.9	53.1	-58.2	53.0
$\angle H7$ [/] -O7 [/] -C7 [/] -C2 [/]	57.3	57.6	57.0	167.2	166.4
$\angle O7$ [/] -C7 [/] -C2 [/] -C1 [/]	64.6	64.2	64.7	65.8	66.2

^aDistances (d_e , d_i , d_l , d_s , r_O and r_H) are in Å and angles (θ_e , θ_i , θ_l , θ_s) are in degrees.

In all three conformers, the equatorial hydroxy groups of the sugar moiety adopt the gauche orientation. Equatorial OH groups are linked with each other through a chain of weak O-H...O hydrogen bonds. This is evident through their hydrogen bond distances (d_e) and angles (θ_e), which are around 2.5 Å and 106°, respectively, in all observed conformers. However, all three conformers (I, II and III) have a strong intramolecular hydrogen bond between the hydroxy group (O2-H2) of the sugar moiety and the oxygen atom (O7[/]) of the

benzyl alcohol unit (O2-H2 \cdots O7'). The O2-H2 \cdots O7' hydrogen bond distance (~ 1.9 Å) and angle ($\sim 164^\circ$) lie close to the ideal geometrical conditions required for strong hydrogen bonding interaction in all three conformers. This indicates that the O2-H2 \cdots O7' hydrogen bond is much stronger than the hydrogen bonds between the equatorial OH groups.

Although only the three lowest energy conformers (I, II, and III) are observed in the experiment, analysis of the hydrogen bonding parameters in a few higher energy conformers reveals interesting information that is the focus of the present section. From Figure 6.3 it can be seen that conformer V is the next highest energy conformer after I and II in group P, while conformer VIII is the next highest energy conformer after III in group Q. It is evident from the comparison of the geometrical parameters of the conformers presented in Table 6.5 that the O2-H2 \cdots O7' hydrogen bond in both conformers V and VIII ($\angle \text{O2-H2}\cdots\text{O7}' \sim 172^\circ$) is stronger than that in conformers I, II, and III ($\angle \text{O2-H2}\cdots\text{O7}' \sim 162^\circ$). This suggests that the other O-H \cdots O hydrogen bond interactions in conformers V and VIII are similar in strength to those of I/II and III. In spite of this, it is interesting to note that conformers V and VIII are relatively high in energy compared to conformers I, II, and III. Basically, conformer V belongs to the same group of conformers as both I and II (group P in Figure 6.4), while conformer VIII is in group Q with conformer III.

It is apparent from the structures of salicin provided in Figure 6.4 that the structures of conformers V and VIII differ from those of conformers I/II and III, respectively, due solely to the orientation of the O7'-H7' group of the benzyl alcohol moiety of salicin. In all three observed conformers of salicin, i.e. conformers I, II, and III, the O7'-H7' group of the benzyl alcohol unit has gauche orientation ($^d\angle \text{H7}'\text{-O7}'\text{-C7}'\text{-C2}' \sim 56.8^\circ$) and the distance of the O7'-H7' group from the center of the aromatic ring ($r_{\text{O7}'\text{-H7}'\cdots\text{Ar}}$) is ~ 3.6 Å. In fact, the gauche orientation of the O7'-H7' group of conformer I, II and III resembles the orientation of the OH group in the gauche conformer of isolated benzyl alcohol.¹⁷⁹ On the other hand, conformers

V and VIII have trans orientation of the $O_7'-H_7'$ group ($\angle H_7'-O_7'-C_7'-C_2' \sim 167^\circ$) which resembles the orientation of the OH group in the trans conformer of isolated benzyl alcohol. The gauche conformer of benzyl alcohol is reported to be more stable than the trans conformer based on both experimental and theoretical data.¹⁷⁹ Interestingly, conformers I, II, and III of salicin (gauche orientation of the $O_7'-H_7'$ group) are also more stable than conformers V and VIII of salicin, which have trans orientation of the $O_7'-H_7'$ group. Based on this, it appears that the gauche orientation of the benzylic OH group plays an important role in governing the conformational preferences of salicin.

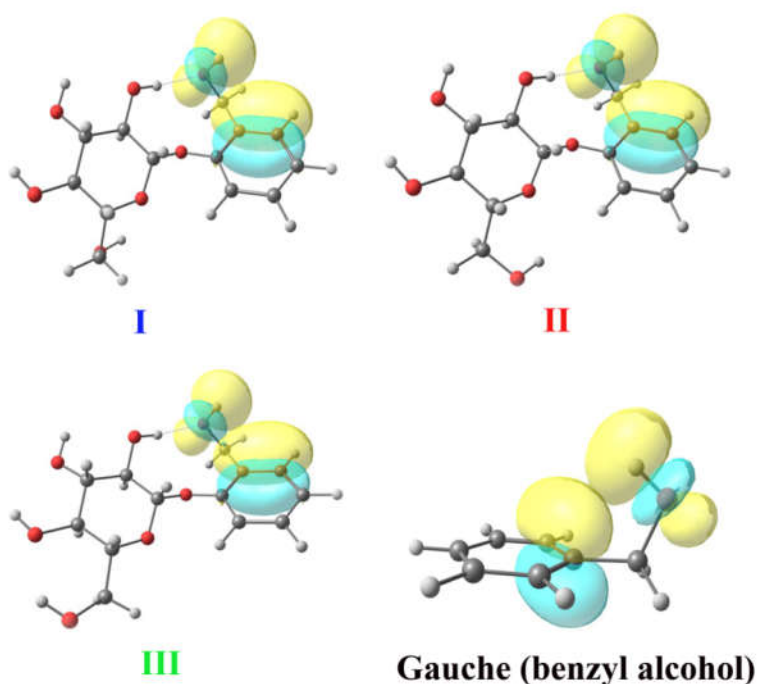


Figure 6.8. NBOs of the three lowest energy conformers (I, II, and III) of salicin and the gauche conformer of benzyl alcohol, showing no overlap between the π orbitals of the aromatic ring and σ^* orbital of the benzylic OH group. The electron density was calculated at the M06-2X/6-311++G(d,p) level of theory.

The stability of the gauche conformer of benzyl alcohol over the trans conformer has previously been rationalized by the presence of an O-H... π interaction in the former.¹⁷⁹

However, an NBO analysis on the gauche conformer of benzyl alcohol, as well as conformers I, II, and III of salicin having gauche orientation of the benzylic OH group, does not reveal any signature of an O-H...π interaction (see Figure 6.8). Generally, the presence of an O-H...π interaction is manifest through the overlap of π-orbitals with the antibonding O-H orbital. On the contrary, NBO analysis reveals that the lone pair orbitals (both s and p-types) on the oxygen atom of the OH group of the gauche conformer of benzyl alcohol, as well as for salicin conformers I, II, and III, have significant overlap with the π* orbitals of the phenyl group and this non-covalent interaction is termed n→π*. NBOs for the n→π* interaction as well as the O2-H2...O7' hydrogen bonding interaction in conformers I, II, III, V and VIII of salicin are shown in Figure 6.9(a). NBOs for the n→π* interaction in gauche and trans conformers of benzyl alcohol are also shown in Figure 6(b). NBO second-order perturbative estimates of donor-acceptor interactions ($E_{i→j*}^{(2)}$) for all the O-H...O hydrogen bonds and n→π* interactions in conformers I, II, III, V and VIII of salicin are listed in Table 6.6.

Table 6.6. NBO second-order perturbative estimates of donor-acceptor interactions ($E_{i→j*}^{(2)}$) of all hydrogen bonding and n→π* interactions observed in conformers I, II, III, V and VIII of salicin. NBO calculations were performed at the M06-2X/6-311++G(d,p) level of theory.

	$E_{i→j*}^{(2)}$ (kcal/mol)				
	I	II	III	V	VIII
n _p (O7')→σ*(O2-H2)	5.65	5.35	5.90	7.07	7.61
n _s (O7')→σ*(O2-H2)	3.28	3.24	3.27	2.39	2.40
n _p (O2)→σ*(O3-H3)	0.15	0.22	0.22	0.33	0.32
n _s (O2)→σ*(O3-H3)	0.21	0.16	0.15	0.18	0.18
n _p (O3)→σ*(O4-H4)	0.15	0.20	0.20	0.23	0.22
n _s (O3)→σ*(O4-H4)	0.18	0.20	0.24	0.20	0.24
n _p (O5)→σ*(O6-H6)	0.18	0.16	-	-	0.10
n _s (O5)→σ*(O6-H6)	0.17	0.15	-	0.15	0.14
n _p (O4)→σ*(O6-H6)	-	-	0.69	-	0.68
n _s (O4)→σ*(O6-H6)	-	-	2.60	-	2.61
n _p (O7')→π*(C2'/-C3')	0.80	0.83	0.78	-	-
n _s (O7')→π*(C2'/-C3')	0.33	0.32	0.35	0.31	0.31

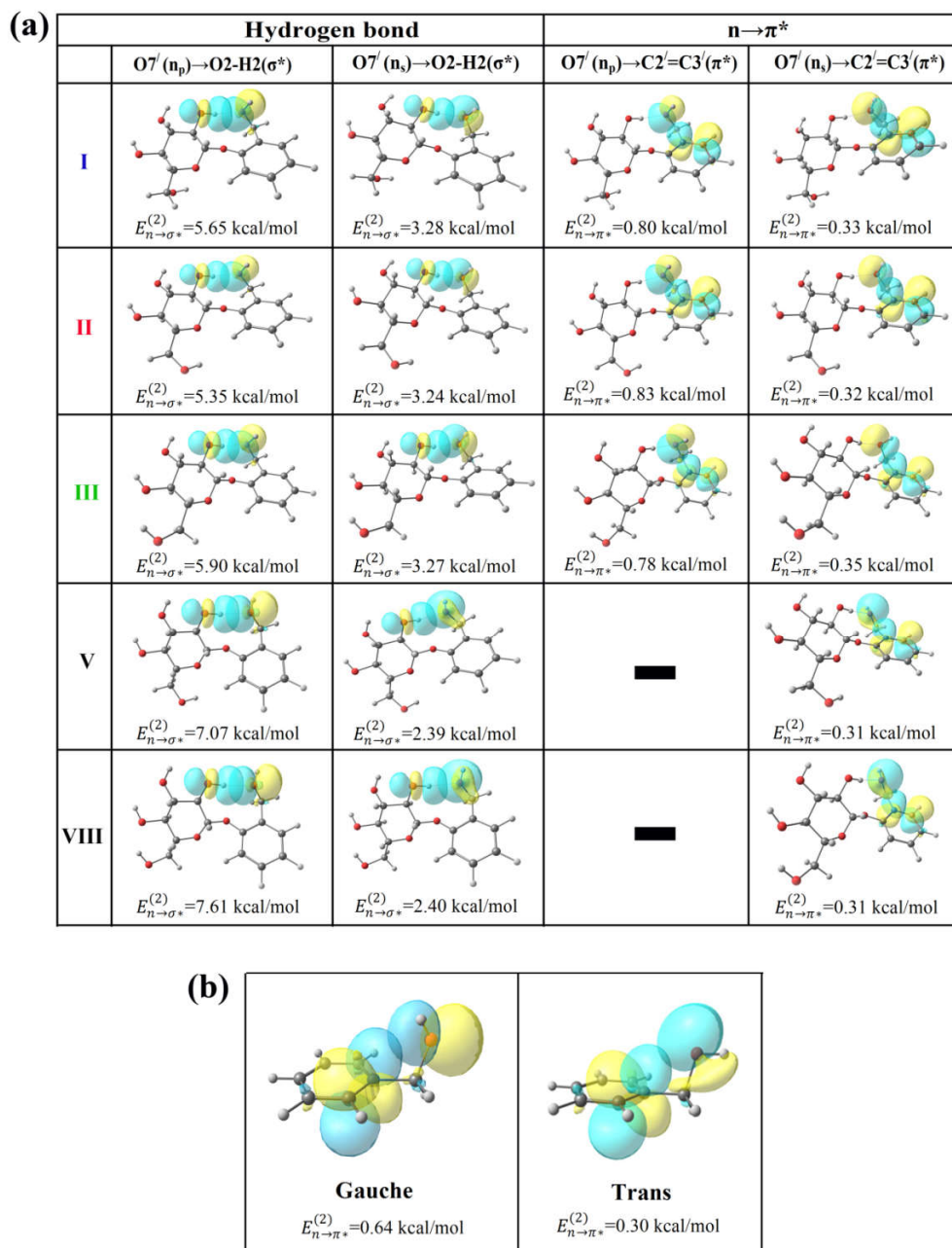


Figure 6.9 (a) NBOs of the O2-H2...O7' hydrogen bonding interaction and $n \rightarrow \pi^*$ interaction in various conformers (I, II, III, V and VIII) of salicin calculated at the M06-2X/6-311++G(d,p) level of theory. The NBOs of the $n \rightarrow \pi^*$ interaction show overlap between the lone pair orbitals (n_s and n_p) of O7' atom with the π^* orbital of C2'=C3' bond of the aromatic ring. The NBOs of the hydrogen bonding interaction show overlap between lone pair orbitals (n_s and n_p) of O7' atom with the σ^* orbital of the O2-H2 bond. (b) NBOs of the $n \rightarrow \pi^*$ interaction between the lone pair orbital of (n_s and n_p) oxygen atom and the aromatic ring in the gauche and trans conformers of benzyl alcohol.

The sum of the $E_{i \rightarrow j}^{(2)}$ values for the $n \rightarrow \pi^*$ interactions in the gauche conformer of benzyl alcohol and conformers I, II, and III of salicin is about 1.2 kcal/mol. The trans conformer of benzyl alcohol, as well as conformers V and VIII of salicin, also have an $n \rightarrow \pi^*$ interaction, albeit significantly weaker at around 0.4 kcal/mol (see below). Interestingly, NBO derived estimates for the strong hydrogen bond O2-H2...O7' in different conformers of salicin listed in Table 6.6 also highlight that the O2-H2...O7' hydrogen bond in conformers V and VII of salicin is stronger than that in conformers I, II, and III. This indicates that conformational preferences of conformers I, II, and III over conformers V and VIII of salicin are due to the presence of significant $n \rightarrow \pi^*$ interaction in the former, which have the benzylic OH group in gauche orientation.

A further interesting point from Table 6.6 is that both s-type and p-type lone pair electrons (n_s and n_p) on the O7' atom of the benzylic O-H group in conformers I, II, and III of salicin simultaneously participate in hydrogen bonding as well as the $n \rightarrow \pi^*$ interaction. The $n \rightarrow \pi^*$ interaction involving the n_p -type electrons is stronger than that involving the n_s -type electrons on the O7' atom in conformers I, II, and III of salicin. On the other hand, the n_p -type electrons on the O7' atom in conformers V and VIII do not take part in the $n \rightarrow \pi^*$ interaction. As the n_p -type electrons on O7' atom are involved in the stronger $n \rightarrow \pi^*$ interaction in conformers I, II and III, its availability for overlap with the σ^* orbital of the O2-H2 bond to form a O2-H2...O7' hydrogen bond slightly decreases. This accounts for the slightly weaker O2-H2...O7' hydrogen bond strength in the three observed salicin conformers (I, II, and III) compared to V and VIII. It is important to mention here that other higher energy conformers of salicin in the P and Q groups also have $n \rightarrow \pi^*$ interactions, albeit much weaker in strength compared to those in the observed conformers. This shows that the $n \rightarrow \pi^*$ interaction plays an important role in the preferential stabilization of the three lowest energy conformers.

Based on the experimental observation of the small red-shift in the O-H stretching frequency of gauche conformer of benzyl alcohol, the presence of O-H...π interaction could be expected however, NBO analysis suggest that n→π* interaction have major contribution towards the stability of gauche conformer of benzyl alcohol over the trans conformer. We have also looked at the occupancies of the σ* orbital of benzylic O-H bond in the most stable conformers (I, II, and III) and higher energy conformers (V, VIII) of salicin (see table 6.7). Through table it is revealed that occupancy of the σ* orbital of benzylic O-H bond is more in the most stable conformers of salicin (I, II, III) which have gauche conformation of the benzyl alcohol unit, compared to that of the higher energy conformers (V, VIII) which have trans conformation of the benzyl alcohol unit. Increase in the occupancy of the σ* orbital of benzylic O-H bond in the gauche conformer could be due to the O-H...π interaction or n→π* interaction.

Table 6.7. Occupancy of σ* orbital of benzylic O-H group in the conformers of salicin

Conformers	Occupancy of σ* _{Benzylic OH} orbital
I	0.0075
II	0.0075
III	0.0076
V	0.0052
VIII	0.0052

6.2.6 Biological perspective

In general, the role of the n→π* interaction in providing conformational preferences of biomolecules and biomolecular complexes is also revealed from protein data bank (PDB) searches.^{3-5,7,8,12} We have found that the preference for the gauche conformation of the isolated benzyl alcohol is retained in the benzylic alcohol moiety of not only isolated salicin

but also salicin bound to β-glucosidase enzyme (*NkBg1*), which is in the glycosyl hydrolase family.¹⁸² This enzyme plays an important role in the cleavage of the β-glucosidic linkage in salicin (a glucose substituted molecule) or any disaccharide. The X-ray crystal structure of the salicin bound complex of β-glucosidase enzyme (PDB ID: 3VIL) shows that the benzylic alcohol moiety of salicin adopts a gauche conformation.¹⁸² An NBO analysis of the unoptimized geometry of the salicin moiety obtained from the crystal structure of the

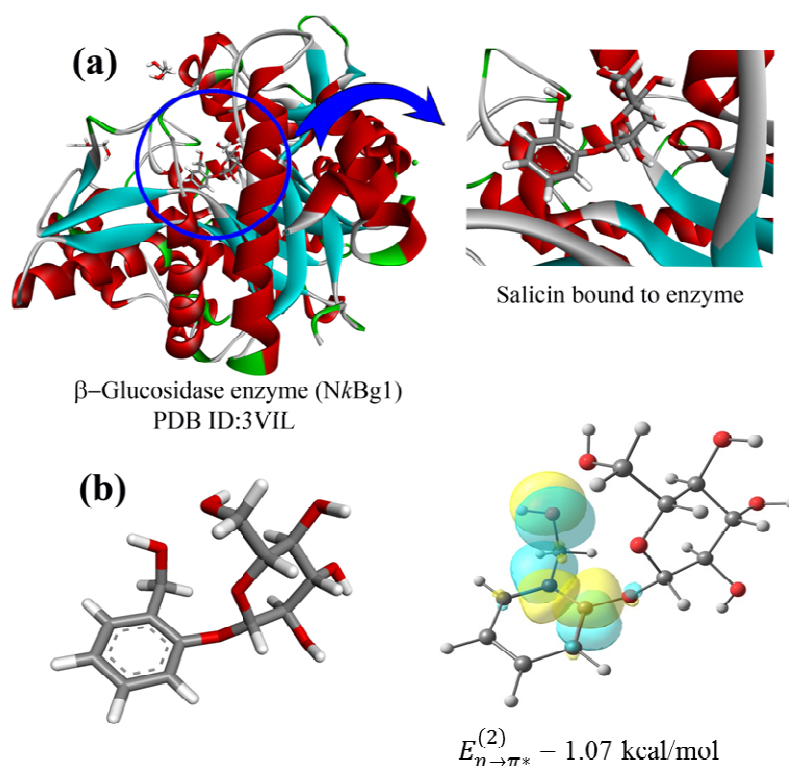


Figure 6.10. (a) X-ray crystal structure of the β-Glucosidase enzyme...salicin complex (PDB ID: 3VIL). (b) Structure of salicin in the enzyme bound state and one of its NBOs showing an n→π* interaction between the oxygen atom of the benzylic OH and the aromatic ring. The electron density has been calculated at the M06-2X/6-311++G(d,p) level of theory.

salicin...β-glucosidase complex carried out at the M06-2X/6-311++G(d,p) level provides an n→π* interaction energy of 1.07 kcal/mol, which is similar to that presented in Table 6.6 for isolated salicin. The PDB structure highlighting the binding pocket of the enzyme with salicin and NBOs of the salicin moiety are presented in Figure 6.10.

The propensity of the $n \rightarrow \pi^*$ interaction and hydrogen bonds to both stabilize and influence the shape of protein structures has been pointed out by Raines and coworkers as a result of analyzing the crystal structure of proteins in the PDB.^{7,12} Hydrogen bonding ($n \rightarrow \sigma^*$) and $n \rightarrow \pi^*$ interactions are interrelated as both interactions originate from the delocalization of lone pair electrons. In proteins, mostly in α -helices, lone pair electrons of the same oxygen atom of a C=O group are often shared by both hydrogen bonding and an $n \rightarrow \pi^*$ interaction. For example, there is a 50:50 sharing of the p-type lone pair electrons of the carbonyl oxygen atom by the hydrogen bond and the $n \rightarrow \pi^*$ interaction in the asparagine residues of a human carbonic anhydrase-II protein (PDB ID: 3KS3).¹² Similar results were obtained for the salicin in this work. In the case of the three observed conformers of salicin, p-type lone pair electrons on the oxygen atom of the benzylic alcohol moiety participate in both O...H-O hydrogen bonding and the $n \rightarrow \pi^*$ interaction. It is also observed that the strength of the hydrogen bond in the three observed conformers of salicin decreases due to the presence of a significant amount of $n \rightarrow \pi^*$ interaction compared to that in the other conformers of salicin.

6.3 Conclusion

Conformational preferences of salicin induced by the $n \rightarrow \pi^*$ interactions in the presence of multiple hydrogen bonding interactions have been studied using isolated gas phase electronic and vibrational spectroscopy combined with quantum chemistry calculations. Three low energy conformers of salicin, which are observed in the experiment, have a significant amount of $n \rightarrow \pi^*$ interaction along with the hydrogen bonding interactions when compared to other higher energy conformers. The latter have stronger hydrogen bonding interactions, but weaker $n \rightarrow \pi^*$ interactions. Sharing of lone pair electrons on a single oxygen atom between hydrogen bonding and $n \rightarrow \pi^*$ interactions reported for the stabilization of protein structures has also been observed in salicin here. Thus, the present research suggests that the presence of a hydrogen bonding interaction in a molecular system

can very often indicate the possibility of the existence of a $n \rightarrow \pi^*$ interaction as these two non-covalent interactions are quite analogous in terms of electron delocalization. This indicates that the $n \rightarrow \pi^*$ interaction should be incorporated into the simulation of biomolecules to obtain more accurate results for their structures and dynamics.

The present work also adds further evidence of competition and cooperation between weak intermolecular interactions in determining the low-energy conformers of floppy drug molecules. In this case a compromise in the strength of the hydrogen bonding interaction favours the $n \rightarrow \pi^*$ interaction in the overall stability of the molecular structures. Another intriguing finding of this study is that the conformational preference of the gauche conformer of either isolated benzyl alcohol or the benzyl alcohol moiety of salicin over the trans conformer is not due to the O-H... π interaction, but rather an $n \rightarrow \pi^*$ interaction. Therefore, it is proposed that the $n \rightarrow \pi^*$ interaction could have a significant contribution in the stabilization of molecular systems that have previously been reported to be stabilized by O-H... π interactions. The contribution of the $n \rightarrow \pi^*$ interaction in O-H... π bound systems has largely been overlooked in previous studies. In future, it will be interesting to reinvestigate systems containing O-H... π interactions to probe for the presence of an $n \rightarrow \pi^*$ interaction there.



Chapter 7

SUMMARY AND FUTURE
DIRECTION

Summary:

In summary, we have studied $n \rightarrow \pi^*$ interaction in various molecular systems (7-azaindole...2,6-substituted fluoropyridines, phenyl formate, Cbz-Hyp-OMe, and salicin) in the gas phase using R2PI, RIDIRS, IR-UV hole-burn and UV-UV hole-burn spectroscopic techniques combined with quantum chemistry calculations.

We have investigated the interplay between hydrogen bonding and $n \rightarrow \pi^*$ interaction in the complexes of 7-AI and 2,6-substituted fluoropyridines by probing the strength of the N-H...N hydrogen bonding interaction present there. The $n \rightarrow \pi^*$ and hydrogen bonding interactions present in the complexes are strongly interrelated because one interaction affects the strength of the other. Even though $n \rightarrow \pi^*$ interaction is weaker in strength compared to hydrogen bonding, the former interaction modulate the overall structural motif of the complexes. This study provides an experimental evidence for the interplay between hydrogen bonding and $n \rightarrow \pi^*$ interaction through the study of a model complex. Interplay between these two energetically disparate non-covalent interactions has been reported earlier in proteins on the basis of crystal structure analysis in the protein data bank (PDB). The present study of $n \rightarrow \pi^*$ interaction as an intermolecular non-covalent interaction shows that it can exist in a molecular moiety independently and it is not just a short contact imposed by geometric constraint of the macromolecular system. This study demonstrates an indirect spectroscopic approach to show the evidence of $n \rightarrow \pi^*$ interaction in the complex. However, direct spectroscopic signature of $n \rightarrow \pi^*$ interaction in a molecular moiety is more desirable.

Direct spectroscopic signature for an $n \rightarrow \pi^*$ interaction has been achieved by probing the C=O stretching frequency of phenyl formate using gas phase IR spectroscopy. We have observed two conformers (cis and trans) of phenyl formate in the experiment. The cis conformer having $n \rightarrow \pi^*_{Ar}$ interaction between the C=O group and the aromatic ring shows red-shift in the C=O stretching frequency relative to that of the trans conformer where

$n \rightarrow \pi_{Ar}^*$ interaction is absent. This study provides the first gas phase IR spectroscopic evidence of the $n \rightarrow \pi_{Ar}^*$ interaction in a molecular moiety.

Later, we have used the same gas-phase IR spectroscopic technique to show the evidence of $n \rightarrow \pi_{Am}^*$ interaction between two carbonyl groups ($C=O \dots C=O$), which is widely present in proteins including collagen. For this study, we chose carboxybenzyl(Cbz)-Hyp-OMe, a proline derivative, which is an important amino acid residue of collagen. Four conformers of Cbz-Hyp-OMe are observed in the experiment. Two of the observed conformers have trans orientation of the amide bond with $n \rightarrow \pi^*$ interaction while the other two conformers have cis orientation of the amide bond with no $n \rightarrow \pi^*$ interaction between the neighboring carbonyl groups. The stretching frequencies of both the carbonyl groups of the trans conformers show red-shift relative to those of the cis conformers due to the presence of $n \rightarrow \pi^*$ interaction in the former conformers. This study shows the first IR spectroscopic evidence of the $n \rightarrow \pi_{Am}^*$ interaction present in the most important amino acid residue of collagen and PP-II helix. The $n \rightarrow \pi_{Ar}^*$ or $n \rightarrow \pi_{Am}^*$ interactions in a molecular system has been probed directly by measuring the red-shift in the stretching frequency of the carbonyl group of the conformer which has $n \rightarrow \pi^*$ interaction relative to that of the conformer with no $n \rightarrow \pi^*$ interaction. These studies on model systems also demonstrate the importance of $n \rightarrow \pi^*$ interaction in governing the conformational preferences. However, it is more desirable to study the role of $n \rightarrow \pi^*$ interaction in governing the structures and functions of molecules which have biological significance using similar spectroscopic techniques.

Therefore, we have studied the conformational preferences of an analgesics drug salicin in isolated gas phase using R2PI, IR-UV and UV-UV double resonance spectroscopic techniques. Salicin, also known as “nature’s aspirin”, has been used as a medicine for the treatment of pain, fever, as well as inflammation in our body and it is obtained naturally from

the bark of the willow tree. We have observed three lowest energy conformers of salicin in our experiment. All the three conformers observed in the experiment have significant amount of $n \rightarrow \pi^*$ interaction energy along with the hydrogen bonding interaction. Other higher energy conformers of salicin having relatively stronger hydrogen bonding interaction but weaker $n \rightarrow \pi^*$ interaction are not observed in the experiment. This shows that $n \rightarrow \pi^*$ interaction play a vital role in governing the conformational preferences of salicin even in the presence of strong hydrogen bonding interaction. The $n \rightarrow \pi^*$ interaction in the structure of salicin is retained even when the salicin is bound to glycosidase enzyme. Another significant finding of this study is that the $n \rightarrow \pi^*$ interaction in comparison to the $O-H \dots \pi$ interaction may have significant contribution to the stability of the gauche conformer of either isolated benzyl alcohol or the benzyl alcohol moiety of salicin over the trans conformer.

Future perspective:

In future, it will be interesting to investigate the $n \rightarrow \pi^*$ interaction in the repeating sequence of collagen (XaaYaaGly) triple helix, where Xaa is usually proline (Pro) and Yaa is 4R-Hydroxyproline (Hyp), using gas-phase spectroscopic techniques. Figure 7.1 shows the crystal structure of Pro-Hyp-Gly sequence of collagen. To study the electronic spectroscopy,

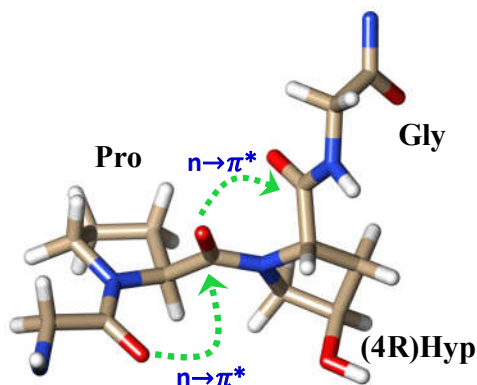


Figure 7.1 Crystal structure of Pro-Hyp-Gly sequence of collagen triple helix (PDB ID – 1CAG).

an aromatic chromophore will be attached with the tripeptide. It has been reported that $n \rightarrow \pi^*$

interaction is present all along the poly peptide chain of the collagen triple helix. Further, the position of Hyp in the tripeptide sequence is very crucial in the stability of the helical structure. For example if the positions of Hyp and Pro are interchanged, the helical structure of the collagen is lost. Similarly, if the 4R-hydroxyproline is replaced with 4S-hydroxyproline (hyp) in the peptide sequence of collagen, the helical structure is not retained. We want to study the structures of ProHypGly and HypProGly sequences to investigate the effect on the strength of $n \rightarrow \pi^*$ interaction upon changing the position of Hyp, using gas-phase spectroscopic techniques and quantum chemical calculations.

Strength of the $n \rightarrow \pi^*$ interaction is weak compared to that of other non-covalent interactions. Therefore, it is challenging to probe this interaction in a given molecular moiety. It will be interesting to investigate the ways to increase the strength of the $n \rightarrow \pi^*$ interaction. One of the ways is to induce geometric constraint on the donor atom and acceptor group to have better overlap of lone pair and π^* orbitals. One such example is shown in Figure 7.2(a)

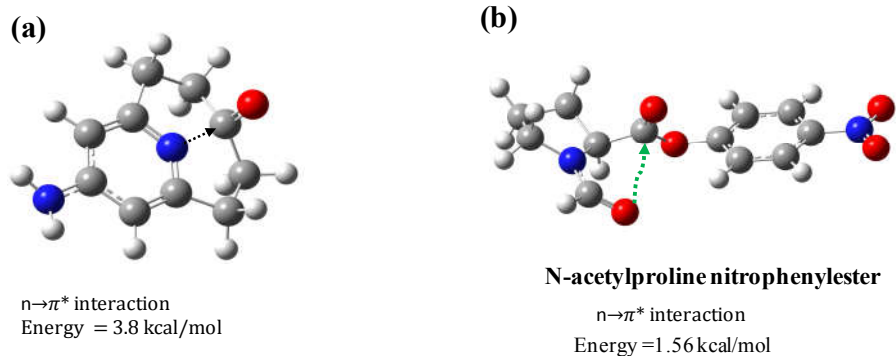


Figure 7.2 (a) Calculated structure of a molecule showing close proximity between donor nitrogen atom and acceptor carbonyl C=O group which is imposed by geometrical constraint of the molecule. Structure is calculated at the M05-2X/aVDZ level of theory. (b) is the calculated structure of N-acetylproline nitrophenylester at the M05-2X/cc-pVTZ level of theory.

where the nitrogen atom and the acceptor carbonyl group are in a geometric constraint that allows better overlap of lone pair orbital of nitrogen atom and π^* orbital of the carbonyl

group. The $n \rightarrow \pi^*$ interaction energy in this molecule is about 3.8 kcal/mol. Another way to enhance the $n \rightarrow \pi^*$ interaction is to include electron withdrawing substituents on the acceptor side. Electron withdrawing groups make the acceptor group more electrophilic and hence better electron pair acceptor. Figure 7.2 (b) shows calculated structure of N-acetylproline nitrophenylester where, nitro group is substituted on the phenyl ring to make the acceptor carbon more electrophilic. Similarly one choose different functional groups substitution on the acceptor carbonyl group to tune the strength of $n \rightarrow \pi^*$ interaction.

On the theoretical front, extensive computational studies are required for detailed understanding of the physical nature of the $n \rightarrow \pi^*$ non-covalent interaction.

References

- (1) Gorske, B. C.; Bastian, B. L.; Geske, G. D.; Blackwell, H. E. Local and tunable $n \rightarrow \pi^*$ interactions regulate amide isomerism in the peptoid backbone. *J. Am. Chem. Soc.* **2007**, *129*, 8928-8929.
- (2) Newberry, R. W.; Raines, R. T. The $n \rightarrow \pi^*$ Interaction. *Acc. Chem. Res.* **2017**, *50*, 1838-1846.
- (3) Egli, M.; Sarkhel, S. Lone Pair–Aromatic Interactions: To Stabilize or Not to Stabilize. *Acc. Chem. Res.* **2007**, *40*, 197-205.
- (4) Jain, A.; Ramanathan, V.; Sankararamakrishnan, R. Lone pair $\cdots \pi$ interactions between water oxygens and aromatic residues: Quantum chemical studies based on high-resolution protein structures and model compounds. *Protein Sci.* **2009**, *18*, 595-605.
- (5) Jain, A.; Purohit, C. S.; Verma, S.; Sankararamakrishnan, R. Close contacts between carbonyl oxygen atoms and aromatic centers in protein structures: $\pi \cdots \pi$ or lone-pair $\cdots \pi$ interactions? *J. Phys. Chem. B* **2007**, *111*, 8680-8683.
- (6) Pal, T. K.; Sankararamakrishnan, R. Quantum chemical investigations on intraresidue carbonyl - carbonyl contacts in aspartates of high-resolution protein structures. *J. Phys. Chem. B* **2010**, *114*, 1038-1049.
- (7) Bartlett, G. J.; Choudhary, A.; Raines, R. T.; Woolfson, D. N. $n \rightarrow \pi^*$ interactions in proteins. *Nat. Chem. Biol.* **2010**, *6*, 615-620.
- (8) Egli, M.; Gessner, R. V. Stereoelectronic effects of deoxyribose O4' on DNA conformation. *Proc. Natl. Acad. Sci. U.S.A.* **1995**, *92*, 180-184.
- (9) Jain, A.; Krishna Deepak, R. N. V.; Sankararamakrishnan, R. Oxygen–aromatic contacts in intra-strand base pairs: Analysis of high-resolution DNA crystal structures and quantum chemical calculations. *J. Struct. Biol.* **2014**, *187*, 49-57.
- (10) DeRider, M. L.; Wilkens, S. J.; Waddell, M. J.; Bretscher, L. E.; Weinhold, F.; Raines, R. T.; Markley, J. L. Collagen stability: Insights from NMR spectroscopic and hybrid density functional computational investigations of the effect of electronegative substituents on prolyl ring conformations. *J. Am. Chem. Soc.* **2002**, *124*, 2497-2505.
- (11) Mooibroek, T. J.; Gamez, P.; Reedijk, J. Lone pair- π interactions: A new supramolecular bond? *CrystEngComm* **2008**, *10*, 1501-1515.
- (12) Bartlett, G. J.; Newberry, R. W.; VanVeller, B.; Raines, R. T.; Woolfson, D. N. Interplay of Hydrogen Bonds and $n \rightarrow \pi^*$ Interactions in Proteins. *J. Am. Chem. Soc.* **2013**, *135*, 18682-18688.
- (13) Hodges, J. A.; Raines, R. T. Energetics of an $n \rightarrow \pi^*$ interaction that impacts protein structure. *Org. Lett.* **2006**, *8*, 4695-4697.
- (14) Desiraju, G. R.; Steiner, T. *The Weak Hydrogen Bond in Structural Chemistry and Biology*; Oxford University Press, New York, 1999.
- (15) Jeffrey, G. A.; Saenger, W. *Hydrogen Bonding in Biological Structures*; Springer: Berlin, 1991.
- (16) Jeffrey, G. A. *An Introduction to Hydrogen Bonding*; Oxford University Press: New York, 1997.
- (17) Steed, J. W.; Atwood, J. L. *Supramolecular Chemistry: A Concise Introduction*; John Wiley & Sons Inc, New York, 2000.
- (18) Lehn, J.-M. *Supramolecular Chemistry: Concepts and Perspectives*; John Wiley & Sons, New York, 1996.

- (19) Anfinsen, C. B. Principles That Govern Folding of Protein Chains. *Science* **1973**, *181*, 223-230.
- (20) Saenger, W. *Principles of Nucleic Acid Structure*; Springer-Verlag: New York, 1984.
- (21) Salonen, L. M.; Ellermann, M.; Diederich, F. Aromatic Rings in Chemical and Biological Recognition: Energetics and Structures. *Angew. Chem. Int. Ed.* **2011**, *50*, 4808-4842.
- (22) Desiraju, G. R. Supramolecular Synthons in Crystal Engineering—A New Organic Synthesis. *Angew. Chem. Int. Ed.* **1995**, *34*, 2311-2327.
- (23) Desiraju, G. R. Crystal engineering: From molecule to crystal. *J. Am. Chem. Soc.* **2013**, *135*, 9952-9967.
- (24) Burley, S. K.; Petsko, G. A. Weakly Polar Interactions In Proteins. *Adv. Protein Chem.* **1988**, *39*, 125-189.
- (25) Desiraju, G. R. Crystal Engineering: A Holistic View. *Angew. Chem. Int. Ed.* **2007**, *46*, 8342-8356.
- (26) Karshikoff, A. *Non-covalent Interactions in Proteins*; Imperial College Press, 2006.
- (27) Burley, S. K.; Petsko, G. A. Aromatic-aromatic interaction: a mechanism of protein structure stabilization. *Science* **1985**, *229*, 23-28.
- (28) Dougherty, D. A. The cation- π interaction. *Acc. Chem. Res.* **2013**, *46*, 885-893.
- (29) Ma, J. C.; Dougherty, D. A. The Cation- π Interaction. *Chem. Rev.* **1997**, *97*, 1303-1324.
- (30) Chifotides, H. T.; Dunbar, K. R. Anion- π Interactions in Supramolecular Architectures. *Acc. Chem. Res.* **2013**, *46*, 894-906.
- (31) Frontera, A.; Gamez, P.; Mascal, M.; Mooibroek, T. J.; Reedijk, J. Putting Anion- π Interactions Into Perspective. *Angew. Chem. Int. Ed.* **2011**, *50*, 9564-9583.
- (32) Seo, J.-I.; Kim, I.; Lee, Y. S. π - π Interaction energies in monosubstituted-benzene dimers in parallel- and antiparallel-displaced conformations. *Chem. Phys. Lett.* **2009**, *474*, 101-106.
- (33) Tiekink, E. R. T.; Zuckerman-Schpector, J. *The Importance of π -Interactions in Crystal Engineering: Frontiers in Crystal Engineering*; John Wiley and Sons, New York, 2012.
- (34) Hunter, C. A. Meldola Lecture. The role of aromatic interactions in molecular recognition. *Chem. Soc. Rev.* **1994**, *23*, 101-109.
- (35) Sinnokrot, M. O.; Sherrill, C. D. Substituent effects in π - π interactions: sandwich and T-shaped configurations. *J. Am. Chem. Soc.* **2004**, *126*, 7690-7697.
- (36) Scheiner, S. *Hydrogen Bonding. A Theoretical Perspective*; Oxford University Press: Oxford, 1997.
- (37) Dougherty, D. A. Cation- π interactions involving aromatic amino acids. *Journal of Nutrition* **2007**, *137*, 1504S-1508S.
- (38) Nishio, M. The CH/[small pi] hydrogen bond in chemistry. Conformation, supramolecules, optical resolution and interactions involving carbohydrates. *Phys. Chem. Chem. Phys.* **2011**, *13*, 13873-13900.
- (39) Nishio, M.; Umezawa, Y.; Fantini, J.; Weiss, M. S.; Chakrabarti, P. CH-[small pi] hydrogen bonds in biological macromolecules. *Phys. Chem. Chem. Phys.* **2014**, *16*, 12648-12683.

- (40) Pfaffen, C.; Frey, H.-M.; Ottiger, P.; Leutwyler, S.; Bachorz, R. A.; Kloppe, W. Large-amplitude vibrations of an N–H... π hydrogen bonded cis-amide-benzene complex. *Phys. Chem. Chem. Phys.* **2010**, *12*, 8208-8218.
- (41) Steiner, T.; Koellner, G. Hydrogen bonds with π -acceptors in proteins: frequencies and role in stabilizing local 3D structures. *J. Mol. Biol.* **2001**, *305*, 535-557.
- (42) Neel, A. J.; Hilton, M. J.; Sigman, M. S.; Toste, F. D. Exploiting non-covalent π interactions for catalyst design. *Nature* **2017**, *543*, 637-646.
- (43) Quiñero, D.; Garau, C.; Rotger, C.; Frontera, A.; Ballester, P.; Costa, A.; Deyà, P. M. Anion– π Interactions: Do They Exist? *Angew. Chem. Int. Ed.* **2002**, *41*, 3389-3392.
- (44) Hunter, C. A.; Sanders, J. K. M. The nature of π - π interactions. *J. Am. Chem. Soc.* **1990**, *112*, 5525-5534.
- (45) Cockroft, S. L.; Perkins, J.; Zonta, C.; Adams, H.; Spey, S. E.; Low, C. M. R.; Vinter, J. G.; Lawson, K. R.; Urch, C. J.; Hunter, C. A. Substituent effects on aromatic stacking interactions. *Org. Biomol. Chem.* **2007**, *5*, 1062-1080.
- (46) Arunan, E.; Desiraju, G. R.; Klein, R. A.; Sadlej, J.; Scheiner, S.; Alkorta, I.; Clary, D. C.; Crabtree, R. H.; Dannenber, J. J.; Hobza, P.; Kjaergaard, H. G.; Legon, A. C.; Mennucci, B.; Nesbitt, D. J. Definition of the hydrogen bond (IUPAC Recommendations 2011). *Pure and Applied Chemistry* **2011**, *83*, 1637-1641.
- (47) Ottiger, P.; Pfaffen, C.; Leist, R.; Leutwyler, S.; Bachorz, R. A.; Kloppe, W. Strong N–H... π Hydrogen Bonding in Amide–Benzene Interactions. *J. Phys. Chem. B* **2009**, *113*, 2937-2943.
- (48) Kumar, S.; Das, A. Mimicking trimeric interactions in the aromatic side chains of the proteins: A gas phase study of indole...(pyrrole)₂ heterotrimer. *J. Chem. Phys.* **2012**, *136*, 174302-174309.
- (49) Sinnokrot, M. O.; Sherrill, C. D. High-Accuracy Quantum Mechanical Studies of π - π Interactions in Benzene Dimers. *J. Phys. Chem. A* **2006**, *110*, 10656-10668.
- (50) Wagner, J. P.; Schreiner, P. R. London Dispersion in Molecular Chemistry—Reconsidering Steric Effects. *Angew. Chem. Int. Ed.* **2015**, *54*, 12274-12296.
- (51) Wheeler, S. E. Understanding Substituent Effects in Noncovalent Interactions Involving Aromatic Rings. *Acc. Chem. Res.* **2012**, *46*, 1029-1038.
- (52) Mecozzi, S.; West, A. P.; Dougherty, D. A. Cation– π Interactions in Simple Aromatics: Electrostatics Provide a Predictive Tool. *J. Am. Chem. Soc.* **1996**, *118*, 2307-2308.
- (53) Singh, S. K.; Das, A. The $n \rightarrow \pi^*$ interaction: a rapidly emerging non-covalent interaction. *Phys. Chem. Chem. Phys.* **2015**, *17*, 9596-9612.
- (54) Jenkins, C. L.; Raines, R. T. Insights on the conformational stability of collagen. *Nat. Prod. Rep.* **2002**, *19*, 49-59.
- (55) Sarkhel, S.; Rich, A.; Egli, M. Water-nucleobase "stacking": H– π and lone pair– π interactions in the atomic resolution crystal structure of an RNA pseudoknot. *J. Am. Chem. Soc.* **2003**, *125*, 8998-8999.
- (56) Choudhary, A.; Raines, R. T. Signature of $n \rightarrow \pi^*$ interactions in α -helices. *Protein Sci.* **2011**, *20*, 1077-1081.
- (57) Newberry, R. W.; Bartlett, G. J.; VanVeller, B.; Woolfson, D. N.; Raines, R. T. Signatures of $n \rightarrow \pi^*$ interactions in proteins. *Protein Sci.* **2014**, *23*, 284-288.
- (58) Choudhary, A.; Gandla, D.; Krow, G. R.; Raines, R. T. Nature of amide carbonyl-carbonyl interactions in proteins. *J. Am. Chem. Soc.* **2009**, *131*, 7244-7246.

- (59) Hodgest, J. A.; Raines, R. T. Stereoelectronic effects on collagen stability: The dichotomy of 4-fluoroproline diastereomers. *J. Am. Chem. Soc.* **2003**, *125*, 9262-9263.
- (60) Newberry, R. W.; VanVeller, B.; Guzei, I. A.; Raines, R. T. $n \rightarrow \pi^*$ Interactions of Amides and Thioamides: Implications for Protein Stability. *J. Am. Chem. Soc.* **2013**, *135*, 7843-7846.
- (61) Newberry, R. W.; Raines, R. T. A Key $n \rightarrow \pi^*$ Interaction in N-Acyl Homoserine Lactones. *ACS Chem. Biol.* **2014**, *9*, 880-883.
- (62) Newberry, R. W.; Raines, R. T. $N \rightarrow \pi^*$ interactions in poly(lactic acid) suggest a role in protein folding. *Chem Commun* **2013**, *49*, 7699-7701.
- (63) Choudhary, A.; Kamer, K. J.; Raines, R. T. An $n \rightarrow \pi^*$ interaction in Aspirin: Implications for structure and reactivity. *J. Org. Chem.* **2011**, *76*, 7933-7937.
- (64) Jakobsche, C. E.; Choudhary, A.; Miller, S. J.; Raines, R. T. $N \rightarrow \phi^*$ Interaction and $n(\phi)$ Pauli repulsion are antagonistic for protein stability. *J. Am. Chem. Soc.* **2010**, *132*, 6651-6653.
- (65) Kamer, K. J.; Choudhary, A.; Raines, R. T. Intimate interactions with carbonyl groups: Dipole-dipole or $n \rightarrow \pi^*$? *J. Org. Chem.* **2013**, *78*, 2099-2103.
- (66) Choudhary, A.; Fry, C. G.; Raines, R. T. Modulation of an np^* interaction with α -fluoro groups. *Arkivoc* **2010**, *2010*, 251-262.
- (67) Choudhary, A.; Newberry, R. W.; Raines, R. T. $n \rightarrow \pi^*$ Interactions Engender Chirality in Carbonyl Groups. *Org. Lett.* **2014**, *16*, 3421-3423.
- (68) Fufezan, C. The role of Bürgi-Dunitz interactions in the structural stability of proteins. *Proteins: Structure, Function and Bioinformatics* **2010**, *78*, 2831-2838.
- (69) Shoulders, M. D.; Kotch, F. W.; Choudhary, A.; Guzei, I. A.; Raines, R. T. The aberrance of the 4S diastereomer of 4-hydroxyproline. *J. Am. Chem. Soc.* **2010**, *132*, 10857-10865.
- (70) Gorske, B. C.; Nelson, R. C.; Bowden, Z. S.; Kufe, T. A.; Childs, A. M. "Bridged" $n \rightarrow \pi^*$ Interactions Can Stabilize Peptoid Helices. *J. Org. Chem.* **2013**, *78*, 11172-11183.
- (71) Hinderaker, M. P.; Raines, R. T. An electronic effect on protein structure. *Protein Sci.* **2003**, *12*, 1188-1194.
- (72) Cabezas, C.; Alonso, J. L.; López, J. C.; Mata, S. Unveiling the shape of aspirin in the gas phase. *Angew. Chem. Int. Ed.* **2012**, *51*, 1375-1378.
- (73) Lesarri, A.; Cocinero, E. J.; López, J. C.; Alonso, J. L. Shape of 4(S)- and 4(R)-hydroxyproline in gas phase. *J. Am. Chem. Soc.* **2005**, *127*, 2572-2579.
- (74) Sanz, M. E.; Lesarri, A.; Peña, M. I.; Vaquero, V.; Cortijo, V.; López, J. C.; Alonso, J. L. The shape of β -alanine. *J. Am. Chem. Soc.* **2006**, *128*, 3812-3817.
- (75) Blanco, S.; López, J. C.; Mata, S.; Alonso, J. L. Conformations of γ -aminobutyric acid (gaba): The role of the $n \rightarrow \pi^*$ interaction. *Angew. Chem. Int. Ed.* **2010**, *49*, 9187-9192.
- (76) Shoulders, M. D.; Raines, R. T. Modulating collagen triple-helix stability with 4-chloro, 4-fluoro, and 4-methylprolines. *Advances in experimental medicine and biology* **2009**, *611*, 251-252.
- (77) Singh, S. K.; Kumar, S.; Das, A. Competition between n [rightward arrow] [small pi]Ar* and conventional hydrogen bonding (N-HN) interactions: an ab initio study of the complexes of 7-azaindole and fluorosubstituted pyridines. *Phys. Chem. Chem. Phys.* **2014**, *16*, 8819-8827.

- (78) Singh, S. K.; Vaishnav, J. K.; Das, A. Experimental observation of structures with subtle balance between strong hydrogen bond and weak $n \rightarrow \pi^*$ interaction: Gas phase laser spectroscopy of 7-azaindole...fluorosubstituted pyridines. *J. Chem. Phys.* **2016**, *145*, 104302.
- (79) Singh, S. K.; Mishra, K. K.; Sharma, N.; Das, A. Direct spectroscopic evidence of $n\text{-}\pi^*$ interaction. *Angew. Chem. Int. Ed.* **2016**, DOI: 10.1002/anie.201511925
- (80) Mooibroek, T. J.; Teat, S. J.; Massera, C.; Gamez, P.; Reedijk, J. Crystallographic and Theoretical Evidence of Acetonitrile- π Interactions with the Electron-Deficient 1,3,5-Triazine Ring. *Cryst. Growth Des.* **2006**, *6*, 1569-1574.
- (81) Costa, J. S.; Castro, A. G.; Pievo, R.; Roubeau, O.; Modéc, B.; Kozlevcar, B.; Teat, S. J.; Gamez, P.; Reedijk, J. Proficiency of the electron-deficient 1,3,5-triazine ring to generate anion- π and lone pair- π interactions. *CrystEngComm* **2010**, *12*, 3057-3064.
- (82) Newberry, R. W.; Orke, S. J.; Raines, R. T. $n \rightarrow \pi^*$ Interactions Are Competitive with Hydrogen Bonds. *Org. Lett.* **2016**, *18*, 3614-3617.
- (83) Rahim, A.; Saha, P.; Jha, K. K.; Sukumar, N.; Sarma, B. K. Reciprocal carbonyl-carbonyl interactions in small molecules and proteins. *Nat. Commun.* **2017**, *8*.
- (84) Bella, J.; Eaton, M.; Brodsky, B.; Berman, H. Crystal and molecular structure of a collagen-like peptide at 1.9 Å resolution. *Science* **1994**, *266*, 75-81.
- (85) Kuemin, M.; Nagel, Y. A.; Schweizer, S.; Monnard, F. W.; Ochsenfeld, C.; Wennemers, H. Tuning the cis/trans Conformer Ratio of Xaa-Pro Amide Bonds by Intramolecular Hydrogen Bonds: The Effect on PPII Helix Stability. *Angew. Chem. Int. Ed.* **2010**, *49*, 6324-6327.
- (86) Wilhelm, P.; Lewandowski, B.; Trapp, N.; Wennemers, H. A Crystal Structure of an Oligoproline PPII-Helix, at Last. *J. Am. Chem. Soc.* **2014**, *136*, 15829-15832.
- (87) Holmgren, S. K.; Taylor, K. M.; Bretscher, L. E.; Raines, R. T. Code for collagen's stability deciphered [9]. *Nature* **1998**, *392*, 666-667.
- (88) Lu, Z.; Gamez, P.; Mutikainen, I.; Turpeinen, U.; Reedijk, J. Supramolecular assemblies generated from both lone-pair... π and C-H... π binding interactions. *Cryst. Growth Des.* **2007**, *7*, 1669-1671.
- (89) Costa, J. S.; Castro, A. G.; Pievo, R.; Roubeau, O.; Modéc, B.; Kozlevčar, B.; Teat, S. J.; Gamez, P.; Reedijk, J. Proficiency of the electron-deficient 1,3,5-triazine ring to generate anion- π and lone pair- π interactions. *CrystEngComm* **2010**, *12*, 3057-3064.
- (90) Das, A.; Choudhury, S. R.; Estarellas, C.; Dey, B.; Frontera, A.; Hemming, J.; Helliwell, M.; Gamez, P.; Mukhopadhyay, S. Supramolecular assemblies involving anion-[small pi] and lone pair-[small pi] interactions: experimental observation and theoretical analysis. *CrystEngComm* **2011**, *13*, 4519-4527.
- (91) Biswas, C.; Drew, M. G. B.; Escudero, D.; Frontera, A.; Ghosh, A. Anion- π , lone-Pair- π , π - π and hydrogen-bonding interactions in a Cu^{II} Complex of 2-picolinate and protonated 4,4-bipyridine: Crystal structure and theoretical studies. *Eur J Inorg Chem* **2009**, 2238-2246.
- (92) Caracelli, I.; Haiduc, I.; Zukerman-Schpector, J.; Tiekink, E. R. T. Delocalised antimony(lone pair)- and bismuth-(lone pair)... π (arene) interactions: Supramolecular assembly and other considerations. *Coordination Chemistry Reviews* **2013**, *257*, 2863-2879.
- (93) Caracelli, I.; Zukerman-Schpector, J.; Tiekink, E. R. T. Supramolecular aggregation patterns based on the bio-inspired Se(lone pair)... π (aryl) synthon. *Coord. Chem. Rev.* **2012**, *256*, 412-438.

- (94) Gorske, B. C.; Stringer, J. R.; Bastian, B. L.; Fowler, S. A.; Blackwell, H. E. New strategies for the design of folded peptoids revealed by a survey of noncovalent interactions in model systems. *J. Am. Chem. Soc.* **2009**, *131*, 16555-16567.
- (95) Gallivan, J. P.; Dougherty, D. A. Can Lone Pairs Bind to a π System? The Water...Hexafluorobenzene Interaction. *Org. Lett.* **1999**, *1*, 103-106.
- (96) Gung, B. W.; Zou, Y.; Xu, Z.; Amicangelo, J. C.; Irwin, D. G.; Ma, S.; Zhou, H. C. Quantitative study of interactions between oxygen lone pair and aromatic rings: Substituent effect and the importance of closeness of contact. *J. Org. Chem.* **2008**, *73*, 689-693.
- (97) Amicangelo, J. C.; Gung, B. W.; Irwin, D. G.; Romano, N. C. Ab initio study of substituent effects in the interactions of dimethyl ether with aromatic rings. *Phys. Chem. Chem. Phys.* **2008**, *10*, 2695-2705.
- (98) Yang, T.; An, J. J.; Wang, X.; Wu, D. Y.; Chen, W.; Fossey, J. S. A theoretical exploration of unexpected amine... π interactions. *Phys. Chem. Chem. Phys.* **2012**, *14*, 10747-10753.
- (99) Cabaleiro-Lago, E. M.; Carrazana-García, J. A.; Rodríguez-Otero, J. Study of the interaction between water and hydrogen sulfide with polycyclic aromatic hydrocarbons. *J. Chem. Phys.* **2009**, *130*, 234307.
- (100) Rubeš, M.; Nachtigall, P.; Vondrášek, J.; Bludský, O. Structure and Stability of the Water-Graphite Complexes. *J. Phys. Chem. C* **2009**, *113*, 8412-8419.
- (101) Gung, B. W.; Xue, X.; Reich, H. J. Off-center oxygen-arene interactions in solution: A quantitative study. *J. Org. Chem.* **2005**, *70*, 7232-7237.
- (102) Levy, D. H. Laser Spectroscopy of Cold Gas-Phase Molecules. *Annual Review of Physical Chemistry* **1980**, *31*, 197-225.
- (103) Smalley, R. E.; Wharton, L.; Levy, D. H. Molecular optical spectroscopy with supersonic beams and jets. *Acc. Chem. Res.* **1977**, *10*, 139-145.
- (104) Levy, D. H. The spectroscopy of very cold gases. *Science* **1981**, *214*, 263-269.
- (105) Anderson, J. B.; Fenn, J. B. Velocity Distributions in Molecular Beams from Nozzle Sources. *The Physics of Fluids* **1965**, *8*, 780-787.
- (106) Wiley, W. C.; McLaren, I. H. Time - of - Flight Mass Spectrometer with Improved Resolution. *Review of Scientific Instruments* **1955**, *26*, 1150-1157.
- (107) Duarte, F. J. K., P.; Hillman, L. W.; Liao, P. F. *Dye laser principles*; Elsevier Science, 2012.
- (108) Liao, P. F. K., P.; Duarte, F. J.; Hillman, L. W. *Dye Laser Principles: With Applications*; Elsevier, 2012.
- (109) Sorokin, P. L., J. *IBM J. Res. Dev.* **1966**, *10*.
- (110) Piuze, F.; Dimicoli, I.; Mons, M.; Tardivel, B.; Zhao, Q. A simple laser vaporization source for thermally fragile molecules coupled to a supersonic expansion: application to the spectroscopy of tryptophan. *Chem. Phys. Lett.* **2000**, *320*, 282-288.
- (111) Meijer, G.; de Vries, M. S.; Hunziker, H. E.; Wendt, H. R. Laser desorption jet-cooling of organic molecules. *Applied Physics B* **1990**, *51*, 395-403.
- (112) Dean, J. C.; Buchanan, E. G.; Zwier, T. S. Mixed 14/16 Helices in the Gas Phase: Conformation-Specific Spectroscopy of Z-(Gly)(n), n=1, 3, 5. *J. Am. Chem. Soc.* **2012**, *134*, 17186-17201.
- (113) Hall, R. B. Pulsed-laser-induced desorption studies of the kinetics of surface reactions. *J. Phys. Chem.* **1987**, *91*, 1007-1015.
- (114) Lubman, D. M. Optically selective molecular mass spectrometry. *Anal Chem* **1987**, *59*, 31A-40A.

- (115) Page, R. H.; Shen, Y. R.; Lee, Y. T. Infrared–ultraviolet double resonance studies of benzene molecules in a supersonic beam. *J. Chem. Phys.* **1988**, *88*, 5362-5376.
- (116) Frisch, M. J.; Trucks, G. W.; Schlegel, H. B.; Scuseria, G. E.; Robb, M. A.; Cheeseman, J. R.; Scalmani, G.; Barone, V.; Mennucci, B.; Petersson, G. A.; et. al. Gaussian 09, revision D.01, Gaussian Inc.: Wallingford, CT, 2009.
- (117) Glendening, E. D.; Landis, C. R.; Weinhold, F. NBO 6.0: Natural bond orbital analysis program. *J. Comput. Chem.* **2013**, *34*, 1429-1437.
- (118) Schmidt, M. W.; Baldridge, K. K.; Boatz, J. A.; Elbert, S. T.; Gordon, M. S.; Jensen, J. H.; Koseki, S.; Matsunaga, N.; Nguyen, K. A.; Su, S.; Windus, T. L.; Dupuis, M.; Montgomery, J. A. General atomic and molecular electronic structure system. *J. Comput. Chem.* **1993**, *14*, 1347-1363.
- (119) Grimme, S.; Waletzke, M. Multi-reference Moller-Plesset theory: computational strategies for large molecules. *Phys. Chem. Chem. Phys.* **2000**, *2*, 2075-2081.
- (120) Ehrlich, S.; Moellmann, J.; Grimme, S. Dispersion-Corrected Density Functional Theory for Aromatic Interactions in Complex Systems. *Acc. Chem. Res.* **2012**, *46*, 916-926.
- (121) Zhao, Y.; Truhlar, D. G. Density Functionals for Noncovalent Interaction Energies of Biological Importance. *J. Chem. Theory Comput.* **2006**, *3*, 289-300.
- (122) Grimme, S. Semiempirical GGA-type density functional constructed with a long-range dispersion correction. *J. Comput. Chem.* **2006**, *27*, 1787-1799.
- (123) Grimme, S.; Ehrlich, S.; Goerigk, L. Effect of the Damping Function in Dispersion Corrected Density Functional Theory. *J. Comput. Chem.* **2011**, *32*, 1456-1465.
- (124) Mardirossian, N.; Head-Gordon, M. How Accurate Are the Minnesota Density Functionals for Noncovalent Interactions, Isomerization Energies, Thermochemistry, and Barrier Heights Involving Molecules Composed of Main-Group Elements? *J. Chem. Theory Comput.* **2016**, *12*, 4303-4325.
- (125) Goto, H.; Osawa, E. CONFLEX 3 evaluation version, JCPE, P40.
- (126) Goto, H.; Osawa, E. Corner flapping: a simple and fast algorithm for exhaustive generation of ring conformations. *J. Am. Chem. Soc.* **1989**, *111*, 8950-8951.
- (127) Goto, H.; Osawa, E. An efficient algorithm for searching low-energy conformers of cyclic and acyclic molecules. *J. Chem. Society Perkin Trans. 2* **1993**, 187-198.
- (128) Boys, S. F.; Bernardi, F. The calculation of small molecular interactions by the differences of separate total energies. Some procedures with reduced errors. *Mol. Phys.* **1970**, *19*, 553-566.
- (129) Su, P.; Li, H. Energy decomposition analysis of covalent bonds and intermolecular interactions. *J. Chem. Phys.* **2009**, *131*, 14102-14115.
- (130) Weinhold, F.; Landis, C. R. *Valency and Bonding: A Natural Bond Orbital Donor-Acceptor Perspective*, Cambridge University Press, 2005.
- (131) Reed, A. E.; Curtiss, L. A.; Weinhold, F. Intermolecular interactions from a natural bond orbital, donor-acceptor viewpoint. *Chem. Rev.* **1988**, *88*, 899-926.
- (132) Meyer, E. A.; Castellano, R. K.; Diederich, F. Interactions with Aromatic Rings in Chemical and Biological Recognition. *Angew. Chem. Int. Ed.* **2003**, *42*, 1210-1250.
- (133) Dean, J. C.; Buchanan, E. G.; Zwier, T. S. Mixed 14/16 Helices in the Gas Phase: Conformation-Specific Spectroscopy of Z-(Gly)_n, n = 1, 3, 5. *J. Am. Chem. Soc.* **2012**, *134*, 17186-17201.
- (134) Buchanan, E. G.; James, W. H.; Choi, S. H.; Guo, L.; Gellman, S. H.; Muller, C. W.; Zwier, T. S. Single-conformation infrared spectra of model peptides in the amide I and

amide II regions: Experiment-based determination of local mode frequencies and inter-mode coupling. *J. Chem. Phys.* **2012**, *137*, 094301.

(135) Leist, R.; Frey, J. A.; Ottiger, P.; Frey, H.-M.; Leutwyler, S.; Bachorz, R. A.; Klopper, W. Nucleobase–Fluorobenzene Interactions: Hydrogen Bonding Wins over π Stacking. *Angew. Chem. Int. Ed.* **2007**, *46*, 7449-7452.

(136) Dauster, I.; Rice, C. A.; Zielke, P.; Suhm, M. A. N–H $\cdots\pi$ interactions in pyrroles: systematic trends from the vibrational spectroscopy of clusters. *Phys. Chem. Chem. Phys.* **2008**, *10*, 2827-2835.

(137) Kumar, S.; Pande, V.; Das, A. π -Hydrogen Bonding Wins over Conventional Hydrogen Bonding Interaction: A Jet-Cooled Study of Indole \cdots Furan Heterodimer. *J. Phys. Chem. A* **2012**, *116*, 1368-1374.

(138) Kumar, S.; Biswas, P.; Kaul, I.; Das, A. Competition between Hydrogen Bonding and Dispersion Interactions in the Indole \cdots Pyridine Dimer and (Indole) $_2\cdots$ Pyridine Trimer Studied in a Supersonic Jet. *J. Phys. Chem. A* **2011**, *115*, 7461.

(139) Hobza, P.; Riehn, C.; Weichert, A.; Brutschy, B. Structure and binding energy of the phenol dimer: correlated ab initio calculations compared with results from rotational coherence spectroscopy. *Chem. Phys.* **2002**, *283*, 331-339.

(140) Pfaffen, C.; Infanger, D.; Ottiger, P.; Frey, H.-M.; Leutwyler, S. N–H $\cdots\pi$ hydrogen-bonding and large-amplitude tipping vibrations in jet-cooled pyrrole-benzene. *Phys. Chem. Chem. Phys.* **2011**, *13*, 14110-14118.

(141) Kumar, S.; Kaul, I.; Biswas, P.; Das, A. Structure of 7-Azaindole \cdots 2-Fluoropyridine Dimer in a Supersonic Jet: Competition between N–H \cdots N and N–H \cdots F Interactions. *J. Phys. Chem. A* **2011**, *115*, 10299-10308.

(142) Lee Lin, J.; Tzeng, W. B. Mass analyzed threshold ionization spectroscopy of 7-azaindole cation. *Chem. Phys. Lett.* **2003**, *380*, 503-511.

(143) Fuke, K.; Yoshiuchi, H.; Kaya, K. Electronic spectra and tautomerism of hydrogen-bonded complexes of 7-azaindole in a supersonic jet. *J. Phys. Chem.* **1984**, *88*, 5840-5844.

(144) Muzangwa, L.; Nyambo, S.; Uhler, B.; Reid, S. A. On π -stacking, C-H/ π , and halogen bonding interactions in halobenzene clusters: Resonant two-photon ionization studies of chlorobenzene. *J. Chem. Phys.* **2012**, *137*, 184307.

(145) Yokoyama, H.; Watanabe, H.; Omi, T.; Ishiuchi, S.-i.; Fujii, M. Structure of Hydrogen-Bonded Clusters of 7-Azaindole Studied by IR Dip Spectroscopy and ab Initio Molecular Orbital Calculation. *J. Phys. Chem. A* **2001**, *105*, 9366-9374.

(146) Pribble, R. N.; Zwier, T. S. Size-Specific Infrared Spectra of Benzene-(H $_2$ O) $_n$ Clusters ($n = 1$ through 7): Evidence for Noncyclic (H $_2$ O) $_n$ Structures. *Science* **1994**, *265*, 75-79.

(147) Zwier, T. S. Laser Spectroscopy of Jet-Cooled Biomolecules and Their Water-Containing Clusters: Water Bridges and Molecular Conformation. *J. Phys. Chem. A* **2001**, *105*, 8827-8839.

(148) Pillsbury, N. R.; Stearns, J. A.; Müller, C. W.; Plusquellic, D. F.; Zwier, T. S. State-specific studies of internal mixing in a prototypical flexible bichromophore: Diphenylmethane. *J. Chem. Phys.* **2008**, *129*, 114301.

(149) Brinckmann, J. In *Collagen: Primer in Structure, Processing and Assembly*; Brinckmann, J., Notbohm, H., Müller, P. K., Eds.; Springer Berlin Heidelberg: Berlin, Heidelberg, 2005, p 1-6.

- (150) Engel, J.; Bächinger, H. P. In *Collagen: Primer in Structure, Processing and Assembly*; Brinckmann, J., Notbohm, H., Müller, P. K., Eds.; Springer Berlin Heidelberg: Berlin, Heidelberg, 2005, p 7-33.
- (151) Raines, R. T. 2005 Emil Thomas Kaiser Award. *Protein Science* **2006**, *15*, 1219-1225.
- (152) Shoulders, M. D.; Raines, R. T. Collagen Structure and Stability. *Annu. Rev. Biochem.* **2009**, *78*, 929-958.
- (153) Bretscher, L. E.; Jenkins, C. L.; Taylor, K. M.; DeRider, M. L.; Raines, R. T. Conformational stability of collagen relies on a stereoelectronic effect. *J. Am. Chem. Soc.* **2001**, *123*, 777-778.
- (154) Bella, J.; Brodsky, B.; Berman, H. M. Hydration structure of a collagen peptide. *Structure*, *3*, 893-906.
- (155) Engel, J.; Chen, H.-T.; Prockop, D. J.; Klump, H. The triple helix \rightleftharpoons coil conversion of collagen-like polytripeptides in aqueous and nonaqueous solvents. Comparison of the thermodynamic parameters and the binding of water to (L-Pro-L-Pro-Gly)_n and (L-Pro-L-Hyp-Gly)_n. *Biopolymers* **1977**, *16*, 601-622.
- (156) Berg, R. A.; Prockop, D. J. The thermal transition of a non-hydroxylated form of collagen. Evidence for a role for hydroxyproline in stabilizing the triple-helix of collagen. *Biochem. Biophys. Res. Commun.* **1973**, *52*, 115-120.
- (157) Erdmann, R. S.; Wennemers, H. Importance of Ring Puckering versus Interstrand Hydrogen Bonds for the Conformational Stability of Collagen. *Angew. Chem. Int. Ed.* **2011**, *50*, 6835-6838.
- (158) Jenkins, C. L.; Bretscher, L. E.; Guzei, I. A.; Raines, R. T. Effect of 3-hydroxyproline residues on collagen stability. *J. Am. Chem. Soc.* **2003**, *125*, 6422-6427.
- (159) Horng, J. C.; Raines, R. T. Stereoelectronic effects on polyproline conformation. *Protein Sci.* **2006**, *15*, 74-83.
- (160) Kuemin, M.; Schweizer, S.; Ochsenfeld, C.; Wennemers, H. Effects of Terminal Functional Groups on the Stability of the Polyproline II Structure: A Combined Experimental and Theoretical Study. *J. Am. Chem. Soc.* **2009**, *131*, 15474-15482.
- (161) Walsh, P. S.; Blodgett, K. N.; McBurney, C.; Gellman, S. H.; Zwier, T. S. Inherent Conformational Preferences of Ac-Gln-Gln-NHBn: Sidechain Hydrogen Bonding Supports a β -Turn in the Gas Phase. *Angew. Chem. Int. Ed.* **2016**, *55*, 14618-14622.
- (162) Kusaka, R.; Zhang, D.; Walsh, P. S.; Gord, J. R.; Fisher, B. F.; Gellman, S. H.; Zwier, T. S. Role of Ring-Constrained γ -Amino Acid Residues in α/γ -Peptide Folding: Single-Conformation UV and IR Spectroscopy. *J. Phys. Chem. A* **2013**, *117*, 10847-10862.
- (163) Shara, M.; Stohs, S. J. Efficacy and Safety of White Willow Bark (*Salix alba*) Extracts. *Phytother. Res.* **2015**, *29*, 1112-1116.
- (164) Vlachoianis, J.; Magora, F.; Chrubasik, S. Willow Species and Aspirin: Different Mechanism of Actions. *Phytother. Res.* **2011**, *25*, 1102-1104.
- (165) Ali, G.; Subhan, F.; Wadood, A.; Khan, A.; Ullah, N.; Islam, N. U.; Khan, I. *Afr. J. Pharm. Pharmacol.* **2013**, *7*, 585-596.
- (166) Mahdi, J. G. *J. Saudi Chem. Soc.* **2010**, *14*, 317-322.
- (167) Mahdi, J. G. Biosynthesis and metabolism of β -d-salicin: A novel molecule that exerts biological function in humans and plants. *Biotechnol. Rep.* **2014**, *4*, 73-79.
- (168) Julkunen-Tiitto, R.; Meier, B. The Enzymatic Decomposition of Salicin and Its Derivatives Obtained from Salicaceae Species. *J. Nat. Prod.* **1992**, *55*, 1204-1212.

- (169) Kong, C.-S.; Kim, K.-H.; Choi, J.-S.; Kim, J.-E.; Park, C.; Jeong, J.-W. Salicin, an Extract from White Willow Bark, Inhibits Angiogenesis by Blocking the ROS-ERK Pathways. *Phytother. Res.* **2014**, *28*, 1246-1251.
- (170) Wölfle, U.; Haarhaus, B.; Kersten, A.; Fiebich, B.; Hug, M. J.; Schempp, C. M. Salicin from Willow Bark can Modulate Neurite Outgrowth in Human Neuroblastoma SH-SY5Y Cells. *Phytother. Res.* **2015**, *29*, 1494-1500.
- (171) Hostanska, K.; Jürgenliemk, G.; Abel, G.; Nahrstedt, A.; Saller, R. Willow bark extract (BNO1455) and its fractions suppress growth and induce apoptosis in human colon and lung cancer cells. *Cancer Detect Prev.* **2007**, *31*, 129-139.
- (172) Preeti, S.; Singh, V. K.; Brahma Deo, S.; Gaurava, S.; Misra, B. B.; Vyasji, T. - Screening and Identification of Salicin Compound from *Desmodium gangeticum* and its In vivo Anticancer Activity and Docking Studies with Cyclooxygenase (COX) Proteins from *Mus musculus*. *Proteomics Bioinform.* **2013**, *6*, 109-124.
- (173) Bonaterra, G. A.; Heinrich, E. U.; Kelber, O.; Weiser, D.; Metz, J.; Kinscherf, R. Anti-inflammatory effects of the willow bark extract STW 33-I (Proaktiv®) in LPS-activated human monocytes and differentiated macrophages. *Phytomedicine* **2010**, *17*, 1106-1113.
- (174) Kumar, S.; Singh, S. K.; Calabrese, C.; Maris, A.; Melandri, S.; Das, A. Structure of saligenin: microwave, UV and IR spectroscopy studies in a supersonic jet combined with quantum chemistry calculations. *Phys. Chem. Chem. Phys.* **2014**, *16*, 17163-17171.
- (175) Dessent, C. E. H.; Geppert, W. D.; Ullrich, S.; Dethlefs, K. M. *Chem. Phys. Lett.* **2000**, *319*, 375-384.
- (176) Talbot, F. O.; Simons, J. P. Sugars in the gas phase: the spectroscopy and structure of jet-cooled phenyl β -D-glucopyranoside. *Phys. Chem. Chem. Phys.* **2002**, *4*, 3562-3565.
- (177) Jockusch, R. A.; Kroemer, R. T.; Talbot, F. O.; Simons, J. P. Hydrated Sugars in the Gas Phase: Spectroscopy and Conformation of Singly Hydrated Phenyl β -d-Glucopyranoside. *J. Phys. Chem. A* **2003**, *107*, 10725-10732.
- (178) Usabiaga, I.; Gonzalez, J.; Arnaiz, P. F.; Leon, I.; Cocinero, E. J.; Fernandez, J. A. Modeling the tyrosine-sugar interactions in supersonic expansions: glucopyranose-phenol clusters. *Phys. Chem. Chem. Phys.* **2016**, *18*, 12457-12465.
- (179) Mons, M.; Robertson, E. G.; Simons, J. P. Intra- and Intermolecular π -Type Hydrogen Bonding in Aryl Alcohols: UV and IR-UV Ion Dip Spectroscopy. *J. Phys. Chem. A* **2000**, *104*, 1430-1437.
- (180) Gosling, M. P.; Pugliesi, I.; Cockett, M. C. R. The role of the methyl group in stabilising the weak N-H $\cdots\pi$ hydrogen bond in the 4-fluorotoluene-ammonia complex. *Phys. Chem. Chem. Phys.* **2010**, *12*, 132-142.
- (181) Hill, J. G.; Das, A. Interaction in the indole...imidazole heterodimer: Structure, Franck-Condon analysis and energy decomposition. *Phys. Chem. Chem. Phys.* **2014**, *16*, 11754-11762.
- (182) Jeng, W.-Y.; Wang, N.-C.; Lin, C.-T.; Chang, W.-J.; Liu, C.-I.; Wang, A. H. J. High-resolution structures of *Neotermes koshunensis* β -glucosidase mutants provide insights into the catalytic mechanism and the synthesis of glucoconjugates. *Acta Crystallogr., Sect. D* **2012**, *68*, 829-838.

